



# Jordan Journal of P H Y S I C S

An International Peer-Reviewed Research Journal

Volume 14, No. 4, December 2021, Jumada-Al-Awwal 1443 H

**Jordan Journal of Physics (JJP):** An International Peer-Reviewed Research Journal funded by the Scientific Research Support Fund, Jordan, and published quarterly by the Deanship of Research and Graduate Studies, Yarmouk University, Irbid, Jordan.

## EDITOR-IN-CHIEF:

**Ibrahim O. Abu Al-Jarayesh**

*Department of Physics, Yarmouk University, Irbid, Jordan.*

[ijaraysh@yu.edu.jo](mailto:ijaraysh@yu.edu.jo)

EDITORIAL BOARD:	ASSOCIATE EDITORIAL BOARD
<p><b>Prof. Nabil Y. Ayoub</b> <i>President, American University of Madaba, Madaba, Jordan.</i> <a href="mailto:nabil.ayoub@gju.edu.jo">nabil.ayoub@gju.edu.jo</a></p> <p><b>Prof. Tareq F. Hussein</b> <i>Department of Physics, The University of Jordan, Amman, Jordan.</i> <a href="mailto:t.hussein@ju.edu.jo">t.hussein@ju.edu.jo</a></p> <p><b>Prof. Marwan S. Mousa</b> <i>Department of Physics, Mu'tah University, Al-Karak, Jordan.</i> <a href="mailto:mmousa@mutah.edu.jo">mmousa@mutah.edu.jo</a></p> <p><b>Prof. Mohammad Al-Sugheir</b> <i>Department of Physics, The Hashemite University, Zarqa, Jordan.</i> <a href="mailto:msugh@hu.edu.jo">msugh@hu.edu.jo</a></p> <p><b>Prof. Abdalmajeid M. Alyassin</b> <i>Department of Physics, Yarmouk University, Irbid, Jordan.</i> <a href="mailto:alyassin@yu.edu.jo">alyassin@yu.edu.jo</a></p> <p><b>Prof. M-Ali H. Al-Akhras (AL-Omari)</b> <i>Department of Physics, Jordan University of Science &amp; Technology, Irbid, Jordan.</i> <a href="mailto:alakmoh@just.edu.jo">alakmoh@just.edu.jo</a></p> <p><b>Prof. Ibrahim A. Bsoul</b> <i>Department of Physics, Al al-Bayt University, Mafrqa, Jordan.</i> <a href="mailto:Ibrahimbsoul@yahoo.com">Ibrahimbsoul@yahoo.com</a></p>	<p><b>Prof. Mark Haggmann</b> <i>Desert Electronics Research Corporation, 762 Lacey Way, North Salt Lake 84064, Utah, U. S. A.</i> <a href="mailto:MHaggmann@NewPathResearch.Com">MHaggmann@NewPathResearch.Com</a></p> <p><b>Dr. Richard G. Forbes</b> <i>Dept. of Electrical and Electronic Engineering, University of Surrey, Advanced Technology Institute and Guildford, Surrey GU2 7XH, UK.</i> <a href="mailto:r.forbes@surrey.ac.uk">r.forbes@surrey.ac.uk</a></p> <p><b>Prof. Roy Chantrell</b> <i>Physics Department, The University of York, York, YO10 5DD, UK.</i> <a href="mailto:roy.chantrell@york.ac.uk">roy.chantrell@york.ac.uk</a></p> <p><b>Prof. Susamu Taketomi</b> <i>2-35-8 Higashisakamoto, Kagoshima City, 892-0861, Japan.</i> <a href="mailto:staketomi@hotmail.com">staketomi@hotmail.com</a></p>

**Editorial Secretary:** Majdi Al-Shannaq.

**Languages Editor:** Haider Al-Momani

**Manuscripts should be submitted to:**

Prof. Ibrahim O. Abu Al-Jarayesh  
Editor-in-Chief, Jordan Journal of Physics  
Deanship of Research and Graduate Studies  
Yarmouk University-Irbid-Jordan  
Tel. 00 962 2 7211111 Ext. 2075  
E-mail: [jjp@yu.edu.jo](mailto:jjp@yu.edu.jo)  
Website: <http://Journals.yu.edu.jo/jjp>

Jordan Journal of  
P H Y S I C S

An International Peer-Reviewed Research Journal

---

Volume 14, No. 4, December 2021, Jumada-Al-Awwal 1443 H

---

INTERNATIONAL ADVISORY BOARD

**Prof. Dr. Ahmad Saleh**

Department of Physics, Yarmouk University, Irbid, Jordan.  
[salema@yu.edu.jo](mailto:salema@yu.edu.jo)

**Prof. Dr. Aurore Savoy-Navarro**

LPNHE Université de Paris 6/IN2P3-CNRS, Tour 33, RdC 4,  
Place Jussieu, F 75252, Paris Cedex 05, France.  
[auore@lphnep.in2p3.fr](mailto:auore@lphnep.in2p3.fr)

**Prof. Dr. Bernard Barbara**

Laboratoire Louis Neel, Salle/Room: D 108, 25, Avenue des  
Martyrs BP 166, 38042-Grenoble Cedex 9, France.  
[Barbara@grenoble.cnrs.fr](mailto:Barbara@grenoble.cnrs.fr)

**Prof. Dr. Bruno Guiderdoni**

Observatoire Astronomique de Lyon, g, avenue Ch. Antre-F-69561,  
Saint Genis Laval Cedex, France.  
[Bruno.guiderdoni@olos.univ-lyon1.fr](mailto:Bruno.guiderdoni@olos.univ-lyon1.fr)

**Prof. Dr. Buford Price**

Physics Department, University of California, Berkeley, CA 94720,  
U. S. A.  
[bprice@berkeley.edu](mailto:bprice@berkeley.edu)

**Prof. Dr. Colin Cough**

School of Physics and Astronomy, University of Birmingham, B15  
2TT, U. K.  
[c.gough@bham.ac.uk](mailto:c.gough@bham.ac.uk)

**Prof. Dr. Desmond Cook**

Department of Physics, Condensed Matter and Materials Physics  
Research Group, Old Dominion University, Norfolk, Virginia  
23529, U. S. A.  
[Dcook@physics.odu.edu](mailto:Dcook@physics.odu.edu)

**Prof. Dr. Evgeny Sheshin**

MIPT, Institutskij per. 9, Dogoprudnyi 141700, Russia.  
[sheshin@lafeet.mipt.ru](mailto:sheshin@lafeet.mipt.ru)

**Prof. Dr. Hans Ott**

Laboratorium fuer Festkorperphysik, ETH Honggerberg, CH-  
8093 Zurich, Switzerland.  
[ott@solid.phys.ethz.ch](mailto:ott@solid.phys.ethz.ch)

**Prof. Dr. Herwig Schopper**

President SESAME Council, Chairman Scientific Board UNESCO  
IBSP Programme, CERN, 1211 Geneva, Switzerland.  
[Herwig.Schopper@cern.ch](mailto:Herwig.Schopper@cern.ch)

**Prof. Dr. Humam Ghassib**

Department of Physics, The University of Jordan, Amman 11942,  
Jordan.  
[humamg@ju.edu.jo](mailto:humamg@ju.edu.jo)

**Prof. Dr. Khalid Touqan**

Chairman of Jordan Atomic Energy Commission, Amman, Jordan.

**Prof. Dr. Nasr Zubeidey**

President: Al-Zaytoonah University of Jordan, Amman, Jordan.  
[President@alzaytoonah.edu.jo](mailto:President@alzaytoonah.edu.jo)

**Prof. Dr. Patrick Roudeau**

Laboratoire de l'Accelérateur, Lineaire (LAL), Université Paris-  
Sud 11, Batiment 200, 91898 Orsay Cedex, France.  
[roudeau@mail.cern.ch](mailto:roudeau@mail.cern.ch)

**Prof. Dr. Paul Chu**

Department of Physics, University of Houston, Houston, Texas  
77204-5005, U. S. A.  
[Ching-Wu.Chu@mail.uh.edu](mailto:Ching-Wu.Chu@mail.uh.edu)

**Prof. Dr. Peter Dowben**

Nebraska Center for Materials and Nanoscience, Department of  
Physics and Astronomy, 255 Behlen Laboratory (10th and R  
Streets), 116 Brace Lab., P. O. Box 880111, Lincoln, NE 68588-  
0111, U. S. A.  
[pdowben@unl.edu](mailto:pdowben@unl.edu)

**Prof. Dr. Peter Mulser**

Institute fuer Physik, T.U. Darmstadt, Hochschulstr. 4a, 64289  
Darmstadt, Germany.  
[Peter.mulser@physik.tu-darmstadt.de](mailto:Peter.mulser@physik.tu-darmstadt.de)

**Prof. Dr. Rasheed Azzam**

Department of Electrical Engineering, University of New Orleans  
New Orleans, Louisiana 70148, U. S. A.  
[razzam@uno.edu](mailto:razzam@uno.edu)

**Prof. Dr. Shawqi Al-Dallal**

Department of Physics, Faculty of Science, University of Bahrain,  
Manamah, Kingdom of Bahrain.

**Prof. Dr. Wolfgang Nolting**

Institute of Physics / Chair: Solid State Theory, Humboldt-  
University at Berlin, Newtonstr. 15 D-12489 Berlin, Germany  
[Wolfgang.nolting@physik.hu-berlin.de](mailto:Wolfgang.nolting@physik.hu-berlin.de)

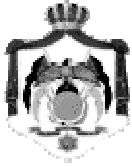
**Prof. Dr. Ingo Hofmann**

GSI Darmstadt, Planckstr. 1, 64291, Darmstadt, Germany.  
[i.hofmann@gsi.de](mailto:i.hofmann@gsi.de)

**Prof. Dr. Jozef Lipka**

Department of Nuclear Physics and Technology, Slovak University  
of Technology, Bratislava, Ilkovicova 3, 812 19 Bratislava,  
Slovakia.  
[Lipka@elf.stuba.sk](mailto:Lipka@elf.stuba.sk)





The Hashemite Kingdom of Jordan



Yarmouk University

Jordan Journal of  
**PHYSICS**

An International Peer-Reviewed Research Journal  
Funded by the Scientific Research Support Fund

**Volume 14, No. 4, December 2021, Jumada-Al-Awwal 1443 H**



## Instructions to Authors

Instructions to authors concerning manuscript organization and format apply to hardcopy submission by mail, and also to electronic online submission via the Journal homepage website (<http://jip.yu.edu.jo>).

### Manuscript Submission

1- **E-mail to** : [jip@yu.edu.jo](mailto:jip@yu.edu.jo)

2- **Online**: Follow the instructions at the journal homepage website.

Original *Research Articles*, *Communications* and *Technical Notes* are subject to critical review by minimum of two competent referees. Authors are encouraged to suggest names of competent reviewers. *Feature Articles* in active Physics research fields, in which the author's own contribution and its relationship to other work in the field constitute the main body of the article, appear as a result of an invitation from the Editorial Board, and will be so designated. The author of a *Feature Article* will be asked to provide a clear, concise and critical status report of the field as an introduction to the article. *Review Articles* on active and rapidly changing Physics research fields will also be published. Authors of *Review Articles* are encouraged to submit two-page proposals to the Editor-in-Chief for approval. Manuscripts submitted in *Arabic* should be accompanied by an Abstract and Keywords in English.

### Organization of the Manuscript

Manuscripts should be typed double spaced on one side of A4 sheets (21.6 x 27.9 cm) with 3.71 cm margins, using Microsoft Word 2000 or a later version thereof. The author should adhere to the following order of presentation: Article Title, Author(s), Full Address and E-mail, Abstract, PACS and Keywords, Main Text, Acknowledgment. Only the first letters of words in the Title, Headings and Subheadings are capitalized. Headings should be in **bold** while subheadings in *italic* fonts.

**Title Page**: Includes the title of the article, authors' first names, middle initials and surnames and affiliations. The affiliation should comprise the department, institution (university or company), city, zip code and state and should be typed as a footnote to the author's name. The name and complete mailing address, telephone and fax numbers, and e-mail address of the author responsible for correspondence (designated with an asterisk) should also be included for official use. The title should be carefully, concisely and clearly constructed to highlight the emphasis and content of the manuscript, which is very important for information retrieval.

**Abstract**: A one paragraph abstract not exceeding 200 words is required, which should be arranged to highlight the purpose, methods used, results and major findings.

**Keywords**: A list of 4-6 keywords, which expresses the precise content of the manuscript for indexing purposes, should follow the abstract.

**PACS**: Authors should supply one or more relevant PACS-2006 classification codes, (available at <http://www.aip.org/pacs/pacs06/pacs06-toc.html>)

**Introduction**: Should present the purpose of the submitted work and its relationship to earlier work in the field, but it should not be an extensive review of the literature (e.g., should not exceed 1 ½ typed pages).

**Experimental Methods**: Should be sufficiently informative to allow competent reproduction of the experimental procedures presented; yet concise enough not to be repetitive of earlier published procedures.

**Results**: should present the results clearly and concisely.

**Discussion**: Should be concise and focus on the interpretation of the results.

**Conclusion**: Should be a brief account of the major findings of the study not exceeding one typed page.

**Acknowledgments**: Including those for grant and financial support if any, should be typed in one paragraph directly preceding the References.

**References**: References should be typed double spaced and numbered sequentially in the order in which they are cited in the text. References should be cited in the text by the appropriate Arabic numerals, enclosed in square brackets. Titles of journals are abbreviated according to list of scientific periodicals. The style and punctuation should conform to the following examples:

### **1. Journal Article:**

- a) Heisenberg, W., Z. Phys. 49 (1928) 619.
- b) Bednorz, J. G. and Müller, K. A., Z. Phys. B64 (1986) 189
- c) Bardeen, J., Cooper, L.N. and Schrieffer, J. R., Phys. Rev. 106 (1957) 162.
- d) Asad, J. H., Hijjawi, R. S., Sakaji, A. and Khalifeh, J. M., Int. J. Theor. Phys. 44(4) (2005), 3977.

### **2. Books with Authors, but no Editors:**

- a) Kittel, C., "Introduction to Solid State Physics", 8<sup>th</sup> Ed. (John Wiley and Sons, New York, 2005), chapter 16.
- b) Chikazumi, S., C. D. Graham, JR, "Physics of Ferromagnetism", 2<sup>nd</sup> Ed. (Oxford University Press, Oxford, 1997).

### **3. Books with Authors and Editors:**

- a) Allen, P. B. "Dynamical Properties of Solids", Ed. (1), G. K. Horton and A. A. Maradudin (North-Holland, Amsterdam, 1980), p137.
- b) Chantrell, R. W. and O'Grady, K., "Magnetic Properties of Fine Particles" Eds. J. L. Dormann and D. Fiorani (North-Holland, Amsterdam, 1992), p103.

### **4. Technical Report:**

Purcell, J. "The Superconducting Magnet System for the 12-Foot Bubble Chamber", report ANL/HEP6813, Argonne Natl. Lab., Argonne, III, (1968).

### **5. Patent:**

Bigham, C. B., Schneider, H. R., US patent 3 925 676 (1975).

### **6. Thesis:**

Mahmood, S. H., Ph.D. Thesis, Michigan State University, (1986), USA (Unpublished).

### **7. Conference or Symposium Proceedings:**

Blandin, A. and Lederer, P. Proc. Intern. Conf. on Magnetism, Nottingham (1964), P.71.

### **8. Internet Source:**

Should include authors' names (if any), title, internet website, URL, and date of access.

### **9. Prepublication online articles (already accepted for publication):**

Should include authors' names (if any), title of digital database, database website, URL, and date of access.

For other types of referenced works, provide sufficient information to enable readers to access them.

**Tables:** Tables should be numbered with Arabic numerals and referred to by number in the Text (e.g., Table 1). Each table should be typed on a separate page with the legend above the table, while explanatory footnotes, which are indicated by superscript lowercase letters, should be typed below the table.

**Illustrations:** Figures, drawings, diagrams, charts and photographs are to be numbered in a consecutive series of Arabic numerals in the order in which they are cited in the text. Computer-generated illustrations and good-quality digital photographic prints are accepted. They should be black and white originals (not photocopies) provided on separate pages and identified with their corresponding numbers. Actual size graphics should be provided, which need no further manipulation, with lettering (Arial or Helvetica) not smaller than 8 points, lines no thinner than 0.5 point, and each of uniform density. All colors should be removed from graphics except for those graphics to be considered for publication in color. If graphics are to be submitted digitally, they should conform to the following minimum resolution requirements: 1200 dpi for black and white line art, 600 dpi for grayscale art, and 300 dpi for color art. All graphic files must be saved as TIFF images, and all illustrations must be submitted in the actual size at which they should appear in the journal. Note that good quality hardcopy original illustrations are required for both online and mail submissions of manuscripts.

**Text Footnotes:** The use of text footnotes is to be avoided. When their use is absolutely necessary, they should be typed at the bottom of the page to which they refer, and should be cited in the text by a superscript asterisk or multiples thereof. Place a line above the footnote, so that it is set off from the text.

**Supplementary Material:** Authors are encouraged to provide all supplementary materials that may facilitate the review process, including any detailed mathematical derivations that may not appear in whole in the manuscript.

## Revised Manuscript and Computer Disks

Following the acceptance of a manuscript for publication and the incorporation of all required revisions, authors should submit an original and one more copy of the final disk containing the complete manuscript typed double spaced in Microsoft Word for Windows 2000 or a later version thereof. All graphic files must be saved as PDF, JPG, or TIFF images.

Allen, P.B., “.....”, in: Horton, G.K., and Muradudin, A. A., (eds.), “Dynamical.....”, (North.....), pp....

## Reprints

Twenty (20) reprints free of charge are provided to the corresponding author. For orders of more reprints, a reprint order form and prices will be sent with the article proofs, which should be returned directly to the Editor for processing.

## Copyright

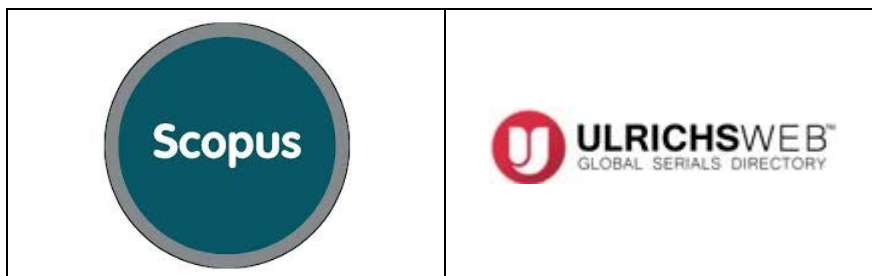
Submission is an admission by the authors that the manuscript has neither been previously published nor is being considered for publication elsewhere. A statement transferring copyright from the authors to Yarmouk University is required before the manuscript can be accepted for publication. The necessary form for such transfer is supplied by the Editor-in-Chief. Reproduction of any part of the contents of a published work is forbidden without a written permission by the Editor-in-Chief.

## Disclaimer

Opinions expressed in this Journal are those of the authors and neither necessarily reflects the opinions of the Editorial Board or the University, nor the policy of the Higher Scientific Research Committee or the Ministry of Higher Education and Scientific Research. The publisher shoulders no responsibility or liability whatsoever for the use or misuse of the information published by JJP.

## Indexing

JJP is currently indexing in:





Jordan Journal of  
P H Y S I C S

An International Peer-Reviewed Research Journal

Volume 14, No. 4, December 2021, Jumada-Al-Awwal 1443 H

Table of Contents:

Articles	Pages
<b>Mid IR Holmium, Praseodymium - doped Fluoride Fiber Laser Pulse Operation</b> Fadi Qamar	275-286
<b>Investigation of the Structural and Magnetic Properties of BaM Hexaferrites Prepared from Scrap Iron Filings</b> Eman S. Al-Hwaitat, Mohammad K. Dmour, Ibrahim Bsoul, Abeer Albgour, Tuqa Alsalti, Raghad Abuawad, Aseel Alajarmah, Rola Al-Buqain and Sami H. Mahmood	287-299
<b>Solution of the Hamilton – Jacobi Equation in a Central Potential Using the Separation of Variables Method with Staeckel Boundary Conditions</b> B. M. Al-Khamiseh, R. S. Hijjawi and J. M. Khalifeh	301-308
<b>The Alpha Particle Doses Received by Students and Staff in Twenty Schools in the North of Hebron Region - Palestine</b> L. A. Mashal, K. M. Thabayneh and M. M. Abu-Samreh	309-316
<b>Single-mode Optical Fiber: An Investigation for the Bending Loss at Wavelength 650 nm</b> Anu Dhupar, Suresh Kumar, Kajal Mittal, Anu, Sanjay K. Sharma, Vandana Sharma and Jatinder K. Sharma	317-322
<b>Applying in-Situ and Laboratory-based Gamma Spectrometry to Determine Activity Concentration and Distribution of <math>^{40}\text{K}</math>, <math>^{226}\text{Ra}</math> and <math>^{232}\text{Th}</math> in Abeokuta, Southwest Nigeria</b> A. O. Mustapha, P. E. Biere, A. E. Ajetunmobi and J. O. Aina	323-331
<b>Calculation of the Electric Quadrupole Moment of <math>^6\text{Li}</math> and <math>^7\text{Li}</math> in Shell Model and Cluster Model</b> Jamshid K. Bizhaem, Nasrin Malekinezhad and Mohammadreza Shojaei	333-338
<b>Study on the Applicability of Varshni Potential to Predict the Mass Spectra of the Quark-Antiquark Systems in a Non-relativistic Framework</b> Etido P. Inyang, Ephraim P. Inyang, Eddy S. William and Etebong E. Ibekwe	339-347
<b>Influence of Solvents on Properties of ZnS Thin Films Synthesized by Chemical Spray Pyrolysis Technique</b> Akintunde A. Ajayi, Aderemi B. Alabi, Olutayo W. Abodunrin, Ibukun S. Akinsola, Olukunle C. Olawole, Abiodun M. Salawu and Adewale Ayeni	349-358
<b>Retrieval of Optical Constants of Undoped Flash-Evaporated Lead Iodide Films from an Analysis of Their Normal Incidence Transmission Spectra Using Swanepoel's Transmission Envelope Theory of Non-Uniform Films</b> Mousa M. A-G. Jafar, Nidal M. Ershaidat, Mais J. A. Ahmad, Mahmoud H. Saleh and Basim N. Bulos	359-378



### Mid IR Holmium, Praseodymium - doped Fluoride Fiber Laser Pulse Operation

**Fadi Qamar**

*Physics Department, Faculty of Sciences, Damascus University, Damascus, Syria.*

**Doi:** <https://doi.org/10.47011/14.4.1>

*Received on: 06/05/2020;*

*Accepted on: 05/11/2020*

---

**Abstract:** Pulsed operation of a novel single-clad mid IR Ho<sup>3+</sup>, Pr<sup>3+</sup> co-doped ZBLAN fiber laser excited by a Nd:YAG laser at 1064 nm has been demonstrated using pulse-pumping. An acousto-optic modulator (AOM) has been used to modulate the CW input pump laser and used in either zero-order or first-order operation. A regular output train of pulses was generated for modulation frequencies over 1 Hz - 100 kHz with zero-order operation of the AOM. A maximum peak power of ~ 50 W and pulse duration of ~200 ns have been obtained for a modulation frequency of 45 kHz and 9.3 W pump power. Single-end and double-end pumping of the first-order AOM operation for the fiber have also been demonstrated to avoid the overheating of the modulator which reduces the modulation efficiency. The same results as the zero AOM operation were obtained when the fiber laser was pumped with a pumping power of about 5 watts.

**Keywords:** Fiber lasers, Pump pulsed operation, Acousto-optic modulator (AOM), Single-end and double-end pumping.

**PACs:** Fiber lasers, 42.55.Wd, Acousto-optical devices, 42.79.Jq.

## Introduction

Pulsed fiber lasers operating near 3 μm hold potential for various sensing [1], spectroscopy [2], metrology [3] and medical [4,5] applications. All studies so far are concerned with pulsed operation of the Er-doped ZBLAN glass fiber laser emitting at 2.7 μm. The first Q-switched Er - ZBLAN laser was reported in [6], where the gain was switched with two different methods; firstly with an acousto-optic modulator (AOM) yielding a pulse length of ~100ns, peak power of 2.2 W and average powers up to 500 μW; secondly with a rotator mirror, producing a minimum pulse width of 270 ns with repetition rates up to 500 Hz. Passive Q-switching of the Er-doped fluoride fiber laser has been demonstrated [7] using an InAs saturable absorber; this yielded a maximum peak power of 1 W and a pulse energy of 1.25 μJ. The pulse intervals in a multi-mode fiber were found to be much longer compared to a single-mode fiber,

indicating better energy storage properties and thus, more efficient Q-switch operation. The limitation of this method was the damage to the InAs absorber at high pump powers. Q-switching of a diode cladding-pumped Er-doped fluoride fiber laser has also been reported [8], with a rotating mirror or an acousto-optic modulator. This generated pulses in the range of 300 - 500 ns, with repetition frequencies between 10 and 136 Hz with the rotating mirror and 1 Hz - 2 kHz with the AOM and produced pulse energies between 1 and 1.5 μJ at an average power of 2 mW (at 2 kHz repetition rate). With these pulse energies, the destruction limit of the fiber was reached.

A pulse-pumped 2.7 μm Er-doped ZBLAN fiber laser has been investigated [9], which was longitudinally pumped by a tuneable, flash-lamp pumped Ti: sapphire pulsed laser operating at a wavelength of around 785 - 795 nm. The

observed relaxation oscillations in the laser output had a peak intensity of approximately 2 kW and a duration of 200 ns when the fiber was pumped by 30 mJ pulses. An energy output of 1.9 mJ at a slope efficiency of 13.5 % with respect to launched pulsed pump energy from a near single transverse mode Er-doped ZBLAN fiber laser was reported. Switching of the output wavelength from 2700 to 2756 and then to 2770 nm was observed in the fiber laser spectrum, attributed to reabsorb losses from the long-lived lower laser level. The limitation of this method is that the output energy is limited by damage of the fiber launch facet due to the short pump-pulse duration. Finally, Q-switched operation of a cladding-pumping Er<sup>3+</sup>/Pr<sup>3+</sup> co-doped ZBLAN fiber laser using mechanical chopper has been demonstrated [10]. A pulse energy of 10 μJ and 250 ns duration were obtained at a relatively low repetition rate of 500 Hz, while a maximum average power of 19 mW was obtained at the higher repetition rate of 19.5 kHz. The maximum power was limited by the switching speed of the pulsed pump and there was no evidence of saturation in the output power due to ASE or ESA. A gain-switched Er:ZBLAN fiber laser based on an active pulsed diode pump system was also reported [11]. The measured pulse duration was 300 ns and nearly independent of the pump repetition frequency. The maximum obtained peak power was 68 W with 2 W of average power at the repetition frequency of 100 kHz. Recently, many Q-switched operations of Er:ZBLAN fiber laser at 2.8 μm using different methods such as acousto-optic modulator [12] and topological insulator Bi<sub>2</sub>Te<sub>3</sub> nanosheets [13] were demonstrated. On the other hand, CW operation of Ho<sup>3+</sup> and Ho<sup>3+</sup>, Pr<sup>3+</sup>-doped ZBLAN fiber lasers has been reported; these are alternative and efficient lasers emitting at 2.85 - 2.87 μm and have been pumped by 1.1 μm or 1064 nm lasers [14-16]. Passively Q-switched Ho<sup>3+</sup>-doped fluoride fiber laser using Fe<sup>2+</sup>:ZnSe crystal and graphene saturable absorbers was latterly reported [17] and 800 ns pulses at 2.93 μm with an energy of 460 nJ and a repetition rate of 105 kHz were obtained. A diode-cladding-pumped mid-infrared passively Q-switched Ho<sup>3+</sup>-doped fluoride fiber laser using a broad band semiconductor saturable mirror (SESAM) was also demonstrated [18]. Maximum pulse energy of 6.65 μJ with a pulse

width of 1.68 μs at a repetition rate of 47.6 kHz was produced at a slope efficiency of 12.1 % with respect to the launched pump power and center wavelength of 2.971 μm. Actively Q-switched Ho<sup>3+</sup>, Pr<sup>3+</sup>-doped fluoride fiber laser by a TeO<sub>2</sub> acousto-optic modulator, producing a peak power of 77 W, with a pulse width of 78 ns and a slope efficiency of 20 % with respect to the launched pump power was achieved. The modulator allowed continuous tunability of the pulse repetition frequency from 40 to 300 kHz and the fibre pumped 1150 nm diode laser [19].

In this paper, the first description of pulsed operation of an Ho<sup>3+</sup>, Pr<sup>3+</sup>-doped ZBLAN fiber laser emitting at 2.874 μm is reported using low peak power pulse pumped excitation by a 1064 nm Nd: YAG laser. The modulation of the CW input power was controlled by an AOM, which allowed variation of the duration and energy of the pump to obtain optimum gain switched laser. In addition, double-end pumping with CW input into one end has been used to create a gain pedestal onto which the pulsed excitation is impressed.

## Experimental

The fiber laser used was a heavily doped single-clad fluoride fiber, manufactured by Fiber-labs, Japan, with concentrations of 30000 ppm molar Ho and 3000 ppm molar Pr. The fiber had a core diameter of 15 μm supporting single mode operation, a numerical aperture (NA) of 0.13 and an intrinsic loss of ~ 30 dB/km at 800 nm. The fiber was pumped by 10 W single transverse mode vertically polarized Nd: YAG laser output operating at 1064 nm. A polarization-insensitive bulk TeO<sub>2</sub> Bragg cell acousto-optic modulator (AOM, NEOS Model N36027) was used to modulate the input beam. The AOM modulator system had the following crystal specifications: transmission of ~93 % and efficiency (loss modulation) of > 50 % at 1064 nm, active aperture of 5 mm, extinction ratio of -76 dB, able to be driven up to 27 MHz and rise/fall times of 182/40 ns and opening times in the order of 50 ns to few microseconds.

The experimental setups are shown in Fig. 1.

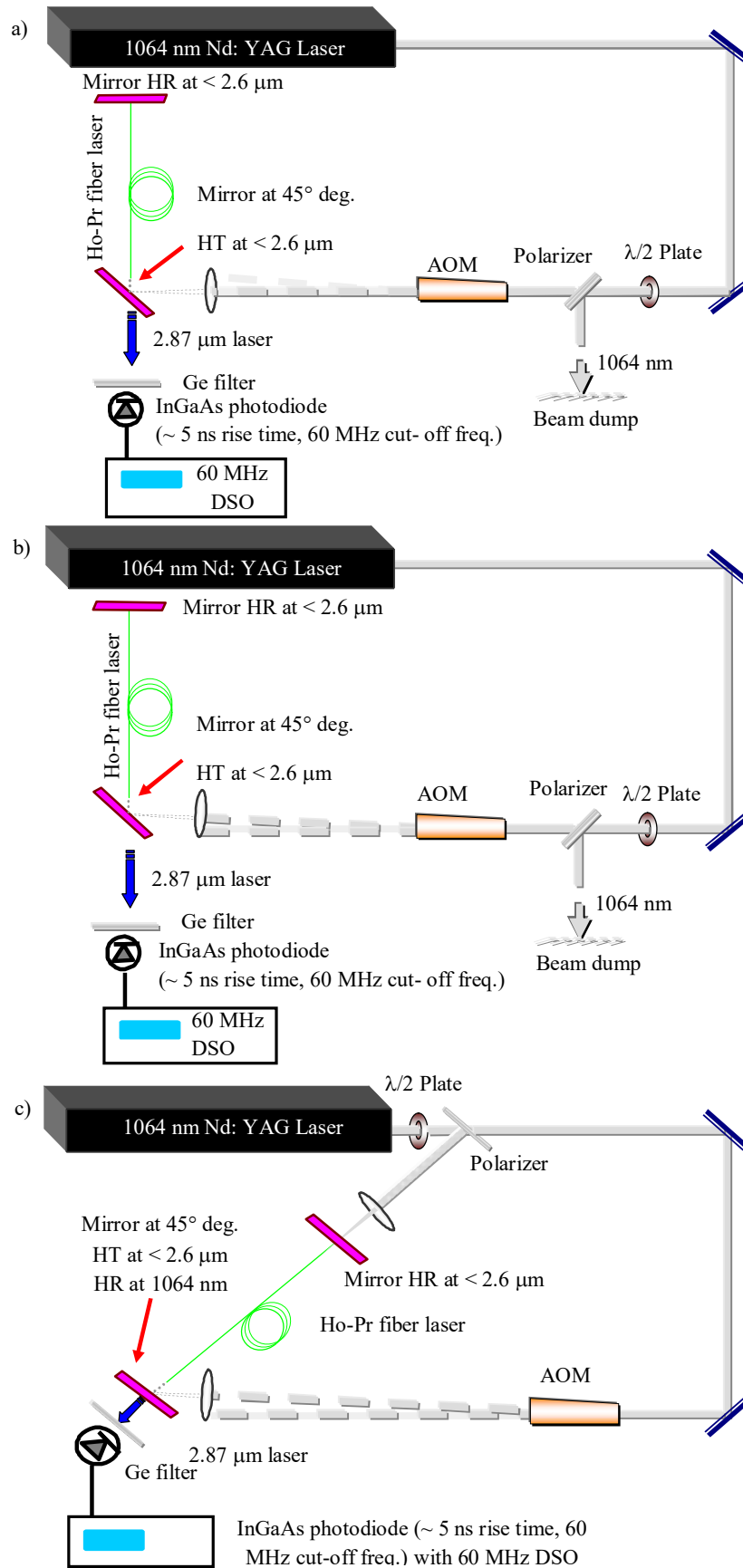


FIG. 1. Experimental setups for pulse pumping a single-clad  $\text{Ho}^{3+}$ ,  $\text{Pr}^{3+}$  co-doped ZBLAN fiber laser. a) zero-order AOM operation, b) first-order AOM operation, c) first-order AOM operation with simultaneous CW pumping of the second fiber facet.

Three different designs have been used to suit different forms of fiber laser operation. Fig. 1a shows the experimental configuration with zero-order operation of the AOM. The modulated beam was focused by an objective lens with NA of 0.25 and reflected by a 45° dichroic mirror for launching into the fiber. The dichroic mirror was HR (~99 %) at the pump wavelength and HT (~97 %) with an anti-reflection coating at the lasing wavelength. The distal facet of the fiber was butted with a mirror HR at both the pump and lasing wavelengths, so that the cavity consisted of Fresnel reflection and a highly reflecting mirror. The output temporal profile of the laser was measured using an unamplified, liquid nitrogen-cooled InAs photodiode (Judson J12D) with a response time of approximately 2 ns, connected to a 60 MHz digital storage oscilloscope (Tektronix TDS210). A Ge filter before the detector was required to eliminate the input pump. Fig. 1b shows a similar design, but with first-order operation of the AOM, where the diffracted light is launched into the fiber. In Fig. 1c, the setup is re-arranged to be double end-pumped, allowing a low intensity of CW pump light into the second facet of the fiber. A focusing lens with NA 0.25 has been used to launch the reflected pump light transmitting from the polarizer into the second facet of the fiber which butted to a mirror; this was HT at the pump wavelength and HR at lasing wavelength. The half wave plate and the polarizer in these arrangements have been used to control the pump power as well as to control the double-end pumping in the third design.

## Pulsed Fiber Laser Operation, Results and Discussions

### Zero-order AOM Operation

The zero-order operation of the AOM was applied in the first experiment, where the laser intensity built up with the AOM in the off position allowing all the input power to be launched into the fiber. On the other hand, when the modulator switched to the on position, more than 50 % of the input power was diffracted with the remainder being transmitted to be stored inside the fiber until it was released as a narrow pulse. The method required the AOM to be kept in the on position for a period of time determined

by the modulation frequency, so that power was stored inside the fiber and then it was switched to the off position for another period of time (defining the opening time). This was determined experimentally by adjusting the modulated pump pulse width from the pulse generator to avoid multi-pulse emissions and thus produce single, short, high-peak power pulses and hence achieve efficient pulsed emission. The opening time was adjusted dependent on the length of the fiber as well as on the doping concentration and pump power.

Fig. 2a shows that the opening time decreased for shorter lengths. For a shorter length of fiber, a greater energy density can be stored (at the same time) compared with a longer fiber. As the amount of stored energy increased, the time required to achieve the population inversion inside the fiber decreased so that a reduced opening time was required. Fig. 2b shows that a shorter opening time is necessary for a single pulse to be produced when more pump power is used. Increasing the input power leads to faster development of population inversion and reduced radiative loss from the fiber, thus a shorter opening time is required to avoid multiple-pulse emission.

The peak power and pulse duration were also studied as a function of the modulation frequency for two fiber lengths of 12 m and 9.25 m (which is the optimum length of the CW process) pumped by a 9.3 watt laser beam, as shown in Fig. 3a and Fig. 3 b.

Comparing the behavior shown in these figures, it can be deduced that the peak power of the pulses increased and the pulse duration decreased when shorter length fiber or higher pump power was used. Individually, each fig. shows that changes in the duration and the peak power are small for low modulation frequencies, while they increase at high frequency towards 40 - 45 kHz and then decrease again. This suggests that the system is most efficient when the modulation frequency is in the range of the relaxation oscillation frequency of the system, which is between 40 - 80 kHz. The range of the relaxation oscillation frequency was measured for the long opening period of AOM. The shorter pulse duration of 200 ns, the higher peak power ~ 50 W with about 93 % pulse-to-pulse stability and average

power of 450 mW were obtained for the 9.25 m fiber length and at a modulation frequency of 45 kHz, as shown in Fig. 4.

However the optimum length of the fiber for pulsed operation has not been determined in this experiment. This method has the advantage that no extra components are required inside the cavity to achieve the pulsed operation; it is

straight forward to operate and align and leads to achieve a compact pulsed fiber system, especially when combined with diode pumping. On the other hand, a disadvantage of this method is that high-efficiency pulsing occurs for higher modulation frequencies, even though the pulsing starts at a low repetition rate (1 Hz).

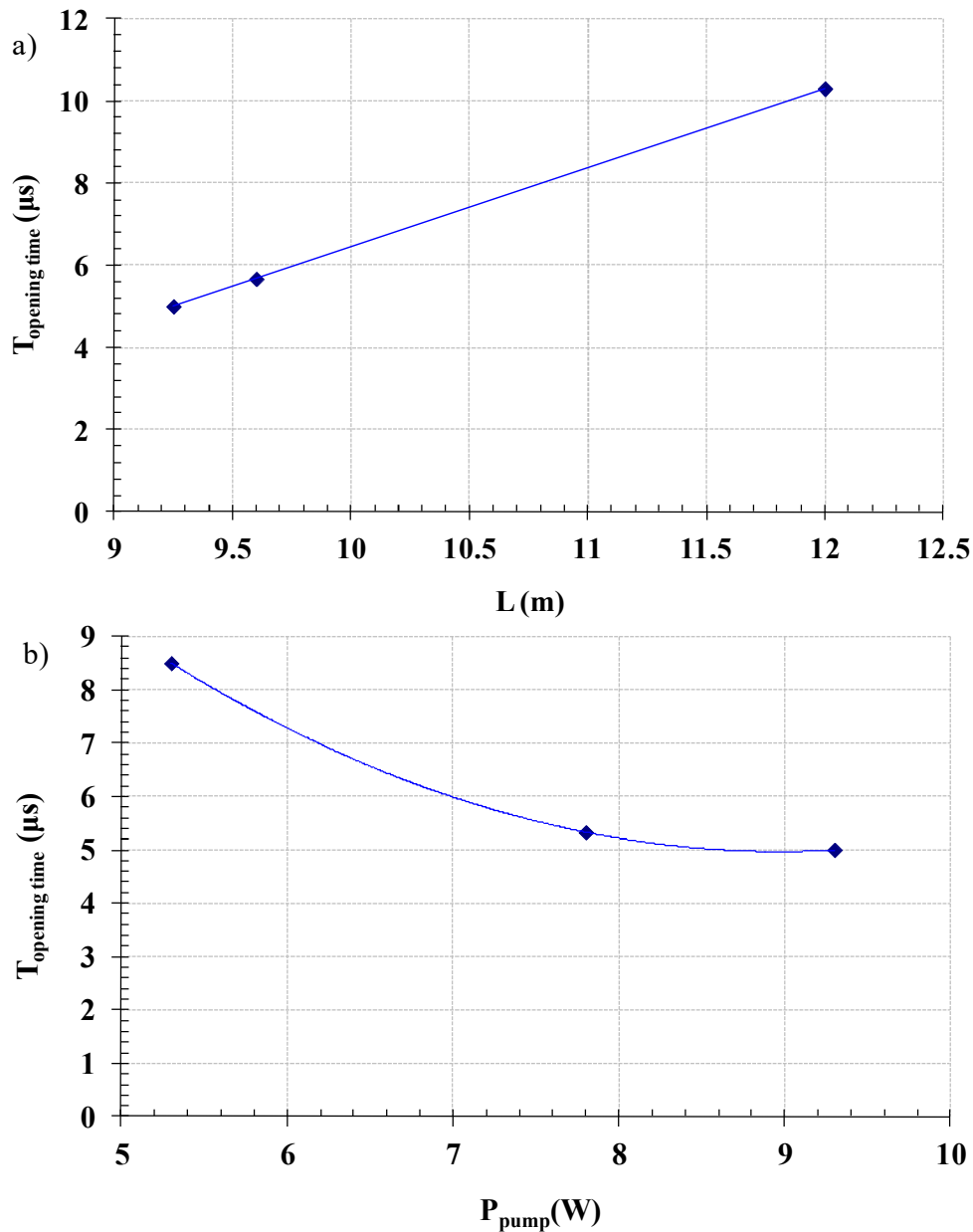


FIG. 2. Opening time of zero-order AOM operation required to produce a single pulse at 50 kHz modulation frequency as a function of a) fiber length and b) pump power.

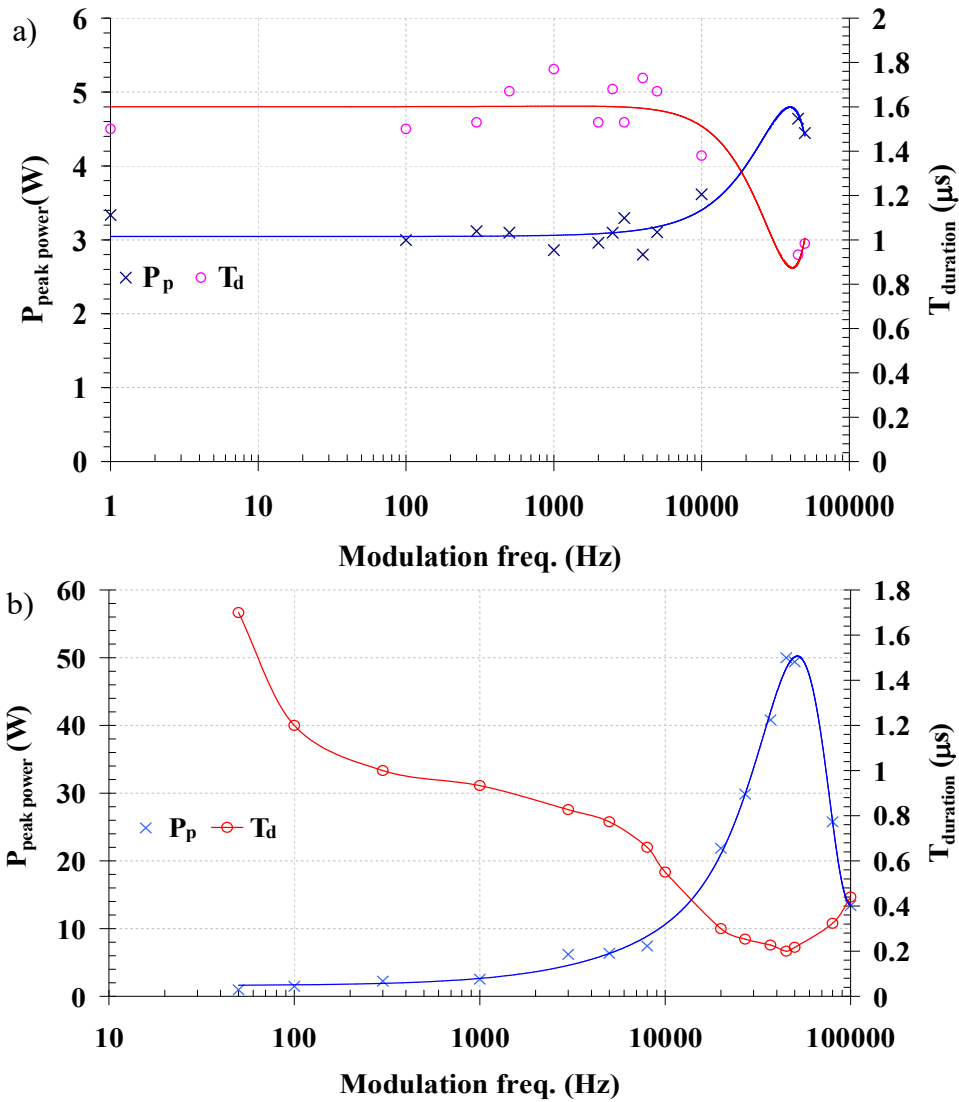


FIG. 3. Peak power and pulse duration as a function of modulation frequency for zero-order AOM operation and for a) 12 m fiber length and 9.3 W pump power and b) 9.25 m fiber length and pump power of 9.3 W.

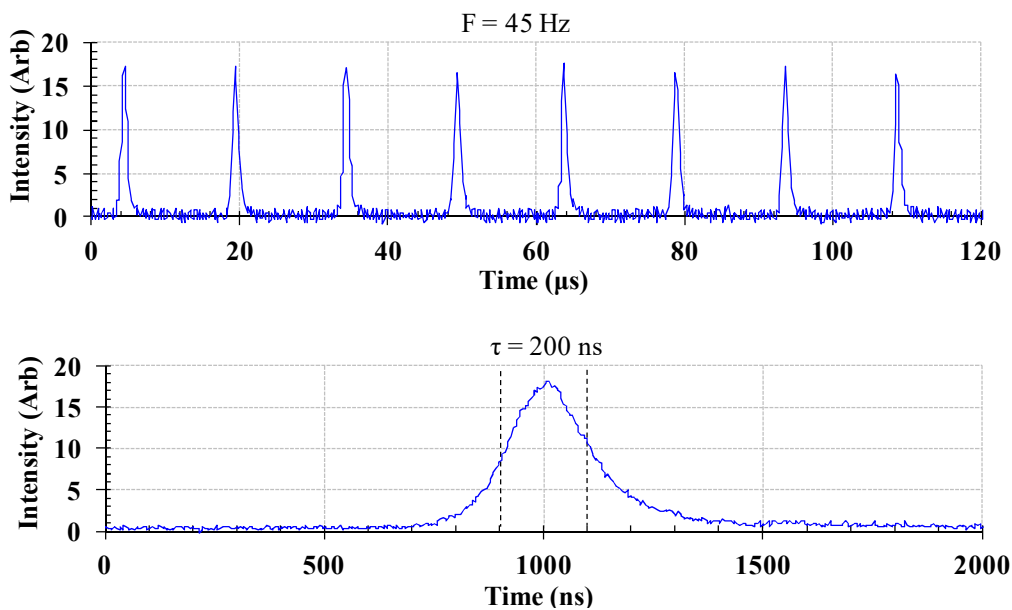


FIG. 4. A pulse train for zero-order AOM operation with modulation frequency of 45 kHz; the duration of each pulse is 200 ns.

### First-order AOM Operation

Operating the AOM in zero-order results in overheating of the modulator, which reduces the modulation efficiency and thus cooling is required. Another major disadvantage is that, in this mode, the stored power (non - diffracted power) cannot be controlled separately, unless the input power is reduced or a longer fiber is used. Both solutions will lower the overall efficiency of the laser. Controlling the amount of non-diffracted power is important in order to avoid simultaneous CW and pulsed lasing, as well as to prevent extra pulses to be created in between the main switched pulses. However, the amount of non-diffracted power also affects the pulse-to-pulse stability and needs to be adjusted for high stability.

The dependence of efficient and stable pulse operation on the stored energy was demonstrated experimentally using first-order operation of the AOM with single-end pumping (SEP) and with double-end pumping (DEP). The simultaneous pumping into the second end was used to vary the energy that was stored in the fiber.

In first-order operation without DEP, only the diffracted power is launched into the fiber, so that pumping of the fiber will occur when the modulator is on and the time required for lasing depends on the build-up time of the laser intensity and on the modulation frequency. Thus, the opening time should be adjusted each time the modulation frequency changes to obtain a single pulse train. The value of the opening time as a function of modulation frequency has been measured for the 13.25 m and 9.25 m fiber lengths, as shown in Fig. 5. For the 13.25 m fiber, Fig. 5a, the opening time for 1Hz modulation frequency was 480  $\mu$ s, while it was only 16  $\mu$ s at a modulation frequency of 50 kHz. In comparison, for the 9.25 m length, the opening time becomes 300  $\mu$ s at 1 Hz and 8  $\mu$ s at 50 kHz modulation frequency. Thus, using a shorter fiber results in reduction of the opening time; that is because the energy density which is required for pulse operation in a short fiber is less than the energy required for a longer fiber.

Fig. 5b shows the comparison between first-order operation when there is no CW pumping of the second facet of the fiber and when this end is pumped by a 300 mW CW laser beam. It shows

that the pumping of both ends helped stabilize the output and fixed the opening time that was required for pulsed operation at one value of  $\approx 8 \mu$ s for all modulation frequencies.

As a result, pumping both ends of the fiber increases stored energy in the fiber which, without second facet pumping (SEP) in first-order AOM operation, depends only on the length of the modulated pulse which is diffracted from the AOM. The power which is pumped into the second facet has the same function as the CW leakage power in zero-order operation under AOM-on operation. To observe the effect of CW power pumping on the performance of the system, the power pumped into the second facet of the fiber (SEP) has been changed when using a short fiber with 1.5 m length (Fig. 6). It was found that, with SEP, a pure CW output was obtained, Fig. 6a. Applying a small degree of second facet pumping (SFP) power resulted in pulsed operation of the system. A train of pulses has been obtained for feedback power up to 2W and 5 kHz modulation frequency, Fig. 6b. Providing more SFP resulted in a multiple pulsing train, Fig. 6c; further increase in SFP leads to quasi-CW operation, Fig. 6d and then to CW operation of the output, Fig. 6e.

The peak power and pulse duration have been measured as a function of modulation frequency for both conditions; first-order operation without SFP and with 300 mW SFP pump. A fiber length of 9.25 m has been used, which is near to the optimum length for CW operation when the pump power was 9.3 W. Maximum peak pulse powers of 3.3 W and 2.7 W, minimum pulse durations of 1.01  $\mu$ s and 1.03  $\mu$ s, as well as average powers of 211 and 266 mW have been obtained for operation with 300 mW SFP and without SFP, respectively. The last result suggests that the amount of the modulation loss should be chosen carefully to ensure successful pulsed operation, especially if the AOM will be used in transmission (zero-order) mode of operation.

Fig. 7 shows that the peak power of the pulse improved with SFP, provided the pulse duration is nearly the same. Pulse-to-pulse stability ratios with and without SFP were 95 % and 92.5 %, respectively.

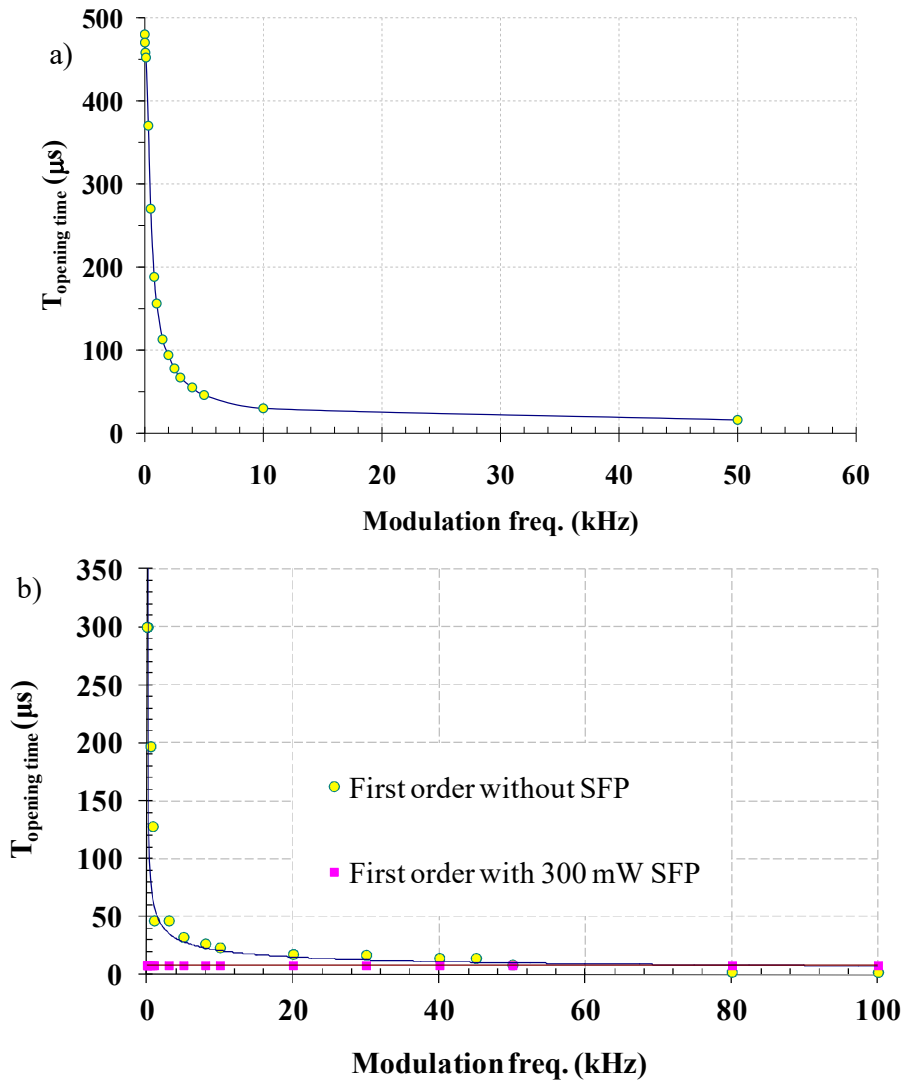


FIG. 5. Opening time as a function of frequency modulation for first-order AOM operation, (a) 13.25 m fiber length, b) 9.25 m fiber length, without second facet pumping (SFP) and with 300 mW SFP.

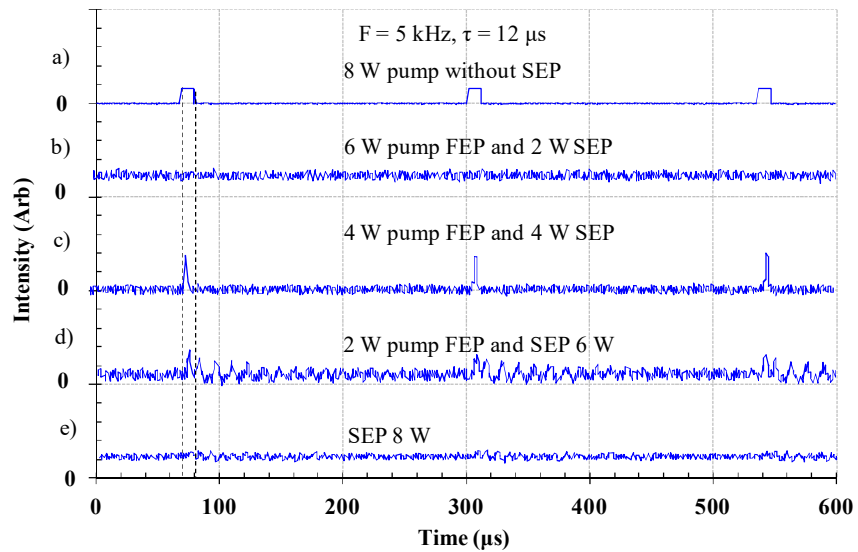


FIG. 6. Temporal profiles of the output of the laser for changes in the degree of double-end pumping, first-order AOM operation for fiber length of 1.5 m. a) CW output, when small opening time is applied with single-end pumping (SEP), b) train of pulses when less than 2 W second facet pumping (SFP) is applied, with 6 W first-end pumping (FEP), c) train of relaxation oscillations for 4W SFP, d) quasi-CW and e) CW output with less than 6W SFP pumping.

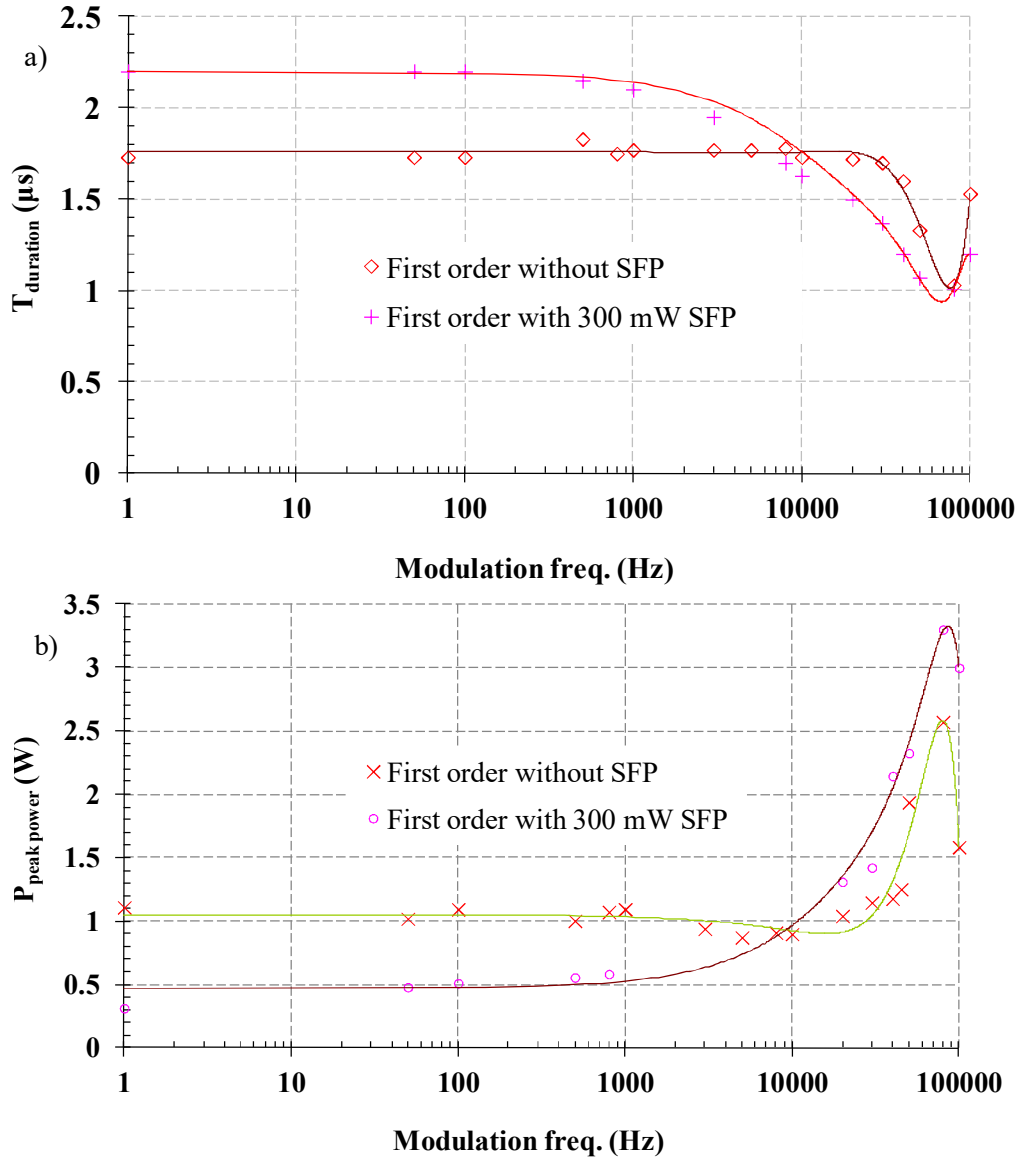


FIG. 7. The comparison between a) pulse durations and b) peak powers as a function of modulation frequency for first-order AOM operation with 300 mW SFP and without SFP, respectively.

Fig. 8 shows a typical pulse train with modulation frequency of 80 kHz and a single-pulse duration of 1.01  $\mu\text{s}$ . A train of short-duration sub-pulses was found within the main pulses. The study of self-locking in this fiber is out of the scope of this paper and will be reported in detail in another paper.

Since only  $\sim 50\%$  of the pump power is diffracted in first-order AOM operation, the first-order AOM results were comparable to the zero-order AOM results when the fiber was pumped at  $\sim 5$  W (Fig.9).

The highest peak power and the lowest pulse duration values for the first-order AOM operation, when pumped at  $\sim 9$  W with SFP of 300mW, are found to be consistent with the

values obtained for zero-order AOM operation when pumped at 5 W; however, a higher modulation frequency is required to reach these values in first-order AOM operation.

With pulsed pumping, the fiber laser output is, in general, characterized by a series of relaxation oscillations which, at a certain launched pump energy, show good pulse-to-pulse reproducibility. The  $1/e$  damping time of these oscillations can be given as [20]:

$$\tau_{\text{damping}} = (\tau_{\text{ul}} / r) \quad (1)$$

where  $r$  is the pump-to-threshold ratio and  $\tau_{\text{ul}}$  is the lifetime of the upper laser level. The upper laser level lifetime is  $\sim 300$   $\mu\text{s}$  and the pump ratio  $r$  is assumed to be 16 for zero-order AOM operation, so that  $\tau_{\text{damping}} \sim 18.7$   $\mu\text{s}$ . This value is

in the range of the values found experimentally of between 15 - 22  $\mu\text{s}$ . Thus, from Eq. (1), stronger pumping shows fast decay until, for a certain pump power, the output becomes CW. The reduction in pump power can be achieved by reducing the opening time  $T_{\text{ot}}$ . The pulsed behaviour of the laser can be well understood by comparing the opening time of the AOM with the pulse build-up time  $T_{\text{bu}}$  after the switch is opened.  $T_{\text{bu}}$  can be calculated by [21]:

$$T_{\text{bu}} \approx (25 \pm 5) \tau_c / (r-1) \tag{2}$$

Here,  $\tau_c$  is the round-trip period, which is about 93 ns for a fiber laser length of 9.25 m. The build-up time for the previous length of the fiber is in the range of  $\approx 0.155 \mu\text{s}$  and shows good agreement with the experimental results, which are in the range of 0 - 2  $\mu\text{s}$ , dependent on the modulation frequency.

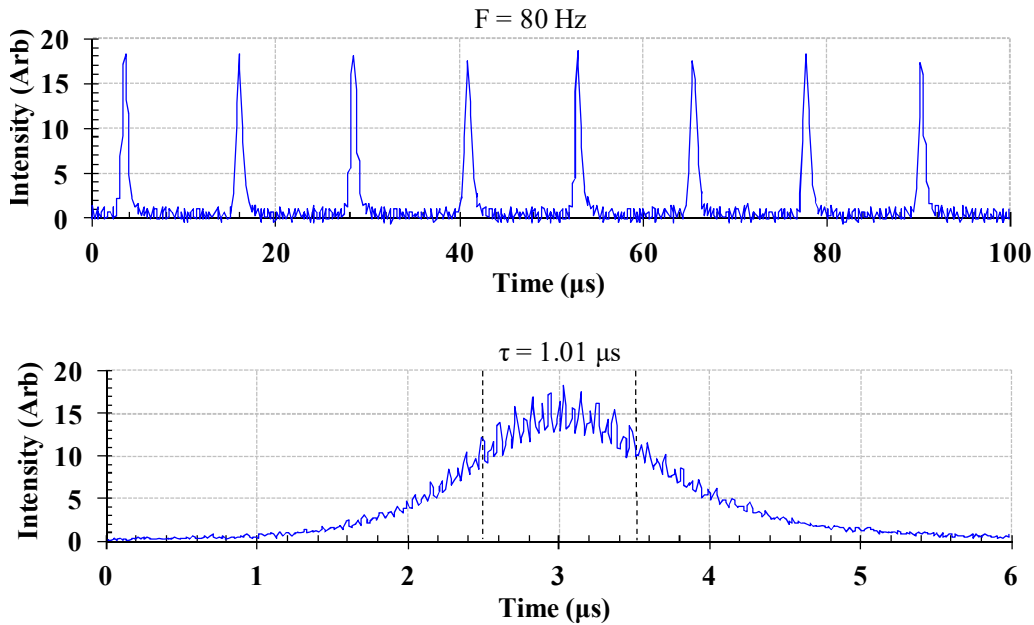


FIG. 8. Temporal profiles for first-order AOM operation: a pulse train with a modulation frequency of 80 kHz and a single pulse with a duration of 1.01  $\mu\text{s}$ .

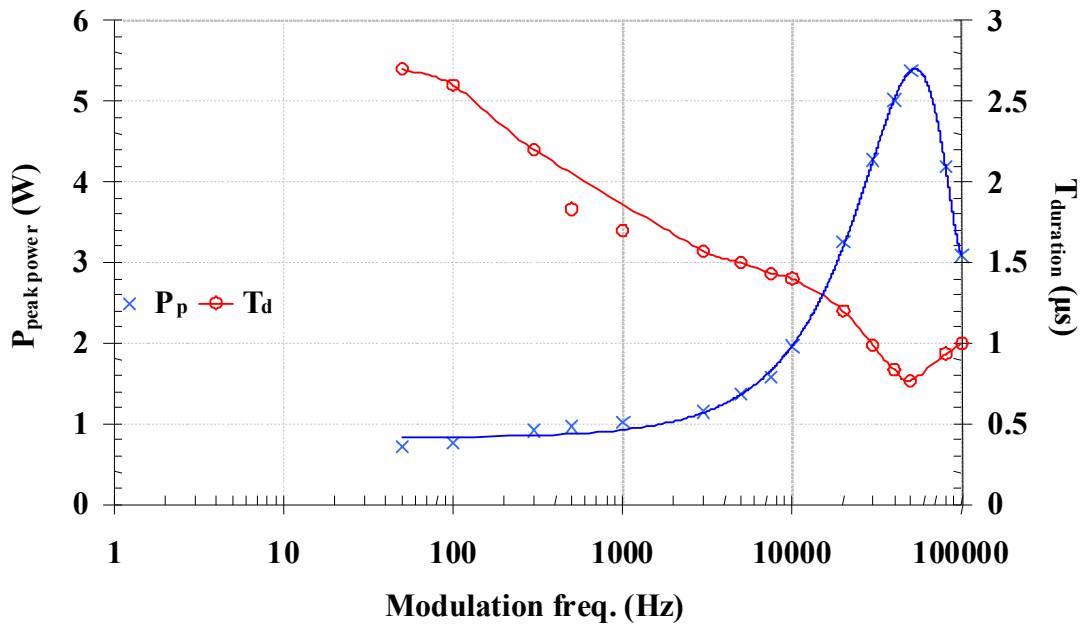


FIG. 9. Peak power and pulse duration as a function of modulation frequency for zero-order AOM operation and for 9.25 m and 5 W pump power.

For opening times longer than the build-up time,  $T_{ot} > T_{bu}$ , and shorter than the damping time, the formation of the pulse is undisturbed and smooth gain-switched pulses are generated. Multiple pulses or relaxation-oscillation pulses with and without CW in the output appear for opening times longer than the damping time. When the opening time is equal to, or slightly shorter than the build-up time,  $T_{ot} \leq T_{bu}$ ; i.e., a critical opening time, a high-intensity pulse does not have enough time to form and, in consequence, pulses with unstable and reduced amplitude are emitted. The critical opening time is equal to the build-up time and is defined very sharply and can be measured within  $\pm 5 - 10$  % accuracy. The build-up time increases at higher repetition rate due to the reduction in the population inversion induced by the pumping light [22]. At low repetition rates (below 40 kHz), the build-up time for a particular cavity configuration remains nearly constant due to the effect of population inversion saturation.

Acousto-optic modulation (AOM) to switch the cavity finesse has been the preferred method of Q-switching in fiber laser and has been used in one of two configurations, zero- or first-order modes. Such modulators offer the advantage of short switching times and electronic control of both the repetition rate and mark-to-space ratio. Their main disadvantage is limited diffraction efficiency, resulting in an increase in the transmitted pump power (CW base intensity) for zero-order operation when the modulator is set to the on position (i.e., almost the light should be diffracted outside the fiber); this transmitted power might become sufficient to set off CW lasing. The pump power must therefore be kept low enough to avoid CW lasing, thus effectively putting an upper limit on the maximum energy and peak power of the gain-switched pulses. First-order operation of the AOM is one effective solution to this problem, but in this case, suppression of CW oscillation is bought at the expense of significantly increased loss in launched power. In the zero-order

configuration, the loss is due just to the transmission loss of the modulator, of order of 0.3 dB. In the first-order configuration, the loss is given by the product of the transmission loss and the diffraction efficiency, of the order of 3.3 dB. Since the stored power comes only from the diffracted light, then more input power is needed to reach the lasing threshold. Providing SFP is an effective solution to lower the threshold and improve the pulsed efficiency. First-order operation offers another advantage that the AOM is on only for a small fraction of time. This narrow time window reduces problems associated with thermal effects in the acousto-optic material, which have been seen in this system under zero-order operation.

## Conclusion

A novel single-clad  $\text{Ho}^{3+}$ ,  $\text{Pr}^{3+}$  co-doped ZBLAN fiber laser pumped by a CW Nd: YAG laser at 1064 nm has been pulsed using pulse pump extraction. An AOM with a modulation efficiency of more than 50 % at 1064 nm has been utilized to modulate the CW pump. The AOM is able to generate modulated pulses ranging from a few ns to sub-ms at frequencies from 1Hz to 27 MHz. Operation of the AOM in zero order and in first-order has been demonstrated. A train of pulses of 200 ns duration, 50 W peak power and 450 mW average power at 45 kHz modulation frequency has been obtained for zero-order operation and an un-optimized fiber length of 9.25 m. No evidence of secondary pulses or CW lasing in zero-order AOM operation has been observed, suggesting that the pump power is completely absorbed inside the fiber and there is no need for further reduction in the pump power to avoid multiple pulsing. Pumping of both facets of the fiber in first-order AOM operation has been used to determine the best ratio between the modulated pump pulse and the CW base intensity of the pump power that is required for efficient pulsed operation.

## References

- [1] Bawden, N., Matsukuma, H., Henderson-Sapir, O., Klantsataya, E., Tokita, S. and Ottaway, D.J., *Optics Letters*, 43 (11) (2018) 2724.
- [2] Tittel, F.K., Richter, D. and Fried, A., *Topics Appl. Phys.*, 89 (2003) 445.
- [3] Keilmann, F. and Amarie, S., *Journal of Infrared, Millimeter and Terahertz Waves*, 33 (2012) 479.
- [4] Petersen, C.R., Møller, U., Kubat, I., Zhou, B.S., Dupont, Ramsay, J., Enson, T., Sujecki, S., Abdel-Moneim, N., Tang, Z., Furniss, D., Seddon, A. and Bang, O., *Nature Photonics*, 8 (2014) 830.
- [5] Abu-Sardana, S.O., Subramaniam, C., Abbasi, S. and Haji Reza, P., *Proceedings, Photons Plus Ultrasound: Imaging and Sensing*, 11240 (2020).
- [6] Frerichs, C. and Tauermaun, T., *Electron. Lett.*, 30 (1994) 706.
- [7] Frerichs, C. and Unrau, U.B., *Opt. Fib. Tech.: Mat., Dev. and Sys.*, 2 (1996) 358.
- [8] Huber, T., Luthy, W., Weber, H.P. and Hochstrasser, D.F., *Opt. and Quantum Electron.*, 31 (1999) 1171.
- [9] Dickinson, B.C., Golding, P.S., Jackson, S.D. and King, T.A., *Conference on Lasers and Electro-Optics (CLEO 2000). Technical Digest*, 39 (2000) 77.
- [10] Coleman, D.J., King, T.A., Do-Kyeong, K. and Jongmin, L., *Opt. Commun.*, 236 (2004) 379.
- [11] Gorjan, M., Petkovšek, R., Marinček, M. and Čopič, M., *Opt. Lett.*, 36 (2011) 1923.
- [12] Tokita, M., Murakami, M., Shimizu, S., Hashida, M. and Sakabe, S., *Opt. Lett.*, 36 (2011) 2812.
- [13] Tang, P., Wu, M., Wang, Q., Miao, L., Huang, B., Liu, J., Zhao, C. and Wen, S., *IEEE Photonics Technology Lett.*, 28 (2016) 1573.
- [14] Sumiyoshi, T., Sekita, H., Arai, T., Sato, S., Ishihara, M. and Kikuchi, M., *IEEE J. Select. Top. in Quantum Electron.*, 5 (1999) 936.
- [15] Jackson, S.D., *Opt. Lett.*, 29, (2004) 334.
- [16] Qamar, F.Z., King, T.A., Jackson, S.D. and Tsang, Y.H., *Journal of Light-wave Tech.*, 23 (2005) 4315.
- [17] Zhu, G., Zhu, X., Balakrishnan, K., Norwood, R.A. and Peyghambarian, N., *Opt. Matt. Exp.*, 3 (2013) 1365.
- [18] Li, J.F., Luo, H.Y., He, Y.L., Liu, Y., Zhang, L., Zhou, K.M., Rozhin, A.G. and Turistyn, S.K., *Las. Phys. Lett.*, 11 (2014) 065102.
- [19] Hu, T., Hudson, D.D. and Jackson, S.D., *Opt. Lett.*, 38 (2012) 2145.
- [20] Siegman, A.E. "Lasers". (Oxford: Oxford University Press, 1986) p. 414.
- [21] Morkel, P.R., Jdrzejewski, K.P., Taylor, E.R. and Payne, D.N., *IEEE Photon. Tech. Lett.*, 4 (1992) 545.
- [22] Myslinski, P., Chrostowski, J., Koningstein, J.A. and Simpson, J.R., *IEEE J. Quantum Electron.*, 28 (1992) 371.

### Investigation of the Structural and Magnetic Properties of BaM Hexaferrites Prepared from Scrap Iron Filings

Eman S. Al-Hwaitat<sup>a</sup>, Mohammad K. Dmour<sup>a</sup>, Ibrahim Bsoul<sup>b</sup>, Abeer Albgour<sup>a</sup>, Tuqa Alsalti<sup>a</sup>, Raghad Abuawad<sup>a</sup>, Aseel Alajarmah<sup>a</sup>, Rola Al-Buqain<sup>c</sup> and Sami H. Mahmood<sup>a,d</sup>

<sup>a</sup> Physics Department, The University of Jordan, Amman 11942, Jordan.

<sup>b</sup> Physics Department, Al al-Bayt University, Al-Mafraq 13040, Jordan.

<sup>a</sup> The Cell Therapy Center, The University of Jordan, Amman 11942, Jordan.

<sup>b</sup> Department of Physics and Astronomy, Michigan State University, East Lansing, MI 48824, USA.

**Doi:** <https://doi.org/10.47011/14.4.2>

Received on: 07/05/2020;

Accepted on: 12/11/2020

---

**Abstract:** In this work, we demonstrate the feasibility of preparing a commercially important type of magnetic oxide, BaM (BaFe<sub>12</sub>O<sub>19</sub>) hexaferrite, using scrap iron filings as an iron source. The hexaferrites were prepared by conventional solid state reaction and characterized by X-ray diffraction (XRD), scanning electron microscopy (SEM) and magnetization measurements. XRD patterns of samples prepared by mixing powders extracted from the iron filings with appropriate amounts of barium carbonate and sintering at 1200 °C revealed the presence of a major BaM hexaferrite with small amounts of nonmagnetic  $\alpha$ -Fe<sub>2</sub>O<sub>3</sub> oxide phase. On the other hand, SEM images of the samples showed clear crystallization of perfect hexagonal platelets of BaM hexaferrite, which was further confirmed by the Curie temperature determined from the thermomagnetic measurements. The saturation magnetization of the samples was in the range of 45.1– 52.1 emu/g and the remnant magnetization in the range of 14.8 – 19.0 emu/g. These values and the moderate coercivity of ~ 1 kOe suggest that the prepared samples could potentially be useful for high-density magnetic recording.

**Keywords:** Hexaferrite, Solid waste, Magnetic Properties, Structural properties, Magnetic recording.

## Introduction

The revolutionary growth in modern industrialization, mining and technological advances did not proceed without leaving behind negative impacts on the environment, partially caused by the accumulation of hazardous solid wastes [1-4]. For example, the industry connected to canned food, steel and iron production plants, disposable parts of vehicles and utilities and by-products of machining contribute significantly to the increasing level of such solid waste on planet Earth. Wise planning for avoiding this problem should not be limited

to wise disposal of such waste, but should also benefit from the feasibility of recycling solid wastes in the production lines. This process would provide alternative sources of materials necessary for the industry, thus reducing both the demand for mining in search of naturally occurring minerals and the level of solid waste.

For decades, magnetic oxides have been widely used in a wide range of applications in our everyday life [5-9], thus contributing significantly to efficient achievement of tasks and convenience in human societies. The

competitiveness of magnetic oxides in the industrial market was not established by their performance only, but also by their cost effectiveness. The cost of production of materials for applications is determined by several parameters, including the cost of raw materials and processing. Thus, adopting successful strategies for cost-effective use of recyclable materials provides additional benefits in producing high-performance materials, while conserving natural resources and significantly reducing cost. Specifically, magnetic oxides could be produced from recycled iron-rich scrap, thus cutting down the cost of raw materials. The aim of this article is to demonstrate an effective procedure for the use of scrap iron in the production of beneficial materials for permanent magnet applications. While this procedure is concerned with the use of a specific iron scrap (iron filings resulting from machining processes), the procedure could be extended to other iron scrap sources, including iron-rich food cans, metal parts and byproducts of mining and industrialization.

M-type hexagonal ferrite ( $MFe_{12}O_{19}$ , where  $M = Ba, Sr, Pb$ ) is an important functional magnetic oxide possessing high magnetocrystalline anisotropy and relatively high saturation and remanence magnetization. The large annual production of these materials was motivated by their cost-effectiveness and suitability for a wide range of applications [5-8, 10-14]. Consequently, the production of these ferrites and investigation of their structural and physical properties have received an exponentially increasing interest in the last few decades [15-21]. In this article, we describe the preparation of M-type barium hexaferrite using iron-rich scrap metal filings without the need for prior knowledge of the exact elemental contents of this iron source. The large-scale employment of this procedure is promising for providing important magnetic materials at low cost and efficient disposal of solid wastes.

## Experimental Work

### Preparation of the Starting Iron-rich (F) Powder

Scrap iron filings resulting from machining iron rods and objects in the mechanical workshop at the Physics Department, the University of Jordan, were collected using a bar magnet to avoid nonmagnetic particles in the

collected raw material. The collected filings are expected to consist of mainly metallic iron, but may also contain small amounts of other elements due to impurities in the machined iron objects and contamination due to possible mixing with small amounts of particles of other materials such as Al and brass, which are normally processed by the same device. The filings were washed with water and preheated at 500 °C for 2 h to get rid of moisture, oils and other non-metallic burnable materials. The preheated material was subsequently hand-ground in an agate mortar and pestle for 1 h. The resulting powder (labelled F) was strongly attracted to a small magnet, indicating that the above heat treatment did not result in appreciable conversion of metallic iron into a non-magnetic ( $\alpha\text{-Fe}_2\text{O}_3$ ) oxide phase. This (F) powder was used as a starting iron source for the preparation of BaM hexaferrites.

### Preparation of BaM Samples

BaM hexaferrites ( $BaFe_{12}O_{19}$ ) were prepared by conventional solid state reaction using precursor powder mixtures of the F powder and  $BaCO_3$  (Sigma-Aldrich made, ~ 99% pure). The production of BaM hexaferrite with high purity can be achieved by sintering a precursor mixture with F/ $BaCO_3$  mass ratio (R) consistent with the Fe:Ba stoichiometric molar ratio of 12:1 in BaM. If the F powder consists of pure metallic iron, the stoichiometric composition of BaM requires F/ $BaCO_3$  mass ratio of  $R = 3.40$  ( $= 12 \times M(Fe) / M(BaCO_3)$ ), where  $M$  is the molar mass). However, if the F powder consists of iron oxide ( $Fe_2O_3$ ), the required F/ $BaCO_3$  mass ratio should be  $R = 4.85$  ( $= 6 \times M(Fe_2O_3) / M(BaCO_3)$ ). Accordingly, in the absence of prior knowledge of the exact nature (level of oxidation) and composition of the F powder, three powder mixtures with F/ $BaCO_3$  mass ratios of  $R = 3.0$  (BFO3),  $R = 3.5$  (BFO3.5) and  $R = 5.0$  (BFO5) were prepared to cover the range between the value corresponding to pure metallic iron and that corresponding to fully oxidized iron. The ratios of  $R = 3.0$  and  $3.5$  were chosen around the stoichiometric ratio corresponding to pure iron, where slightly lower and higher values were adopted to account for possible presence of small amounts of elements with lower or higher molar masses compared to iron, small amounts of non-reacting impurities or low-levels of oxidation in the F powder. However, the mixture with  $R = 5.0$  was made

slightly higher than the stoichiometric mass ratio for  $\text{Fe}_2\text{O}_3$  to account for possible presence of small amounts of non-reacting impurities in a fully oxidized iron powder. These powder mixtures were hand-ground in an agate mortar and pestle for 1 h and disk-like pellets (1.25 cm in diameter and  $\sim 2$  mm thick) were prepared from the finely ground powder mixtures using a force of 50 kN. The disks were then sintered in air at 1200 °C for 2 h, using a heating rate of 10 °C/min. For the sake of comparison, a pellet of the F powder (without the addition of  $\text{BaCO}_3$ ) was prepared and sintered in air at 1200 °C for 2 h (resulting in the sample labelled FO). All sintered samples were then characterized structurally and magnetically to investigate the structural phases in the samples and draw conclusions regarding the nature of the filings used as an iron source and the purity of BaM phase in the prepared hexaferrite samples.

The results of the characterization revealed that the FO sample consists of high-purity  $\alpha$ - $\text{Fe}_2\text{O}_3$  phase (as discussed in a forthcoming subsection). Accordingly, the FO powder was used as a known iron source to prepare a forth BaM sample using a mixture with FO/ $\text{BaCO}_3$  mass ratio of  $R = 4.8$  (sample BFO4.8), slightly lower than the theoretical ratio ( $R = 4.85$ ) to account for possible existence of traces of un-oxidized iron at the core of the particles. This powder mixture was pelletized following the abovementioned procedure for the F/ $\text{BaCO}_3$  mixtures and similarly sintered at 1200 °C for 2 h.

### Characterization Techniques

The XRD patterns of the samples were recorded at room temperature using XRD 7000-Shimadzu diffractometer with  $\text{Cu-K}_\alpha$  radiation ( $\lambda = 1.5406 \text{ \AA}$ ). The structural phases in the samples were identified by analyzing the XRD patterns using X'pert HighScore software, whereas the refined structural parameters were obtained by Rietveld analysis [22] using FullProf software [23, 24]. The XRD patterns were collected in the angular range  $20^\circ \leq 2\theta \leq 70^\circ$  in steps of  $0.01^\circ$  and using a scanning speed of  $0.5^\circ/\text{min}$ . Scanning electron microscopy (SEM) using Versa 3D, FEI electron microscope was

employed to further characterize the samples by examining the morphology and particle size distribution. The magnetic properties of the samples were investigated by room-temperature hysteresis loop measurements using a conventional vibrating sample magnetometry (VSM MicroMag 3900, Princeton Measurements Corporation) operating under an applied magnetic field up to  $\pm 10$  kOe. To further confirm the identity of the magnetic phases in the samples, thermomagnetic measurements were performed by measuring the temperature-dependent magnetization under an applied field of 100 Oe in a temperature range up to 550 °C.

## Results and Discussion

### Characterization of the FO Powder

The sintered FO sample was characterized by XRD, SEM and magnetic measurements. Fig. 1a revealed that the diffraction pattern of the FO powder matches the standard pattern (01-086-2368) for  $\alpha$ - $\text{Fe}_2\text{O}_3$  oxide phase, confirming the oxidation of the sintered filings. The SEM image in Fig. 1b revealed the presence of rhombohedral, sharp-edged particles with typical size in the range of 1 – 4  $\mu\text{m}$ . These particles are characteristic of  $\alpha$ - $\text{Fe}_2\text{O}_3$  iron oxide as confirmed by Energy Dispersive X-ray spectroscopic analysis in a previous study [25]. However, the magnetic hysteresis loop in Fig. 1c indicated the presence of a soft magnetic component, which may be associated with small amounts of un-oxidized iron. The saturation magnetization ( $\sigma_s$ ) of the sintered powder is  $\sim 6$  emu/g, which is  $\sim 3\%$  of the saturation magnetization for metallic iron ( $\sigma_s = 197$  emu/g) [5]. This is an indication that the wt.% of un-oxidized iron in the FO powder is a few percent and the likelihood that this magnetic phase is at the core of the powder particles made it undetectable by XRD measurements. Similarly, in a recent article [26], the ferromagnetic-like behaviour of  $\alpha$ - $\text{Fe}_2\text{O}_3$  was attributed to Fe-containing impurity with relatively high saturation magnetization. However, in an earlier study, this behaviour was associated with magnetic disorder in the shell of the hematite nanoparticles [27].

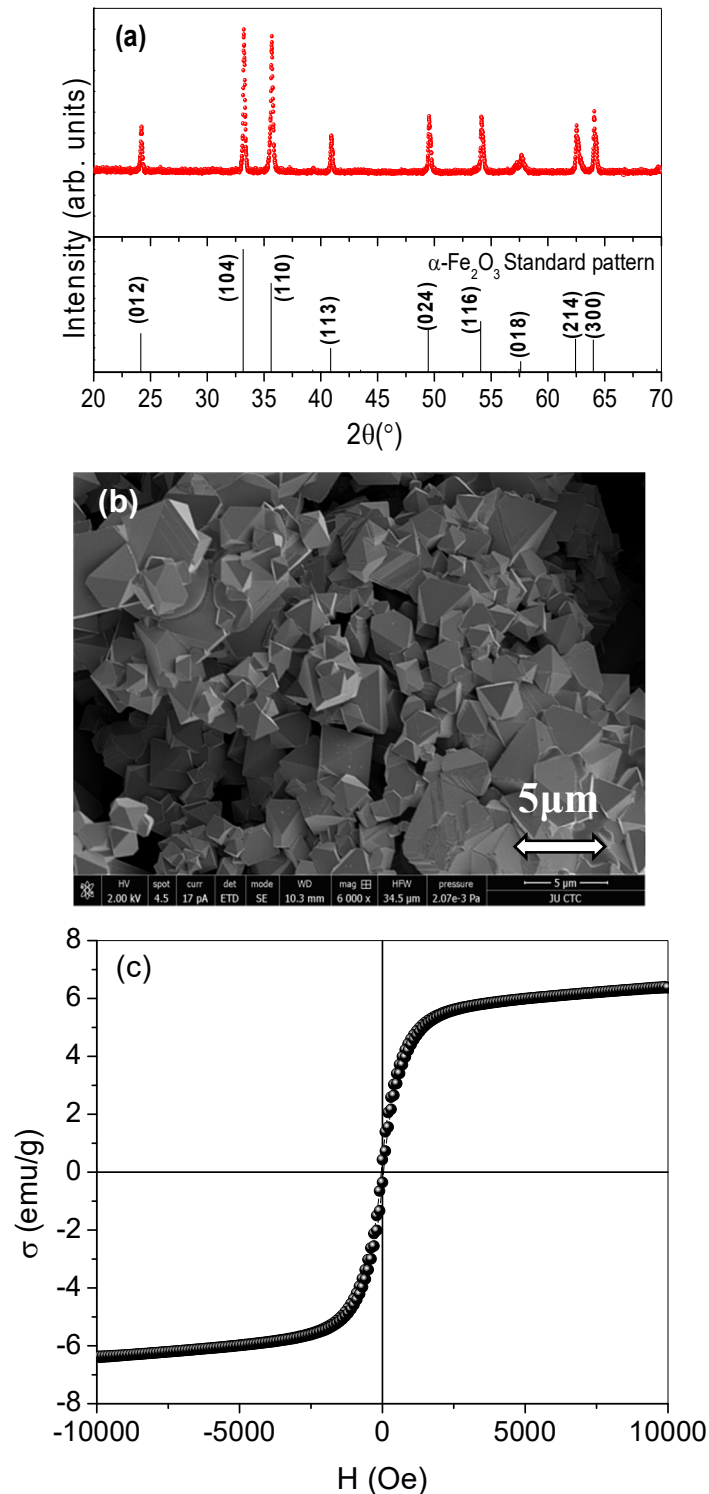


FIG. 1. (a) XRD pattern, (b) SEM image and (c) magnetization curve of the FO sample.

### Structural analysis of BaM samples

The three M-type hexaferrites prepared from the F powder (BFO3, BFO3.5, and BFO5) and the fourth prepared from the FO powder (BFO4.8) were examined by XRD to investigate the phase purity and the structural characteristics of the hexaferrite phase in these samples. Fig. 2 shows

XRD patterns with Rietveld refinement for the BFO3 and BFO3.5 samples. The patterns revealed structural peaks corresponding to a major BaM phase matching the standard pattern (00-043-0002) and a minor nonmagnetic  $\alpha$ -Fe<sub>2</sub>O<sub>3</sub> oxide phase matching the standard pattern (01-086-2368). The expanded pattern in Fig. 3a indicated that the BFO3 sample contained

additional traces of  $\text{BaFe}_2\text{O}_4$  phase as indicated by the weak peak labeled by (B) and of an unidentified phase represented by the weak peak labeled by (\*). These trace phases were not observed in the pattern of the sample BFO3.5 (Fig. 3b), indicating that these phases most probably contain Ba, which was incorporated in the production of the hexaferrite phase in this sample. The diffraction peaks of the M-type phase are slightly shifted to higher angles by  $\sim 0.05^\circ$  compared with the Bragg positions of the standard pattern (Fig. 3), indicating a slight decrease of the lattice constants. Also, the relative intensities of the (006) and (008) Bragg peaks in the pattern of the sample BFO3 (Fig. 2) are obviously higher than in the standard pattern, indicating structural texture along the  $c$ -axis [28]. In addition, the higher intensities of the peaks corresponding to  $\alpha$ - $\text{Fe}_2\text{O}_3$  phase in the pattern of the sample BFO3.5 indicated a surplus of Fe in this sample, which forms an extra amount of the  $\text{Fe}_2\text{O}_3$  oxide phase. The weight ratios of the BaM and  $\alpha$ - $\text{Fe}_2\text{O}_3$  oxide phase in these samples were determined by Rietveld analysis and are listed in Table 1. The relatively low values of the reliability factors ( $R_B$  and  $R_F$ )

and goodness of fit ( $\chi^2$ ) indicate a reliable fit as demonstrated by the (almost) horizontal difference curve (blue line in Fig. 2). The results indicated that the BaM hexaferrite is a major phase in these samples, with 91.7 wt.% in sample BFO3 and 86.3% in sample BFO3.5. The wt.% of the  $\alpha$ - $\text{Fe}_2\text{O}_3$  phase of 8.3% and 13.7% in these samples, respectively, is in agreement with the detailed structural analysis of the BaM/ $\text{Fe}_2\text{O}_3$  composites [29]. These results demonstrated that the required mass ratio of the F powder to produce a high purity BaM hexaferrite is lower than the stoichiometric ratio of  $R = 3.40$  for pure iron, which leads to two conclusions regarding the iron filings used in this study. First, the filings in the F powder were mostly in the form of metallic iron, since progressive oxidation should increase the required F/ $\text{BaCO}_3$  mass ratio up to 4.85 for full oxidation. Second, the filings contain impurity elements having lower atomic masses compared to iron, since the required  $R$  is lower than the stoichiometric ratio for pure metallic iron. Notably, when these elements occupy the  $\text{Fe}^{3+}$  sites in the hexaferrite lattice, they may lead to modifications of the magnetic properties of the hexaferrites.

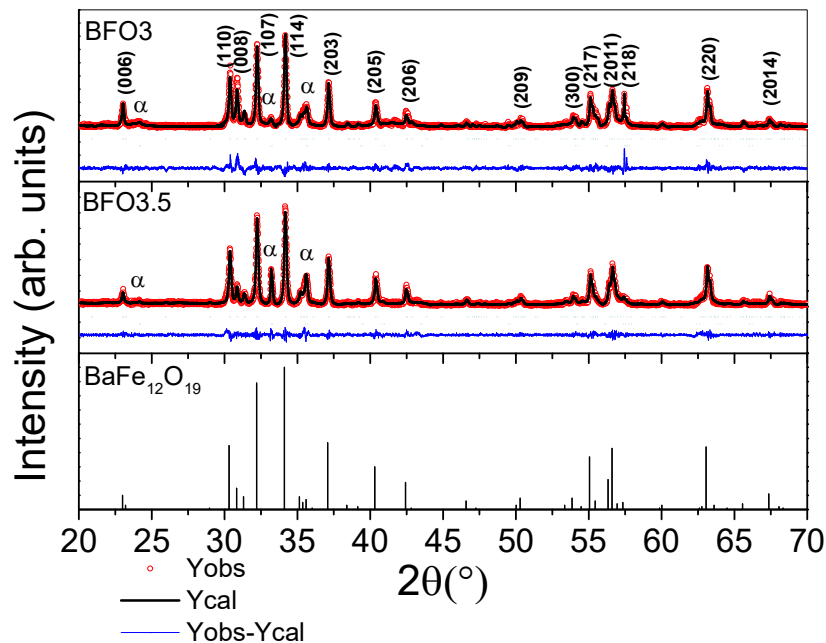


FIG. 2. XRD patterns with Rietveld refinement for sintered BFO3 and BFO3.5 samples. The red open circles represent the experimental data, the black line represents the calculated pattern and the blue line below the pattern represents the difference between the experimental and calculated patterns. The reflections corresponding to  $\alpha$ - $\text{Fe}_2\text{O}_3$  oxide phase are labeled ( $\alpha$ ). The standard patterns of M-type hexaferrite is shown for comparison.

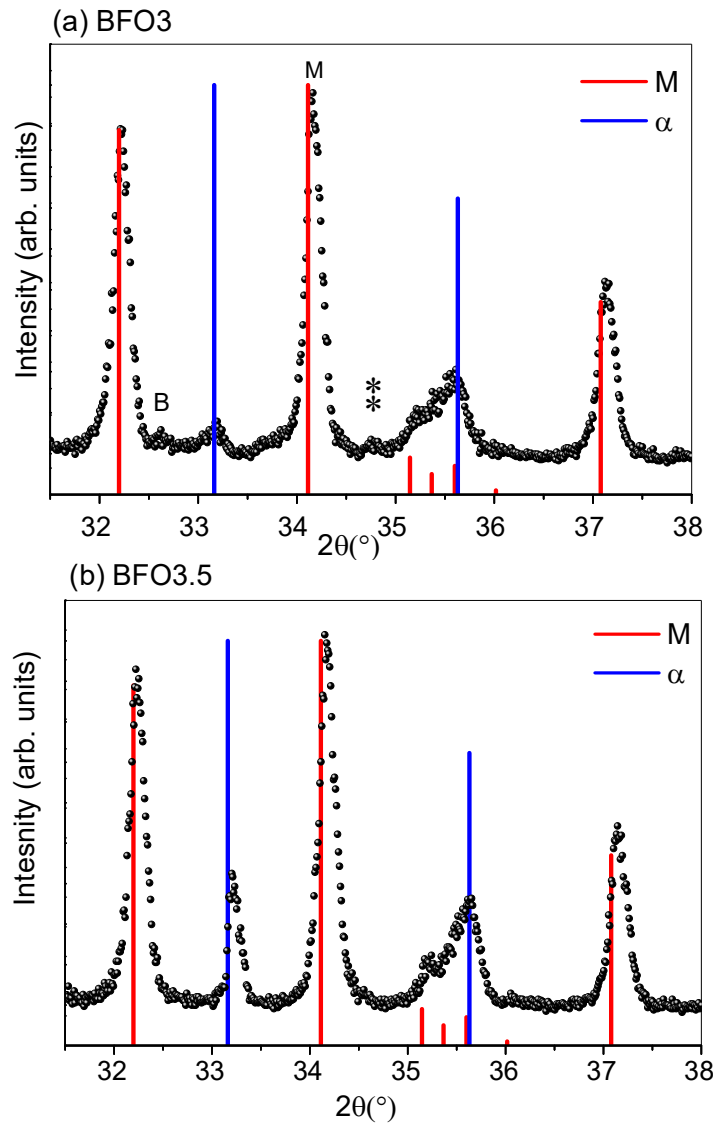


FIG. 3. Expanded view of the diffraction patterns for the samples with F/BaCO<sub>3</sub> mass ratio of (a) 3.0:1.0 and (b) 3.5:1.0. The red bars represent the structural peaks in the standard pattern of the M-type, whereas the blue bars are the structural peaks in the standard pattern of  $\alpha$ -Fe<sub>2</sub>O<sub>3</sub> phase. The peak labeled B corresponds to BaFe<sub>2</sub>O<sub>4</sub> phase.

TABLE 1. The fractions of the phases (in wt.%) as obtained by Rietveld analysis. The reliability factors and goodness of fit ( $R_B$ ,  $R_F$ , and  $\chi^2$ ) are also listed.

Sample	Phase	Wt.%	$R_B$	$R_F$	$\chi^2$
BFO3	BaM	91.7	6.84	5.33	0.61
	$\alpha$ -Fe <sub>2</sub> O <sub>3</sub>	8.3	6.60	6.21	
BFO3.5	BaM	86.3	3.55	4.12	0.40
	$\alpha$ -Fe <sub>2</sub> O <sub>3</sub>	13.7	5.56	4.32	
BFO5	BaM	84.1	5.20	5.02	0.69
	$\alpha$ -Fe <sub>2</sub> O <sub>3</sub>	15.9	6.53	4.92	
BFO4.8	BaM	98.7	4.10	4.87	0.47
	$\alpha$ -Fe <sub>2</sub> O <sub>3</sub>	1.3	9.83	8.10	

On the other hand, Fig. 4 shows XRD patterns of the samples BFO5 (prepared from the F powder) and BFO4.8 (prepared from the FO powder) with mass ratio close to the

stoichiometric ratio for  $\alpha$ -Fe<sub>2</sub>O<sub>3</sub>. The diffraction pattern of sample BFO5 in Fig. 4 (a) revealed the presence of a significant amount of  $\alpha$ -Fe<sub>2</sub>O<sub>3</sub> phase compared with sample BFO3. The wt.% of

iron oxide phase in the sample was determined by Rietveld analysis and found to be 15.9% (Table 1). This is an indication that the F/BaCO<sub>3</sub> mass ratio in this sample is significantly higher than the stoichiometric ratio in BaM, confirming the above results which revealed that the F powder is mostly metallic iron, rather than iron oxide. However, Rietveld analysis revealed that the sample BFO4.8 prepared from the pre-oxidized (FO) powder is almost a pure BaM

phase (98.7%), confirming that this starting powder consists of  $\alpha$ -Fe<sub>2</sub>O<sub>3</sub>, in agreement with the structural analysis of this powder. The expanded view (Fig. 5) shows that the sample consists of almost a pure M-type phase, with very small amounts of iron oxide impurity phase revealed by the very weak peak at  $2\theta \sim 33.2^\circ$  corresponding to the main structural peak of  $\alpha$ -Fe<sub>2</sub>O<sub>3</sub> phase.

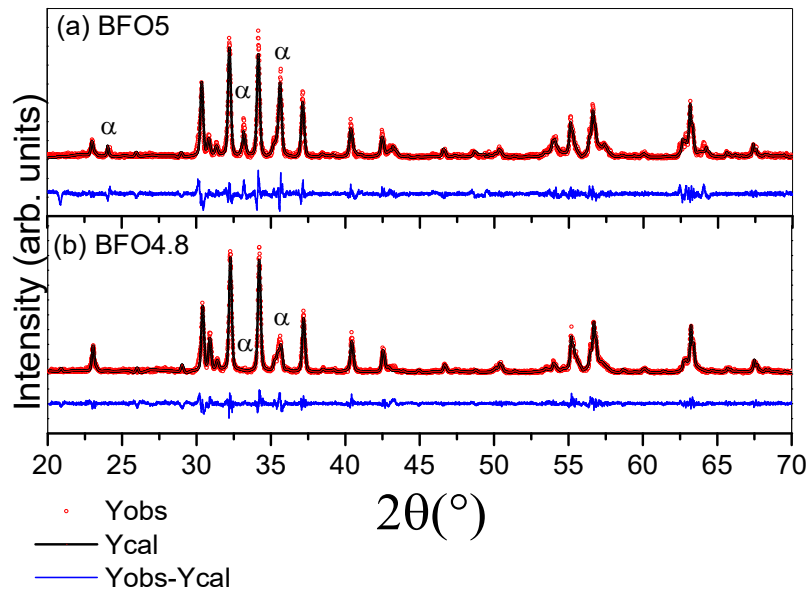


FIG. 4. XRD patterns with Rietveld refinement for the samples BFO5 and BFO4.8.

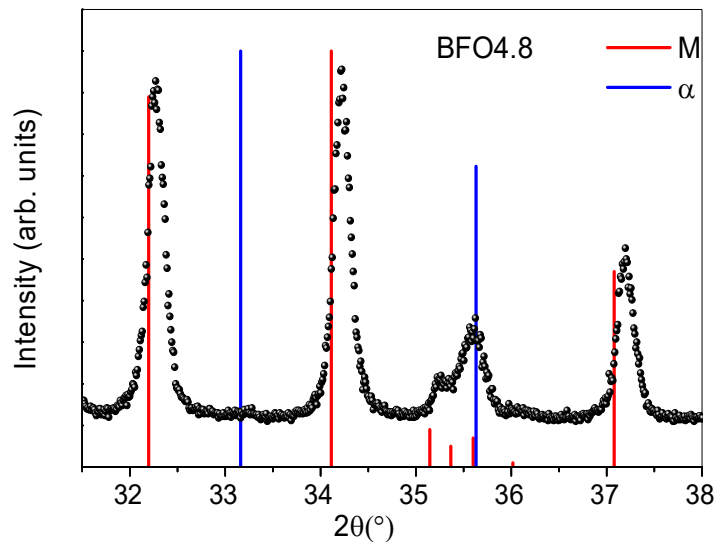


FIG. 5. Expanded view of the diffraction pattern of the sample BFO4.8 in the angular range of the main structural peaks of BaM and  $\alpha$ -Fe<sub>2</sub>O<sub>3</sub> phases. The Bragg positions and relative intensities of the standard patterns of BaM and  $\alpha$ -Fe<sub>2</sub>O<sub>3</sub> phases are shown for comparison.

The refined lattice parameters of  $a = 5.88 - 5.89 \text{ \AA}$  and  $c = 23.18 - 23.19 \text{ \AA}$  for BFO3, BFO3.5 and BFO5 (Table 2) are in good agreement with the standard values of  $a = 5.89 \text{ \AA}$  and  $c = 23.18 \text{ \AA}$  [30] and the previously reported values of  $a = 5.897 - 5.899 \text{ \AA}$  and  $c = 23.175 -$

$23.179 \text{ \AA}$  [31], but the lattice parameter  $c$  is slightly smaller than values in the range of  $23.20 - 23.24 \text{ \AA}$  reported by others [32-34]. However, the lattice parameters of  $a = 5.88 \text{ \AA}$  and  $c = 23.16 \text{ \AA}$  for BFO4.8 are slightly lower as revealed by the peak shifts in Fig. 5.

TABLE 2. Lattice parameters, cell volume, bulk density, x-ray density and porosity for the samples.

Sample	$a$ (Å)	$c$ (Å)	$V$ (Å <sup>3</sup> )	$\rho_x$ (g/cm <sup>3</sup> )	$\rho_b$ (g/cm <sup>3</sup> )	$P\%$
BFO3	5.89	23.19	696.7	5.30	3.20	40
BFO3.5	5.88	23.18	694.1	5.32	4.13	22
BFO4.8	5.88	23.16	693.5	5.32	4.69	12
BFO5	5.89	23.19	696.7	5.30	4.03	24

The x-ray density was calculated from the molecular weight ( $M_w$ ) of BaM and the refined cell volume  $V$  (Table 2) using the formula:

$$\rho_x = \frac{Z(M_w)}{N_A V} \quad (1)$$

Here,  $Z = 2$  is the number of molecules per unit cell and  $N_A$  is Avogadro's number. The x-ray density of 5.30 g/cm<sup>3</sup> for BaM phase in BFO3 and BFO5 samples was in agreement with the reported values of 5.28 – 5.29 g/cm<sup>3</sup> [32, 34]. However, the x-ray density of 5.32 g/cm<sup>3</sup> for BaM phase in BFO3.5 and BFO4.8 samples was slightly higher, which is consistent with the slightly lower cell volume in these samples. The bulk density ( $\rho_b$ ) was measured by Archimedes method and the porosity was calculated using the formula:

$$P\% = \left(1 - \frac{\rho_b}{\rho_x}\right) \times 100 \quad (2)$$

The results in Table 2 indicate that the porosity of the sample BFO3 is significantly higher than in the other samples. However, the range of the observed porosity is slightly lower than the range of 25.8 – 48.4% reported for Mg-Ti substituted BaM [35].

In order to calculate the crystallite size of the BaM phase along the direction perpendicular to the  $(hkl)$  plane using Stokes and Wilson approach, the corresponding diffraction peak area ( $A$ ) and maximum peak intensity ( $I_0$ ) were determined by fitting the peak with a Lorentzian line shape. The integral breadth ( $\beta = A/I_0$ ) was then calculated and the corrected breadth ( $\beta_c$ ) was determined by subtracting the instrumental broadening obtained by using a standard Si sample [32]. According to the formulation of Stokes and Wilson, the crystallite size ( $D$ ) is given by [36]:

$$D = \frac{\lambda}{\beta_c \cos \theta} \quad (3)$$

Here,  $\lambda = 0.15406$  nm and  $\theta$  is the Bragg angle of diffraction peak.

The crystallite size of the BaM phase was determined from its three main reflections (110), (107) and (114) and the results are listed in Table 3. Clearly, the crystallite size along the hexagonal plane (perpendicular to the (110) planes) was not larger than that along the other directions, indicating that the crystallites are not platelet-like in shape.

TABLE 3. Crystallite size of BaM phase along different crystallographic directions.

Sample	Crystallite size ( $D$ ) nm		
	(110)	(107)	(114)
BFO3	151	134	169
BFO3.5	101	141	153
BFO4.8	114	111	115
BFO5	57	98	111

## SEM Results

SEM images of the samples revealed the presence of platelet-like particles, some of which exhibiting clear hexagonal symmetry as indicated by the representative images in Fig. 6. Typical particle size in the range of 0.5 – 3.0  $\mu\text{m}$  was observed in all samples except BFO3, which revealed the presence of larger particles with some  $\sim 10$   $\mu\text{m}$  in diameter. In addition, the platelet-like particles are generally thick, the thickness reaching about half the in-plane dimension in some cases. Compared with the crystallite size obtained from analysis of the XRD peaks, the physical particle size is significantly larger, indicating that these particles are polycrystalline.

## Magnetic Measurements

The hysteresis loops for the samples are shown in Fig. 7, together with the central part of the loops for clarity. The hysteresis loops revealed that all samples are magnetically semi-hard, with monotonically increasing magnetization in the high-field range, indicating high magnetocrystalline anisotropy field ( $H_a$ ) in all samples. The coercivity of all samples was in the range of 878 – 966 Oe (Table 4), which is significantly lower than values of 4 – 5 kOe

reported for single-domain BaM hexaferrites [37, 38]. However, our observed values are in agreement with values of 860 and 1005 Oe reported by others for samples consisting of large particles as a consequence of the high-temperature sintering at 1300 °C [35, 39]. The reduction of the coercivity in our samples could therefore be due to the multi-domain nature of their constituent particles, in agreement with the SEM images which revealed the presence of a large fraction of particles with size greater than the single-domain critical size of  $\sim 0.5 - 1 \mu\text{m}$

[6, 40]. The remanence magnetization ( $\sigma_r$ ) was also determined from the hysteresis loops and the results are listed in Table 4. These materials with  $\sigma_r$  in the range of 14.8 – 19.0 emu/g and intermediate values of the coercivity could be used for the production of cost-effective low-performance permanent magnets for applications that do not require high flux and magnetic hardness. However, these characteristics are better suited for high-density magnetic recording applications [21, 41].

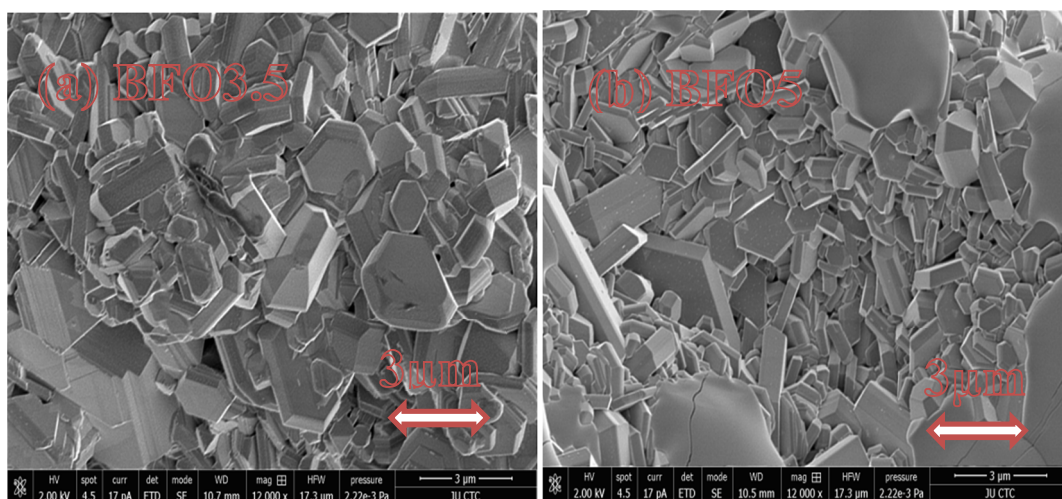


FIG. 6. Representative SEM images for BFO3.5 and BFO5 samples.

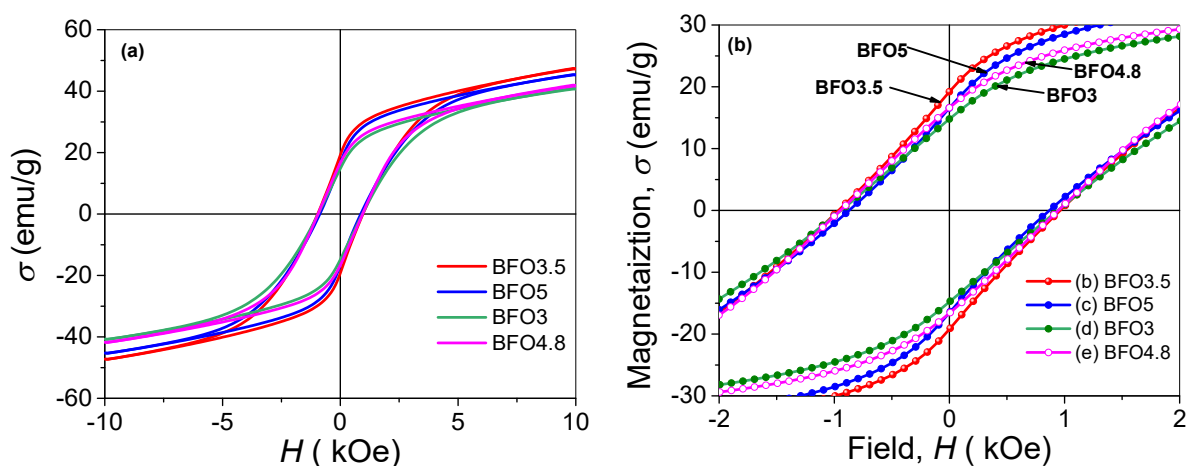


FIG. 7. (a) hysteresis loops and (b) expanded view of the hysteresis loops for the samples.

TABLE 4. Saturation magnetization ( $\sigma_s$ ), remanence ( $\sigma_r$ ), squareness ratio ( $\sigma_r/\sigma_s$ ), coercive field ( $H_c$ ), and anisotropy field ( $H_a$ ) for the samples.

Sample	$\sigma_s$ (emu/g)	$\sigma_r$ (emu/g)	$\sigma_r/\sigma_s$	$H_c$ (Oe)	$H_a$ (kOe)
BFO3	45.1	14.8	0.33	947	12.1
BFO3.5	52.1	19.0	0.36	966	11.8
BFO4.8	46.2	16.6	0.35	947	12.1
BFO5	49.9	16.6	0.33	878	11.7

Other magnetic parameters such as the saturation magnetization ( $\sigma_s$ ) and magnetocrystalline anisotropy field ( $H_a$ ) were obtained from the law of approach to saturation. At high fields, the magnetization behavior is determined by the rotation of the domain magnetization into the direction of the applied field and the magnetization can be approximated by the polynomial [42, 43]:

$$M = M_s \left( 1 - \frac{A}{H} - \frac{B}{H^2} \right) + \chi H \quad (4)$$

Here,  $M_s = \rho_x \sigma_s$  is the saturation magnetization per unit volume, the constant  $A$  represents the contribution of crystal imperfections and the constant  $B$  represents the contribution of the magnetocrystalline anisotropy ( $B = H_a^2/15$ ). At high fields, the contributions of the crystal imperfections and the forced magnetization term,  $\chi H$ , are negligible, leading to a linear relation between  $M$  and  $1/H^2$ , which can also be expressed as a linear relation between  $\sigma$  and  $1/H^2$  as follows:

$$\sigma = \sigma_s \left( 1 - \frac{B}{H^2} \right) \quad (5)$$

Note that this simple equation which involves the directly measured magnetization  $\sigma(H)$  is obtained by canceling the density on the two sides of the equation. The straight line fit to the experimental data in the field range  $8.5 \text{ kOe} \leq H \leq 10 \text{ kOe}$  allowed determination of the best estimate of the saturation magnetization ( $\sigma_s =$  the intercept of the line with the magnetization axis) and the magnetocrystalline anisotropy (from the slope of the straight line) and the results are listed in Table 4. The saturation magnetization of the samples (45.1 to 52.1 emu/g) were in agreement with reported values of 49 and 51 emu/g [35, 44], but lower than the best values of 70 – 72 emu/g obtained by our group [38, 45, 46]. The squareness ratio ( $\sigma_r/\sigma_s$ ) for all samples was in the range of 0.33 – 0.36, appreciably lower than the value characteristic of randomly oriented single-domain particles of 0.5, which confirms the multi-domain nature of a significant fraction of the particles in our samples. Among these samples, the highest and best magnetic parameters for high-density magnetic recording were exhibited by the sample BFO3.5, with  $\sigma_s = 52.1 \text{ emu/g}$ ,  $\sigma_r = 19.0 \text{ emu/g}$  and  $H_c = 966 \text{ Oe}$ .

The magnetocrystalline anisotropy field ( $H_a$ ) was almost the same ( $11.9 \pm 0.2 \text{ kOe}$ ) for all

samples. These values are in good agreement with values reported for a variety of BaM hexaferrites exhibiting high coercivity ( $> 4 \text{ kOe}$ ) [47]. This indicates that the observed reduction of the coercivity of the samples in this study is not caused by lowering the magnetocrystalline anisotropy, which is a further confirmation that this reduction is associated with particle size [48].

### Thermomagnetic Measurements

Fig. 8 shows the thermomagnetic curves for the samples at a constant applied field of 100 Oe. The curves exhibited normal slow decrease of the magnetization with the increase of temperature and then a sudden drop associated with ferrimagnetic to paramagnetic phase transition at the Curie temperature. The Curie temperature (indicated by the arrow in Fig. 8) of all samples was  $(455 \pm 5) \text{ }^\circ\text{C}$ , characteristic of barium M-type hexaferrite [34]. All curves, with the exception of that for the sample BFO5, exhibited a normal behavior characteristic of a single magnetic phase. Notice that  $\alpha\text{-Fe}_2\text{O}_3$  undergoes a transition from antiferromagnetic to paramagnetic state above Neel temperature ( $T_N \sim 687 \text{ }^\circ\text{C}$ ) and thus does not exhibit magnetic phase transition in the temperature range adopted in this study. The curve of the sample BFO5, however, exhibited a small peak just below the Curie temperature (Hopkinson peak), indicating the presence of a small fraction of superparamagnetic particles [49]. Also, the curve is flattened above the Curie temperature, indicating the possibility of existence of magnetic inhomogeneity in this sample.

### Conclusion

We have demonstrated that iron-rich powders extracted from solid wastes such as scrap iron filings can profitably replace other costly iron sources in the production of important magnetic oxides. The results of this study clearly indicated that powders obtained by firing iron filings at  $500 \text{ }^\circ\text{C}$  provide a useful metallic iron source, whereas the powder obtained by sintering at  $1200 \text{ }^\circ\text{C}$  can be reliably used as an iron oxide source. Both sources were successfully used in this study for the production of high-quality BaM hexaferrites. The magnetic parameters of the prepared hexaferrites were characteristic of materials suitable for high-density magnetic storage media and permanent magnets for applications that do not require high-flux and

magnetically hard materials. The procedure adopted in this study can be modified and extended to other metal scrap for the production

of important materials, thus reducing the level of hazardous solid waste and lowering the cost of production.

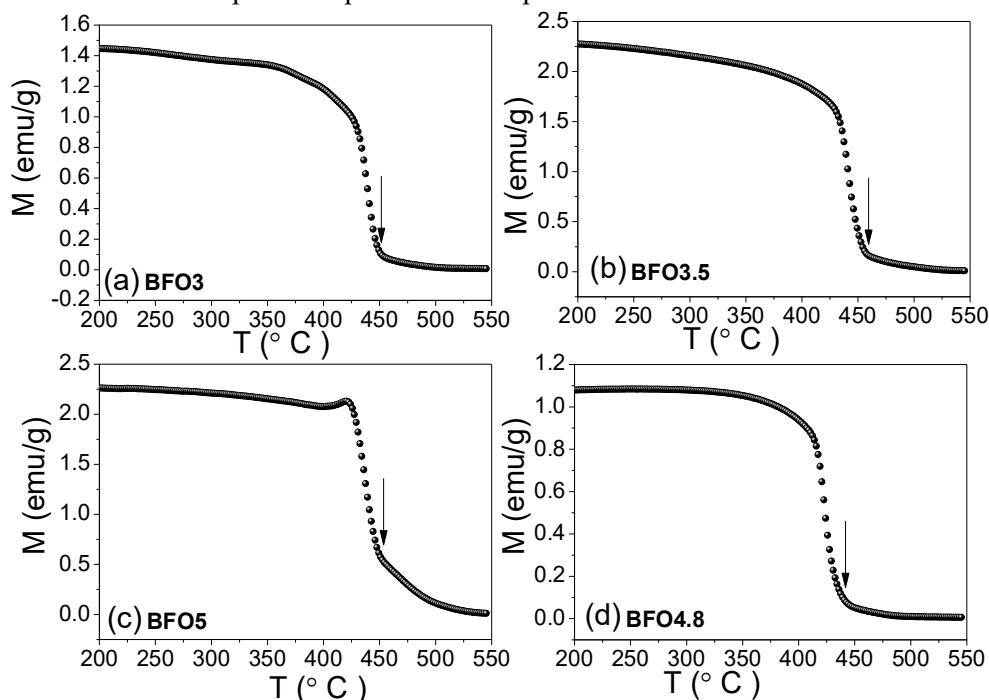


FIG.8. Thermomagnetic curves (at an applied field of 100 Oe) for the samples.

## Acknowledgement

S.H. Mahmood would like to acknowledge the support provided by the University of Jordan during his sabbatical leave at Michigan State University. The technical assistance of Y. Abu Salha (the University of Jordan) in performing

XRD measurements is acknowledged. Also, the assistance of Zaid Al-Degess (the mechanical workshop at the Physics Department, the University of Jordan) in collecting iron filings for this study is acknowledged.

## References

- [1] Ohimain, E.I., *Journal of Environmental Management and Public Safety*, 2 (2013) 1.
- [2] Carvalheiras, J., Novais, R.M., Mohseni, F., Amaral, J.S., Seabra, M.P., Labrincha, J.A. and Pullar, R.C., *Ceramics International*, 46 (2020) 5757.
- [3] Liu, Z. and Li, H., *Hydrometallurgy*, 155 (2015) 29.
- [4] Khairul, M.A., Zanganeh, J. and Moghtaderi, B., *Conservation & Recycling*, 141 (2019) 483.
- [5] Özgür, Ü., Alivov, Y. and Morkoç, H., *Journal of Materials Science: Materials in Electronics*, 20 (2009) 789.
- [6] Pullar, R.C., *Progress in Materials Science*, 57 (2012) 1191.
- [7] Harris, V.G., Geiler, A., Chen, Y., Yoon, S.D., Wu, M., Yang, A., Chen, Z., He, P., Parimi, P.V. and Zuo, X., *Journal of Magnetism and Magnetic Materials*, 321 (2009) 2035.
- [8] Mahmood, S.H., "Permanent Magnet Applications", In: S.H. Mahmood and I. Abu-Aljarayesh (Eds.), "Hexaferrite Permanent Magnetic Materials", (Materials Research Forum LLC, Millersville, PA, 2016), pp. 153-165.
- [9] Gutfleisch, O., Willard, M.A., Brück, E., Chen, C.H., Sankar, S. and Liu, J.P., *Advanced Materials*, 23 (2011) 821.
- [10] Strnat, K.J., *Proceedings of the IEEE*, 78 (1990) 923.

- [11] Meng, P., Xiong, K., Wang, L., Li, S., Cheng, Y. and Xu, G., *Journal of Alloys and Compounds*, 628 (2015) 75.
- [12] Lee, J., Hong, Y.-K., Lee, W., Abo, G.S., Park, J., Neveu, N., Seong, W.-M., Park, S.-H. and Ahn, W.-K., *Journal of Applied Physics*, 111 (2012) 07A520.
- [13] Cui, J., Kramer, M., Zhou, L., Liu, F., Gabay, A., Hadjipanayis, G., Balasubramanian, B. and Sellmyer, D., *Acta Materialia*, 158 (2018) 118.
- [14] Sugimoto, S., Okayama, K., Kondo, S.-I., Ota, H., Kimura, M., Yoshida, Y., Nakamura, H., Book, D., Kagotani, T. and Homma, M., *Materials Transactions, JIM*, 39 (1998) 1080.
- [15] Chikazumi, S., "Physics of Ferromagnetism", 2<sup>nd</sup> edn., (Oxford University Press Oxford, 2009).
- [16] Mahmood, S.H., Aloqaily, A.N., Maswadeh, Y., Awadallah, A.M., Bsoul, I., Awawdeh, M. and Juwhari, H.K., *Solid State Phenomena*, 232 (2015) 65.
- [17] Mahmood, S.H., Zaqsaw, M.D., Mohsen, O.E., Awadallah, A.M., Bsoul, I., Awawdeh, M. and Mohaidat, Q.I., *Solid State Phenomena*, 241 (2016) 93.
- [18] Albanese, G., *Le Journal de Physique Colloques*, 38 (1977) 85.
- [19] Mahmood, S.H., "High-performance Permanent Magnets", In: S.H. Mahmood and I. Abu-Aljarayesh (Eds.), "Hexaferrite Permanent Magnetic Materials", (Materials Research Forum LLC, Millersville, PA, 2016), pp. 47-73.
- [20] Mahmood, S.H. and Bsoul, I., "Tuning the magnetic properties of M-type hexaferrites", In: R.B. Jotania and S.H. Mahmood (Eds.), "Magnetic Oxides and Composites", (Materials Research Forum LLC, Millersville, PA, USA, 2018), pp. 49-100.
- [21] Mahmood, S.H., "Ferrites with High Magnetic Parameters", In: S.H. Mahmood and I. Abu-Aljarayesh (Eds.), "Hexaferrite Permanent Magnetic Materials", (Materials Research Forum LLC, Millersville, PA, 2016), pp. 111-152.
- [22] Rietveld, H.M., *Journal of Applied Crystallography*, 2 (1969) 65.
- [23] Rodriguez-Carvajal, J., *IUCR Newsletter*, 26 (2001) 12.
- [24] Roisnel, T. and Rodriguez-Carvajal, J., "A Windows Tool for Powder Diffraction Patterns Analysis", In: R. Delhez and E.J. Mittemeijer (Eds.), "The Seventh European Powder Diffraction Conference (EPDIC 7)", (Trans Tech Publications, Barcelona, Spain, 2000), pp. 118-123.
- [25] Mahmood, S.H., Awadallah, A.M., Maswadeh, Y. and Bsoul, I., *IOP Conference Series: Materials Science and Engineering*, 92 (2015) 012008.
- [26] Ahmadzadeh, M., Romero, C. and McCloy, J., *AIP Advances*, 8 (2018) 056807.
- [27] Tadic, M., Panjanb, M., Damnjanovic, V. and Milosevic, I., *Applied Surface Science*, 320 (2014) 183.
- [28] Mahmood, S.H., Ghanem, A.A., Bsoul, I., Awadallah, A. and Maswadeh, Y., *Materials Research Express*, 4 (2017) 036105.
- [29] Maswadeh, Y., Mahmood, S.H., Awadallah, A.M. and Aloqaily, A.N., *IOP Conference Series: Materials Science and Engineering*, 92 (2015) 012019.
- [30] Shin, S.S. and Kwon, S.-J., *Powder Diffraction*, 7 (1992) 212.
- [31] Stergiou, A.C., Samaras, D., Kalogirou, O., Vincent, H. and Bekka, A., *Solid State Ionics*, 50 (1992) 11.
- [32] Awadallah, A.M., Mahmood, S.H., Maswadeh, Y., Bsoul, I. and Aloqaily, A.N., *IOP Conference Series: Materials Science and Engineering*, 92 (2015) 012006.
- [33] Albanese, G. and Deriu, A., *Ceramics International*, 5 (1979) 3.
- [34] Smit, J. and Wijn, H.P.J., "Ferrites", (Wiley, New York, 1959).
- [35] Soman, V.V., Nanoti, V.M. and Kulkarni, D.K., *Ceramics International*, 39 (2013) 5713.
- [36] Warren, B.E., "X-ray Diffraction", (Addison-Wesley, Reading, Massachusetts, 1969).
- [37] An, S.Y., Shim, I.-B. and Kim, C.S., *Journal of Applied Physics*, 91 (2002) 8465.

- [38] Bsoul, I. and Mahmood, S., *Jordan J. Phys.*, 2 (2009) 171.
- [39] Shepherd, P., Mallick, K.K. and Green, R.J., *Journal of Magnetism and Magnetic Materials*, 311 (2007) 683.
- [40] Rezlescu, L., Rezlescu, E., Popa, P. and Rezlescu, N., *Journal of Magnetism and Magnetic Materials*, 193 (1999) 288.
- [41] Abu-Aljarayesh, I., "Magnetic Recording", In: S.H. Mahmood and I. Abu-Aljarayesh (Eds.), "Hexaferrite Permanent Magnetic Materials", (Materials Research Forum LLC, Millersville, PA, 2016), pp. 166-181.
- [42] Cullity, B.D. and Graham, C.D., "Introduction to Magnetic Materials, 2<sup>nd</sup> edn., (John Wiley & Sons, Hoboken, NJ, 2011).
- [43] Grössinger, R., *Physica Status Solidi (a)*, 66 (1981) 665.
- [44] Topal, U., *Materials Science and Engineering: B*, 176 (2011) 1531.
- [45] Mahmood, S.H., Aloqaily, A.N., Maswadeh, Y., Awadallah, A., Bsoul, I. and Juwhari, H., *Material Science Research India*, 11 (2014) 09.
- [46] Bsoul, I. and Mahmood, S., *Journal of Alloys and Compounds*, 489 (2010) 110.
- [47] Awawdeh, M., Bsoul, I. and Mahmood, S.H., *Journal of Alloys and Compounds*, 585 (2014) 465.
- [48] Sharma, P., Roch, R.A., Medeiros, S.N., Hallouche, B. and Paesano Jr, A., *Journal of Magnetism and Magnetic Materials*, 316 (2007) 29.
- [49] Mahmood, S.H. and Bsoul, I., *EPJ Web of Conferences*, 29 (2012) 00039.



### **Solution of the Hamilton – Jacobi Equation in a Central Potential Using the Separation of Variables Method with Staeckel Boundary Conditions**

**B. M. Al-Khamiseh<sup>a</sup>, R. S. Hijjawi<sup>b</sup> and J. M. Khalifeh<sup>a</sup>**

<sup>a</sup> *Department of Physics, The University of Jordan, 11942-Amman, Jordan.*

<sup>b</sup> *Department of Physics, Mutah University, Al-Karak, Jordan.*

**Doi:** <https://doi.org/10.47011/14.4.3>

*Received on: 12/05/2020;*

*Accepted on: 29/11/2020*

---

**Abstract:** This manuscript aims at solving Hamilton-Jacobi equation in a central potential using the separation of variables technique with Staeckel boundary conditions. Our results show that the Hamilton – Jacobi variables can be completely separated, which agrees with other results employing different methods.

**Keywords:** Lagrangian mechanics, Hamilton-Jacobi, Staeckel boundary conditions, Staeckel matrix, Staeckel vector, Hamilton's characteristic function, Hamilton's principal function.

## **Introduction**

The Hamilton-Jacobi equation is based not just on the physical problems included, but also on the choice of generalized coordinate system. Thus, the one-body central force problem is detachable in polar coordinates, but not in Cartesian coordinates. In some problems, it is not at all possible to completely separate the Hamilton-Jacobi equation, the known three-body problem being one illustration. Otherwise, in many fundamental problems of mechanics and atomic physics, one can carry out the separation in more than one set of coordinates. When the variables are completely separable, it is feasible to solve the Hamilton-Jacobi equation [1].

One of the methods to separate variables is the Staeckel approach. This method applies to some Hamiltonians in which certain conditions are satisfied, such as: conservative Hamiltonian and orthogonal coordinates. This method also helps find the complete solution of the differential equations which are not easy to solve.

It was not known what is the most comprehensive separation system with  $n$  degrees of freedom. However, it is now known what a detachable orthogonal system is with  $n$  degrees of freedom. This was discovered by Staeckel in his habilitation thesis [2]. These systems are now called Staeckel systems. The theory of Staeckel systems can be found in several publications, such as references [3-22].

The first major contribution by Staeckel [3] was to find all the separable metrics for an arbitrary two-dimensional Riemannian manifold. He proved the theorem connecting the integrability of a Staeckel system with the existence of a matrix  $S$  called a Staeckel matrix for the system. Staeckel [2] showed how to determine the quantities  $H_i$  (Eq. 3) in the Hamilton- Jacobi equation so that the variables are separable.

Benet [23] presented basic definitions and theorems concerning the algebra of contravariant symmetric tensors and killing tensors.

Benenti *et al.* [24] showed that the three-body Calogero system is in fact separable in infinitely many ways; thus, it is super-separable.

This work aims at solving the Hamilton-Jacobi equation using the separation of variables method. We will use the Staeckel boundary conditions to separate variables.

This paper is organized as follows: the following section presents some basic definitions of the Hamilton-Jacobi equation of a Staeckel system. The next section presents how to solve the Hamilton-Jacobi equation by the method of Staeckel boundary conditions. Finally, the last section is dedicated to our conclusions.

## Basic Definitions

In this part of the manuscript, we briefly introduce some of the fundamental definitions used in this work [25].

### A- Staeckel Matrix $\Phi$ and Staeckel Vector $\Psi$

In a Staeckel system with  $n$  degrees of freedom, we will assume an  $(n \times n)$  matrix  $\Phi$  and a vector  $\Psi$  with  $n$  components  $\Psi_r$ . Actually,  $n^2 + n$  components of  $\Phi$  and  $\Psi$  solve completely the Staeckel system and that's why we will call them the Staeckel matrix and the Staeckel vector. The elements are all functions of the coordinate  $q_r$ , but in the upcoming way:

$$\Phi_{rl} = \Phi_{rl}(q_r), \Psi_r = \Psi_r(q_r). \quad (1)$$

In short, one coordinate consists of a row  $r$  of both  $\Phi$  and  $\Psi$ . We will say that the rows of  $\Phi$  are with separated variables; that is, the rows of  $\Phi$  are separated. This indicates that this separation property controls the whole theory of Staeckel system.

First, we will need the cofactors  $C_{ij}$  of the matrix elements  $\Phi_{ij}$  of the matrix  $\Phi$ , in addition to the determinant  $\Delta$  and the inverse  $v$  of matrix  $\Phi$ . We will set the elements of the inverse  $v = \Phi^{-1}$  of the matrix  $\Phi$  by  $(\Phi^{-1})_{ij}$  or call them  $v_{ij}$ .

We may need some well-known properties of determinants and matrices, such as:

$$\sum_j \Phi_{ij} v_{jk} = \sum_j v_{ij} \Phi_{jk} = \delta_{ik} \quad (2)$$

$$v_{ij} = \frac{C_{ij}}{\Delta} \quad (3)$$

$$\sum_i \Phi_{ji} C_{ik} = \Delta \sum_i \Phi_{ji} v_{ik} = \Delta \delta_{jk}. \quad (4)$$

The result of the separation property (1) is that the cofactor  $C_{ij}$  will depend on  $(n-1)$  coordinates only;  $C_{ij}$  is independent of the variable  $q_i$ . This will simplify many partial derivatives; for example:

$$\frac{\partial \Delta}{\partial q_k} = \sum_i C_{ki} \frac{\partial \Phi_{ik}}{\partial q_k}. \quad (5)$$

### B- The Hamiltonian of a Staeckel System

In terms of the notations and initial developments (given in sub-section A), we can now easily define a Staeckel system. The Staeckel system can be defined as:

$$H = \sum_{k=1}^n \left[ \frac{\dot{q}_k^2}{2v_{1k}} + v_{1k} \Psi_k \right] = \sum_{k=1}^n v_{1k} \left[ \frac{\dot{q}_k^2}{2v_{1k}^2} + \Psi_k \right], \quad (6)$$

where the kinetic energy is given by:  $T = \sum_{k=1}^n \frac{\dot{q}_k^2}{2v_{1k}}$  and the potential energy is:  $V = \sum_{k=1}^n v_{1k} \Psi_k$ .

We can see that all the ingredients are the Staeckel vector  $\Psi$  and the first row of the inverse of the Staeckel matrix  $\Phi$ . The second form of the Hamiltonian shown in Eq. (6) is the product of a row vector,  $v_{1k}$ , by a column vector,  $\Psi_k$ . The elements  $g_{kk}$  of the diagonal metric tensor are thus given by:

$$g_{kk} = \frac{1}{v_{1k}} = \frac{1}{(\Phi^{-1})_{1k}} = \frac{\Delta}{C_{k1}} \quad (\text{with } \sum_k \frac{\Phi_{ks}}{g_{kk}} = \delta_{1k}). \quad (7)$$

As a result of the notes of sub-section A, we have:

$$\frac{\partial g_{kk}}{\partial q_k} = \frac{1}{C_{k1}} \frac{\partial \Delta}{\partial q_k} = \sum_i \frac{C_{ki}}{C_{k1}} \frac{\partial \Phi_{ki}}{\partial q_k}. \quad (8)$$

In the following, we simply derive the Hamiltonian equations of motion,  $\dot{P}_l = -\frac{\partial H}{\partial q^l}$  from Eq. (6); thus:

$$\frac{d}{dt} \left[ \frac{\dot{q}_l}{v_{1l}} \right] = - \sum_{k=1}^n \left[ \frac{\dot{q}_k^2}{2v_{1k}^2} - \Psi_k \right] \frac{\partial v_{1k}}{\partial q_l} + v_{1l} \frac{\partial \Psi_l}{\partial q_l}. \quad (9)$$

The Staeckel Hamiltonian does not depend explicitly on time; that is, we have a conservative system with the classical energy integral given as follows:

$$\sum_{k=1}^n v_{1k} \left[ \frac{\dot{q}_k^2}{2v_{1k}^2} + \Psi_k \right] = \alpha_1 = \text{constant}. \quad (10)$$

It will be useful to write this first integral also in a different form. Let us take benefit of the

relation in Eq. (2) and add to Eq. (10) some terms which are zeros or ones:

$$\sum_{k=1}^n v_{1k} \left[ \frac{\dot{q}_k^2}{2v_{1k}^2} + \Psi_k \right] = \alpha_1 \sum_k v_{1k} \Phi_{k1} + \alpha_2 \sum_k v_{1k} \Phi_{k2} + \dots + \alpha_n \sum_k v_{1k} \Phi_{kn}, \quad (11)$$

where the  $\alpha$ 's are all arbitrary constants. Compiling the terms differently leads to:

$$\sum_{k=1}^n v_{1k} \left[ \frac{\dot{q}_k^2}{2v_{1k}^2} + \Psi_k - \sum_{r=1}^n \Phi_{kr} \alpha_r \right] = 0, \quad (12)$$

where the constants  $\alpha$ 's are sometimes called separation constants. The interest of the above form of energy integral is actually in that the last two terms in the brackets are now with separated variables.

The most important property of Staeckel systems exists in the following theorem:

"Not only the expression given in Eq. (12) is zero, but also each bracket separately" [8]:

$$\frac{\dot{q}_k^2}{2v_{1k}^2} + \Psi_k = \sum_{r=1}^n \Phi_{kr} \alpha_r. \quad (13)$$

### C- Completion of the Solution of the Staeckel System

The first integral in Eq. (12) can be written in another form as:

$$\frac{\dot{q}_k^2}{v_{1k}^2} = 2(\sum_{r=1}^n \Phi_{kr} \alpha_r - \Psi_k) = f_k(q_k). \quad (14)$$

We have also:

$$\frac{\dot{q}_k}{\sqrt{f_k(q_k)}} = v_{1k}. \quad (15)$$

Multiplying by  $\Phi_{kr}$  and summing over  $k$  produce:

$$\sum_{k=1}^n \frac{\dot{q}_k \Phi_{kr}}{\sqrt{f_k(q_k)}} = \sum_{k=1}^n v_{1k} \Phi_{kr} = \delta_{1r}. \quad (16)$$

We see that each term in the sum on the left-hand side is a function of one variable  $q_k$  only:

$$\sum_{k=1}^n \int \frac{\varphi_{kr} dq_k}{\sqrt{f_k(q_k)}} = \beta_r = \text{constant } r = 2, 3, 4, \dots, n \quad (17.A)$$

$$\sum_{k=1}^n \int \frac{\Phi_{k1} dq_k}{\sqrt{f_k(q_k)}} = t - t_0. \quad (17.B)$$

This inserts  $n$  new constants of integration; altogether  $2n$  constants of integration are inserted. Finally,  $n$  equations can be solved and give the  $n$  coordinates  $q_k$  as a function of time  $t$  and the constants,  $\beta_r$ . The velocities are then given by Eq. (13). We have to use Eqs. (17.A) and (17.B) to calculate the values of the

constants of integrations with the initial conditions.

### D- Separation of Variables of Hamilton-Jacobi Equation Using Staeckel Boundary Conditions

The separation of Hamilton-Jacobi equations is a characteristic of the dynamic system as well as the coordinates that are described. A simple criterion cannot be given to refer to a coordinate system those results in a separate Hamilton Jacobi equation for a particular system. However, if

- The Hamiltonian is conserved and takes the form:

$$H = \frac{1}{2}(\mathbf{P} - \mathbf{a})\mathbf{T}^{-1}(\mathbf{P} - \mathbf{a}) + V(\mathbf{q}). \quad (A)$$

Here,  $\mathbf{a}$  is a column matrix,  $\mathbf{T}$  is a square  $n \times n$  matrix and  $\mathbf{p}$  is a row matrix.

- The set of generalized coordinates  $q_i$  forms an orthogonal system of coordinates, so that the matrix  $\mathbf{T}$  is diagonal. It follows that the inverse matrix  $\mathbf{T}^{-1}$  is also diagonal with non-vanishing elements:

$$(\mathbf{T}^{-1})_{ii} = \frac{1}{T_{ii}}. \quad (B)$$

- For problems and coordinates satisfying this description, the Staeckel conditions state that the Hamilton-Jacobi equation will be completely separable if the vector  $\mathbf{a}$  has elements  $\mathbf{a}_i$  that are functions only of the corresponding coordinate; that is,  $\mathbf{a}_i = \mathbf{a}_i(q_i)$  and the potential function  $V(\mathbf{q})$  can be written as a sum of the form:

$$V(\mathbf{q}) = \frac{V_i(q_i)}{T_{ii}}. \quad (C)$$

- There exists an  $n \times n$  matrix  $\Phi$  with elements  $\Phi_{ij} = \Phi_{ij}(q_i)$ , such that:

$$(\Phi^{-1})_{1j} = \frac{1}{T_{jj}}. \quad (D)$$

Consider the motion of a particle of mass  $m$  in a central force field with potential  $V = -\frac{k}{r} + \frac{h}{r^2}$ . The Hamilton – Jacobi equation is:

$$H = T + V = \frac{1}{2m} \left[ p_r^2 + \frac{p_\theta^2}{r^2} + \frac{p_\phi^2}{r^2 \sin^2 \theta} \right] - \frac{k}{r} + \frac{h}{r^2}. \quad (18)$$

Comparing Eq. (18) with the equation:  $H = \frac{1}{2}(\mathbf{P} - \mathbf{a})\mathbf{T}^{-1}(\mathbf{P} - \mathbf{a}) + V(\mathbf{q})$ , we get:

$$T^{-1} = \begin{pmatrix} \frac{1}{m} & 0 & 0 \\ 0 & \frac{1}{mr^2} & 0 \\ 0 & 0 & \frac{1}{mr^2 \sin^2 \theta} \end{pmatrix}. \tag{19}$$

Applying Staeckel boundary conditions, we satisfy:

$$(T^{-1})_{ii} = \frac{1}{T_{ii}} = \begin{pmatrix} \frac{1}{m} & 0 & 0 \\ 0 & \frac{1}{mr^2} & 0 \\ 0 & 0 & \frac{1}{mr^2 \sin^2 \theta} \end{pmatrix}, \tag{20}$$

in addition to the following two conditions:

$$(\Phi^{-1})_{1j} = \frac{1}{T_{jj}} = \begin{pmatrix} \frac{1}{m} & \frac{1}{mr^2} & \frac{1}{mr^2 \sin^2 \theta} \\ 0 & \frac{1}{m} & \frac{1}{mr^2 \sin^2 \theta} \\ 0 & \frac{-1}{m^2} & \frac{1}{m} \end{pmatrix} \tag{21}$$

and we get:

$$V(q) = \frac{V_i(q_i)}{T_{ii}} = \left( \frac{\psi_1(r)}{m} \right). \tag{22}$$

If the Staeckel conditions are satisfied, then Hamilton's characteristic function is completely separable:

$$W(q) = \sum_i W_i(q_i). \tag{23}$$

Inserting H from Eq. (18) into equation  $H\left(q, \frac{\partial W}{\partial q}\right) + \frac{\partial S_0}{\partial t} = 0$  and using the definition of momentum  $p = \frac{\partial W}{\partial q}$ , we obtain:

$$\frac{1}{2m} \left[ \left[ \frac{\partial W_r}{\partial r} \right]^2 + \frac{1}{r^2} \left[ \frac{\partial W_\theta}{\partial \theta} \right]^2 + \frac{1}{r^2 \sin^2 \theta} \left[ \frac{\partial W_\varphi}{\partial \varphi} \right]^2 \right] - \frac{k}{r} + \frac{h}{r^2} = \alpha. \tag{24}$$

Here,  $\varphi$  is a cyclic coordinate. We get:

$$\left[ \frac{\partial W_\varphi}{\partial \varphi} \right]^2 = \alpha_\varphi^2. \tag{25}$$

Integrating Eq. (25), we find:

$$W_{\varphi'} = \int_0^\varphi \alpha_\varphi d\varphi = \alpha_\varphi \varphi'. \tag{26}$$

Substituting Eq. (25) into Eq. (24), we get:

$$\frac{1}{2m} \left[ r^2 \left[ \frac{\partial W_r}{\partial r} \right]^2 + \left[ \frac{\partial W_\theta}{\partial \theta} \right]^2 + \frac{\alpha_\varphi^2}{\sin^2 \theta} \right] - kr + h = \alpha r^2. \tag{27}$$

$$\text{We replace } \left[ \frac{\partial W_\theta}{\partial \theta} \right]^2 + \frac{\alpha_\varphi^2}{\sin^2 \theta} = \alpha_\theta^2 \tag{28}$$

in Eq. (27); we obtain:

$$\left[ \frac{\partial W_r}{\partial r} \right]^2 = 2m\alpha + \frac{2mk}{r} - \frac{2mh}{r^2} - \frac{\alpha_\theta^2}{r^2}. \tag{29}$$

Integrating Eqs. (28) and (29), we have:

$$W_{\theta'} = \int_0^{\theta'} \sqrt{\left( \alpha_\theta^2 - \frac{\alpha_\varphi^2}{\sin^2 \theta} \right)} d\theta \tag{30}$$

$$W_{r'} = \int_{r_0}^{r'} \sqrt{\left( 2m\alpha + \frac{2mk}{r} - \frac{2mh}{r^2} - \frac{\alpha_\theta^2}{r^2} \right)} dr \tag{31}$$

The Hamilton's characteristic function becomes  $W = W_{r'} + W_{\theta'} + W_{\varphi'}$

$$W = \int_{r_0}^{r'} \sqrt{\left( 2m\alpha + \frac{2mk}{r} - \frac{2mh}{r^2} - \frac{\alpha_\theta^2}{r^2} \right)} dr + \int_0^{\theta'} \sqrt{\left( \alpha_\theta^2 - \frac{\alpha_\varphi^2}{\sin^2 \theta} \right)} d\theta + \alpha_\varphi \varphi' \tag{32}$$

Solving Eq. (30):

$$W_{\theta'} = \int_0^{\theta'} \sqrt{\left( \alpha_\theta^2 - \frac{\alpha_\varphi^2}{\sin^2 \theta} \right)} d\theta = \alpha_\theta \int_0^{\theta'} \sqrt{\left( 1 - \frac{\alpha_\varphi^2}{\alpha_\theta^2 \sin^2 \theta} \right)} d\theta. \tag{33}$$

We replace  $\cos \gamma = \frac{\alpha_\varphi}{\alpha_\theta}$  and the identity  $\sin^2 \theta = 1 - \cos^2 \theta$  in Eq. (33); we find:

$$W_{\theta'} = \alpha_\theta \int_0^{\theta'} \frac{1}{\sin \theta} \sqrt{(\sin^2 \gamma - \cos^2 \theta)} d\theta. \tag{34}$$

Let  $\cos \theta = \sin \gamma \sin \psi$  and substituting in Eq. (34), we get:

$$W_{\theta'} = \alpha_\theta \int_{\psi_1}^{\psi_2} \frac{\sin^2 \gamma \cos^2 \psi}{\sin^2 \theta} d\psi, \tag{35}$$

where  $\psi_1 = \sin^{-1} \left[ \frac{1}{\sin \gamma} \right]$  and  $\psi_2 = \sin^{-1} \left[ \frac{\cos \theta}{\sin \gamma} \right]$ .

Assume that  $u = \tan \psi$  and substitute in Eq. (35); we obtain:

$$W_{\theta'} = \alpha_\theta \int_{u_1}^{u_2} \frac{\sin^2 \gamma \cos^4 \psi}{1 - \sin^2 \gamma \sin^2 \psi} du = \alpha_\theta \sin^2 \gamma \int_{u_1}^{u_2} \frac{1}{\frac{1 - \sin^2 \gamma \sin^2 \psi}{\cos^4 \psi}} du, \tag{36}$$

where  $u_1 = \tan \left[ \sin^{-1} \left( \frac{1}{\sin \theta} \right) \right]$  and  $u_2 = \tan \left[ \sin^{-1} \left( \frac{\cos \theta}{\sin \theta} \right) \right]$ .

We replace  $\frac{1 - \sin^2 \gamma \sin^2 \psi}{\cos^4 \psi} = \frac{1}{(1+u^2)(1+u^2 \cos^2 \gamma)}$  and  $\sin^2 \gamma = 1 - \cos^2 \gamma$  in Eq. (36); we get:

$$W_{\theta'} = \alpha_\theta \int_{u_1}^{u_2} \frac{1 - \cos^2 \gamma}{(1+u^2)(1+u^2 \cos^2 \gamma)} du = \alpha_\theta \int_{u_1}^{u_2} \left( \frac{1}{(1+u^2)} - \frac{\cos^2 \gamma}{(1+u^2 \cos^2 \gamma)} \right) du. \tag{37}$$

This last form involves only well-known integrals and the final result is:

$$W_{\theta'} = \alpha_\theta (\tan^{-1}(u) - \cos \gamma \tan^{-1}(u \cos \gamma)). \tag{38}$$

Substituting integration limits in Eq. (38), we obtain:

$$W_{\theta'} = \alpha_{\theta'}(\psi - \cos\gamma \tan^{-1}(\tan\psi \cos\gamma)) = \alpha_{\theta'}\left(\sin^{-1}\left[\frac{\sin\gamma}{\cos\theta'}\right] - \cos\gamma \tan^{-1}\left(\tan\left[\sin^{-1}\left[\frac{\sin\gamma}{\cos\theta'}\right]\right] \cos\gamma\right) - \alpha_{\theta'}(\gamma - \cos\gamma \tan^{-1}(\sin\gamma)). \quad (39)$$

Solving Eq. (31), we obtain:

$$W_{r'} = \sqrt{2m} \int_{r_0}^{r'} \sqrt{\left(\alpha + \frac{k}{r} - \frac{(\alpha_{\theta'}^2 + 2mh)}{2mr^2}\right)} dr. \quad (40)$$

Using the relation  $\frac{(\sqrt{\quad})^2}{\sqrt{\quad}}$  to solve Eq. (40), we get:

$$W_{r'} = \sqrt{2m} \int_{r_0}^{r'} \frac{\alpha + \frac{k}{2r} + \frac{k}{2r} - \frac{(\alpha_{\theta'}^2 + 2mh)}{2mr^2}}{\sqrt{\left(\alpha + \frac{k}{r} - \frac{(\alpha_{\theta'}^2 + 2mh)}{2mr^2}\right)}} dr. \quad (41)$$

Rewrite Eq. (41) as:

$$W_{r'} = \sqrt{2m} \left[ \int_{r_0}^{r'} \frac{\alpha + \frac{k}{2r}}{\sqrt{\left(\alpha + \frac{k}{r} - \frac{(\alpha_{\theta'}^2 + 2mh)}{2mr^2}\right)}} dr + \int_{r_0}^{r'} \frac{\frac{k}{2r}}{\sqrt{\left(\alpha + \frac{k}{r} - \frac{(\alpha_{\theta'}^2 + 2mh)}{2mr^2}\right)}} dr + \int_{r_0}^{r'} \frac{\frac{(\alpha_{\theta'}^2 + 2mh)}{2mr^2}}{\sqrt{\left(\alpha + \frac{k}{r} - \frac{(\alpha_{\theta'}^2 + 2mh)}{2mr^2}\right)}} dr \right]. \quad (42)$$

The first integral in Eq. (42) can be solved as:

$$\begin{aligned} \int_{r_0}^{r'} \frac{\alpha + \frac{k}{2r}}{\sqrt{\left(\alpha + \frac{k}{r} - \frac{(\alpha_{\theta'}^2 + 2mh)}{2mr^2}\right)}} dr &= \\ \int_{r_0}^{r'} d\left(r \sqrt{\left(\alpha + \frac{k}{r} - \frac{(\alpha_{\theta'}^2 + 2mh)}{2mr^2}\right)}\right) &= \\ r' \sqrt{\left(\alpha + \frac{k}{r'} - \frac{(\alpha_{\theta'}^2 + 2mh)}{2mr'^2}\right)} - & \\ r_0 \sqrt{\left(\alpha + \frac{k}{r_0} - \frac{(\alpha_{\theta'}^2 + 2mh)}{2mr_0^2}\right)}. & \end{aligned} \quad (43)$$

Similarly, the second integral in Eq. (42) can be solved as:

$$\begin{aligned} \int_{r_0}^{r'} \frac{\frac{k}{2r}}{\sqrt{\left(\alpha + \frac{k}{r} - \frac{(\alpha_{\theta'}^2 + 2mh)}{2mr^2}\right)}} dr &= \\ \frac{\sqrt{2mk}}{2\sqrt{\alpha_{\theta'}^2 + 2mh}} \int_{r_0}^{r'} \frac{1}{\sqrt{\left(\frac{2mar^2}{\alpha_{\theta'}^2 + 2mh} + \frac{2mkr}{\alpha_{\theta'}^2 + 2mh} - 1\right)}} dr &= \\ \frac{\sqrt{2mk}}{2\sqrt{\alpha_{\theta'}^2 + 2mh}} \int_{r_0}^{r'} \frac{1}{r \sqrt{\left(\frac{2m\alpha}{\alpha_{\theta'}^2 + 2mh} + \frac{2mk}{(\alpha_{\theta'}^2 + 2mh)r} - \frac{1}{r^2}\right)}} dr. & \end{aligned} \quad (44)$$

Let  $u = \frac{1}{r}$  and substitute in Eq. (44) to get:

$$\frac{\sqrt{2mk}}{2\sqrt{\alpha_{\theta'}^2 + 2mh}} \int_{u_0}^u \frac{-rdu}{\sqrt{\left(\frac{2m\alpha}{\alpha_{\theta'}^2 + 2mh} + \frac{2mku}{(\alpha_{\theta'}^2 + 2mh)} - u^2\right)}}. \quad (45)$$

We can replace  $\frac{2m\alpha}{\alpha_{\theta'}^2 + 2mh} + \frac{2mku}{(\alpha_{\theta'}^2 + 2mh)} - u^2 = \frac{1}{\alpha_{\theta'}^2 + 2mh} \left[2m\alpha + \frac{m^2k^2}{\alpha_{\theta'}^2 + 2mh}\right] - \left(u - \frac{mk}{\alpha_{\theta'}^2 + 2mh}\right)^2$  in Eq. (45); we obtain:

$$\frac{\sqrt{2mk}}{2\sqrt{\alpha_{\theta'}^2 + 2mh}} \int_{u_0}^u \frac{-rdu}{\sqrt{\left(\frac{1}{\alpha_{\theta'}^2 + 2mh} \left[2m\alpha + \frac{m^2k^2}{\alpha_{\theta'}^2 + 2mh}\right] - \left(u - \frac{mk}{\alpha_{\theta'}^2 + 2mh}\right)^2\right)}}. \quad (46)$$

Rewrite:

$$u - \frac{mk}{\alpha_{\theta'}^2 + 2mh} = \sqrt{\frac{1}{\alpha_{\theta'}^2 + 2mh} \left[2m\alpha + \frac{m^2k^2}{\alpha_{\theta'}^2 + 2mh}\right]} \sin\theta$$

and substituting in Eq. (46), we get:

$$\frac{\sqrt{2mk}}{2\sqrt{\alpha_{\theta'}^2 + 2mh}} \int_{\theta_0}^{\theta} -rd\theta, \quad (47)$$

$$\text{where } \theta_0 = \sin^{-1} \left( \frac{u_0 - \frac{mk}{\alpha_{\theta'}^2 + 2mh}}{\sqrt{\frac{1}{\alpha_{\theta'}^2 + 2mh} \left[2m\alpha + \frac{m^2k^2}{\alpha_{\theta'}^2 + 2mh}\right]}} \right) \text{ and}$$

$$\theta = \sin^{-1} \left( \frac{u - \frac{mk}{\alpha_{\theta'}^2 + 2mh}}{\sqrt{\frac{1}{\alpha_{\theta'}^2 + 2mh} \left[2m\alpha + \frac{m^2k^2}{\alpha_{\theta'}^2 + 2mh}\right]}} \right).$$

Let  $\frac{r}{a} = 1 - e \cos\theta$ , where  $a = \frac{k}{-2\alpha}$  and eccentricity  $e = \sqrt{1 + \frac{2(\alpha_{\theta'}^2 + 2mh)\alpha}{mk^2}}$  and let

$e = 0$  because the path is circular and substitute  $\sqrt{\alpha_{\theta'}^2 + 2mh} = \sqrt{\frac{-mk}{2\alpha}}$ , we can rewrite Eq. (47):

$$\sqrt{k\alpha} \int_{\theta_0}^{\theta} a d\theta = a\sqrt{-k\alpha} \cos^{-1} \left( \frac{1}{e} \left( 1 - \frac{r'}{a} \right) \right) - a\sqrt{-k\alpha} \cos^{-1} \left( \frac{1}{e} \left( 1 - \frac{r_0}{a} \right) \right). \tag{48}$$

The third integral in Eq. (42) can be solved as:

$$\int_{r_0}^{r'} \frac{\frac{(\alpha_{\theta'}^2 + 2mh)}{2mr^2}}{\sqrt{\left( \alpha + \frac{k}{r} - \frac{(\alpha_{\theta'}^2 + 2mh)}{2mr^2} \right)}} dr = \int_{r_0}^{r'} \frac{\frac{(\alpha_{\theta'}^2 + 2mh)}{2mr^2} \sqrt{2mr^2}}{\sqrt{\alpha_{\theta'}^2 + 2mh} \sqrt{\left( \frac{2ma r^2}{\alpha_{\theta'}^2 + 2mh} + \frac{2mkr}{\alpha_{\theta'}^2 + 2mh} - 1 \right)}} dr = -\sqrt{\frac{\alpha_{\theta'}^2 + 2mh}{2m}} \int_{r_0}^{r'} \frac{dr}{r^2 \sqrt{\left( \frac{2m\alpha}{\alpha_{\theta'}^2 + 2mh} + \frac{2mk}{(\alpha_{\theta'}^2 + 2mh)r} - \frac{1}{r^2} \right)}}. \tag{49}$$

Let  $u = \frac{1}{r}$  and substitute in Eq. (49); we get:

$$\sqrt{\frac{\alpha_{\theta'}^2 + 2mh}{2m}} \int_{u_0}^u \frac{du}{\sqrt{\left( \frac{2m\alpha}{\alpha_{\theta'}^2 + 2mh} + \frac{2mku}{(\alpha_{\theta'}^2 + 2mh)} - u^2 \right)}}. \tag{50}$$

We can replace  $\frac{2m\alpha}{\alpha_{\theta'}^2 + 2mh} + \frac{2mku}{(\alpha_{\theta'}^2 + 2mh)} - u^2 = \frac{1}{\alpha_{\theta'}^2 + 2mh} \left[ 2m\alpha + \frac{m^2 k^2}{\alpha_{\theta'}^2 + 2mh} \right] - \left( u - \frac{mk}{\alpha_{\theta'}^2 + 2mh} \right)^2$  in Eq. (50) to find:

$$\sqrt{\frac{\alpha_{\theta'}^2 + 2mh}{2m}} \int_{u_0}^u \frac{du}{\sqrt{\left( \frac{1}{\alpha_{\theta'}^2 + 2mh} \left[ 2m\alpha + \frac{m^2 k^2}{\alpha_{\theta'}^2 + 2mh} \right] - \left( u - \frac{mk}{\alpha_{\theta'}^2 + 2mh} \right)^2 \right)}}. \tag{51}$$

Let:

$$u - \frac{mk}{\alpha_{\theta'}^2 + 2mh} = \sqrt{\frac{1}{\alpha_{\theta'}^2 + 2mh} \left[ 2m\alpha + \frac{m^2 k^2}{\alpha_{\theta'}^2 + 2mh} \right]} \sin\theta$$

and substituting in Eq. (51), we can get:

$$\sqrt{\frac{\alpha_{\theta'}^2 + 2mh}{2m}} \sin^{-1} \left( \frac{\frac{\alpha_{\theta'}^2 + 2mh}{r'} - mk}{\sqrt{2m\alpha(\alpha_{\theta'}^2 + 2mh) + m^2 k^2}} \right) - \sqrt{\frac{\alpha_{\theta'}^2 + 2mh}{2m}} \sin^{-1} \left( \frac{\frac{\alpha_{\theta'}^2 + 2mh}{r_0} - mk}{\sqrt{2m\alpha(\alpha_{\theta'}^2 + 2mh) + m^2 k^2}} \right). \tag{52}$$

Substituting Eqs. (43), (48) and (52) in Eq. (42), we get:

$$W_{r'} = \sqrt{2m} r' \sqrt{\left( \alpha + \frac{k}{r'} - \frac{(\alpha_{\theta'}^2 + 2mh)}{2mr'^2} \right)} - \sqrt{2m} r_0 \sqrt{\left( \alpha + \frac{k}{r_0} - \frac{(\alpha_{\theta'}^2 + 2mh)}{2mr_0^2} \right)} + \sqrt{2m} a\sqrt{-k\alpha} \cos^{-1} \left( \frac{1}{e} \left( 1 - \frac{r'}{a} \right) \right) - \sqrt{2m} a\sqrt{-k\alpha} \cos^{-1} \left( \frac{1}{e} \left( 1 - \frac{r_0}{a} \right) \right) + \sqrt{\alpha_{\theta'}^2 + 2mh} \sin^{-1} \left( \frac{\frac{\alpha_{\theta'}^2 + 2mh}{r'} - mk}{\sqrt{2m\alpha(\alpha_{\theta'}^2 + 2mh) + m^2 k^2}} \right) - \sqrt{\alpha_{\theta'}^2 + 2mh} \sin^{-1} \left( \frac{\frac{\alpha_{\theta'}^2 + 2mh}{r_0} - mk}{\sqrt{2m\alpha(\alpha_{\theta'}^2 + 2mh) + m^2 k^2}} \right). \tag{53}$$

The complete characteristic function is:

$$W = \sqrt{2m} r' \sqrt{\left( \alpha + \frac{k}{r'} - \frac{(\alpha_{\theta'}^2 + 2mh)}{2mr'^2} \right)} - \sqrt{2m} r_0 \sqrt{\left( \alpha + \frac{k}{r_0} - \frac{(\alpha_{\theta'}^2 + 2mh)}{2mr_0^2} \right)} + \sqrt{2m} a\sqrt{-k\alpha} \cos^{-1} \left( \frac{1}{e} \left( 1 - \frac{r'}{a} \right) \right) - \sqrt{2m} a\sqrt{-k\alpha} \cos^{-1} \left( \frac{1}{e} \left( 1 - \frac{r_0}{a} \right) \right) + \sqrt{\alpha_{\theta'}^2 + 2mh} \sin^{-1} \left( \frac{\frac{\alpha_{\theta'}^2 + 2mh}{r'} - mk}{\sqrt{2m\alpha(\alpha_{\theta'}^2 + 2mh) + m^2 k^2}} \right) - \sqrt{\alpha_{\theta'}^2 + 2mh} \sin^{-1} \left( \frac{\frac{\alpha_{\theta'}^2 + 2mh}{r_0} - mk}{\sqrt{2m\alpha(\alpha_{\theta'}^2 + 2mh) + m^2 k^2}} \right) + \alpha_{\theta'} \left( \sin^{-1} \left[ \frac{\sin\gamma}{\cos\theta} \right] - \cos\gamma \tan^{-1} \left( \tan \left[ \sin^{-1} \left[ \frac{\sin\gamma}{\cos\theta} \right] \right] \cos\gamma \right) \right) - \alpha_{\theta'} (\gamma - \cos\gamma \tan^{-1}(\sin\gamma)) + \alpha_{\theta'} \varphi'. \tag{54}$$

Substituting Eq. (54) in Eq.  $S(q, \alpha, t) = W(q, \alpha) - at$ , we obtain:

$$\begin{aligned}
 S(q, \alpha, t) = & \sqrt{2m} r' \sqrt{\left(\alpha + \frac{k}{r'} - \frac{(\alpha_\theta^2 + 2mh)}{2mr'^2}\right)} - \\
 & \sqrt{2m} r_0 \sqrt{\left(\alpha + \frac{k}{r_0} - \frac{(\alpha_\theta^2 + 2mh)}{2mr_0^2}\right)} + \\
 & \sqrt{2m} a \sqrt{-k\alpha} \cos^{-1} \left(\frac{1}{e} \left(1 - \frac{r'}{a}\right)\right) - \\
 & \sqrt{2m} a \sqrt{-k\alpha} \cos^{-1} \left(\frac{1}{e} \left(1 - \frac{r_0}{a}\right)\right) + \\
 & \sqrt{\alpha_\theta^2 + 2mh} \sin^{-1} \left(\frac{\frac{\alpha_\theta^2 + 2mh}{r'} - mk}{\sqrt{2m\alpha(\alpha_\theta^2 + 2mh) + m^2 k^2}}\right) - \\
 & \sqrt{\alpha_\theta^2 + 2mh} \sin^{-1} \left(\frac{\frac{\alpha_\theta^2 + 2mh}{r_0} - mk}{\sqrt{2m\alpha(\alpha_\theta^2 + 2mh) + m^2 k^2}}\right) + \\
 & \alpha_\theta' \left(\sin^{-1} \left[\frac{\sin \gamma}{\cos \theta'}\right] - \right. \\
 & \left. \cos \gamma \tan^{-1} \left(\tan \left[\sin^{-1} \left[\frac{\sin \gamma}{\cos \theta'}\right]\right] \cos \gamma\right)\right) - \\
 & \alpha_\theta' (\gamma - \cos \gamma \tan^{-1}(\sin \gamma)) + \alpha_\phi' \varphi' - \alpha t.
 \end{aligned} \tag{55}$$

Differentiating Eq. (55) with respect to  $\alpha_i$ , we obtain:

$$\begin{aligned}
 \beta_r + t = \frac{\partial S}{\partial \alpha} = & \frac{\sqrt{\left(\frac{m}{2}\right) r'}}{\sqrt{\left(\alpha + \frac{k}{r'} - \frac{(\alpha_\theta^2 + 2mh)}{2mr'^2}\right)}} + \\
 & a \sqrt{\frac{-mk}{2\alpha}} \cos^{-1} \left(\frac{1}{e} \left(1 - \frac{r'}{a}\right)\right) + \\
 & \frac{2m(\alpha_\theta^2 + 2mh) \left(mk - \frac{(\alpha_\theta^2 + 2mh)}{r'}\right)}{\sqrt{\left(\left(2m\alpha(\alpha_\theta^2 + 2mh) + m^2 k^2\right)^2 - \left(2m(\alpha_\theta^2 + 2mh) \left(mk - \frac{(\alpha_\theta^2 + 2mh)}{r'}\right)\right)^2\right)}} - \\
 & \frac{\sqrt{\left(\frac{m}{2}\right) r_0}}{\sqrt{\left(\alpha + \frac{k}{r_0} - \frac{(\alpha_\theta^2 + 2mh)}{2mr_0^2}\right)}} - \\
 & a \sqrt{\frac{-mk}{2\alpha}} \cos^{-1} \left(\frac{1}{e} \left(1 - \frac{r_0}{a}\right)\right) - \\
 & \frac{2m(\alpha_\theta^2 + 2mh) \left(mk - \frac{(\alpha_\theta^2 + 2mh)}{r_0}\right)}{\sqrt{\left(\left(2m\alpha(\alpha_\theta^2 + 2mh) + m^2 k^2\right)^2 - \left(2m(\alpha_\theta^2 + 2mh) \left(mk - \frac{(\alpha_\theta^2 + 2mh)}{r_0}\right)\right)^2\right)}}
 \end{aligned} \tag{56.A}$$

$$\begin{aligned}
 \beta_{\theta'} = & \sqrt{\alpha_\theta^2 + 2mh} \times \\
 & \left( \frac{\frac{2\alpha_\theta'}{r'} \left(\sqrt{2m\alpha(\alpha_\theta^2 + 2mh) + m^2 k^2}\right) - 4m\alpha\alpha_\theta' \left(\frac{(\alpha_\theta^2 + 2mh)}{r'} - mk\right)}{\sqrt{\left(\left(2m\alpha(\alpha_\theta^2 + 2mh) + m^2 k^2\right)^2 - \left(\frac{2\alpha_\theta'}{r'} \left(\sqrt{2m\alpha(\alpha_\theta^2 + 2mh) + m^2 k^2}\right) - 4m\alpha\alpha_\theta' \left(\frac{(\alpha_\theta^2 + 2mh)}{r'} - mk\right)\right)^2\right)}} \right) - \\
 & \sqrt{\alpha_\theta^2 + 2mh} \times \\
 & \left( \frac{\frac{2\alpha_\theta'}{r_0} \left(\sqrt{2m\alpha(\alpha_\theta^2 + 2mh) + m^2 k^2}\right) - 4m\alpha\alpha_\theta' \left(\frac{(\alpha_\theta^2 + 2mh)}{r_0} - mk\right)}{\sqrt{\left(\left(2m\alpha(\alpha_\theta^2 + 2mh) + m^2 k^2\right)^2 - \left(\frac{2\alpha_\theta'}{r_0} \left(\sqrt{2m\alpha(\alpha_\theta^2 + 2mh) + m^2 k^2}\right) - 4m\alpha\alpha_\theta' \left(\frac{(\alpha_\theta^2 + 2mh)}{r_0} - mk\right)\right)^2\right)}} \right) + \\
 & \frac{\alpha_\theta'}{\sqrt{\alpha_\theta^2 + 2mh}} \sin^{-1} \left(\frac{\frac{\alpha_\theta^2 + 2mh}{r'} - mk}{\sqrt{2m\alpha(\alpha_\theta^2 + 2mh) + m^2 k^2}}\right) - \\
 & \frac{\alpha_\theta'}{\sqrt{\alpha_\theta^2 + 2mh}} \sin^{-1} \left(\frac{\frac{\alpha_\theta^2 + 2mh}{r_0} - mk}{\sqrt{2m\alpha(\alpha_\theta^2 + 2mh) + m^2 k^2}}\right) + \\
 & \sin^{-1} \left[\frac{\sin \gamma}{\cos \theta'}\right] - \gamma - \\
 & \cos \gamma \tan^{-1} \left(\tan \left[\sin^{-1} \left[\frac{\sin \gamma}{\cos \theta'}\right]\right] \cos \gamma\right) + \\
 & \cos \gamma \tan^{-1}(\sin \gamma)
 \end{aligned} \tag{56.B}$$

$$\beta_{\phi'} = \alpha_{\phi'}'. \tag{56.C}$$

## Conclusion

We have chosen the Hamilton – Jacobi equation of a central potential example and separated the variables using Staeckel boundary conditions. This method applies to some Hamiltonians in which certain conditions are satisfied, such as: conservative Hamiltonian and orthogonal coordinates.

After doing the application of Staeckel boundary conditions, we found Hamilton's characteristic function and Hamilton's principal function, then we separated completely the

variables of the Hamilton – Jacobi equation in a central potential. Our results, as expected, are found in agreement with those obtained using other methods [26].

## References

- [1] Goldstein, H., "Classical Mechanics", 2<sup>nd</sup> Edition, (Addison-Wesley, Reading, 1980).
- [2] Staeckel, P. "Über die Integration der Hamilton-Jacobischen Differentialgleichung mittels Separation der Variablen". (Habilitationsschrift, Halle, 1891).
- [3] Stackel, P., Math. Ann., 35 (1890) 91.
- [4] Staeckel, P., Journal für die Reine und Angewandte Mathematik, 111 (1893) 290.
- [5] Charlier, C.V.L., "Die Mechanik des Himmels: Vorlesungen", 1, (Veit., 1902).
- [6] Eisenhart, L.P., Annals of Mathematics, 35 (1934) 284.
- [7] Pars, L.A., The American Mathematical Monthly, 56 (6) (1949) 394.
- [8] Pars, L.A., "A Treatise on Analytical Dynamics", (John Wiley and Sons, New York, 1965), pp. 320-326.
- [9] Ibort, A., Magri, F. and Marmo, G., Journal of Geometry and Physics, 33 (3-4) (2000) 210.
- [10] Daskaloyannis, C. and Tanoudis, Y., Physics of Atomic Nuclei, 71 (5) (2008) 853.
- [11] Błaszak, M. and Marciniak, K., Journal of Mathematical Physics, 47 (3) (2006) 032904.
- [12] Ballesteros, Á., Enciso, A., Herranz, F.J., Ragnisco, O. and Riglioni, D., SIGMA-Symmetry, Integrability and Geometry: Methods and Applications, 7 (2011) 048.
- [13] Famaey, B. and Dejonghe, H., Monthly Notices of the Royal Astronomical Society, 340 (3) (2003) 752.
- [14] Garfinkel, B., Space Mathematics, Part 1 (1966) 40.
- [15] Rauch-Wojciechowski, S. and Waksjö, C., "Staeckel Separability for Newton Systems of Cofactor Type". arXiv preprint nlin/0309048 (2003).
- [16] Kalnins, E.G., Kress, J.M. and Miller Jr, W., Journal of Mathematical Physics, 47 (4) (2006) 043514.
- [17] Marikhin, V.G., Journal of Physics A: Mathematical and Theoretical, 47 (17) (2014) 175201.
- [18] Marikhin, V.G. and Sokolov, V.V., Russian Mathematical Surveys, 60 (5) (2005) 981.
- [19] Minesaki, Y. and Nakamura, Y., Journal of Physics A: Mathematical and General, 39 (30) (2006) 9453.
- [20] Prus, R. and Sym, A., Physics Letters A, 336 (6) (2005) 459.
- [21] Sergyeyev, A. and Błaszak, M., Journal of Physics A: Mathematical and Theoretical, 41 (10) (2008) 105205.
- [22] Tsiganov, A.V., "Transformation of the Staeckel Matrices Preserving Superintegrability". arXiv preprint arXiv:1809.05824 (2018).
- [23] Benenti, S., Note di Matem. Suppl., 9 (1989) 39.
- [24] Benenti, S., Chanu, C. and Rastelli, G., Journal of Mathematical Physics, 41 (7) (2000) 4654.
- [25] Broucke, R., Celestial Mechanics, 25 (2) (1981) 185.
- [26] Calkin, M.G., "Lagrangian and Hamiltonian Mechanics". (World Scientific Publishing Company, 1996).

### The Alpha Particle Doses Received by Students and Staff in Twenty Schools in the North of Hebron Region - Palestine

L. A. Mashal<sup>a</sup>, K. M. Thabayneh<sup>a</sup> and M. M. Abu-Samreh<sup>b</sup>

<sup>a</sup> Faculty of Science and Technology, Hebron University, P.O. Box 40, Hebron, Palestine.

<sup>b</sup> Faculty of Arts and Sciences, Arab American University-Jenin (AAUJ), Jenin, Palestine.

**Doi:** <https://doi.org/10.47011/14.4.4>

Received on: 09/06/2020;

Accepted on: 5/11/2020

---

**Abstract:** The aim of the current study was to measure indoor radon concentration levels and its resulting doses received by the students and staff in schools of the directorate of education in the north of Hebron region- Palestine, during the summer months from June to September (2018), using CR-39 detectors. In this study, a total of 567 CR-39-based radon detectors were installed in the selected schools. The average radon concentrations were found to be 90.0, 66.5 and 58.0 Bqm<sup>-3</sup> in Halhul, Beit Umar and Alarrub camp schools, respectively. Based on the measured indoor radon data, the overall average effective dose for the studied area was found to be 0.31 mSvy<sup>-1</sup>. Reported values for radon concentrations and corresponding doses are lower than ICRP recommended limits for workplaces. The results show no significant radiological risk for the pupils and staff in the schools under investigation. Consequently, the health hazards related to radiation are expected to be negligible.

**Keywords:** Radon concentration, Alpha particles, Annual effective dose, Schools.

**PACs:** 29.40.–n.

## Introduction

Radon is a naturally occurring radioactive gas that is tasteless, odorless and colorless, and its decay products represent the most important source of natural radioactivity for human exposure [1]. It is the second leading cause of lung cancer in the world and the primary cause of lung cancer for individuals who have never smoked [2]. Measurement of the indoor radon level is highly desirable, because the radiation dose received by the human population due to the inhalation and ingestion of radon and its progeny contribute more than 53% of the total dose from natural sources [3].

The most important isotope of radon, in terms of environmental effects, is (<sup>222</sup>Rn), which is formed from the  $\alpha$ -decay of radium (<sup>226</sup>Ra), which is a decay product of Uranium (<sup>238</sup>U) [1].

<sup>222</sup>Rn has a half-life of 3.82 days, allowing it to diffuse through earth crust and into the air before decaying by the emission of  $\alpha$ - particles into a series of short- lived radioactive progeny. However, as radon concentrations increase, the quantity that decays in the lung increases, resulting in a greater health risk [4].

Radon gas naturally dissipates from the rock and soil out to the atmosphere. Building materials, the water supply and natural gas can all be sources of radon in home and atmosphere. The concentration of atmospheric <sup>222</sup>Rn, therefore, depends on the rate of diffusion from the ground and diffusion in the air [5]. The radon gas can enter the body *via* respiring, drinking and eating. The alpha particles emitted by radon gas and other radiations emitted by its daughter

products increase the absorbed dose in respiratory and digestion systems [6]. Exposure of persons to high concentration of radon and its short-lived progeny for a long period leads to health problems, particularly lung cancer [2].

The knowledge of radon levels in classrooms is important in assessing students and staff exposure and has a considerable public health impact, where the concentrations of indoor radon are almost always higher than outdoor concentrations. Once inside a building, radon cannot easily escape. The sealing of buildings to conserve energy reduces the intake of outside air and worsens the situation, although radon levels are generally highest in basements and ground floors, because these areas are nearest to the source and are usually poorly ventilated.

Schools may be a significant source of radon exposure for children and working staff. However, because occupancy patterns in schools differ from those in homes, the actual exposures received by each individual, or even by the entire school population, are difficult to determine. In another previous work, Dabayneh measured the radon concentration in 62 classrooms in Palestine; he claimed that the harmful levels of radon and radon progeny can accumulate in confined air spaces, such as basements and crawl spaces [7].

Our laboratory previously conducted a series of studies with the objective to determine radon concentration levels in homes, hospitals, schools, tobacco, soils and building materials [6, 9, 10-24].

The aim of the present work is to determine radon concentrations in schools in the Directorate of Education in the north of Hebron region - Palestine, during the summer months from June to September, using CR-39 track etch detectors. It is worth mentioning here that this study is part of a nationwide survey and measurement of indoor radon levels in workplaces and studies which so far have not been conducted in this region, to provide data for drawing a national radon map in Palestine.

## Materials and Methods

Solid State Nuclear Track Detectors (SSNTDs) (CR-39 detectors) were installed in various rooms in twenty elementary and secondary schools in the Directorate of Education in the north of Hebron region – Palestine (Fig. 1).

The typical dosimeter is shown in Fig. 2 [2, 10]. Five detectors were used for the determination of background track density. This track density was subtracted from all the measurements before the determination of radon concentration. The CR-39-based radon detector was calibrated according to the standard source facility at the National Radiological Protection Board (NRPB), UK [6, 7]. Following this technique, dosimeters were prepared and distributed in three sites (Halhul, Beit Umar and Alarrub camp) in Hebron region. The detectors were installed in the classrooms, teachers' office, director's office, kitchens, stores, laboratories, libraries, corridors, bathrooms, canteens, ... etc. In each room two passive detectors were installed ~ 1.25 – 1.5 m above the ground. The first detector was placed 0.5 m behind the door to prevent air currents and the second detector was placed against the windows.

The schools of the studied area, as almost all Palestinian schools, are structures of masonry (concrete and brick) from inside and stones from outside, where rooms are ventilated only by operable windows (natural ventilation).

The main zones and the statistical information on detectors and schools in the Directorate of Education in the north of Hebron region - Palestine, during the summer season, are exhibited in Table 1.

Three months later; i.e., after 90 days of exposure, the detectors were collected and chemically etched in a 6.25 M, NaOH solution at  $72 \pm 2$  °C and 8 h etching time to reach high resolution latent tracks [2, 8]. The detectors were washed by distilled water and then dried out. The number of tracks per cm<sup>2</sup> in each detector was counted manually using an optical microscope of 160 times magnification (160×). The tracks were counted twice for each detector and the average was calculated [2].

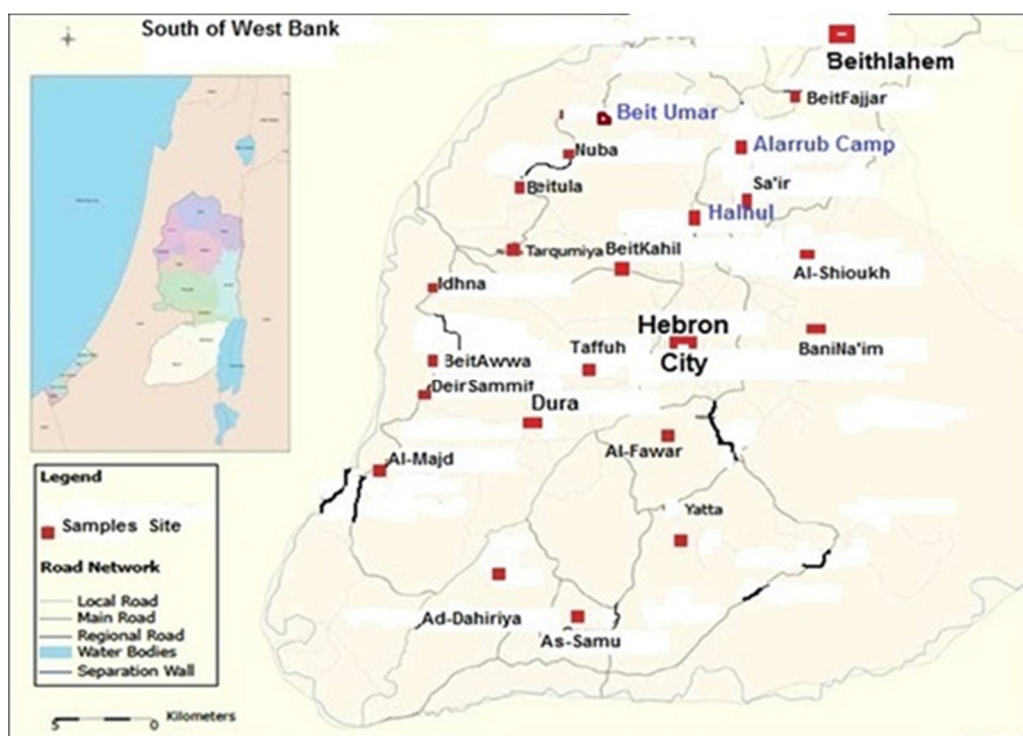


FIG. 1. West Bank geographical map showing the studied region.

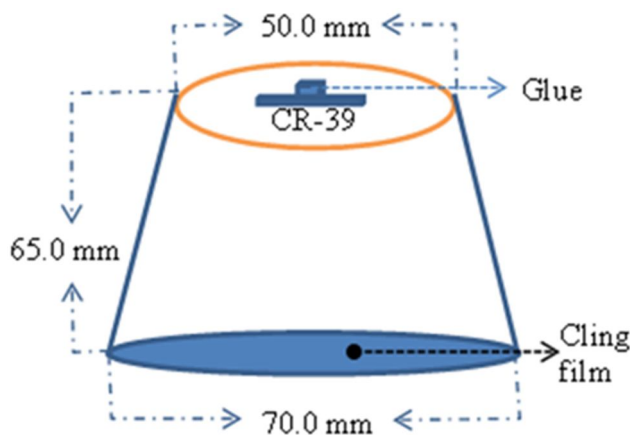


FIG. 2: CR-39 dosimeter.

TABLE 1. Number of the schools, rooms and dosimeters distributed in the area under investigation.

Zone	No. of schools	No. of rooms	No. of dosimeters distributed	No. of dosimeters lost	No. of dosimeters collected
Halhul	10	118	262	28	234
Beit Umar	9	129	270	29	241
Alarrub Camp	1	16	35	8	27
Total	20	263	567	65	502

## Results and Discussion

### The Indoor Radon Concentrations

The track density,  $\rho$ , is generally defined as the average number of scratches in section divided by the section area. The obtained track densities were converted into indoor radon

concentration levels,  $C_{Rn}$ , in  $Bqm^{-3}$  by applying the following calibration formula [2]:

$$C_{Rn} = \frac{C_0 t_0 \rho}{\rho_0 t} \quad (1)$$

where  $C_0$  is the radon concentration of the calibration chamber ( $90 \text{ kBqm}^{-3}$ ),  $t_0$  is the calibration exposure time (48 h),  $\rho$  is the

measured track number density per  $\text{cm}^2$  on the CR-39 detectors inside the used dosimeters,  $\rho_0$  is the measured track number density per  $\text{cm}^2$  on those of the calibrated dosimeters ( $3.3 \times 10^4$  tracks  $\text{cm}^{-2}$ ) and  $t$  is the exposure time (2160 h).

The radon concentration levels data were assessed from 502 dosimeters over a total of 567 as 65 detectors were lost. The range of radon concentrations and the frequency distributions of indoor  $^{222}\text{Rn}$  in twenty schools (263 rooms) are listed in Table 2.

TABLE 2. Range and frequency of radon concentrations of selected schools in the 3 investigated zones in the area under investigation.

Zone	Frequency range ( $\text{Bqm}^{-3}$ )			
	0 - 49	50-99	100-199	$\geq 200$
Halhul	36	154	28	16
Beit Umar	79	145	14	3
Alarrub Camp	8	19	---	---
Total	123	318	42	19
%	24.5	63.3	8.4	3.8

As can be seen from Table 2, about 24.5% of indoor  $^{222}\text{Rn}$  levels are found to vary between 0 and 29  $\text{Bqm}^{-3}$ . Radon concentration levels between 50 and 99  $\text{Bqm}^{-3}$  were observed in 63.3% of the studied classrooms, while about 8.4% are found to vary between 100 and 199  $\text{Bqm}^{-3}$ . Nearly 3.8% of rooms show radon concentrations  $\geq 200$   $\text{Bqm}^{-3}$ , with a maximum value of 306.4  $\text{Bqm}^{-3}$ .

The results show that the concentrations in 12.2% of the studied rooms are above the reference level of 100  $\text{Bqm}^{-3}$  assigned by WHO [23]. The minimum, the maximum and the average concentrations of  $^{222}\text{Rn}$  in the investigated rooms in 20 schools in 3 different zones are listed in Table 3.

TABLE 3. Statistical parameters of the  $^{222}\text{Rn}$  concentrations ( $C_{\text{Rn}}$ ) in different rooms of schools.

Zone	Halhul		Beit Umar		Alarrub Camp	
	$C_{\text{Rn}}$ ( $\text{Bqm}^{-3}$ )		$C_{\text{Rn}}$ ( $\text{Bqm}^{-3}$ )		$C_{\text{Rn}}$ ( $\text{Bqm}^{-3}$ )	
Rooms Type	Min	Max Av.	Min	Max Av.	Min	Max Av.
Classrooms	37.5	257.0 80.3	25.2	286.0 65.2	35.0	93.0 49.2
Administration and Teacher rooms	32.5	306.4 109.6	35.7	164.6 79.3	51.9	64.5 58.2
Bathrooms	46.5	99.5 73.4	20.5	93.2 52.4	-----	----- 55.5
Kitchens	45.5	84.5 62.2	16.6	107.1 58.4	52.0	60.0 56.0
Stores	52.5	305.2 110.6	34.2	164.6 79.4	60.9	91.7 76.3
Computer and scientific labs and libraries	48.1	289.0 103.6	35.6	99.0 64.6	-----	----- 52.5
Total Average	90.0		66.5		58.0	

The data presented in Table 3 shows that the average indoor radon concentrations obtained varied from 62.2  $\text{Bqm}^{-3}$  (in kitchens) to 110.6  $\text{Bqm}^{-3}$  (in stores) in Halhul zone; from 52.4  $\text{Bqm}^{-3}$  (in bathrooms) to 79.4  $\text{Bqm}^{-3}$  (in stores) in Beit Umar zone and from 49.2  $\text{Bqm}^{-3}$  (in classrooms) to 76.3  $\text{Bqm}^{-3}$  (in stores) in Alarrub camp, with overall average values of 90.0, 66.5 and 58.0  $\text{Bqm}^{-3}$ , respectively. Generally speaking, almost 83% of average values are below the reference level [23], for the remedial action to be taken, and all the average values are higher than the world average radon concentration of 40  $\text{Bqm}^{-3}$  [3].

According to the data in Table 3, the differences between the minimum and maximum of indoor concentration levels in the surveyed schools are relatively high. This large variation is mainly due to the difference in the ventilation methods used, the difference in the school's altitude and the difference in the number of floors. Small values of concentration levels are generally reported in schools newly built under the supervision of Western countries (USA, Germany) and Japan as donations for Palestinian pupils.

Table 4 shows the average concentrations of  $^{222}\text{Rn}$  and other radiological effects, in the schools in three zones in different floors of the regions under investigation. Fig. 3 shows the comparison of radon average concentrations in different floors in the studied regions.

The first floor is generally characterized by a high radon concentration level compared to the other floor levels. This may be due to several reasons. Firstly, upper floors have better ventilation than lower ones. Secondly, the chances for radon to reach upper floors are very small compared to its chances to reach lower ones. Finally, the radon exhalation rates from the ground decrease fast as going to higher floors.

However, there is a large variation in the radon concentration levels within the same floors, especially the ground and the first floors.

We can see from Tables 4 and 5 that radon concentration was found to be higher in old schools, poorly ventilated, rather than in newly constructed schools, having good ventilation. In addition, a higher concentration of radon in lower floors in comparison to values measured in higher floors, is observed. The ground floor of such schools is directly constructed on top of soil with a coating of concrete, which allows more radon to diffuse inside the rooms because of the higher porosity of the construction materials used.

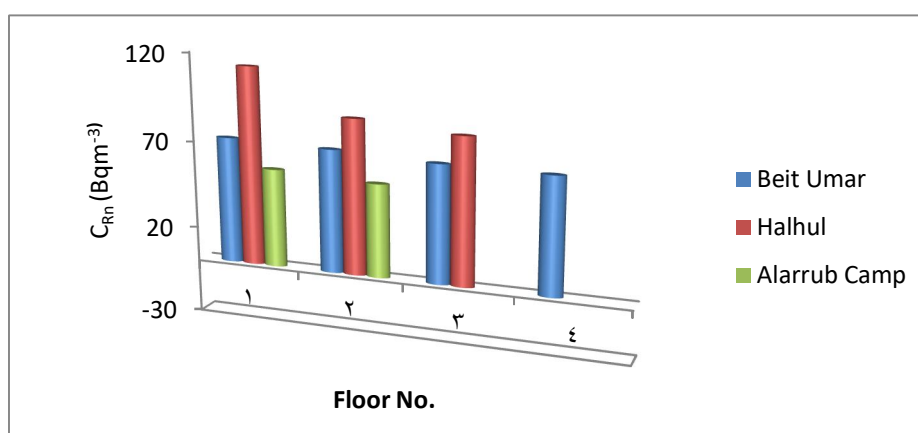


FIG. 3: Comparison of the average radon concentrations in different floors in the studied zones.

TABLE 4. Comparison of the present study results in the schools with those of other studies.

Country	$C_{\text{Rn}}$ (Bqm <sup>-3</sup> )	Reference
Palestine:		
- Tarqumia schools	34	[7]
- Tulkarem schools	40	[25]
- Bethlehem schools	125	[26]
- North-east of Hebron	71	[2]
- North of Hebron schools	74	Present study
Jordan	77	[27]
Algiers	26	[28]
Kuwait:		
- 1 <sup>st</sup> Floor	16	[29]
- 2 <sup>nd</sup> Floor	19	
Saudi Arabia	75	[30]
Greece	231	[31]
Pakistan:		
- Kashmir schools	78	[32]
- Punjab schools	52	[33]
Tunisia	27	[34]
Nigeria	45	[35]
Portugal	400	[36]
ICRP action level, 1993	200	[37]
UNSCEAR, 2000	40	[3]
WHO	100	[23]

TABLE 5. The  $^{222}\text{Rn}$  concentrations levels ( $C_{\text{Rn}}$ ), the annual effective dose ( $E_{\text{Rn}}$ ), the lifetime risk (LTR) and the radon content of the lung air ( $H_{\text{lung}}$ ) belonging to different floors in the surveyed schools.

Zone	Floor No.	$C_{\text{Rn}}$ ( $\text{Bqm}^{-3}$ )			$E_{\text{Rn}}$ ( $\text{mSvy}^{-1}$ )			LTR ( $\times 10^{-4}$ )			$H_{\text{lung}}$ ( $\times 10^{-8}$ ) ( $\text{Svy}^{-1}$ )		
		Min	Max	Av.	Min	Max	Av.	Min	Max	Av.	Min	Max	Av.
Halhul	1	53.5	289.0	113.3	0.22	1.20	0.47	12.5	67.3	26.3	4.3	23.1	9.1
	2	37.5	306.4	88.2	0.16	1.27	0.37	8.7	71.4	20.6	3.0	24.5	7.1
	3	32.5	248.5	83.0	0.14	1.03	0.34	7.6	57.9	19.4	2.6	19.9	6.6
Beit Umar	1	20.5	325.2	72.0	0.09	1.35	0.30	4.8	75.8	16.8	1.6	26.0	5.8
	2	48.6	286.0	70.0	0.20	1.19	0.29	11.3	66.6	16.3	3.9	22.9	5.6
	3	35.7	101.4	67.0	0.15	0.42	0.28	8.3	23.6	15.6	2.9	8.1	5.4
	4	16.6	81.0	66.0	0.07	0.34	0.27	3.9	18.9	15.4	1.3	6.5	5.3
Alarrub Camp	1	35.0	93.0	56.0	0.15	0.39	0.23	8.2	21.7	13.1	2.8	7.4	4.5
	2	38.0	91.7	53.0	0.16	0.38	0.22	8.9	21.4	12.3	3.0	7.3	4.2
Total Average		74.3			0.31			17.3			6.0		

The observed variations of radon concentrations among various regions can be attributed to many factors, such as the geological structure of the site, the various types of building materials used for the construction of the schools, the number of floors, painting and ventilation rates and the aging effect on the building. Other variations of the radon concentration levels may be attributed to human activities, such as opening windows and doors. Human activities are definitively different for schools from those for homes. Schools in Palestine mainly are operated from 5 to 6 hours and closed for the rest of the day. In addition, except for weekends, there are also long periods in the year when schools are closed, especially during summer holidays. When schools are closed, an increase of radon concentration is expected due to poor ventilation. Accordingly, indoor radon concentrations in schools are expected to be higher than in houses.

The relatively high concentrations found in some rooms may be due to the structure of the soil and rocks, which consist mainly of limestone. Also, it may be due to the geological and topographical nature of the school site. Finally, the general results obtained were less than the ICRP standard level, the standard reference level set by WHO and the US EPA for the USA assigned level in general [23, 24].

For the sake of comparison, the radon concentration levels were compared with those of other schools in different countries. The obtained radon concentration levels in the region under consideration are within the majority results of some other national and international areas, as can be seen in Table 4.

## The Radiological Effects of Radon

### The Effective Dose in Schools

To obtain the annual effective dose ( $E_{\text{Rn}}$ ), due to the indoor radon and its progeny received by the pupils and staff, one has to take into account the conversion coefficient from the absorbed dose and the occupancy factor. According to the UNSCEAR 2000 report [3], the effective dose at any location depends upon the occupancy factor. The occupancy factor for the students and the teachers of north Hebron schools was calculated using the following equation:

$$5.5 \frac{\text{h}}{\text{day}} \times 5 \frac{\text{day}}{\text{wk}} \times 36 \frac{\text{wk}}{\text{yr}} = 990 \frac{\text{h}}{\text{yr}} \quad (2)$$

Thus, the school occupancy factor ( $H_s$ ) =  $990\text{h} / 8760\text{h} = 0.113$ .

The expected annual effective doses received by students and teachers in the surveyed areas were calculated by using Eq. (3), the UNSCEAR model [3, 25] as shown below:

$$E_{\text{Rn}} (\text{mSvy}^{-1}) = C_{\text{Rn}} \times H_s \times F \times D \times T \quad (3)$$

where  $C_{\text{Rn}}$  is the radon concentration ( $\text{Bqm}^{-3}$ ),  $H_s$  is the occupancy factor (0.113),  $F$  is the equilibrium factor (0.4),  $T$  is hours in a year (8760) and  $D$  is the dose conversion factor ( $9.1 \times 10^{-6}$  mSv/h per  $\text{Bqm}^{-3}$ ).

By using Eq. (3) and Table (4), the results for the average annual effective dose in all schools are as follows: from  $0.34 \text{ mSvy}^{-1}$  (in third floor) to  $0.47 \text{ mSvy}^{-1}$  (in first floor) in Halhul zone; from  $0.27 \text{ mSvy}^{-1}$  (in fourth floor) to  $0.30 \text{ mSvy}^{-1}$  (in first floor) in Beit Umar zone; and from  $0.22 \text{ mSvy}^{-1}$  (in second floor) to  $0.23 \text{ mSvy}^{-1}$  in (in first floor) in Alarrub camp.

In recent reports, UNSCEAR and WHO [3, 23] recommended that the action levels of radon should be set around 1.3 and 2.5 mSv<sup>-1</sup>, respectively. Based on these recommendations, it has been observed that all of the annual effective doses show lower values than the action levels. Therefore, the results show no significant radiological health risk to the students and staff. We think that this low effective dose value may reflect the very low occupancy rate as students and teachers spend just 11.3% of the year in the schools.

### The Lifetime Risk

The estimate of lifetime risk used in the ICRP Publication 115 [38] is the lifetime excess absolute risk (LTR) associated with a chronic exposure scenario, expressed in a number of deaths 10<sup>-4</sup> per Working Level per Month (WLM). According to the ICRP, an LTR of 5 × 10<sup>-4</sup> per WLM should now be used as the nominal probability coefficient for radon- and radon progeny-induced lung cancer, replacing the ICRP Publication 65 value of 2.8 × 10<sup>-4</sup> per WLM [25, 38].

$$LTR = \frac{WLM}{Life} \times 5 \times 10^{-4} \quad (4)$$

The students and staff of the schools in the north of Hebron region are subjected to the total average of a lifetime lung cancer risk of about 17.3% to chronic exposure to indoor radon. Another study in Palestine reported a lifetime lung cancer risk variation of 0.02% to 0.09% [25, 39].

### The Annual Equivalent Dose to the Lungs

The annual effective dose to lung, H<sub>E</sub>, is calculated using an equation of the form [40]:

$$H_E (mSv y^{-1}) = E_{Rn} \times W_R \times W_T \quad (5)$$

where  $W_R$  is the radiation weighting factor for alpha particles ( $W_R = 20$ ) and  $W_T$  is the tissue weighting factor for the lung ( $W_T = 0.12$ ).

In case the radon content of the lung air is taken into account, Eq. (5) reduces to [3]:

$$H_{lung} (Sv) = 8 \times 10^{10} C_{Rn} (Bqm^{-3}). \quad (6)$$

The total average value of radon content in the lung air ( $H_{lung}$ ) is 6 × 10<sup>-8</sup> Sv<sup>-1</sup> in the region under investigation. The results show no significant radiological risk for pupils and staff in the schools in this region [41].

### Conclusions

The results of the present research led to the following conclusions: the average radon concentrations for the three zones were found to be 90.0, 66.5 and 58.0 Bqm<sup>-3</sup> in Halhul, Beit Umar and Alarrub camp schools, respectively. The total average annual effective dose due to the radon received by the pupils and staff in the studied area was 0.31 mSv<sup>-1</sup>.

Since most radon comes from the ground, the highest concentrations of radon are found in ground floor rooms compared to values measured in the first and upper floors. Variations in radon concentration from one room to another in the same floor level may be explained by human activities. As the annual mean effective dose for students and staff at the schools is consistent with the normal dose as regarded by ICRP and WHO recommendations, health hazards related to radiation are expected to be negligible.

### Acknowledgments

We gratefully acknowledge the Deanship of Scientific Research and Graduate Studies at Hebron University for supporting this research. Sincere thanks are also extended to the working staff in the chemistry lab at Hebron University who helped us in the etching process of the detectors before taking their readings

### References

- [1] Shoqwara, F., Dwaikat, N. and Saffarini, G., Research & Reviews: Journal of Physics, 2 (1) (2013) 10.
- [2] Thabayneh, K.M., Abu-Samreh, M.M. and Mashal, L.A., Environ. Sci., 10 (2015) 260.
- [3] UNSCEAR Report to General Assembly, with Scientific Annexes, United Nations. New York (2000).
- [4] Cao, X., Mac Naughton, P., Laurent, J. and Allen, J., Plos One, 12 (2017) e0184298.
- [5] Youssef, H., Embaby, A., El-Farrash, H. and Laken, A., Int. J. of Recent Scient. Res., 6 (2015) 3440.
- [6] Al-Khalifa, I. and Aood, H., Internat. J. of Resear. in Appl., Nat. and Social Scien., 2 (2014) 117.

- [7] Dabayneh, K.M., *Isot. and Radiat. Res. J.*, 38 (2006) 1067.
- [8] Dabayneh, K.M. and Awawdeh, K.M., *Al-Azhar J. of Sci.*, 18 (2007) 17.
- [9] Dabayneh, K.M., *Isot. and Radiat. Res. J.*, 40 (2008) 277.
- [10] Thabayneh, K.M., Abu-Samreh, M.M. and Elian, M.M., *Hebron Univ. Resear. J. (A)*, 6 (2012) 47.
- [11] Thabayneh, K.M., *Arab J. Sci. Eng.*, 38 (2013) 201.
- [12] Shoeb, M.Y. and Thabayneh, K.M., *J. of Radiat. Res. and Appl. Sci.*, 7 (2014) 174.
- [13] Jazzar, M.M. and Thabayneh, K.M., *Inter. J. of Environ. Engin. and Nat. Resour.*, 1 (2014) 171.
- [14] Thabayneh, K.M., *Appli. Radiat. Isot.*, 103 (2015) 48.
- [15] Thabayneh, K.M. and Arar, A.M., *Ulutas Med. J.*, 1(2015) 31.
- [16] Thabayneh, K.M., Nawajah, I.M. and Ighraib, A.A., *SDRP J. of Earth Sci. and Environ. Stud.*, 1 (2015) 1.
- [17] Thabayneh, K.M., *Sains Malaysiana*, 45 (2016) 699.
- [18] Thabayneh, K.M., Mashal, L.A. and Arar, A.M., *Asian J. of Sci. and Tech.*, 7 (2016) 2502.
- [19] Abu-Samreh, M., Hussain, A., Daraghme, M. and Thabayneh, K., *Hebron Univ. Res. J. (A)*, 7 (2017) 41.
- [20] Thabayneh, K.M., Mashal, L.A., Arar, M.A. and Buss, F.M., *J. of Scient. and Engin. Res.*, 4 (2017) 66.
- [21] Thabayneh, K.M., *J. of Environ. Heal. Sci. and Engin.*, 16 (2018) 121.
- [22] Thabayneh, K., Khalilia, W. and Jaradat, A., *Hebron Univ. Res. J. (A)*, 8 (2019) 40.
- [23] [https://www.who.int/phe/radiation/background\\_under\\_radon/en/](https://www.who.int/phe/radiation/background_under_radon/en/). WHO calls for tighter standards on indoor radon, World Health Organization.
- [24] US EPA, *Environments Division (6609J). A citizen's guide to Radon: The guide to protecting yourself and your family from Radon.* Washington DC (2004).
- [25] Al-Zabadi, H., Mallah, K. and Saffarini, G., *Inter. J. of Radi. Res.*, 13 (2015) 221.
- [26] Leghrouz, A., Abu-Samreh, M. and Shehadeh, A., *Heal. Phys.*, 104 (2013) 163.
- [27] Kullab, M., Al-Bataina, B., Ismail, A., Abumurad, K. and Ghaith, A., *Radi. Measur.*, 28 (1997) 699.
- [28] Amrani, D., *Rad. Protec. Dosim.*, 87 (2000) 1333.
- [29] Maged, A., *Heal. Phys.*, 90 (2006) 258.
- [30] Al-Mosa, T., MSc thesis, King Saud University (2007). Saudi Arabia (Unpublished).
- [31] Clouvas, A., Takoudis, G., Xanthos, S., Potiriadis, C. and Kolovou, M., *Rad. Protec. Dosim.*, 136 (2009) 127.
- [32] Rafique, M., Rahman, S.U., Rahman, S., Matiullah, Shahzad, I., Ahmed, N., Iqbal, J., Ahmed, B., Ahmed, T. and Akhtar, N., *Rad. Protec. Dosim.*, 142 (2010) 339.
- [33] Rahman, S., Anwar, J., Jabbar, A. and Rfique, M., *Indoor and Built Environ.*, 19 (2010) 214.
- [34] Labidi, S., Al-Azmi, D., Mahjoubi, H. and Ben Salah, B., *Radioprotection*, 45 (2010) 209.
- [35] Obed, I., Ademola, K., Vascotto, M. and Gianrossano, G., *Environ. Radioactiv.*, 102 (2011) 1012.
- [36] Antão, A., *Earth and Planetary Sci.*, 8 (2014) 7.
- [37] ICRP, *Publication 65, Annals of the ICRP.23*, Pergamon Press, Oxford (1993).
- [38] ICRP, *Publication 115, Annals ICRP 40 (1)*, Pergamon Press, Oxford (2010).
- [39] Dwaikat, N., M.Sc. Thesis, An-Najah National University, (2001), Palestine (Unpublished).
- [40] ICRP, *Recommendations of the ICRP, Publication 60. Annals of the ICRP, 21*, Pergamon Press, Oxford (1991).
- [41] Rafique, M., Manzoor, N., Rahman, S., Rahman, S.U., Rajput, M.U. and Matiullah, *Iran. J. Radiat. Res.*, 10 (2012) 19.

### Single-mode Optical Fiber: An Investigation for the Bending Loss at Wavelength 650 nm

Anu Dhupar<sup>a</sup>, Suresh Kumar<sup>b,c</sup>, Kajal Mittal<sup>c</sup>, Anu<sup>d</sup>, Sanjay K. Sharma<sup>e</sup>, Vandana Sharma<sup>b</sup> and Jatinder K. Sharma<sup>b</sup>

<sup>a</sup> Department of Physics, Chandigarh University, Gharuan, Mohali – 140413, Punjab, India.

<sup>b</sup> Department of Physics, MMEC, Maharishi Markandeshwar (Deemed to be University), Mullana – 133207, Haryana, India.

<sup>c</sup> Department of Physics, Maharishi Markandeshwar University, Sadopur, Ambala – 134007, Haryana, India.

<sup>d</sup> School of Physics and Materials Science, Thapar University, Patiala – 147004, Punjab, India.

<sup>e</sup> School of ICT, Gautam Buddha University, Greater Noida – 201308, Uttar Pradesh, India.

**Doi:** <https://doi.org/10.47011/14.4.5>

Received on: 11/08/2020;

Accepted on: 29/11/2020

---

**Abstract:** In modern time, the optical fiber communication has revolutionized the data transmission process and contributed vitally to the development of qualitative and speedy telecommunication systems. The arteries of this system are optical fibers which carry information as light signals and as fast as speed of light. But these light signals suffer energy losses during their propagation through the optical fibers. For the effective functioning of an optical fiber communication, it is necessary to know and prevent the prevailing energy losses (especially external bending losses) of the optical fibers. In this paper, the external bending loss of optical power while propagating through a single-mode optical fiber has been investigated. Further, the effects of wrapping turns (1 to 6 turns) and bending diameters ( $2\text{ cm} \leq D \leq 12\text{ cm}$ ) on the power loss of laser at a wavelength of 650 nm have been studied.

**Keywords:** Single-mode optical fiber, Bending loss, Attenuation coefficient, Wrapping turns, Bending diameter.

**PACs:** 42.81.-I, 78.67.Pt, 42.25.Bs.

## Introduction

Optical fibers are transparent and flexible strands which possess thicknesses of few microns and are fabricated from materials like glass, plastic ... etc., [1]. They are spherical dielectric waveguides that efficiently transport optical energy and information in the form of light signals. They are especially designed to transmit signals over larger distances and at higher bandwidths than conventional electrical

wires or cables. These fibers have many advantages over conventional wires and cables, such as less signal attenuation, less power loss, electrical isolation, high volume capacity, being free from electromagnetic interference of signals ... etc. Specially designed optical fibers are also used in a variety of applications, including communication, optical sensors, fiber lasers, power transmission ... etc. [2]. An optical fiber consists of typically three regions; namely, core,

cladding and outer material. A core material having a high refractive index is surrounded by a transparent cladding material having a low refractive index and an outer polymer material which acts as protection jacket for inner materials and provides mechanical strength to the fiber. Light propagates through the core obeying the total internal reflection phenomenon which turns the fiber into an optical waveguide [3]. Optical fibers that uphold numerous propagation paths are called multimode fibers, while those that maintain only a single path are called single-mode fibers. In general, multimode fibers have a wider core diameter and are more suitable in short-distance communication links, high power transmission ... etc. [4]. Single-mode optical fibers having smaller core diameters are mostly preferred for communication links longer than 1,000 meters [5]. The light gathering ability of an optical fiber, also known as numerical aperture, is more for multimode fibers than that of single-mode fibers. However, the information transmission ability of single-mode optical fibers is much larger than that of multimode cables [6, 7]. There are many factors responsible for high transmission ability of single-mode fibers, but the most important property is the comparatively low signal attenuation [8, 9]. Attenuation is the reduction in signal strength when it propagates through the channel medium. It has proved to be one of the important factors for the widespread acceptance of optical fibers in communication systems. It is affected by various mechanisms: absorption, scattering, bending, dispersion, misalignment ... etc. However, the bending losses are particularly important in single-mode fibers, because they work internally and externally [6, 9]. In optical fibers, two types of bending occur: macro-bending (large-scale bending occurs externally) and micro-bending (small-scale bending exists in the core cladding interface). The macro-bending or external bending may occur during installation of optical cables, while the localized micro-bending can develop during manufacturing of the fiber [10-14]. Optical fibers are critically designed for the development of high-quality and high-speed networks [11 - 14], but external bending affects their functioning badly if not handled properly.

Hence, in this work, the authors try to investigate the consequence of external bending on the optical power transmission through single-mode fibers of different lengths (1 m, 1.4

m, 1.8 m and 2.2 m). The effects of wrapping turns (1 to 6 turns) and bending diameters (2 cm, 4 cm, 6 cm, 8 cm, 10 cm and 12 cm) on the power loss of laser light of wavelength 650 nm have been studied.

## Experimental Work

The experimental work was carried out using different instruments with specifications such as a laser diode of wavelength ( $\lambda$ ) 650 nm (red color), output power between 3 and 5 mW, operated at voltage  $220 \text{ V} \pm 10\%$  having frequency = 50 Hz, single-mode optical fiber (with plastic core and plastic cladding design) of variable lengths (1 m, 1.4 m, 1.8 m and 2.2 m), a light lens (45 $\times$ ), V grooves and post stands. For bending the optical fiber, aluminum mandrels of different diameters (2 to 12 cm) were used. A composite silicon laser detector acts as a digital micrometer used to measure the output optical power. The single-mode optical fiber was carefully aligned to the laser source and positioned to achieve maximum light intensity. A reference loss that was presented without any bending was recorded and subtracted from the loss obtained after bending of fiber. All the components and instruments are arranged as shown in Fig. 1. The experiment was performed in a dark-room environment to avoid interference of external light with experimental conditions.

## Results and Discussion

The output optical power [11] of single-mode optical fiber is given by  $P_o(L) = P_i \times \exp^{-\alpha L/10}$  dB, where  $P_i$  is input power,  $P_o$  is output power,  $\alpha_{dB}$  is the signal attenuation per unit length in decibels and  $L$  is the length of the optical fiber. The attenuation of light ( $\alpha_{dB}$ ) while propagating through the fiber is expressed in decibels per unit length (*i.e.*, dB/m) which is given by the relation,  $\alpha_{dB}L = 10 \times \log(P_i/P_o)$  [4]. In terms of current, the bending loss in dB is given as,  $dB = 20 \times \log(I/I_o)$  for all values of current corresponding to different bending loop diameters. The values of optical output of laser diode (emitting red light of wavelength,  $\lambda = 650 \text{ nm}$ ) when propagating through single-mode fiber under different experimental investigations, such as different bending diameters (2 cm to 12 cm), different numbers of turns (1 to 6) and different optical fiber lengths; *i.e.*, 1 m, 1.4 m, 1.8 m and 2.2 m are listed in Tables 1 to 4.

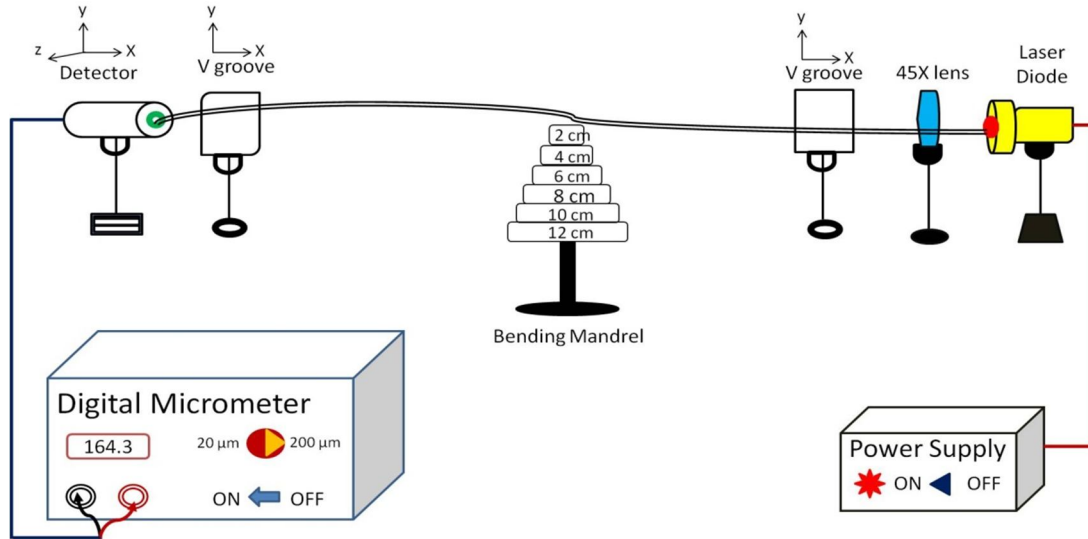


FIG. 1. The experimental setup for measuring optical loss due to macro-bending.

TABLE 1. The effect of number of wrapping turns on the output current of laser source at different bending diameters for single-mode optical fiber of length 1 m.

Sr.	Wrapping turns (N)	Output current ( $\times 10^{-6}$ A)					
		Bending diameter (D)					
		2 cm	4 cm	6 cm	8 cm	10 cm	12 cm
1	0	190	190	190	190	190	190
2	1	164	167	169	172	175	179
3	2	147	150	153	156	160	164
4	3	128	131	137	139	144	147
5	4	108	114	117	121	127	133
6	5	94	98	102	105	111	118
7	6	73	81	86	90	96	102

TABLE 2. The effect of number of wrapping turns on the output current of laser source at different bending diameters for single-mode optical fiber of length 1.4 m.

Sr.	Wrapping turns (N)	Output current ( $\times 10^{-6}$ A)					
		Bending diameter (D)					
		2 cm	4 cm	6 cm	8 cm	10 cm	12 cm
1	0	190	190	190	190	190	190
2	1	158	160	164	169	173	178
3	2	138	144	148	154	158	163
4	3	124	128	132	134	137	146
5	4	104	111	117	122	128	133
6	5	87	95	100	107	113	115
7	6	68	76	81	91	97	101

TABLE 3. The effect of number of wrapping turns on the output current of laser source at different bending diameters for single-mode optical fiber of length 1.8 m

Sr.	Wrapping turns (N)	Output current ( $\times 10^{-6}$ A)					
		Bending diameter (D)					
		2 cm	4 cm	6 cm	8 cm	10 cm	12 cm
1	0	190	190	190	190	190	190
2	1	152	158	162	165	170	177
3	2	133	140	146	152	159	162
4	3	117	121	129	131	139	146
5	4	100	108	115	120	124	135
6	5	85	92	98	105	111	114
7	6	64	72	78	89	95	103

TABLE 4. The effect of number of wrapping turns on the output current of laser source at different bending diameters for single-mode optical fiber of length 2.2 m

Sr.	Wrapping turns (N)	Output current ( $\times 10^{-6}$ A)					
		Bending diameter (D)					
		2 cm	4 cm	6 cm	8 cm	10 cm	12 cm
1	0	190	190	190	190	190	190
2	1	147	153	159	163	168	175
3	2	128	138	144	150	156	162
4	3	111	117	126	130	137	144
5	4	93	104	112	118	127	133
6	5	77	87	95	104	109	117
7	6	60	68	73	77	88	101

A falling trend in output current is observed for all fiber lengths as the numbers of the wrapping turns increased. However, this output is observed to be increased with an increase in macro-bending diameter at a fixed number of wrapping turns. The variations in attenuation coefficient per unit length of single-mode optical fiber at a fixed length; *i.e.*, 1 m, 1.4 m, 1.8 m and 2.2 m with wrapping turns (1 to 6) and bending diameter (2 cm to 12 cm) are shown in Fig. 2. It

is found that attenuation coefficient increased with increase in wrapping turns and decrease in external bending diameter. Moreover, it changed with the length of optical fiber and found highest for fiber length 2.2 m and lowest for 1.0 m. The effect of wrapping turns (1 to 6) and bending diameter (2 cm to 12 cm) on the bending loss of single-mode optical fiber at a particular length; *i.e.*, 1 m, 1.4 m, 1.8 m and 2.2 m is represented in Fig. 3.

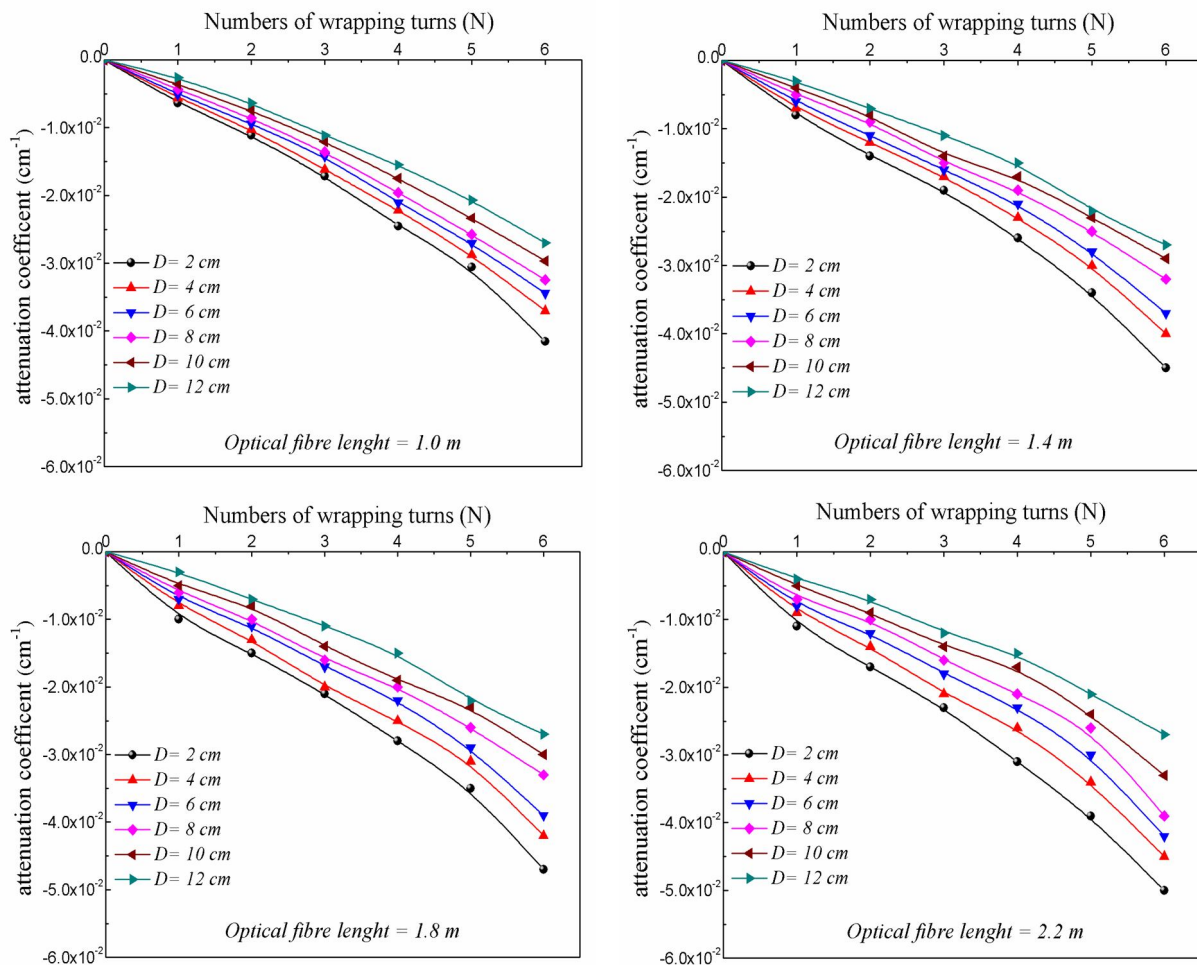


FIG. 2. The effect of wrapping turns (1 to 6) and bending diameter (2 cm to 12 cm) on the attenuation coefficient of single-mode optical fiber at a particular length; *i.e.*, 1 m, 1.4 m, 1.8 m and 2.2 m.

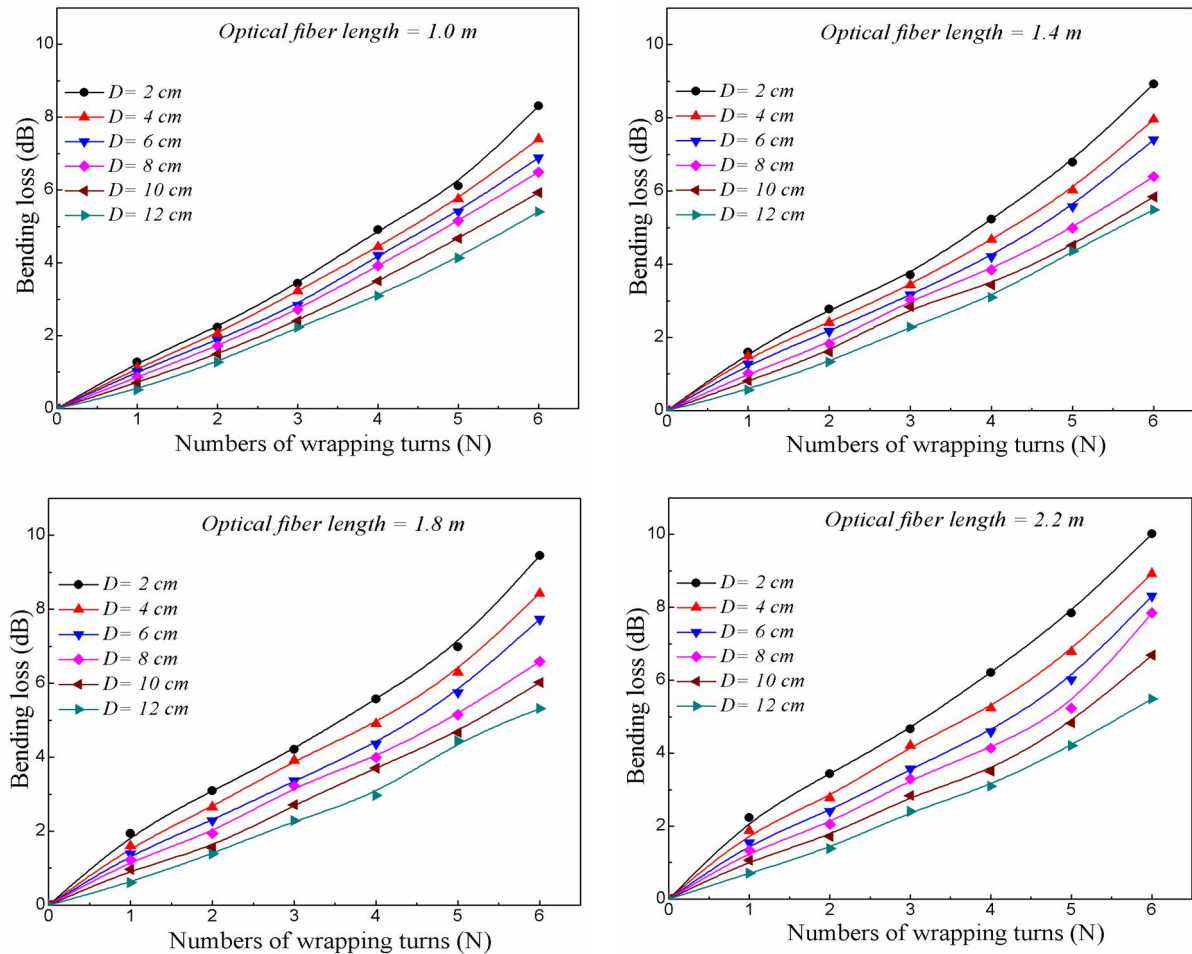


FIG. 3. The effect of wrapping turns (1 to 6) and bending diameter (2 cm to 12 cm) on the bending loss of single-mode optical fiber at a particular length; *i.e.*, 1 m, 1.4 m, 1.8 m and 2.2 m.

It is shown that the bending loss depends on the number of wrapping turns of the single-mode fiber which provides varied values of bending loss with each step size. It is observed that when the wrapping turn increases, the bending loss directly increases. A direct linear relationship between the bending loss and wrapping turn has been estimated. Similar type of variation in bending loss with wrapping turns was also reported in literature [13]. It is also predicted from the results that for a particular length of a single-mode optical fiber, the bending loss decreases with increase in bending diameter from 2 cm to 12 cm (Fig. 4). It has also been observed that for a fixed length of the fiber, as the bending diameter increases, the sharpness in the reduction of bending loss *w.r.t.* number of turns; *i.e.*, slope of the curve slightly decreases, which indicates that susceptibility of the fiber to these losses depends on the bend diameter and

can be minimized by increasing the bending diameter.

Moreover, this loss is found high for smallest bending diameter; *i.e.*, 2 cm and low for the highest bending diameter; *i.e.*, 12 cm, while the attenuation coefficient has the opposite trend for compressible fiber lengths (Fig. 4). This indicates that smaller bending diameter and larger wrapping turns promote higher bending loss which increases with the increase in the length of the fiber, while it decreases with increase in bending diameter. A similar variation in the power loss of the optical fiber with bending radius and wrapping turns at a wavelength of 1550 nm is also reported in literature [4, 14]. The present analysis suggests that to reduce the power loss during transmission, the external bending diameter should be kept large and the number of wrapping turns should be kept small.

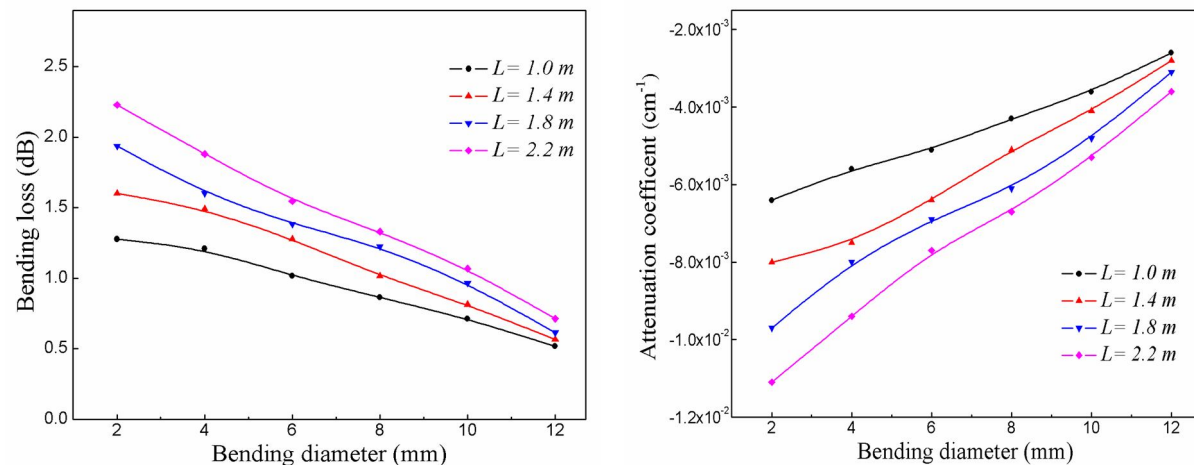


FIG. 4. The effect of bending diameter (2 cm to 12 cm) on the bending loss (left) and the attenuation coefficient (right) of single-mode optical fiber with different lengths (1 m, 1.4 m, 1.8 m and 2.2 m).

## Conclusion

In the present study, the bending loss in the optical power of a single-mode optical fiber because of different wrapping turns and variable bending diameters has been investigated. It has been observed that as the number of wrapping turns of the optical fiber increases and the bending diameter decreases, the bending loss through the fiber increases linearly and sharply. Also, it is observed that as the length of the fiber

increases, the bending loss and attenuation coefficient change up to an appreciable extent. It is found that the external bending loss of optical power, when propagating through the optical fiber, increases as the bending diameter decreases and wrapping turns increase. The accomplished investigation and experimental results are compatible with the theoretical studies within the uncertainty limits.

## References

- [1] Buck, J.A., "Fundamentals of Optical Fibers", (John Wiley & Sons, Inc., New York, United States, 2004).
- [2] Baldini, F., Brenci, M., Chiavaioli, F., Giannetti, A. and Trono, C., *Analytical and Bioanalytical Chemistry*, 402 (1) (2012) 109.
- [3] Willner, A., "Optical Fiber Telecommunications", (Academic Press, New York, United States, 2019).
- [4] Amanu, A.A., *Advances in Applied Sciences*, 1 (1) (2016) 1.
- [5] Yu, S., De, L.Z., Xiao, J.C. and Sia, Y.X., *Optical Fiber Technology*, 50 (2019) 225.
- [6] Okoshi, T., *IEEE Journal of Quantum Electronics*, 17(6) (1981) 879.
- [7] Essiambre, R.J., Tkach, R.W. and Ryf, R., "Fiber Nonlinearity and Capacity: Single-mode and Multimode Fibers", In: "Optical Fiber Telecommunications", VI (eds. Kaminow, N.P., Li, T. & Willner, A.E.), (Academic Press, New York, United States, 2013) pp.1-37.
- [8] Olshansky, R. and Nolan, D.A., *Applied Optics*, 15 (4) (1976) 1045.
- [9] Wang, Q., Farrell, G. and Freir, T., *Optics Express*, Optical Society of America, 12 (2005) 4476.
- [10] Miao, Y., "The Principle and Application of Fiber Optics", (Tsinghua University Press, Beijing, China, 2010).
- [11] Herrera, L.E.Y., Amaral, G.C. and Von der Weid, J.P., *Applied Optics*, 55 (2016) 1177.
- [12] Lustermann, B., Quandt, B.M., Ulrich, S., Spano, F., Rossi, R.M. and Boesel, L.F., *Scientific Reports*, 10 (2020) 11885.
- [13] Tosi, D., Poeggel, S., Iordachita, I. and Schena, E., "Opto-mechanical Fiber Optic Sensors: Research, Technology and Applications in Mechanical Sensing", (Elsevier BV, USA, 2018).
- [14] Zendeenam, A., Mirzaei, M., Farashiani, A. and Farahani, L.H., *Pramana Journal of Physics*, 74 (2010) 591.

### Applying *in-Situ* and Laboratory-based Gamma Spectrometry to Determine Activity Concentration and Distribution of $^{40}\text{K}$ , $^{226}\text{Ra}$ and $^{232}\text{Th}$ in Abeokuta, Southwest Nigeria

A. O. Mustapha<sup>a</sup>, P. E. Biere<sup>b</sup>, A. E. Ajetunmobi<sup>c</sup> and J. O. Aina<sup>a</sup>

<sup>a</sup> Department of Physics, Federal University of Agriculture Abeokuta, Ogun State, Nigeria.

<sup>b</sup> Department of Physics, Niger Delta University, Wilberforce Island, Bayelsa State, Nigeria.

<sup>c</sup> Department of Physics, Olabisi Onabanjo University, Ago-Iwoye, Ogun State, Nigeria.

**Doi:** <https://doi.org/10.47011/14.4.6>

Received on: 02/10/2020;

Accepted on: 29/11/2020

---

**Abstract:** The applications of radionuclides are potential sources of health risk and also a concern in the area of nuclear security. It is therefore imperative to determine the presence of the different radionuclides present in the environment at all times, because it is necessary to control and assess the risk level in the environment. The present study compares activity concentrations of the primordial radionuclides  $^{40}\text{K}$ ,  $^{226}\text{Ra}$  and  $^{232}\text{Th}$  obtained from laboratory gamma spectrometry measurements with the activity concentrations of the radionuclides as obtained from *in-situ* measurements. Soil samples were randomly collected from nineteen different points within Abeokuta city ensuring good coverage of the city area. A mobile gamma spectrometry system was used to collect gamma spectra measurements in the field. The obtained values are presented. The ranges of activity concentrations for  $^{40}\text{K}$ ,  $^{226}\text{Ra}$  and  $^{232}\text{Th}$  have been found to be 113 – 1975, 5 – 128 and 181 – 3284 Bqkg<sup>-1</sup>, respectively for laboratory gamma spectrometry and 104 – 1312, 31 – 121 and 104 – 2578 Bqkg<sup>-1</sup>, respectively for *in-situ* gamma spectrometry measurements. This study showed that the average activity concentrations of the primordial radionuclides in Abeokuta were much higher than worldwide averages of 400, 35 and 30 Bqkg<sup>-1</sup> for  $^{40}\text{K}$ ,  $^{226}\text{Ra}$  and  $^{232}\text{Th}$ , respectively. From both methods,  $^{232}\text{Th}$  is seen to be the major contributor to the environmental radioactivity of Abeokuta. Good correlations also were deduced between the activity concentration results obtained from laboratory and *in-situ* gamma spectrometry, which therefore implies a significant relationship between the two methods used in the study.

**Keywords:** In-situ gamma, Gamma spectrometry, Activity concentration, Radionuclides.

## Introduction

The presence of radionuclides in the environment is both of interest as well as of concern. It is of interest because radionuclides have been widely applied for various purposes, such as medicine, agriculture, electric power and education [1]. Examples of such radionuclides used are  $^{131}\text{I}$ ,  $^{95}\text{Zr}$ ,  $^{241}\text{Am}$ ,  $^{60}\text{Co}$ ,  $^{137}\text{Cs}$ ,  $^{192}\text{Ir}$ ,  $^{232}\text{U}$ ,  $^{14}\text{C}$ , among others. Their presence is a potential source of health risk as well as a concern in the area of nuclear security. It is therefore

imperative to be able to determine the presence of different radionuclides present in the environment at all times so as to control and assess the risk level in the environment. Gamma-ray spectrometry measurements give practical ways to assess dispersed radionuclides in soils to determine possible changes in the radioactivity of the environment [2]. Both laboratory and *in-situ* gamma spectrometry are usually used for the purpose of detection, monitoring and assessment

of levels of radioactivity in the environment and radiation dose rates as a result of natural and artificial sources [3].

The traditional method of evaluating the distribution of radioactivity in the environment is laboratory gamma spectrometry measurements. It is well established and widely used. Samples are extracted from the site, packaged, transported to the laboratory and prepared for analysis. The method has the advantage of being fairly straight forward and the samples can be used for other types of analysis, like elemental analysis. Sampling, however, is labour-intensive with regard to the collection of samples and concerning laboratory measurements. This method suffers from the disadvantages arising from the representative nature of the samples, difficulty in accessing samples, coverage of sampling area, time required for laboratory analyses and delays in obtaining results [4], because all samples will have to be measured in the laboratory before any results are produced. *In-situ* gamma ray spectrometry entails the collection of a spectrum of the ambient gamma ray flux at a given site for analysis, principally to identify and quantify the radionuclides present at the site. Since its development in the late sixties and at the beginning of the seventies, *in-situ* gamma spectrometry has gone through a lot of modifications. It has become a useful method for rapid assessment of radionuclide concentrations of gamma emitters present in the environment [5]. The main advantages of this method include its modest time consumption, its portability and the reasonable cost of the detector compared to laboratory-based gamma spectrometry [6]. *In-situ* gamma-ray spectrometry is however complex and requires a more rigorous calibration procedure [7]. The present study compares activity concentrations of radionuclides calculated from laboratory gamma spectrometry and activity concentrations of radionuclides obtained from *in-situ* measurements.

## Materials and Methods

Abeokuta, the capital of Ogun State, is located in the southwestern part of Nigeria. It is situated between latitudes 7°9'N and 7°39'N and longitudes 3°20'E and 3°54'E [8]. It is made up mainly of two local government areas, which are Abeokuta North and Abeokuta South. It covers a geographical area of 1,256 km<sup>2</sup>. Abeokuta is found in a sub-humid tropical region within

southwestern Nigeria [9]. The city is drained mainly by River Ogun, which passes through it. The drainage pattern is generally dendritic. Geologically, the city is characterized by underlying basement complex rocks which are basically hornblende-biotite gneiss, porphyroblastic gneiss, granite, porphyritic granite and pegmatitic intrusions [8]. These rocks are noted for high content of radionuclides and poor water-bearing properties [10]. Characterizing the city is the Abeokuta formation which is sedimentary and comprises mainly sand with sandstone, siltstone, silt, clay, mudstone and shale interbeds [11]; [8]. The sands are coarse grained, clayey, micaceous and poorly sorted and indicative of short distances of transport and possible derivation from the granite rocks [12].

## Calibration of *in-Situ* Gamma Spectrometer

The calibration of the detector was done in two stages. The first was to convert channel numbers into gamma energy in keV. The calibration procedure involved selecting the calibration option of the maestro digiBASE software and inserting the gamma energies of each of the peaks of interest against their channel numbers. A relation of the gamma energy *versus* channel number was established by the software, thereby calibrating the detector. The second was to convert the count rates (cps) under a photopeak into soil activity concentration (Bqkg<sup>-1</sup>) of the radionuclide. In this stage of the calibration process, factors that related the count rate under a photopeak to soil radioactivity concentration and dose rate in air were determined.

According to [2], the number of counts per second,  $N_f$ , obtained under a photopeak due to a particular gamma energy,  $E$ , is related to the soil radioactivity concentration,  $A$ , of the radionuclide producing the peak by Eq. 1 [13].

$$\frac{N_f}{A} = \frac{N_f N_o \phi}{N_o \phi A} \quad (1)$$

where  $\frac{N_f}{A}$  is the photopeak count rate at the gamma energy per unit activity concentration of the radionuclide in the soil ( $\frac{cps}{Bqkg^{-1}}$ ),  $\frac{N_f}{N_o}$  is called the angular correction factor and accounts for the non-uniformity of the detector response to gamma rays incident at varying angles. This detector-specific quantity is dimensionless and dependent on the source distribution, gamma

energy, soil density and soil composition,  $\frac{N_0}{\phi}$  is the on-axis response of the detector (normal to detector face) given in count rate per uncollided flux of parallel gamma rays ( $\frac{\text{cps}}{\gamma\text{m}^{-2}\text{s}^{-1}}$ ),  $\frac{\phi}{A}$  represents the total un-collided flux per unit source activity concentration ( $\frac{\gamma\text{m}^{-2}\text{s}^{-1}}{\text{Bqkg}^{-1}}$ ) and  $\phi$  is the gamma ray un-scattered flux on the detector ( $\gamma\text{m}^{-2}\text{s}^{-1}$ ).

### ***In-Situ* Gamma Spectrometry**

The mobile gamma spectrometry system was used to collect gamma spectra measurements in the field. Concerted efforts were made to make sure that the sites where measurements were carried out were well spread across Abeokuta, ensuring also that at each location, the measurement represented the true terrestrial gamma radiation. The NaI(Tl) detector was mounted on the iron stand with the face of the detector pointing downward to receive gamma radiation emanating from the soil below, as shown in Fig. 1. The shield with a thickness of 4 cm and a depth of 17.5 cm was expected to

attenuate radiation from other sources or from outcrops and man-made constructions. Although the shield was not able to eliminate the effect of incident radiation completely, a larger shield would not have been easily movable, so a compromise had to be made between practicability and accuracy of the spectroscopy measurement. The detector itself was accurately folded with shock-resistive material in order to prevent it from possible damage in the field. The central axis of the detector was kept perpendicular to the extended plane of the soil surface while it faced the soil so that it could measure gamma radiation. The distance between the detector and the ground was kept at 140 mm and counting was for a preset time of 600 s. The photo-peaks used were 1460, 1760 and 2614 keV for  $^{40}\text{K}$ ,  $^{226}\text{Ra}$  and  $^{232}\text{Th}$ , respectively. Regions of interest (ROIs) were carefully determined around these photo-peaks in order to obtain total count rate,  $N_f$ , due to each radionuclide under its reference peak.  $N_f$  was converted into soil radioactivity concentration of the radionuclides using the conversion factors.

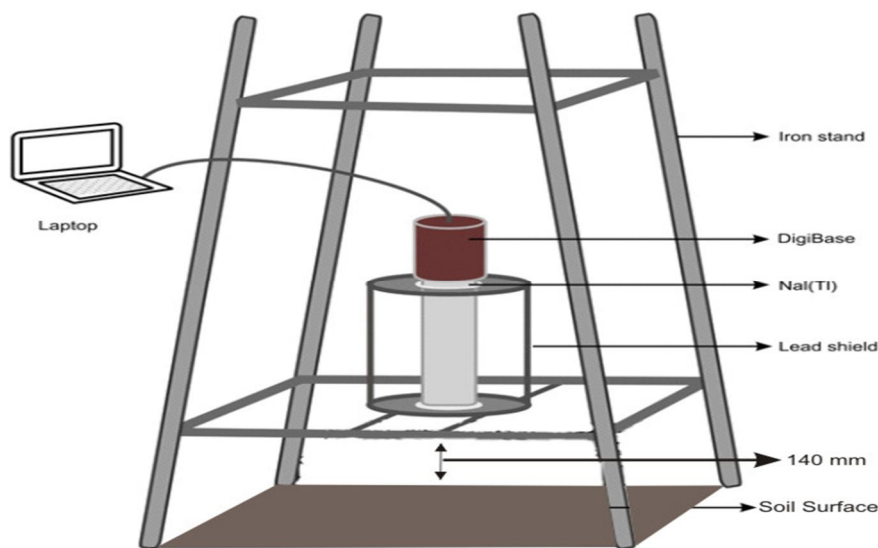


FIG. 1. Schematic diagram showing the arrangement of the detector during *in-situ* measurement.

### **Soil Sampling**

Soil samples were collected from the same *in-situ* measurement points. The soil samples were taken from topsoil within the thickness of 0 – 50 mm from the surface. The collected soil samples were then packed in labeled cellophane bags and taken to the Radiation and Health Physics Laboratory of the Department of Physics, Federal University of Agriculture, Abeokuta (FUNAAB), where they were air-dried at room

temperature [14], pulverized into fine grain sizes and sieved with a 1 mm mesh sieve. The prepared samples were then packed in 0.2 kg of mass in plastic containers of about 80 mm in diameter so that the sample could sit with high geometry on the NaI(Tl) detector, as shown in Fig. 2. The plastic containers were then sealed with adhesive paper tape and kept for about 30 days which was a sufficient time to allow for  $^{226}\text{Ra}$  and its decay products to attain a state of secular radioactive equilibrium.

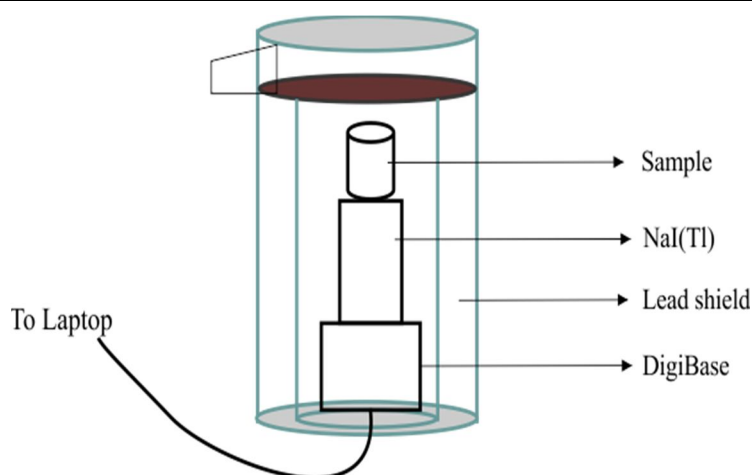


FIG. 2. Schematic diagram showing the soil sample on the NaI(Tl).

### Calibration of Laboratory-based Gamma Spectrometer

Standard material used for energy calibration of the laboratory-based gamma spectrometer consists of RGU-1, RGTh-1 and RGK-1. These are standard materials that were produced under the auspices of the International Atomic Energy Agency (IAEA) and were distributed through its Analytical Control Services (AQCS) program. According to the manufacturers, RGU-1 was prepared from a dilution of Uranium ore (BL-5) with silica sand, RGTh-1 was prepared from a dilution of Britholite material (OKA-2) with silica sand and RGK-1 was prepared from potassium sulphate. The standard materials were put into the sample containers and were kept for about one month to achieve equilibrium between radium and its decay products. The standard materials were counted using the NaI(Tl) detector. Counting was for about 1800 s, which was long enough to capture spectra with well-resolved peaks. Three suitable energy peaks of 352, 609 and 1764 keV were selected. The calibration procedure continued by selecting the calculation option of the maestro digiBase software, calibration option was further selected and the gamma energies of each of the peaks of interest were inserted against their channel numbers. A relation of the gamma energy *versus* channel number was established by the software, then the channel numbers and the corresponding energy values were matched. The activity of each of the three primordial radionuclides was determined by relating the area under each photo-peak in the soil samples to the same photo-peak in the standard materials after counting. The photopeaks used were 1460 keV,

1764 keV and 2614 keV for  $^{40}\text{K}$ ,  $^{226}\text{Ra}$  and  $^{232}\text{Th}$ , respectively.

### Laboratory-based Gamma Spectrometry

Gamma-ray spectrometry analysis of the prepared soil samples was carried out using the NaI(Tl) gamma ray spectrometer in the Radiation and Health Laboratory, Department of Physics, FUNAAB. The counting time was set at 10800 seconds. Regions of interest were carefully determined from the downloaded spectra and were used to obtain total counts under the three major peaks of 1460 keV  $^{40}\text{K}$ , 1764 keV  $^{214}\text{Bi}$  and 2614 keV  $^{208}\text{Tl}$ . The peaks had a range of 160 - 190, 200 - 235 and 295 - 335 keV, respectively. The background count was also determined by counting another container, similar to the one used for the soil samples, filled with distilled water which was sealed and kept for about 30 days. The net area, after background counting was taken away, and was related to the radioactivity concentration of each of the three primordial radionuclides. Activity concentrations of the primordial radionuclides in the soil samples was calculated using Eq. 2 [15].

$$\frac{A_{\text{sample}}}{A_{\text{std}}} = \frac{CR_{\text{sample}} - CR_{\text{Bgd}}}{CR_{\text{std}} - CR_{\text{Bgd}}} \quad (2)$$

where  $A_{\text{sample}}$  is activity concentration of the sample ( $\text{Bqkg}^{-1}$ ),  $A_{\text{std}}$  is activity concentration of the standard ( $\text{Bqkg}^{-1}$ ),  $CR_{\text{sample}}$  is count rate of sample ( $\text{counts sec}^{-1}$ ),  $CR_{\text{Bgd}}$  is count rate of background ( $\text{counts sec}^{-1}$ ),  $CR_{\text{std}}$  is background of standard ( $\text{counts sec}^{-1}$ ),  $CR_{\text{Bgd}}$  is count rate of background ( $\text{counts sec}^{-1}$ ).

Fig. 3 shows the area of the study where both *in-situ* gamma spectrometry as well as the soil sampling were done.

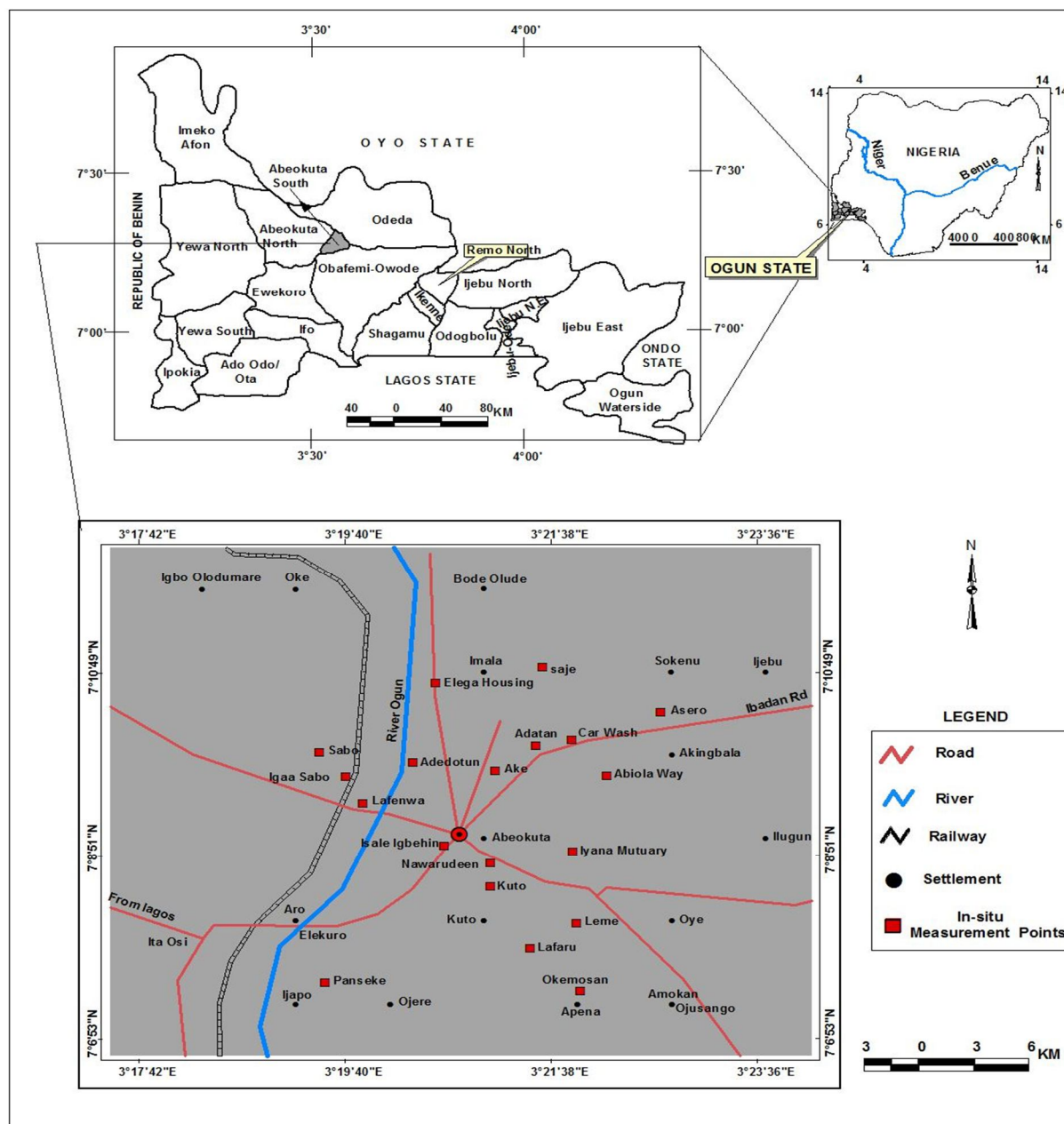


FIG. 3. Map of the study area showing Abeokuta South and Abeokuta North.

## Results and Discussion

The three primordial radionuclides,  $^{40}\text{K}$ ,  $^{226}\text{Ra}$  and  $^{232}\text{Th}$  have been detected and measured. Activity concentrations of the radionuclides from the soil samples as determined in the laboratory and from *in-situ* gamma spectrometry are presented in Table 1. From the laboratory-based gamma spectrometry, of special interest are concentrations of  $^{232}\text{Th}$  at Kuto and Lafaru at 3284 and 2857  $\text{Bqkg}^{-1}$ , respectively which are both over three times the average of the study area and concentrations of  $^{40}\text{K}$  at Kuto and Lafaru at 1924 and 1816  $\text{Bqkg}^{-1}$ , respectively

which are both over two times the average of the study area. From the *in-situ* gamma spectrometry, concentrations of interest are  $^{232}\text{Th}$  at Lafaru and Kuto at 2578 and 2362  $\text{Bqkg}^{-1}$ , respectively which are both over three times the average of the study area and concentrations of  $^{40}\text{K}$  at Leme and Adedotun at 1312 and 1147  $\text{Bqkg}^{-1}$ , respectively which are both over two times the average of the study area. These anomalously high concentrations at some points account for the relatively high activity concentration level of the city. This confirms the general report in different studies carried out by different authors from Nigeria, that Abeokuta

town has a high radiation dose [10]; [16]. Frequency distributions of activity concentrations of  $^{40}\text{K}$ ,  $^{226}\text{Ra}$  and  $^{232}\text{Th}$  from both methods are presented in Figs. 4 to 9. The distributions of the concentrations of the three radionuclides in the study area show significant variations in both laboratory-based spectrometry

and the *in-situ* spectrometry. This shows non-homogenous distributions of  $^{40}\text{K}$ ,  $^{226}\text{Ra}$  and  $^{232}\text{Th}$ . The frequency distributions of the values of the activity concentrations obtained from laboratory and *in-situ* gamma spectrometry show same pattern, where  $^{40}\text{K}$  is near normal,  $^{226}\text{Ra}$  is normal and  $^{232}\text{Th}$  is skewed to the left.

TABLE 1. Results of activity concentrations of naturally occurring radionuclides from both laboratory and *in-situ* gamma spectrometry.

S/N	Location	lab	<i>in-situ</i> $^{40}\text{K}(\text{Bqkg}^{-1})$	lab	<i>in-situ</i> $^{226}\text{Ra}(\text{Bqkg}^{-1})$	lab	<i>in-situ</i> $^{232}\text{Th}(\text{Bqkg}^{-1})$
1	Ake	1796	233	57	68	1432	234
2	Abiola Way	113	219	30	64	181	419
3	Adatan	2036	598	97	79	1826	725
4	Adedotun	1887	1147	35	64	1554	634
5	Asero	482	346	43	54	645	353
6	Car Wash	1082	402	70.3	47	824	222
7	Elega Housing	643	202	64	82	735	626
8	Igaasabo	848	188	34	35	540	185
9	Iyanamutary	768	188	51	42	229	185
10	Isaleigbehin	778	281	5	31	491	1030
11	Kuto	1924	937	68	100	3284	236
12	Lafaru	1816	896	66	90	2857	2578
13	Lafenwa	996	169	10	36	608	104
14	Leme	1975	1312	66	121	1513	1321
15	Nawarudeen	1616	293	128	74	1893	467
16	Okemosan	501	104	31	56	365	200
17	Panseke	680	315	27	65	237	153
18	Sabo	1831	291	26	45	686	191
19	Saje	1240	794	46	85	877	756
MEAN		1211	469	50	65	1094	559
MIN.		113	104	5	31	181	104
MAX.		1975	1312	128	121	3284	2578

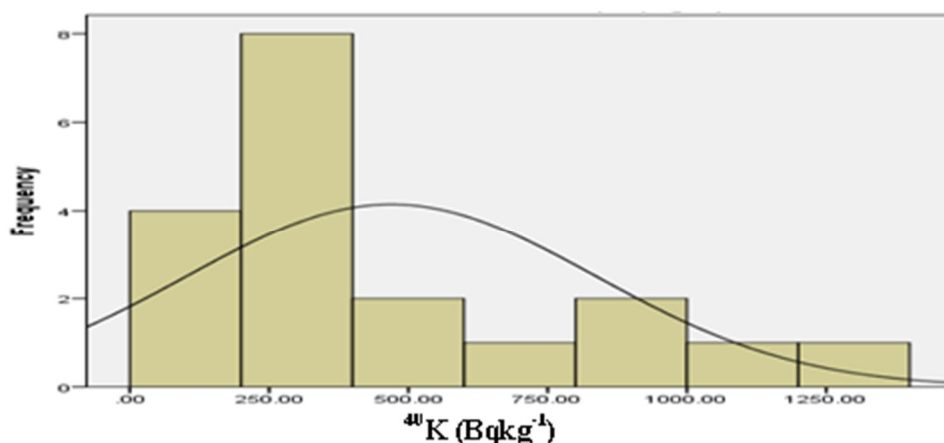


FIG. 4. Frequency distribution of activity concentration of  $^{40}\text{K}$  of *in-situ* gamma spectrometry in Abeokuta.

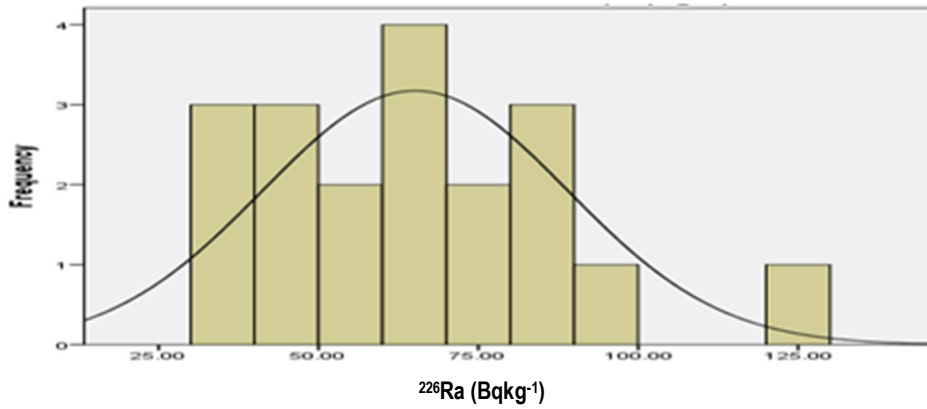


FIG. 5. Frequency distribution of activity concentration of  $^{226}\text{Ra}$  of *in-situ* gamma spectrometry in Abeokuta.

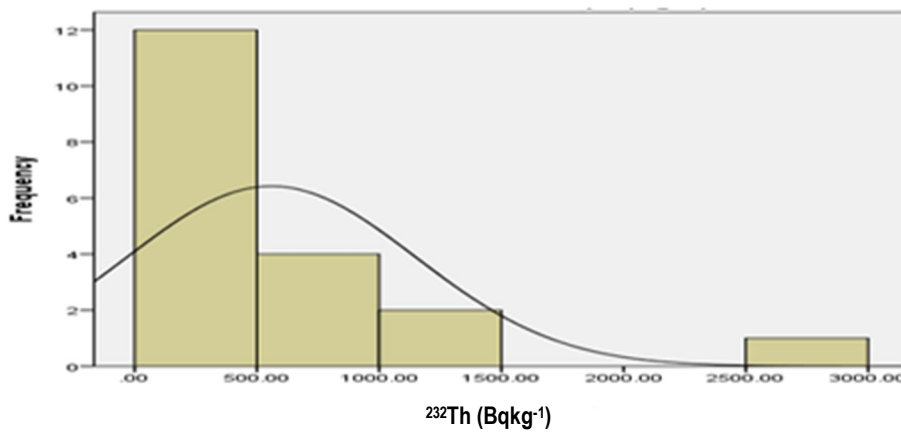


FIG. 6. Frequency distribution of activity concentration of  $^{232}\text{Th}$  of *in-situ* gamma spectrometry in Abeokuta.

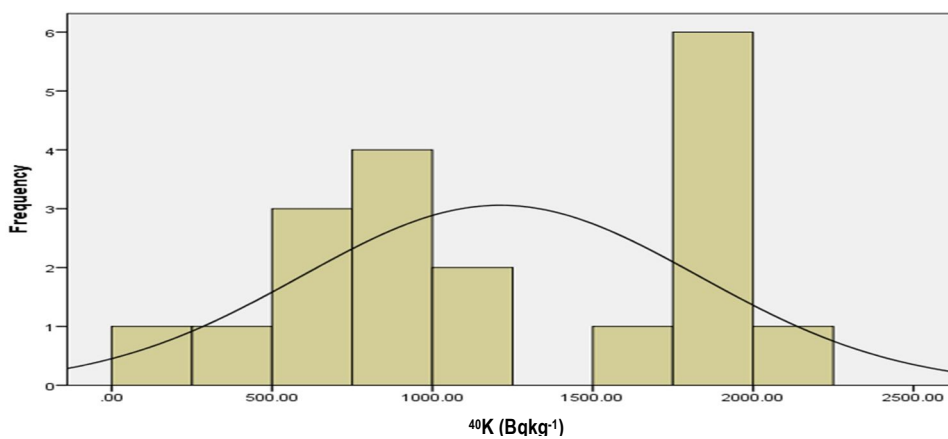


FIG. 7. Frequency distribution of activity concentration of  $^{40}\text{K}$  of laboratory-based gamma spectrometry in Abeokuta.

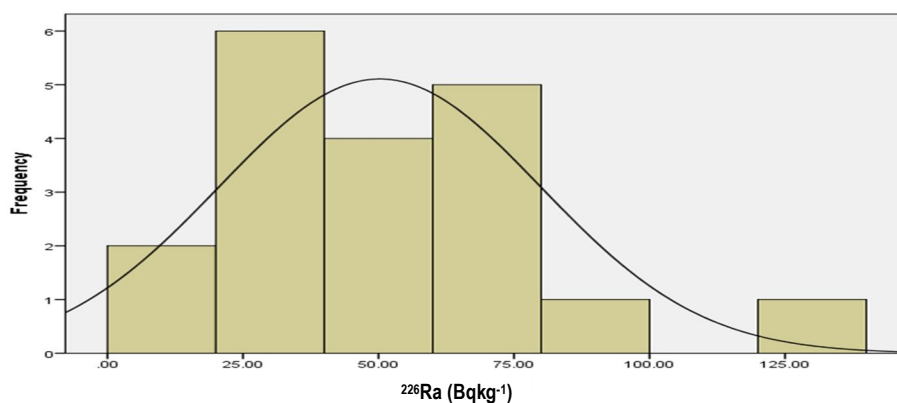


FIG. 8. Frequency distribution of activity concentration of  $^{226}\text{Ra}$  of laboratory-based gamma spectrometry in Abeokuta.

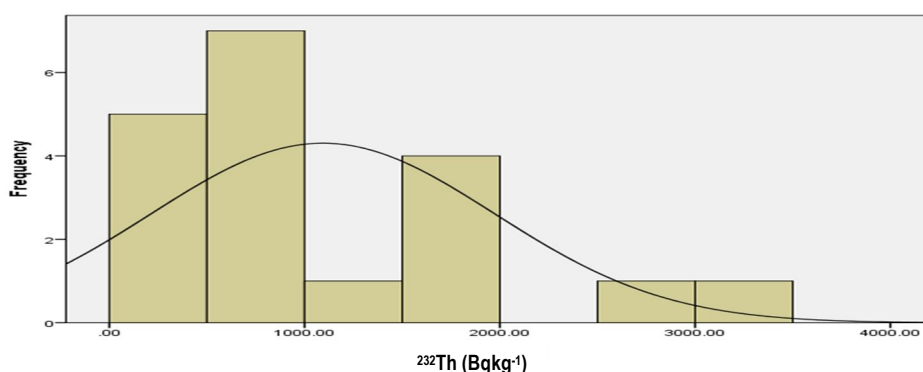


FIG. 9. Frequency distribution of activity concentration of  $^{232}\text{Th}$  of laboratory-based gamma spectrometry in Abeokuta.

## Conclusion

The activity concentrations of primordial radionuclides have been measured using both the laboratory-based and *in-situ* gamma spectrometry methods. The ranges of the activity concentrations for  $^{40}\text{K}$ ,  $^{226}\text{Ra}$  and  $^{232}\text{Th}$  have been found to be 113 – 1975, 5 – 128 and 181 – 3284 Bqkg<sup>-1</sup>, respectively for laboratory-based gamma spectrometry and 104 – 1312, 31 – 121 and 104 – 2578 Bqkg<sup>-1</sup>, respectively for *in-situ* gamma spectrometry. This study determined that the average activity concentrations of the primordial radionuclides in Abeokuta were much higher than worldwide averages of 400, 35 and 30 Bqkg<sup>-1</sup> for  $^{40}\text{K}$ ,  $^{226}\text{Ra}$  and  $^{232}\text{Th}$ , respectively.

From both methods, thorium is seen to be the major contributor to environmental radioactivity of the city Abeokuta. This could be associated to the geological setting of the city. The two methods used in this work have proven to be able to allow for scientific hypothesis to be tested with sufficient statistical power. Good correlations were deduced between the activity concentration results obtained from laboratory-based and *in-situ* gamma spectrometry, which implies a significant relationship between the two methods used in the study area. The *in-situ* gamma spectrometry therefore, is not inferior to the laboratory-based gamma spectrometry.

## References

- [1] Eisenbud, M., "Environmental Radioactivity from Natural, Industrial and Military Sources. (New York: Academic Press, Harcourt Brace Joanovich, 1987).
- [2] Beck, H.L., DeCampo, J. and Gogolak, C., New York: U.S. Department of Energy, Environmental Measurements Laboratory, Report# HASL-258 (1972).
- [3] Othman, I. and Yassine, T., Science of the Total Environment, 170 (1994) 119.
- [4] Sadremomtaz, A., Vahabi, M.M., Khoshbinfar, S. and Moghaddasi, A., Caspian Journal of Environmental Science, 8 (2) (2010) 203.
- [5] Lettner, A., Andradi, A., Hubmer, A.K., Lovranich, E., Steger, F. and Zombori, P., Nuclear Instruments and Methods in Physics Research-Section A: Accelerators, Spectrometers, Detectors and Associated Equipment, 269 (3) (1996) 547.
- [6] Frazier B., "The Use of *in-Situ* Gamma Spectrometer to Save Time, Dose and Money in Operating Nuclear Facilities". Proc. Health Physics Society Midyear Topical Meeting, "Radiation Safety and ALARA Conditions for the 21<sup>st</sup> Century", Anaheim, California, USA (2001).
- [7] Jonas, B., Improving Accuracy of *in-Situ* Gamma-ray Spectrometry, Print and Media 2004940 (2008).
- [8] Aladenola, O.O. and Adeboye, O., Water Resources Management, 24 (10) (2010) 2129.
- [9] Moroofo, O.O. and Gabriel, O.A., Journal of Geography and Geology, 6 (3) (2014) 162.
- [10] Farai, I.P. and Vincent, U.E., Nigerian Journal of Physics, 18 (1) (2006) 121.
- [11] Okeyode, I.C. and Jibiri, N.N., Research Journal of Physics, 7 (1) (2013) 1.
- [12] Falowo, O.O., Materials and Geo-environment, 67 (1) (2020) 21.
- [13] Miller, K.M. and Shebell, P., "In situ Gamma-ray Spectrometry: A Tutorial for Environmental Radiation Scientists". (Environmental Measurements Laboratory, U. S. Department of Energy, New York, NY, 10014-3621 (1993).
- [14] Shittu, H.O., Olarinoye, I.O., Baba-Kutigi, A.N., Olukotun, S.F., Ojo, E.O. and Egga, A., American Institute of Science Physics Journal, 1 (2) (2015) 71.
- [15] Okedeyi, A.S., Gbadebo, A.M., Arowolo, T.A. and Tchokosa, P., Asian Journal of Applied Science, 5 (7) (2012) 506.
- [16] Okeyode, I.C., Towolawi, G.B., Akinboro, F.G., Makinde, V. and Mustapha, A.O., International Journal of Research in Medical and Health Sciences, 2 (2) (2013) 10.



### Calculation of the Electric Quadrupole Moment of ${}^6\text{Li}$ and ${}^7\text{Li}$ in Shell Model and Cluster Model

Jamshid K. Bizhaem, Nasrin Malekinezhad and Mohammadreza Shojaei

*Department of Physics, Shahrood University of Technology, P.O. Box 36155-316, Shahrood, Iran.*

**Doi:** <https://doi.org/10.47011/14.4.7>

*Received on:* 10/10/2020;

*Accepted on:* 01/12/2020

---

**Abstract:** In this paper, we have investigated electric quadrupole moment of  ${}^6\text{Li}$  and  ${}^7\text{Li}$  in both shell model and cluster model. In shell model, the nuclei  ${}^6\text{Li}$  and  ${}^7\text{Li}$  can be modeled as one core plus nucleons. Nucleons outside the closed shell can be considered as a two- and three-particle system. In cluster structure, we have selected alpha clusters and triton or deuteron in interaction with alpha cluster ( ${}^7\text{Li}$  and  ${}^6\text{Li}$  involving  $\alpha + {}^3\text{H}$  and  $\alpha + {}^2\text{H}$ , respectively). By solving Schrödinger equation and using suitable potential for interaction between particles by applying Nikiforov-Uvarov method, potential coefficients have been computed. Then, we have calculated the energy and wave function for nuclei  ${}^6\text{Li}$  and  ${}^7\text{Li}$  and compared the results obtained with experimental results. By having the wave function, we can obtain the quadrupole moment. These values are compared with predictions from shell-model and cluster-model calculations. Although the difference between them is small, the electric quadrupole moment results in the cluster model are in good agreement with experimental results.

**Keywords:** Electric quadrupole moment, Shell-model, Cluster-model, *Li* isotopes, Non-relativistic equation.

## Introduction

Electric quadrupole and magnetic dipole moments can be determined using an experimental method that is based on the nuclear magnetic resonance technique [1, 2, 3]. In nuclear physics, the study of isotopes and calculation of static properties in the different models are the main goals. The most important models in nuclear physics are shell and cluster models. Shell model is acceptable in nuclear physics and  ${}^7\text{Li}$  and  ${}^6\text{Li}$  are described in the shell model with p-shell wave functions. Cluster structure in nuclear physics means that the nucleus behaves as a combination of clusters and cluster means infrastructures with a specific spatial position that are composed of nucleons with strong correlations. From the theoretical point of view, the energy of *Li* isotopes has been studied in many different ways [1, 4]. C. Forssen

*et al.* calculated the charge radii and electromagnetic moments of the  $A \leq 11$  chains of *Li* and *Be* isotopes. They compared the performance of two very different NN interactions: (1) the CD-Bonn 2000 interaction (CDB2k) [5], that is a charge-dependent NN interaction based on one-boson exchange; and (2) the INOY IS-M [6], that is a phenomenological interaction for which non-locality was introduced in certain partial waves, so that the binding energies of  ${}^3\text{H}$  and  ${}^3\text{He}$  are described correctly [1]. It is very useful to describe a suitable model consistent with experience in different trends in physics to solve problems. In nuclear physics, due to the complexity of the potentials, a model must be considered in order to overcome this complexity. Among different nuclear models, cluster model and shell model have considerable answers for

nuclei, especially light nuclei. Since the wave function contains a lot of necessary information for descriptions of quantum system, solving equations such as Schrödinger equation in nonrelativistic quantum mechanics is very important [7]. The lithium isotopes have received much attention due to their rich experimental results in static properties. Recent studies have investigated some of the static properties of lithium isotopes, such as charge radius, energy spectrum and electrical quadrupole moment that present a good picture of their nuclear structure. It is useful to calculate these quantities to test microscopic theory by future experiments [1, 8, 9, 10]. In this work, we calculated electric quadrupole moment of  ${}^7\text{Li}$  and  ${}^6\text{Li}$  in two ways: cluster model and shell model. By selecting a suitable potential in the cluster and shell models, ground-state binding energies, wave functions and finally quadrupole moments of lithium isotopes by solving the non-relativistic equation (Schrödinger) are investigated. In the cluster model, which has recently been considered by many researchers, nucleons are considered as clusters that reduce the complexity of multiparticle systems. The alpha cluster consists of two protons and two neutrons [11].  ${}^7\text{Li}$  And  ${}^6\text{Li}$  involving  $\alpha + {}^3\text{H}$  and  $\alpha + {}^2\text{H}$ , respectively, form a two-particle system. In shell model, we consider  ${}^4\text{He}$  as a closed shell plus few nucleons outside the closed shell. Nucleons outside the closed shell can be considered as a two- and three-particle system; then, we calculated electric quadrupole moment. The results obtained from the calculations in these models compare with the experimental data and other results [1, 2, 3]. To calculate the electric quadrupole moment, we need the wave function of the system, so we use the Schrödinger equation and solve it for these models and then we obtained ground-state binding energies and wave functions.

The cluster model is one of the most important models describing many-particle systems in nuclear models. Studying the properties of many-particle systems is complex and difficult due to high degrees of freedom, so the cluster model is one of the useful solutions to solve this problem. Instead of investigating individual particles, we consider the interaction between clusters. According to the cluster model, the nuclei are a combination of subsystems with a specific spatial position

composed of strongly correlated nucleons. One of the most important clusters is the alpha cluster.

In the shell model, the nucleus energy levels are considered as layers and sublayers in which the nucleons are defined. In the layered model, using the Pauli Exclusion Principle, the structure of the nucleus is expressed based on energy levels, which has been successful in predicting magic numbers. Evidence for the validity of the shell model comes from experimental observations, such as binding energy, spin ... and so on.

## Schrödinger Equation in Cluster Model

To investigate the nuclei, there are two perspectives: relativistic and non-relativistic, each of which is particularly important. In this work, we use a non-relativistic system. In non-relativistic quantum mechanics, the Schrödinger equation is as follows:

$$H\psi = E\psi,$$

$$\left\{-\frac{\hbar^2}{2\mu}\nabla^2 + V(r)\right\}\psi_{n,l}(r) = E_{n,l}\psi_{n,l}(r)$$

where  $H$  is the Hamiltonian system and  $E$  is the energy system.

For a two-cluster system, the Schrödinger equation for the radial potential  $V(r)$  has the following form [12, 13]:

$$\frac{-\hbar^2}{2\mu}\left(\frac{d^2}{dr^2} + \frac{2}{r}\frac{d}{dr}\right)\psi_{n,l}(r) + (V(r) + \frac{\hbar^2 l(l+1)}{2\mu r^2})\psi_{n,l}(r) = E_{n,l}\psi_{n,l}(r) \quad (1)$$

The first step of studying the properties of nuclei in shell model and cluster model is choosing a suitable potential [14]. Due to this reason, in cluster structure, the phenomenological interaction potential between  $\alpha$ -clusters is considered as:

$$V(r) = V_0 \frac{e^{-2ar}}{r^2} + \frac{b}{r^2} e^{-ar} \quad (2)$$

Yukawa potential is one of the most important potentials having been studied by many researchers in physics and chemical physics [15, 16, 17]. In this work, we use inversely quadratic Yukawa (IQY) potential and due to nuclear force saturation at lower distances, we add a repulsive term potential as interaction between particles and clusters.  $V_0$  is

the parameter describing the potential well depth,  $\alpha$  represents the potential range and  $b$  is an adjustable parameter. By substituting Eq. (2) in Eq. (1), the radial Schrödinger equation is obtained as:

$$\frac{d^2R}{dr^2} + \frac{2}{r} \frac{dR}{dr} - \frac{l(l+1)}{r^2} + \frac{2\mu}{\hbar^2} \left[ E - V_0 \frac{e^{-2\alpha r}}{r^2} - \frac{b}{r^2} e^{-\alpha r} \right] R = 0. \quad (3)$$

Then, with further analysis and simplification, Eq. (3) becomes:

$$\frac{d^2R}{dr^2} + \frac{2}{r} \frac{dR}{dr} + \frac{1}{r^2} [-\varepsilon^2 r^2 - \beta r - \gamma] R = 0, \quad (4)$$

$$\begin{cases} -\varepsilon^2 = \frac{2\mu}{\hbar^2} E & \varepsilon > 0 \\ l(l+1) + \frac{2\mu}{\hbar^2} (V_0 + b) = \gamma \\ \frac{2\mu}{\hbar^2} (\alpha b + 2V_0\alpha) = -\beta \end{cases}$$

It is seen from Eq. (4) that the equation has the exponential square and inverse radial square terms, which cannot be solved analytically; then we use the NU method. At this point, we briefly describe the NU method.

## The General Framework of the Nikiforov–Uvarov (NU) Technique

The Nikiforov–Uvarov method offers a powerful mathematical model to solve second-order differential equations [18]. the differential equation can be written in the following form [19, 20]:

$$\psi''_n(s) + \frac{\tilde{\tau}(s)}{\sigma(s)} \psi'_n(s) + \frac{\tilde{\sigma}(s)}{\sigma^2(s)} \psi_n(s) = 0 \quad (5)$$

Where  $\sigma(s)$  and  $\tilde{\sigma}(s)$  are polynomials that can be at most second-degree and  $\tilde{\tau}(s)$  is a first-degree polynomial. To find a particular solution for Eq. (4) by separation of variables, we have the following transformation:

$$\psi(s) = \varphi(s)y(s). \quad (6)$$

It reduces Eq. (5) to a hyper-geometric type function:

$$\sigma(s)y''(s) + \tau(s)y'(s) + \lambda y(s) = 0 \quad (7)$$

where  $\tau(s) = \tilde{\tau}(s) + 2\pi(s)$  and  $\tau'(s) < 0$ , which means that  $\tau(s)$  has a negative derivative. Additionally,  $\lambda$  is a parameter with the following definition:

$$\begin{cases} \lambda_n = -n\tau'(s) - \frac{n(n-1)}{2} \sigma''(s), & n = 0, 1, 2, \dots \\ \lambda = k + \pi'(s) \end{cases} \quad (8)$$

And equality of the two parts in Eq. (8) yields the energy eigenvalues of the intended multi-particle system.

$\pi(s)$  is a polynomial with the parameter  $s$  and the determination of  $k$  is the essential point in the calculation of  $\pi(s)$ . In order to find the value of  $k$ , the expression under the square root must be square of a polynomial:

$$\pi(s) = \frac{\sigma'(s) - \tilde{\tau}(s)}{2} \pm \sqrt{\left(\frac{\sigma'(s) - \tilde{\tau}(s)}{2}\right)^2 - \tilde{\sigma}(s) + k\sigma(s)} \quad (9)$$

The function  $\varphi(s)$  is defined as a logarithmic derivative:

$$\frac{\varphi'(s)}{\varphi(s)} = \frac{\pi(s)}{\sigma(s)} \quad (10)$$

$y(s)$  is the hypergeometric type function the polynomial solutions of which are given by Rodrigues relation:

$$y_n(s) = \frac{B_n}{\rho_n} \frac{d^n}{ds^n} (\sigma^n(s)\rho(s)) \quad (11)$$

$B_n$  is the normalizing constant and the weight function  $\rho$  must satisfy the following condition:

$$(\sigma\rho)' = \tau\rho \quad (12)$$

## Mathematical Calculation and Results

If we apply the NU method based on the discussed model, by comparing (4) and (5), the following expressions are obtained:

$$\tilde{\tau} = 2, \quad \sigma = r, \quad \sigma^2 = r^2, \quad \tilde{\sigma} = -\varepsilon^2 r^2 - \beta r - \gamma \quad (13)$$

Substituting the above expressions into (8) and considering the NU method condition for  $\pi(s)$  with some analysis and simplification, the following equation can be obtained:

$$\pi(r) = -\frac{1}{2} - \frac{1}{2} (2\varepsilon r \pm \sqrt{1 + 4\gamma}) \quad (14)$$

Since we have the polynomial  $\tau(s) = \tilde{\tau}(s) + 2\pi(s)$  with a negative derivative, the suitable form has to be established for this parameter. We have:

$$\tau = 1 - (2\varepsilon r - \sqrt{1 + 4\gamma}) \quad (15)$$

Finally, considering the notations of (8) and Eq. (4), we can write the energy Eigen-values for such a system of  $\alpha$ -clusters as:

$$E = -\frac{2\mu}{\hbar^2} \frac{(ab+2V_0\alpha)^2}{\left[2n+1+\sqrt{1+4l(l+1)+\frac{2\mu}{\hbar^2}(V_0+b)}\right]^2} \quad (16)$$

By using  $\psi(s) = \varphi(s)y(s)$ , the solution of (4) can be written as the wave function of the Schrödinger equation as follows:

$$\psi = B_n r^{-\frac{1}{2}+\sqrt{1+4\gamma}} \exp(-\varepsilon r) L_n^{\sqrt{1+4\gamma}}(2\varepsilon r) \quad (17)$$

where  $B_n$  is the normalization constant. We have obtained the potential parameters by fitting the ground-state energy for the mentioned isotopes. In this way, the chosen parameters for  ${}^6\text{Li}$  in which both  $n$  and  $l$  are set to 1 are:  $V_0 = 42.3 \text{ MeV}$ ,  $b = 1.7 \text{ MeV}$ ,  $\alpha = 0.00125 \text{ fm}^{-1}$  and for  ${}^7\text{Li}$ ,  $V_0 = 35 \text{ MeV}$ ,  $b = 1.15 \text{ MeV}$ ,  $\alpha = 0.00158 \text{ fm}^{-1}$ . The values of ground-state binding energies are shown in Table 1.

### Schrödinger Equation in Shell Model

Studying the nucleon-nucleon interactions is very useful to find the many important properties of multi-nucleon systems. In this section we select a core and consider Eq. (2) for the interaction between nucleons. To study the energy spectrum and wave function for N-body system, we use the time-independent Schrödinger equation [12-21]. That is as follows:

$$\frac{d^2R}{dr^2} + \frac{D-1}{r} \frac{dR}{dr} + \frac{2\mu}{\hbar^2} \left[ E - V_0 \frac{e^{-2\alpha r}}{r^2} - \frac{b}{r^2} e^{-\alpha r} - \frac{\hbar^2 l(l+D-2)}{2\mu r^2} \right] R = 0 \quad (18)$$

where  $R(r)$  and  $V(r)$  are the radial parts of the N-body wave function and the potential, respectively in Eq. (2),  $D = 3N - 3$  and  $\mu$  is the reduced mass.  $E$  represents the energy of the system. In order to solve the above equation, we have:

$$\frac{d^2R}{dr^2} + \frac{D-1}{r} \frac{dR}{dr} + \frac{1}{r^2} \left[ \frac{2\mu}{\hbar^2} E r^2 - \frac{2\mu}{\hbar^2} V_0 + \frac{2\mu}{\hbar^2} V_0 (2\alpha r) - \frac{2\mu}{\hbar^2} b + \frac{2\mu}{\hbar^2} b \alpha r - l(l+D-2) \right] R = 0 \quad (19)$$

Then, with further simplification, Eq. (18) becomes:

$$\frac{d^2R}{dr^2} + \frac{D-1}{r} \frac{dR}{dr} + \frac{1}{r^2} [-\varepsilon^2 r^2 - \beta r - \gamma] R = 0, \quad \begin{cases} \frac{2\mu}{\hbar^2} (V_0 + b) + l(l+D-2) = \gamma \\ \frac{2\mu}{\hbar^2} (2\alpha V_0 + b\alpha) = -\beta \\ \frac{2\mu}{\hbar^2} E = -\varepsilon^2 \quad \varepsilon > 0 \end{cases} \quad (20)$$

There is no exact solution of the Schrödinger equation for most types of interaction. So, various methods, such as super symmetric method [22, 23] and Nikiforov-Uvarov method [18], have been used for the solution of this equation. As mentioned before:

$$\tilde{\tau} = D - 1, \quad \sigma = r, \quad \sigma^2 = r^2, \quad \tilde{\sigma} = -\varepsilon^2 r^2 - \beta r - \gamma \quad (21)$$

Considering the NU method condition for  $\pi(s)$  with some analysis and simplification, the following equation can be obtained:

$$\pi(r) = \frac{2-D}{2} \pm \frac{1}{2} (2\varepsilon r \pm \sqrt{(2-D)^2 + 4\gamma}) \quad (22)$$

And we have:

$$\tau = 1 - (2\varepsilon r - \sqrt{(2-D)^2 + 4\gamma}) \quad (23)$$

As mentioned before, we can use the NU method to acquire the equation of energy. Therefore, we have:

$$E = -\frac{2\mu}{\hbar^2} \frac{(2V_0\alpha + b\alpha)^2}{\left[2n+1+\sqrt{(2-D)^2+4\left(\frac{2\mu}{\hbar^2}(V_0+b)+l(l+D-2)\right)}\right]^2} \quad (24)$$

Having achieved this important equation, we can calculate the energy for  ${}^6\text{Li}$  and  ${}^7\text{Li}$  nuclei in their ground state by assigning appropriate values to coefficients of the potential. It is worth mentioning that in shell model, the nucleons are assumed as a two- and three-particle system.

We have obtained the potential parameters by fitting the ground state of energy. In shell structure, the potential chosen parameters for  ${}^6\text{Li}$  in which both  $n$  and  $l$  are set to 1 are:  $V_0 = 80 \text{ MeV}$ ,  $b = 100 \text{ MeV}$ ,  $\alpha = 1.12 \text{ fm}^{-1}$  and for  ${}^7\text{Li}$ ,  $V_0 = 40 \text{ MeV}$ ,  $b = 1 \text{ MeV}$ ,  $\alpha = 0.00158 \text{ fm}^{-1}$ .

And the wave functions of the quantum system are given by:

$$\psi = B_n r^{\frac{1}{2}((2-D)+\sqrt{(2-D)^2+4\gamma})} \times \exp(-\varepsilon r) L_n^{\sqrt{(2-D)^2+4\gamma}}(2\varepsilon r); \quad \gamma = \frac{2\mu}{\hbar^2} (V_0 + b) + l(l+D-2) \quad (25)$$

Ground-state binding energies ( $E$ ) for the mentioned isotopes are summarized in Table 1. We note that the two different ways used in this study are shell and cluster models. The results obtained from the cluster model are more consistent with the experimental results,

although the difference between the two models is very small.

Since the nuclei at the ground state have spin of  $J^\pi = 1^+, 3/2^-$ , the effect of spin-orbit coupling on the  $L = 1$  states cannot be ignored. Therefore, using Eq. (26), the effect of spin-orbit coupling on the energy levels is calculated as a

first-order disturbing factor. The results of the calculation are shown in Table 1.

$$E_n^{(1)} = \langle n | V_{L,S}(r) \vec{L} \vec{S} | n \rangle$$

$$= \int \psi^*(r) \frac{\hbar^2}{2m_0^2 c^2} \frac{1}{r} \frac{dV(r)}{dr} \vec{L} \vec{S} \psi(r) r^2 dr \quad (26)$$

TABLE 1. Ground-state binding energies ( $E$ ) for Li isotopes in shell and cluster models compared with experiment data and other results.

Isotope	$J^\pi$	$E(\text{MeV})$						
		Shell model	L.S.	Cluster model	L.S.	CDB <sub>2k</sub> [2]	INOY [2]	Exp.[24]
${}^6\text{Li}$	$1^+$	31.6833	31.90	31.7296	31.8301	29.07(41)	32.33(19)	31.99
${}^7\text{Li}$	$3/2^-$	39.6439	39.6857	39.1241	39.1741	35.56(23)	39.62(40)	39.24

### Calculation of Electric Quadrupole Moment

The paired nucleons move in spherically symmetric orbits; they don't contribute to Q. Therefore, we might expect that for many nuclei, the quadrupole moment can be estimated from the valence nucleons which we can assume to orbit near the surface. The electric quadrupole moment has been calculated for the ground state as [25]:

$$eQ = e \int \psi^*(3z^2 - r^2) \psi dv \quad (27)$$

From the above equation, we understand that we need the wave function of the system to calculate the electric quadrupole moment. The radial wave function is obtained from Eqs. (17) and (25), so we can easily calculate the electric quadrupole moment of the studied isotopes by calculating Q in shell model and cluster model. In order to calculate the electric quadrupole moment, it is assumed that the wave function is concentrated in the xy-plane. For this reason, the quantity of quadrupole momentum is obtained negatively (see Table 2). The obtained results are shown in Table 2.

TABLE 2. Ground-state electric quadrupole moments ( $Q$ ).

Isotope	$Q(\text{eb})$					
	Shell model	Cluster model	CDB <sub>2k</sub> [2]	INOY [2]	Exp.[26]	value error
${}^6\text{Li}$	-0.000823	-0.000813	-0.00066(40)	+0.00080(19)	-0.000806	0.0007232/ 0.000007
${}^7\text{Li}$	-0.0413	-0.0406	-0.0320(22)	-0.0279(17)	-0.040	0.0013/0.0006

Finding the forces between the nucleons, the nuclei structure, the nature of the nuclear interactions between them and the electric quadrupole moment are considered as the main aims of studying nuclear physics. Good values obtained of the nuclear ground-state properties of the Li isotopes, such as energy and electric quadrupole moment, are ideal tools for testing the validity of these nuclear models. These values are compared with predictions from shell-

model and cluster-model calculations. Although the difference between them is very small, the electric quadrupole moment results in the cluster model are in good agreement with experimental results. Also, the calculated energy and electric quadrupole moment in cluster model are close to the experimental data. Consequently, the suggested model can also be used for investigating other similar isotopes.

## References

- [1] Forssén, C., Caurier, E. and Navrátil, P., *Phys. Rev. C*, 79 (2009) 021303.
- [2] Borremans, D. et al., *Phys. Rev. C*, 72 (2005) 044309.
- [3] Neugart, R., Balabanski, D.L., Blaum, K., Borremans, D., Himpe, P., Kowalska, M., Lievens, P., Mallion, S., Neyens, G., Vermeulen, N. and Yordanov, D.T., *Phys. Rev. Lett.*, 101 (2008) 132502.
- [4] Roshanbakht, N. and Shojaei, M.R., *Eur. Phys. J. A*, 54 (2018) 134.
- [5] Machleidt, R., *Phys. Rev. C*, 63 (2001) 024001.
- [6] Doleschall, P., *Phys. Rev. C*, 69 (2004) 054001.
- [7] Mousavi, M. and Shojaei, M. R., *Adv. High-energy Phys.*, 2017 (2017) 5841701.
- [8] Cederberg, J., Olson, D., Larson, J., Rakness, G., Jarausch, K., Schmidt, J., Borovsky, B., Larson, P. and Nelson, B., *Phys. Rev. A*, 57 (1998) 2539.
- [9] Stone, N. J., *Atomic Data and Nuclear Data Tables*, 111–112 (2016) 1.
- [10] Tanihata, I., Kobayashi, T., Yamakawa, O., Ekuni, K., Sugimoto, K., Takahashi, N., Shimoda, T. and Sato, H., *Phys. Lett. B*, 206 (4) (1988) 592.
- [11] Beck, C., "Clusters in nuclei", Vols. 1, 2 & 3, (Springer-Verlag, Berlin, Heidelberg, 2010).
- [12] Rajabi, A.A., *Few-body Systems*, 37 (2005) 197.
- [13] Zoghi-Foumani, N., Shojae, M.R. and Rajabi, A.A., *Pramana Journal of Phys.*, 88, (2017) 68.
- [14] Binesh, Z., Shojaei, M.R. and Azadegan, B., *Can. J. Phys.*, 98 (1) (2018) 28.
- [15] Yukawa, H., *Proc. Phys.-Math. Soc. Jpn.*, 17 (1935) 48.
- [16] Rezvani, F. and Shojaei, M.R., *U. P. B. Sci. Bull., Series A*, 79 (2017) 3.
- [17] Hamzavi, H., Ikhdair, S.M. and Ita, B.I., *Physica Scripta*, 85 (4) (2012) 045009.
- [18] Nikiforov, A.F. and Uvarov, V.B., "Special Function of Mathematical Physics", (Birkhäuser Basel, 1988).
- [19] Aslanzadeh, M. and Rajabi, A.A., *Eur. Phys. J. A*, 50 (2014) 1.
- [20] Zhang, M.C., Sun, G.H. and Dong, S.H., *Phys. Lett. A*, 374 (2010) 704.
- [21] Deta, U.A., Suparmi, A. and Cari, C., *Adv. Studies Theor. Phys.*, 7 (2013) 647.
- [22] Cooper, F., Khare, A. and Sukhatme, U., *Phys. Rep.*, 251 (1995) 267.
- [23] Feizi, H., Rajabi, A.A. and Shojaei, M.R., *Acta Physica Polonica B*, 42 (2011) 2143.
- [24] Tilley, D.R., Cheves, C.M., Godwin, J.L., Hale, G.M., Hofmann, H.M., Kelley, J.H., Sheu, C.G. and Weller, H.R., *Nucl. Phys. A*, 708 (2002) 3.
- [25] Krane, K.S., "Introductory Nuclear Physics", (John Wiley and Sons, Ltd., 1987).
- [26] Stone, N.J., *Atomic Data and Nuclear Data Tables*, 90 (1) (2005) 75.

### Study on the Applicability of Varshni Potential to Predict the Mass Spectra of the Quark-Antiquark Systems in a Non-relativistic Framework

Etido P. Inyang<sup>a,c</sup>, Ephraim P. Inyang<sup>a</sup>, Eddy S. William<sup>a</sup> and Etebong E. Ibekwe<sup>b</sup>

<sup>a</sup> *Theoretical Physics Group, Department of Physics, University of Calabar, PMB 1115, Calabar, Nigeria.*

<sup>b</sup> *Department of Physics, Akwa Ibom State University, Ikot Akpaden, P.M.B 1167, Uyo, Nigeria.*

<sup>c</sup> *Department of Physics, National Open University of Nigeria, Jabi, Abuja*

**Doi:** <https://doi.org/10.47011/14.4.8>

*Received on: 14/10/2020;*

*Accepted on: 29/11/2020*

---

**Abstract:** In this work, we obtain the Schrödinger equation solutions for the Varshni potential using the Nikiforov-Uvarov method. The energy eigenvalues are obtained in non-relativistic regime. The corresponding eigenfunction is obtained in terms of Laguerre polynomials. We applied the present results to calculate heavy-meson masses of charmonium  $c\bar{c}$  and bottomonium  $b\bar{b}$ . The mass spectra for charmonium and bottomonium multiplets have been predicted numerically. The results are in good agreement with experimental data and the works of other researchers.

**Keywords:** Schrödinger equation, Varshni potential, Nikiforov-Uvarov method, Heavy meson.

**PACs:** 14.20.Lq; 03.65.-w; 14.40.Pq; 11.80.Fv.

## 1. Introduction

It is a well-known fact by many researchers that quarkonium systems provide deep insight into the essential description of quantum chromodynamics (QCD) theory, particle physics and standard model [1-3]. Quarkonia with heavy quark and antiquark and their interaction are well described by the Schrödinger equation (SE). The solution of this SE with potential is one of the most fundamental problems in quarkonium systems. It is noted that the potentials considered should take into account two important features of the strong interaction; namely, asymptotic freedom and quark confinement [4-8]. The most fundamental potential used in studying quarkonium system is the Cornell potential, also known as Killingbeck potential. Most researchers have carried out works with Cornell potential [9, 10]. For instance, Vega and Flores

[11] solved the Schrödinger equation with the Cornell potential using the variational method and supersymmetric quantum mechanics (SUSYQM). Ciftci and Kisoglu [12] addressed non-relativistic arbitrary  $l$ -states of quark-antiquark through the Asymptotic Iteration Method (AIM). The energy eigenvalues with any  $l \neq 0$  states and mass of the massive quark-antiquark system (quarkonium) were gotten. An analytic solution of the N-dimensional radial Schrödinger equation with the mixture of vector and scalar potentials *via* the Laplace transformation method (LTM) was studied by [13]. Their results were employed to analyze the different properties of the heavy-light mesons. Al-Jamel and Widyan [14] studied heavy quarkonium mass spectra in a Coulomb field plus quadratic potential using the Nikiforov-

Uvarov method. In their work, the spin-averaged mass spectra of heavy quarkonia in a Coulomb plus quadratic potential is analyzed within the non-relativistic Schrödinger equation. Al-Oun *et al.* [15] examined heavy quarkonia characteristics in the general framework of a non-relativistic potential model consisting of a Coulomb plus quadratic potential. Kumar and Chand [16] carried out an asymptotic study to the N-dimensional radial Schrödinger equation for the quark-antiquark interaction potential employing asymptotic iteration method (AIM). Ibekwe *et al.* [17] solved the radial SE with an exponential, generalized, anharmonic Cornell potential using the series expansion method. They applied the bound state eigenvalues to study the energy spectra for CO, NO, CH and N<sub>2</sub> diatomic molecules and the mass spectra of heavy quarkonium systems. Furthermore, Omugbe *et al.* [18] solved the SE with Killingbeck potential plus an inversely quadratic potential model. They obtained the energy eigenvalues and the mass spectra of the heavy and heavy-light meson systems. In addition, Ali *et al.* [19] studied the energy spectra of mesons and hadronic interactions using Numerov's method. Their solutions were used to describe the phenomenological interactions between the charm-anticharm quarks *via* the model. The model accurately predicts the mass spectra of charmed quarkonium as an example of mesonic

systems. Inyang *et al.* [20] obtained the Klein-Gordon equation solutions for the Yukawa potential using the Nikiforov-Uvarov method. The energy eigenvalues were obtained both in relativistic and non-relativistic regime. They applied the results to calculate heavy-meson masses of charmonium and bottomonium.

The Varshni potential is greatly important with applications, cutting across nuclear physics, particle physics and molecular physics [21]. The Varshni potential takes the form:

$$V(r) = a - \frac{abe^{-\alpha r}}{r} \quad (1)$$

where  $a$  and  $b$  are potential strengths for Varshni potential,  $\alpha$  is the screening parameter which controls the shape of the potential energy curve as shown in Fig. 1 and  $r$  is the inter-nuclear separation. The Varshni potential is a short-range repulsive potential energy that plays an important role in chemical, particle and molecular physics [22]. This potential is used generally to describe bound states of the interaction of systems and has been applied in both classical and molecular physics. The Varshni potential was studied by Lim using the 2-body Kaxiras-Pandey parameters. He observed that Kaxiras and Pandey used this potential to describe the 2-body energy portion of multi-body condensed matter [23].

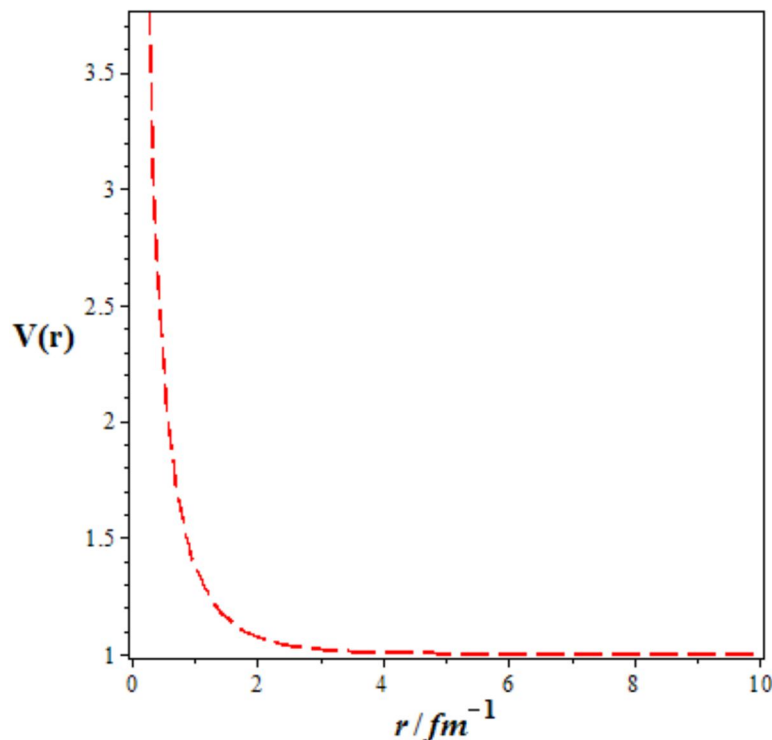


FIG.1. Plots of Varshni potential with  $r$  in ( $\text{fm}^{-1}$ ).

Many researchers have studied heavy mesons with non-exponential type potential like the Cornell without considering the exponential type [11-16]. Therefore, we intend to investigate the SE with the exponential type potential (Varshni potential) in the framework of NU method to obtain the mass spectra of quark- antiquark systems. To the best of our knowledge, this is the first time Varshni potential is being studied with the aim of determining the mass spectra of heavy quarkonia systems using the NU method.

The paper is organized as follows: In Section 2, the Nikiforov-Uvarov (NU) method is reviewed. In Section 3, the bound state energy eigenvalues and the corresponding eigenfunction are calculated. In Section 4, the results are discussed. In Section 5, the conclusion is presented.

## 2. A Brief Review of Nikiforov-Uvarov (NU) Method

The NU method is used to transform Schrödinger -like equations into a second-order differential equation through a coordinate transformation  $y = y(r)$ , of the form [24]:

$$\psi''(y) + \frac{\tilde{\tau}(y)}{\sigma(y)}\psi'(s) + \frac{\tilde{\sigma}(y)}{\sigma^2(y)}\psi(y) = 0 \quad (2)$$

where  $\tilde{\sigma}(y)$  and  $\sigma(y)$  are polynomials, at most second-degree and  $\tilde{\tau}(y)$  is a first-degree polynomial. From Eq. (2), we obtain exact solution by using the transformation:

$$\psi(y) = \phi(y)\chi(y). \quad (3)$$

This transformation reduces Eq. (2) into a hypergeometric-type equation of the form:

$$\sigma(y)\chi''(y) + \tau(y)\chi'(y) + \lambda\chi(y) = 0. \quad (4)$$

The function  $\phi(y)$  can be defined as the logarithm derivative:

$$\frac{\phi'(y)}{\phi(y)} = \frac{\pi(y)}{\sigma(y)} \quad (5)$$

where  $\pi(y)$  is at most a first-degree polynomial. The second part of the wave functions in Eq. (4) is a hypergeometric-type function obtained by Rodriguez relation:

$$\chi_n(y) = \frac{B_n}{\rho(y)} \frac{d^n}{dy^n} [\sigma^n(y)\rho(y)] \quad (6)$$

where  $B_n$  is the normalization constant and  $\rho(y)$  the weight function which satisfies the condition below:

$$\frac{d}{dy} (\sigma(y)\rho(y)) = \tau(y)\rho(y) \quad (7)$$

where also:

$$\tau(y) = \tilde{\tau}(y) + 2\pi(y). \quad (8)$$

For bound solutions, it is required that:

$$\frac{d\tau(y)}{dy} < 0. \quad (9)$$

With  $\pi(y)$  and parameter  $\lambda$ , the eigenfunctions and eigenvalues can be obtained using the definition of the following function:

$$\pi(y) = \frac{\sigma'(y) - \tilde{\tau}(y)}{2} \pm \sqrt{\left(\frac{\sigma'(y) - \tilde{\tau}(y)}{2}\right)^2 - \tilde{\sigma}(y) + k\sigma(y)} \quad (10)$$

and

$$\lambda = k + \pi'(y). \quad (11)$$

The value of  $k$  can be obtained by setting the discriminant in the square root in Eq. (10) equal to zero. As such, the new eigenvalues equation can be given as:

$$\lambda + n\tau'(y) + \frac{n(n-1)}{2}\sigma''(y) = 0, (n = 0,1,2,\dots). \quad (12)$$

## 3. Approximate Solutions of the Schrödinger Equation with Varshni Potential

The Schrödinger equation (SE) for two particles interacting *via* potential  $V(r)$  in three-dimensional space is given by [25]:

$$\frac{d^2 R(r)}{dr^2} + \left[ \frac{2\mu}{\hbar^2} (E_n - V(r)) - \frac{l(l+1)}{r^2} \right] R(r) = 0 \quad (13)$$

where  $l, \mu, r$  and  $\hbar$  are the angular momentum quantum number, the reduced mass for the quarkonium particle, inter-particle distance and reduced plank constant, respectively.

We carry out Taylor series expansion of the exponential term in Eq. (1) up to order three, in order to make the potential interact in the quark-antiquark system and this yields:

$$\frac{e^{-\alpha r}}{r} = \frac{1}{r} - \alpha + \frac{\alpha^2 r}{2} - \frac{\alpha^3 r^2}{6} + \dots \quad (14)$$

We substitute Eq. (14) into Eq. (1) and obtain:

$$V(r) = -\frac{B}{r} - Cr + Dr^2 + A \quad (15)$$

where

$$\left. \begin{aligned} A &= a + ab\alpha, B = ab \\ C &= \frac{ab\alpha^2}{2}, D = \frac{ab\alpha^3}{6} \end{aligned} \right\}. \quad (16)$$

Upon substituting Eq. (15) into Eq. (13), we obtain:

$$\frac{d^2 R(r)}{dr^2} + \left[ \frac{2\mu E_{nl}}{\hbar^2} + \frac{2\mu B}{\hbar^2 r} + \frac{2\mu Cr}{\hbar^2} - \frac{2\mu Dr^2}{\hbar^2} - \frac{2\mu A}{\hbar^2} - \frac{l(l+1)}{r^2} \right] R(r) = 0. \quad (17)$$

In order to transform the coordinate from  $r$  to  $y$  in Eq. (17), we set:

$$y = \frac{1}{r}. \quad (18)$$

This implies that the 2<sup>nd</sup> derivative in Eq. (18) becomes:

$$\frac{d^2 R(r)}{dr^2} = 2y^3 \frac{dR(y)}{dy} + y^4 \frac{d^2 R(y)}{dy^2}. \quad (19)$$

Substituting Eqs. (18) and (19) into Eq. (17), we obtain:

$$\frac{d^2 R(y)}{dy^2} + \frac{2y}{y^2} \frac{dR(y)}{dy} + \frac{1}{y^4} \left[ \frac{2\mu E_{nl}}{\hbar^2} + \frac{2\mu By}{\hbar^2} + \frac{2\mu C}{\hbar^2 y} - \frac{2\mu D}{\hbar^2 y^2} - \frac{2\mu A}{\hbar^2} - l(l+1)y^2 \right] R(y) = 0. \quad (20)$$

Next, we propose the following approximation scheme on the term  $\frac{C}{y}$  and  $\frac{D}{y^2}$ .

Let us assume that there is a characteristic radius  $r_0$  of the meson. Then, the scheme is based on the expansion of  $\frac{C}{y}$  and  $\frac{D}{y^2}$  in a power series around  $r_0$ ; i.e., around  $\delta \equiv \frac{1}{r_0}$ , up to the second order. This is similar to Pekeris approximation, which helps deform the centrifugal term such that the modified potential can be solved by the NU method [26].

Setting  $x = y - \delta$  and around  $x = 0$ , it can be expanded into a series of powers as:

$$\frac{C}{y} = \frac{C}{x + \delta} = \frac{C}{\delta \left( 1 + \frac{x}{\delta} \right)} = \frac{C}{\delta} \left( 1 + \frac{x}{\delta} \right)^{-1} \quad (21)$$

which yields:

$$\frac{C}{y} = C \left( \frac{3}{\delta} - \frac{3y}{\delta^2} + \frac{y^2}{\delta^3} \right). \quad (22)$$

Similarly,

$$\frac{D}{y^2} = D \left( \frac{6}{\delta^2} - \frac{8y}{\delta^3} + \frac{3y^2}{\delta^4} \right). \quad (23)$$

Substituting Eqs. (22) and (23) into Eq.(20) yields:

$$\frac{d^2 R(y)}{dy^2} + \frac{2y}{y^2} \frac{dR(y)}{dy} + \frac{1}{y^4} \left[ -\varepsilon + \alpha y - \beta y^2 \right] R(y) = 0 \quad (24)$$

where

$$\left. \begin{aligned} -\varepsilon &= \left( \frac{2\mu E_{nl}}{\hbar^2} - \frac{2\mu A}{\hbar^2} + \frac{6\mu C}{\hbar^2 \delta} - \frac{12\mu D}{\hbar^2 \delta^2} \right), \\ \alpha &= \left( \frac{2\mu B}{\hbar^2} - \frac{2\mu C}{\hbar^2 \delta^2} + \frac{16\mu D}{\hbar^2 \delta^3} \right) \\ \beta &= \left( \gamma - \frac{2\mu C}{\hbar^2 \delta^3} + \frac{6\mu D}{\hbar^2 \delta^4} \right), \gamma = l(l+1) \end{aligned} \right\}. \quad (25)$$

Comparing Eq. (24) and Eq.(2), we obtain:

$$\left. \begin{aligned} \tilde{\tau}(y) &= 2y, \sigma(y) = y^2, \\ \tilde{\sigma}(y) &= -\varepsilon + \alpha y - \beta y^2 \\ \sigma'(y) &= 2y, \sigma''(y) = 2 \end{aligned} \right\}. \quad (26)$$

Substituting Eq. (26) into Eq. (10) yields:

$$\pi(y) = \pm \sqrt{\varepsilon - \alpha y + (\beta + k)y^2}. \quad (27)$$

To determine  $k$ , we take the discriminant of the function under the square root, which yields:

$$k = \frac{\alpha^2 - 4\beta\varepsilon}{4\varepsilon}. \quad (28)$$

We substitute Eq. (28) into Eq. (27) and have:

$$\pi(y) = \pm \left( \frac{\alpha y}{2\sqrt{\varepsilon}} - \frac{\varepsilon}{\sqrt{\varepsilon}} \right). \quad (29)$$

We take the negative part of Eq. (29) and differentiate, which yields:

$$\pi'_-(y) = -\frac{\alpha}{2\sqrt{\varepsilon}}. \quad (30)$$

By substituting Eqs. (26) and (29) into Eq.(8), we have:

$$\tau(y) = 2y - \frac{\alpha y}{\sqrt{\varepsilon}} + \frac{2\varepsilon}{\sqrt{\varepsilon}}. \quad (31)$$

Differentiating Eq. (31), we have:

$$\tau'(y) = 2 - \frac{\alpha}{\sqrt{\varepsilon}}. \quad (32)$$

By using Eq. (11), we obtain:

$$\lambda = \frac{\alpha^2 - 4\beta\varepsilon}{4\varepsilon} - \frac{\alpha}{2\sqrt{\varepsilon}}. \quad (33)$$

And using Eq. (12), we obtain:

$$\lambda_n = \frac{n\alpha}{\sqrt{\varepsilon}} - n^2 - n. \quad (34)$$

Equating Eqs. (33) and (34), the energy eigenvalue of Eq. (17) is given:

$$E_{nl} = a(1 + b\alpha) - \frac{3ab\alpha^3}{2\delta} + \frac{ab\alpha^3}{\delta^3} - \frac{\hbar^2}{8\mu} \left[ \frac{\frac{2\mu ab}{\hbar^2} - \frac{3\mu ab\alpha^2}{\hbar^2\delta^2} + \frac{16\mu ab\alpha^3}{6\hbar^2\delta^2}}{n + \frac{1}{2} + \sqrt{\left(l + \frac{1}{2}\right)^2 - \frac{ab\mu\alpha^3}{\delta^3\hbar^2} + \frac{16\mu ab\alpha^3}{6\hbar^2\delta^4}}} \right]^2. \quad (35)$$

To determine the wavefunction, we substitute Eqs. (26) and (29) into Eq.(5) and obtain:

$$\frac{d\phi}{\phi} = \left( \frac{\varepsilon}{y^2\sqrt{\varepsilon}} - \frac{\alpha}{2y\sqrt{\varepsilon}} \right) dy. \quad (36)$$

Integrating Eq. (36) gives:

$$\phi(y) = y^{-\frac{\alpha}{2\sqrt{\varepsilon}}} e^{-\frac{\varepsilon}{y\sqrt{\varepsilon}}}. \quad (37)$$

By substituting Eqs. (26) and (29) into Eq. (7), integrating and thereafter simplifying, we obtain:

$$\rho(y) = y^{-\frac{\alpha}{\sqrt{\varepsilon}}} e^{-\frac{2\varepsilon}{y\sqrt{\varepsilon}}}. \quad (38)$$

Substituting Eqs. (26) and (38) into Eq.(6), we have:

$$\chi_n(y) = B_n e^{\frac{2\varepsilon}{y\sqrt{\varepsilon}}} y^{\frac{\alpha}{\sqrt{\varepsilon}}} \frac{d^n}{dy^n} \left[ e^{-\frac{2\varepsilon}{y\sqrt{\varepsilon}}} y^{2n - \frac{\alpha}{\sqrt{\varepsilon}}} \right]. \quad (39)$$

The Rodrigues' formula of the associated Laguerre polynomials is:

$$L_n^{\frac{\alpha}{\sqrt{\varepsilon}}} \left( \frac{2\varepsilon}{y\sqrt{\varepsilon}} \right) = \frac{1}{n!} e^{\frac{2\varepsilon}{y\sqrt{\varepsilon}}} y^{\frac{\alpha}{\sqrt{\varepsilon}}} \frac{d^n}{dy^n} \left( e^{-\frac{2\varepsilon}{y\sqrt{\varepsilon}}} y^{2n - \frac{\alpha}{\sqrt{\varepsilon}}} \right) \quad (40)$$

where

$$\frac{1}{n!} = B_n. \quad (41)$$

Hence,

$$\chi_n(y) \equiv L_n^{\frac{\alpha}{\sqrt{\varepsilon}}} \left( \frac{2\varepsilon}{y\sqrt{\varepsilon}} \right). \quad (42)$$

Substituting Eqs. (37) and (42) into Eq. (3), we obtain the wavefunction of Eq.(17) in terms of Laguerre polynomials as:

$$\psi(y) = N_{nl} y^{-\frac{\alpha}{2\sqrt{\varepsilon}}} e^{-\frac{\varepsilon}{y\sqrt{\varepsilon}}} L_n^{\frac{\alpha}{\sqrt{\varepsilon}}} \left( \frac{2\varepsilon}{y\sqrt{\varepsilon}} \right) \quad (43)$$

where  $N_{nl}$  is normalization constant, which can be obtained from:

$$\int_0^{\infty} |N_{nl}(r)|^2 dr = 1. \quad (44)$$

## 4. Results and Discussion

### 4.1 Results

The mass spectra of the heavy quarkonium system such as charmonium and bottomonium that have the quark and antiquark flavor are calculated and we apply the following relation: [27, 28]

$$M = 2m + E_{nl}, \quad (45)$$

where  $m$  is quarkonium bare mass and  $E_{nl}$  is energy eigenvalue. By substituting Eq. (35) into Eq. (45), we obtain the mass spectra for Varshni potential as:

$$M = 2m + a(1 + b\alpha) - \frac{3ab\alpha^3}{2\delta} + \frac{ab\alpha^3}{\delta^3} - \frac{\hbar^2}{8\mu} \left[ \frac{\frac{2\mu ab}{\hbar^2} - \frac{3\mu ab\alpha^2}{\hbar^2\delta^2} + \frac{16\mu ab\alpha^3}{6\hbar^2\delta^2}}{n + \frac{1}{2} + \sqrt{\left(l + \frac{1}{2}\right)^2 - \frac{ab\mu\alpha^3}{\delta^3\hbar^2} + \frac{16\mu ab\alpha^3}{6\hbar^2\delta^4}}} \right]^2. \quad (46)$$

In order to test for the accuracy of the predicted results determined numerically, we used a Chi square function defined by [29]:

$$\chi^2 = \frac{1}{n} \sum_{i=1}^n \frac{(M_i^{Exp.} - M_i^{Theo.})^2}{\Delta_i} \quad (47)$$

where  $n$  runs over selected samples of heavy mesons,  $M_i^{Exp.}$  is the experimental mass of heavy-mesons, while  $M_i^{Th}$  is the corresponding theoretical prediction. The  $\Delta_i$  quantity is experimental uncertainty of the masses. Intuitively,  $\Delta_i$  should be one. The tendency of overestimating Chi square value is that it reflects some mean error per heavy meson state.

## 4.2 Discussion of Results

We calculate mass spectra of charmonium and bottomonium for states from 1S to 1F by using Eq. (46). We adopt the numerical values of bottomonium ( $b\bar{b}$ ) and charmonium ( $c\bar{c}$ ) masses as  $4.68 \text{ GeV}$  and  $1.488 \text{ GeV}$ , respectively, Ref. [30]. Then, the corresponding reduced masses are  $\mu_b = 2.340 \text{ GeV}$  and  $\mu_c = 0.744 \text{ GeV}$ . The free parameters of Eq.(46) were then obtained by solving two algebraic equations by inserting experimental data of mass spectra for  $2S, 2P$  in the case of charmonium. In the case of bottomonium, the values of the free parameters in Eq. (46) are calculated by solving two algebraic equations, which were obtained by inserting experimental data of mass spectra for  $1S, 2S$ . Experimental data is taken from Ref. [31].

We note that calculations of mass spectra of charmonium and bottomonium are in good agreement with the experimental data, given that the maximum error in comparison with the

experimental data is  $0.0055 \text{ GeV}$ . The values obtained are in good agreement with the works of other researchers, like Ref.[24] and Ref.[18], as shown in Tables 1 and 2. In Ref. [24], the authors investigated the N-radial SE analytically by employing Cornell potential, which was extended to finite temperature. In Ref.[18], the Klein-Gordon equation is solved for the Yukawa potential using the Nikiforov-Uvarov method. The energy eigenvalues were obtained both in relativistic and non-relativistic regime. The results were used to calculate heavy-meson masses of charmonium  $c\bar{c}$  and bottomonium  $b\bar{b}$ . We also plotted mass spectra energy against potential strength ( $a$ ), reduced mass ( $\mu$ ) and screening parameter ( $\alpha$ ), respectively. In Fig. 2, the mass spectra energy converge at the beginning but spread out and there is a monotonic increase in potential strength ( $a$ ). Figs. 3 and 4 show the convergence of the mass spectra energy as the screening parameter ( $\alpha$ ) and reduced mass ( $\mu$ ) increase for various angular momentum quantum numbers. This indicates the energy peak as observable to determine the top quark mass.

TABLE 1. Mass spectra of charmonium in ( $GeV$ ) ( $m_c = 1.488 \text{ GeV}, \mu = 0.744 \text{ GeV}, \alpha = -0.976, \delta = 1.700 \text{ GeV}, \hbar = 1, a = -48.049 \text{ GeV}$  and  $b = 3.020 \text{ GeV}$ ).

State	Present work	[26]	[20]	Experiment[31]
1S	3.096	3.096	3.096	3.096
2S	3.686	3.686	3.672	3.686
1P	3.295	3.255	3.521	3.525
2P	3.802	3.779	3.951	3.773
3S	4.040	4.040	4.085	4.040
4S	4.269	4.269	4.433	4.263
1D	3.583	3.504	3.800	3.770
2D	3.976	-	-	4.159
1F	3.862	-	-	-

TABLE 2. Mass spectra of bottomonium in ( $GeV$ ) ( $m_b = 4.680 \text{ GeV}, \mu = 2.340 \text{ GeV}, \alpha = -0.952, \delta = 1.70 \text{ GeV}, \hbar = 1, a = -14.352 \text{ GeV}$  and  $b = 3.084 \text{ GeV}$ ).

State	Present work	[26]	[20]	Experiment[31]
1S	9.460	9.460	9.462	9.460
2S	10.569	10.023	10.027	10.023
1P	9.661	9.619	9.963	9.899
2P	10.138	10.114	10.299	10.260
3S	10.355	10.355	10.361	10.355
4S	10.567	10.567	10.624	10.580
1D	9.943	9.864	10.209	10.164
2D	10.306	-	-	-
1F	10.209	-	-	-

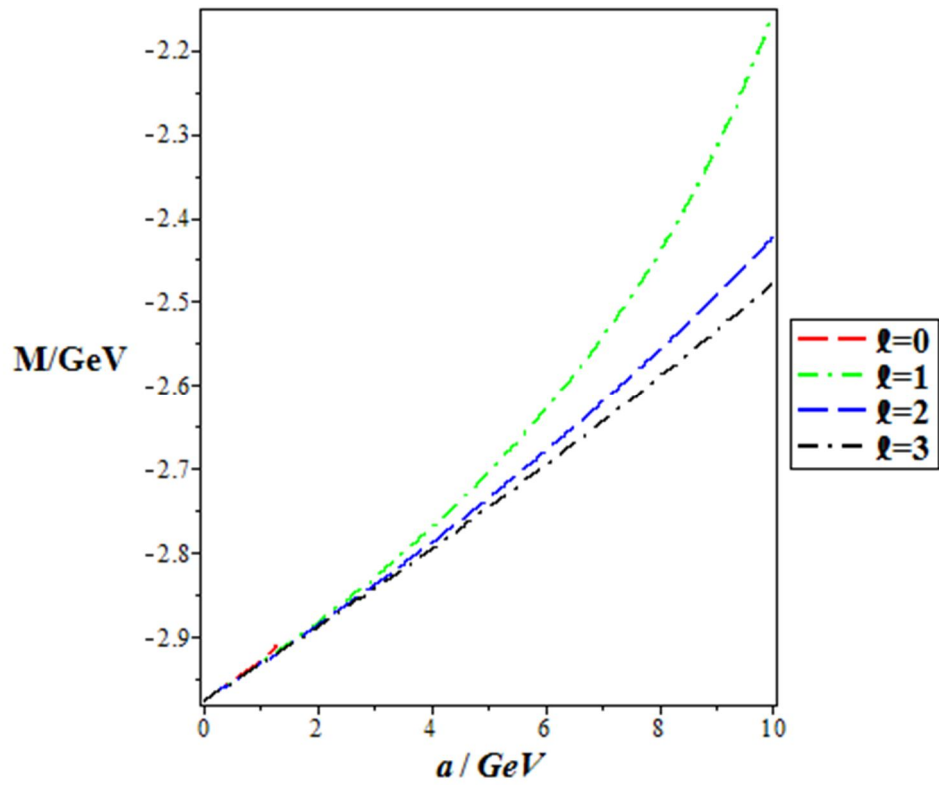


FIG. 2. Variation of mass spectra with potential strength ( $a$ ) for different quantum numbers.

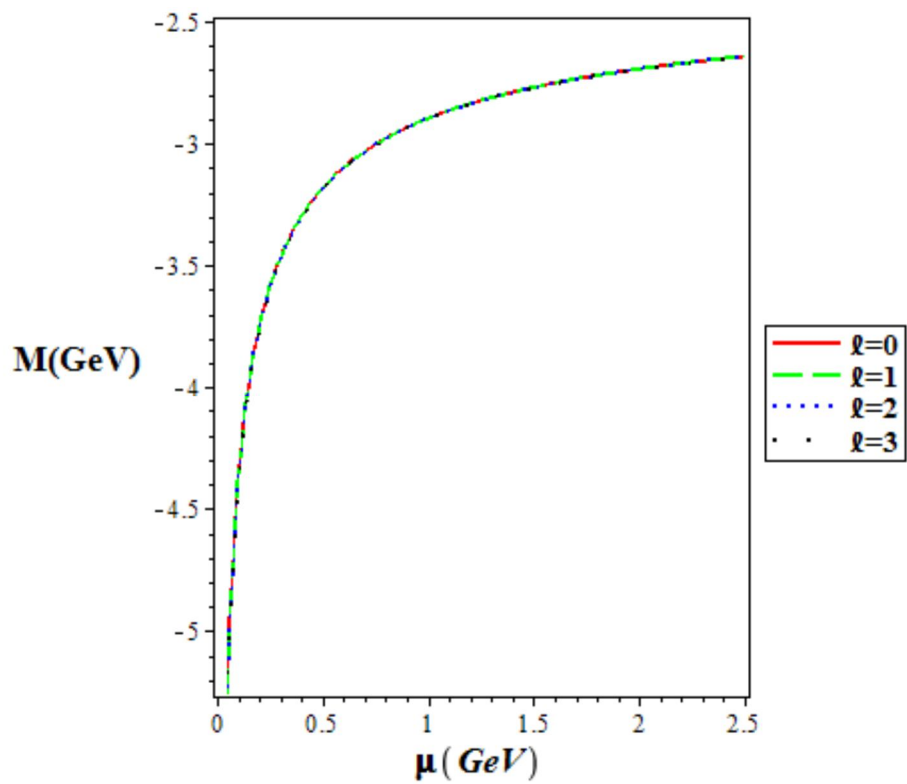


FIG. 3. Variation of mass spectra with reduced mass  $\mu$  for different quantum numbers.

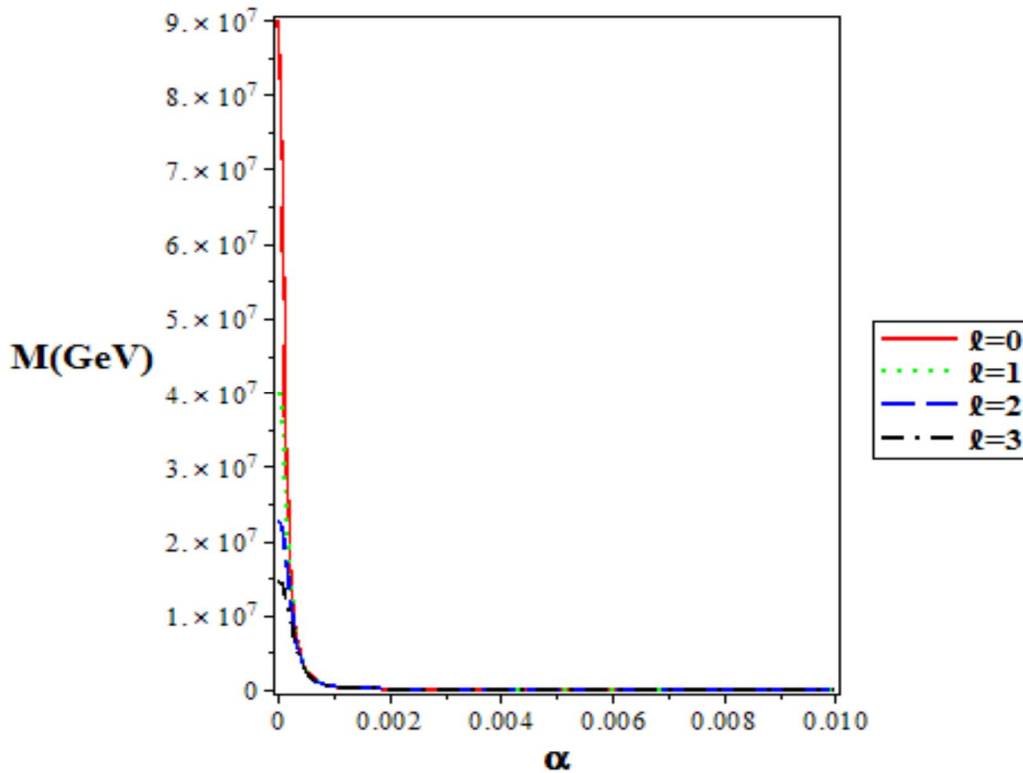


FIG. 4. Variation of mass spectra with screening parameter ( $\alpha$ ) for different quantum numbers.

## 5. Conclusion

In this work, the bound-state solutions of the Schrödinger equation for the Varshni potential using the Nikiforov-Uvarov method were obtained. The corresponding eigenfunction was achieved in terms of Laguerre polynomials. We applied the present results to calculate heavy-meson masses such as charmonium and bottomonium. The energy eigenvalues of charmonium ( $c\bar{c}$ ) and bottomonium ( $b\bar{b}$ ) for

states 1S to 1F were obtained and compared with experimental data and other theoretical works, which are in good agreement with the maximum error of  $0.0055 \text{ GeV}$ . The exponential type potential has been successfully applied in predicting the mass spectra of heavy mesons. The analytical solutions can also be used to describe other characteristics of the quarkonium systems like thermodynamic properties.

## References

- [1] Abu-Shady, M., Abdel-Karim, T.A. and Khokha E.M., *Adv. High-ener. Phys.*, 43 (2018) 843.
- [2] Bhanot, G. and Rudaz, S., *Phys. Lett. B*, 78 (1978) 119.
- [3] Ntibi, J.E., Inyang, E.P., Inyang, E.P. and William, E.S., *Int. J. Innova. Sci. Eng. Tech.*, 11 (2020) 2348.
- [4] Martin, B.R. and Shaw, G.G., "Particle Physics", 2<sup>nd</sup> edition, (The Manchester Physics Series, 1997).
- [5] Perkins, D.H., "Introduction to High-energy Physics", (Cambridge University Press, Cambridge, UK, 20, 2000).
- [6] Griffiths, D., "Introduction to Elementary Particles", (John Wiley & Sons, New York, USA, 1987).
- [7] Bettini, A., "Introduction to Elementary Particle Physics", (Cambridge University Press, 2018).
- [8] Rathsman, J., "Quark and Lepton Interactions", (Acta Universitatis Upsalensis Uppsala, 1996).

- [9] Abu-Shady, M., *Int. J. Appl. Math. and Theor. Phys.*, 2 (2) (2016) 16.
- [10] Omugbe, E., *Cana. J. Phys.*, 98 (12) (2020) 1125.
- [11] Vega, A. and Flores, J., *Pramana J. Phys.*, 56 (2016) 467.
- [12] Ciftci, H. and Kisoglu, H.F., *Pramana J. Phys.*, 57 (2018) 467.
- [13] Abu-Shady, M., *Bos. J. Mod. Phys.*, 55 (2015) 799.
- [14] Al-Jamel, A. and Widyan, H., *Cana. Cent. Sci. Educ.*, 4 (2012) 29.
- [15] Al-Oun, A., Al-Jamel, A. and Widyan, H., *Jordan. J. Phys.*, 8 (4) (2015) 199.
- [16] Kumar, R. and Chand, F., *Comm. Theor. Phys.*, 59 (2013) 467.
- [17] Ibekwe, E.E., Alalibo, T.N., Uduakobong, S.O., Ikot, A.N. and Abdullah, N.Y., *Iran J. Sci. Technol. Trans. Sci.*, 20 (2020) 913.
- [18] Omuge, E., Osafire, O.E. and Onyeajh, M.C., *Adv. High-ener. Phys.*, 10 (2020) 1155.
- [19] Ali, M.S., Hassan, G.S., Abdelmonem, A.M., Elshamndy, S.K., Elmaety, F. and Yasser, A.M., *J. Rad. Appl. Sci.*, 13 (2020) 233.
- [20] Inyang, E.P., Inyang, E.P., Ntibi, J.E., Ibekwe, E.E. and William, E.S., *Indian J. of Phys.*, 1 (2021) 0974.
- [21] Varshni, Y.P., *Rev. Mod. Phys.*, 29 (1957) 682.
- [22] Oluwadare, O.J. and Oyewumi, K.J., *Eur. Phys.*, 53 (2017) 296.
- [23] Lim, T.C., *J. Serb. Chem. Soc.*, 74 (2009) 1423.
- [24] Nikiforov, A.F. and Uvarov, V.B., "Mat. Phys." (ed.) A. Jaffe (Germany: Birkhauser Verlag Basel, 317, 1988).
- [25] William, E.S., Inyang, E.P. and Thompson, E.A., *Rev. Mex. de Fis.*, 66 (6) (2020) 741.
- [26] Abu-Shady, M., *J. Egyp. Math. Soc.*, 23 (2016) 4.
- [27] Kuchin, S.M. and Maksimenko, N.V., *Univ. J. Phys. Appl.*, 7 (2013) 295.
- [28] Abu-Shady, M., Abdel-Karim, T.A. and Khokha, E.M., *J. Quan. Phys.*, 2 (2018) 17.
- [29] Ali, M.S., Yasser, A.M., Hassan, G.S. and Moustakidis, C.C., *Quan. Phys. Lett.*, 5 (2016) 14.
- [30] Barnett, R.M., Carone, C.D., Groom, D.E., Trippe, T.G. and Wohl, C.G., *Phys. Rev. D*, 92 (2012) 656.
- [31] Tanabashi, M., Carone, C.D., Trippe, T.G. and Wohl, C.G., *Phys. Rev. D*, 98 (2018) 548.



### Influence of Solvents on Properties of ZnS Thin Films Synthesized by Chemical Spray Pyrolysis Technique

Akintunde A. Ajayi<sup>a</sup>, Aderemi B. Alabi<sup>b</sup>, Olutayo W. Abodunrin<sup>a</sup>,  
Ibukun S. Akinsola<sup>b,c</sup>, Olukunle C. Olawole<sup>d</sup>, Abiodun M. Salawu<sup>b</sup> and  
Adewale Ayeni<sup>b</sup>

<sup>a</sup> Department of Mathematical and Physical Sciences, Afe Babalola University, Ado-Ekiti, Nigeria.

<sup>b</sup> Department of Physics, University of Ilorin, Ilorin, Nigeria.

<sup>c</sup> Department of Physical and Mathematical Sciences, Crown-Hill University, Ilorin, Nigeria.

<sup>d</sup> Department of Physics, Covenant University, Ota, Nigeria.

**Doi:** <https://doi.org/10.47011/14.4.9>

Received on: 14/10/2020;

Accepted on: 29/11/2020

---

**Abstract:** In this paper, the influence of solvents on the structural, optical, surface and electrical properties of spray-deposited ZnS thin films has been studied. Different precursor mixtures were prepared from ethylene glycol, deionized water and alcohol solvents and sprayed on heated glasses *via* a simple and cost-effective technique known as spray pyrolysis. XRD patterns confirmed cubic and tetragonal phases of synthesized ZnS material. The optical analysis of the synthesized ZnS films showed that films prepared using ethylene glycol solvent have the highest transmittance and the best bandgap (3.61 eV). Surface morphology showed the absence of voids and pinholes in the Scanning Electron Micrograph of ZnS film prepared from ethylene glycol and electrical studies showed that ZnS films prepared using the same solvent have the lowest resistivity.

**Keywords:** ZnS, Thin film, Spray pyrolysis, Bandgap, Morphology.

## Introduction

Zinc sulfide is a group II-VI chalcogenide compound with semiconducting properties. It finds applications as an n-type partner in heterojunction solar cells [1], UV light emitting diodes [2] and as a photoanode in photoelectrochemical water splitting [3]. The aforementioned applications are as a result of ZnS wide bandgap of about 3.70 eV which is the highest among chalcogenide semiconductors [4]. The constituents of ZnS are ecofriendly and abundant and can be a possible replacement for cadmium sulfide which is an n-type partner in commercialized thin-film solar cells, such as Copper Indium Gallium Selenide (CIGS) and Cadmium Telluride (CdTe) solar cells [5]. It can

also be used as a buffer layer in a smart absorber material like Copper Zinc Tin Sulfide (CZTS) [1]. The techniques used in the synthesis of ZnS thin films in most reported works are wet chemical technique which includes spray pyrolysis [6, 7], chemical bath deposition [5, 8], successive ionic layer and reaction (SILAR) [9, 10], chemical vapor deposition (CVD) [11, 12] and sol-gel [13-15]. Among the fore-named chemical methods, spray pyrolysis stands out as a simple technique for low-cost deposition [16]. It is applicable over a wide area, industrially scalable and stoichiometry can be easily controlled. It is well known that deposition parameters in spray pyrolysis play a significant

role in enhancing structural and opto-electronic properties of the final product [16]. One of the deposition parameters is the type of solvent used in preparing starting precursor solution which can be correlated to behavior of the evaporating solution [17]. The use of deionized, distilled or double distilled water in preparation of precursor mixture containing zinc salt and thiourea has been reported in most works on ZnS thin films, though complexing agents are sometimes added to enhance the stability of the solution [18-21]. The effect of solvent on properties of ZnS has not been adequately investigated, though, in 2018, Liu et al. investigated the effect of solvents on spin-coated ZnS films [41]. The aim of this study is to investigate the effect of solvent on properties of ZnS thin films deposited by spray pyrolysis technique with an objective to correlate properties of ZnS thin film to solvent properties.

## Experimental Details

Precursor solutions containing 0.025 M of zinc acetate dihydrate ( $\text{ZnC}_4\text{H}_6\text{O}_4 \cdot 2\text{H}_2\text{O}$ ) and 0.2 M of water-soluble organic compound thiocarbamide ( $\text{CS}(\text{NH}_2)_2$ ) were prepared with solvents; ethylene glycol, deionized water and

alcohol. All reagents are analytical grade and were purchased from Sigma Aldrich. The high concentration of thiocarbamide will compensate for sulphur loss during pyrolysis. Each solution was stirred continuously for an hour until a clear solution was obtained without addition of any complexing agent except for the solution prepared with deionized water in which a drop of  $\text{H}_2\text{SO}_4$  was added to prevent precipitation in the mixture. The solution was sprayed on soda-lime glasses heated to  $400^\circ\text{C}$  at the rate of  $2\text{mL}/\text{minute}$ . The spray assembly is shown in Fig. 1. Air was used as the carrier gas at a pressure of 40 psi. Spray to target distance was maintained at 25 cm. The resulting ZnS thin films were classified as specimens ZG, ZA and ZD, where ZG represents sprayed ZnS thin film sample obtained from ethylene glycol, ZA represents sprayed thin film specimen obtained from alcohol and ZD represents sprayed thin film specimen obtained from deionized water. ZG, ZD and ZA were annealed in a muffled furnace at  $300^\circ\text{C}$  for one hour. Weight of the films and substrates was measured using Adventurer Pro AV313 d = 0.0001g.

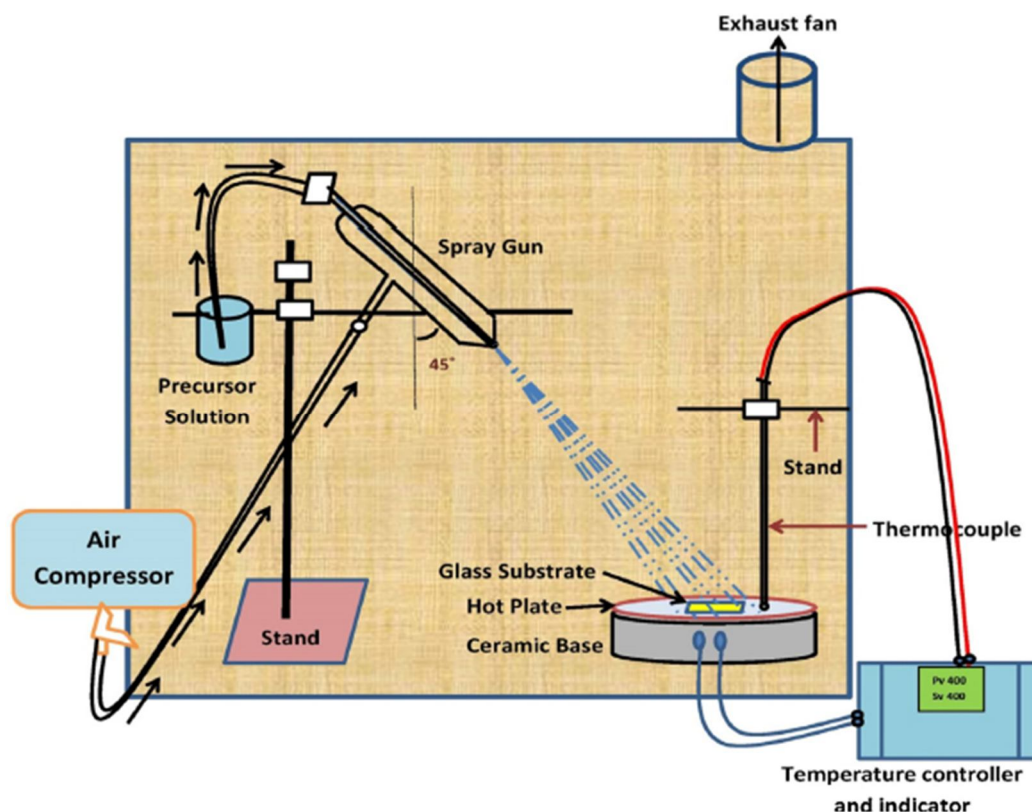


FIG. 1. Schematic diagram of experimental spray pyrolysis assembly [38].

## Characterization of ZnS Thin Films

The structural characterization of the samples was done using a Rigaku D/Max-IIIIC X-ray diffractometer with a lynx eye detector using a copper target ( $\text{Cu}\alpha$ , 1.5418 Å). All X-ray diffraction (XRD) data for the specimens was recorded at current and acceleration voltage of 25mA and 40 kV, respectively. Surface morphology and grain growth analysis of CZTS samples were carried out by using Hitachi scanning electron microscope (SEM) and optical characterization was done using UV-Vis spectrophotometer of CyberLab (model no. UV-100).

## Results and Discussion

### Structural Properties

The XRD patterns of ZG, ZD and ZA are shown in Figs. 2, 3 and 4, respectively. The pattern of ZG shows diffraction peaks corresponding to (111), (220) and (311) reflection planes of cubic ZnS which are observed at  $2\theta$  equaling 28.6°, 48.1° and 57.2°. The peaks matched well with the Crystallography Open Database; American Mineralogist Crystal Structure Database (COD-AMSCD) with Card no. 96-500-5089. The broadening observed at the peaks is an evidence of the nanocrystalline nature of the specimen. There was no evidence of secondary phase in the specimen. Grain size was calculated using Eq. 1 and 2.67 nm was obtained as the grain size of ZD. This result is in agreement with earlier works [20-23]. The pattern of ZD shows diffraction peaks at  $2\theta$  equaling 30.9°, 33.0°, 48.1°, 56.5° and 69.5° which can be indexed to (101), (200), (220), (112) and (400) respective reflection planes which are the planes of cubic and hexagonal structure of ZnS. However, some peaks corresponding to zinc oxide (ZnO) are observed at  $2\theta$  equaling 35.6° and 35.4°. The presence of oxides of zinc can be attributed to decomposition of microsized droplets of

precursor mixture during open air spraying. The calculated grain size for ZD is 66.0 nm. The pattern of ZA shows peaks at  $2\theta$  equaling 28.1°, 30.4° and 33.6° which can be indexed to (111), (101) and (200) reflection planes of cubic and hexagonal phases of ZnS respectively. Other peaks that cannot be indexed to planes of ZnS were observed in the diffractogram of ZA. A grain size of 264.8 nm was obtained for ZA. The results are in agreement with works that have reported cubic and tetragonal crystal structure of ZnS [23] [24]. Variation in grain size from crystalline in ZA and ZD to nanocrystalline in ZG due to solvent influence can be explained by taking the polarity and vapor pressure of the solvents into account. Slower evaporation rate induced by lower vapour pressure may have been responsible for small grain size of ZG (see Fig. 5). Correlation between grain size and vapour pressure has been reported in a very recent work [36]. Increase in grain size with corresponding decrease in polarity can be observed in Fig. 6. It can be suggested that a reduction in solvent polarity causes loose coiling of bonds, which results in higher aggregate formation. The consequence of this is formation of smaller aggregates during drying of specimen prepared using solvent with higher dipole moment. Liu et al. [41] reported a small intensity peak for ethylene glycol against ethanol. We have succeeded in improving the structural properties of ZnS thin film synthesized using ethylene glycol by post-deposition annealing at 300°C and without the use of hydrazine which is toxic. Table 1 shows the polarities and vapour pressures of the solvents used in preparing the ZnS precursor solution.

$$G = \frac{0.9\lambda}{\beta \cos\theta} \quad (1)$$

where G is the grain size,  $\lambda$  is the  $\text{CuK}\alpha$ ,  $\beta$  is the full width at half maximum and  $\theta$  is the angle of diffraction.

TABLE 1. Dipole moments and vapour pressures of solvents [39] [40].

Solvent	Dipole Moment (Debye)	Vapour Pressure (kPa)
Alcohol	1.660	5.950
Water	1.850	2.400
Ethylene Glycol	2.747	0.007

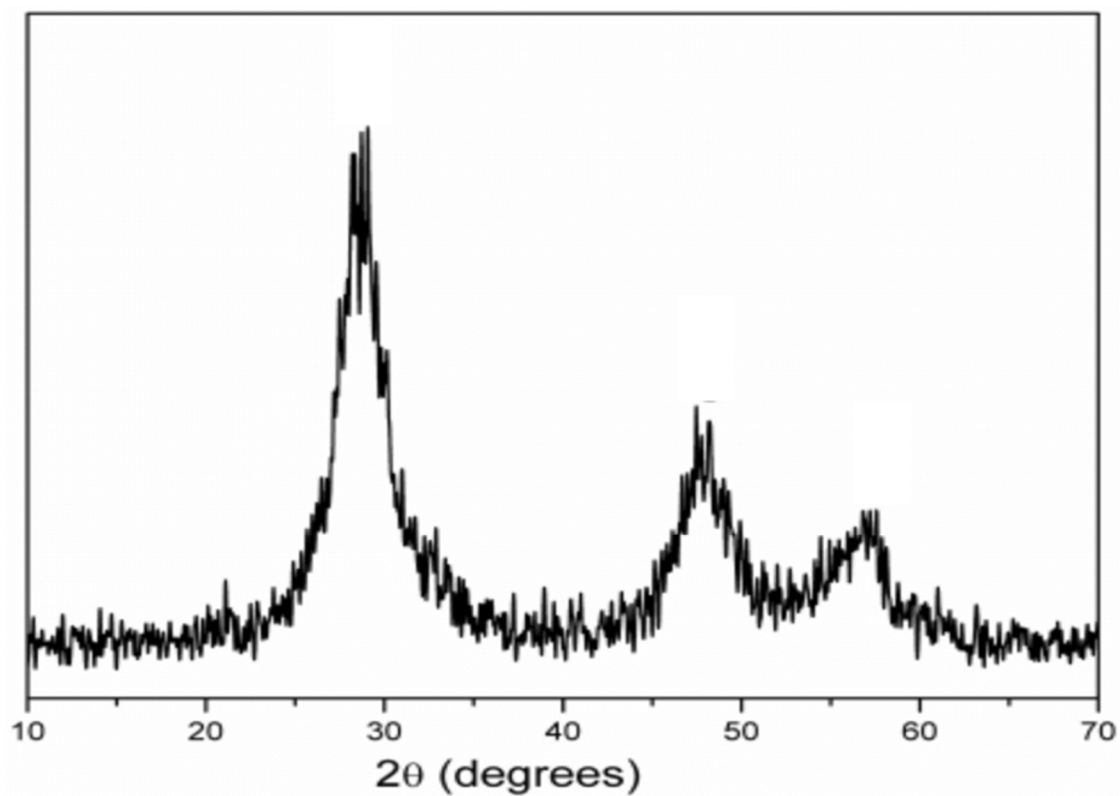


FIG. 2. XRD patterns for ZnS thin films prepared using ethylene glycol solvent.

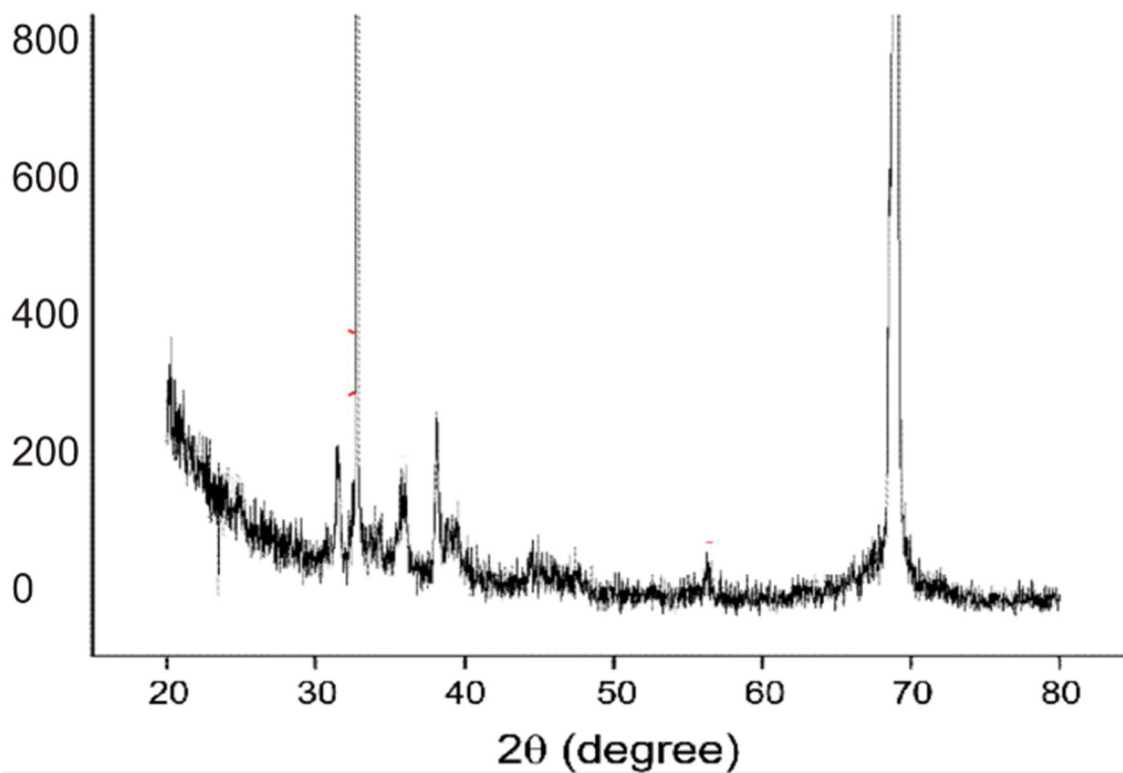


FIG. 3. XRD patterns for ZnS thin films prepared using deionized water solvent.

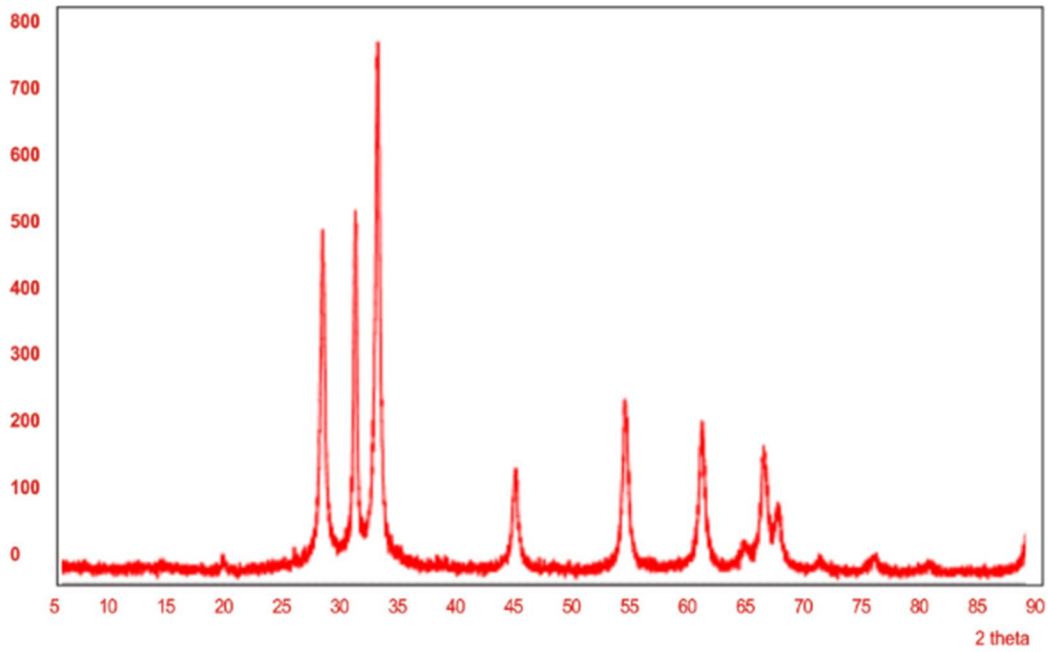


FIG. 4. XRD patterns for ZnS thin films prepared using alcohol solvent.

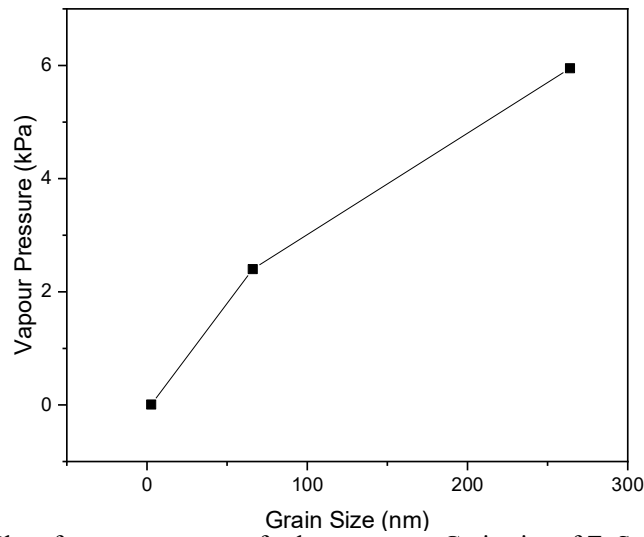


FIG. 5. Plot of vapour pressure of solvents *versus* Grain size of ZnS thin films.

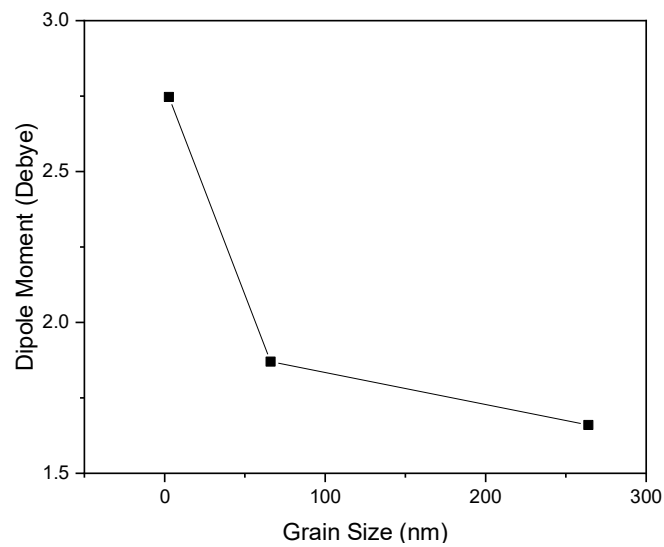


FIG. 6. Plot of dipole moment *versus* grain size of sprayed ZnS thin films.

## Optical Properties

Transmission and absorption spectra of samples ZG, ZD and ZA are shown in Figs. 7 and 8. Transmission data was obtained from ultraviolet-visible spectroscopy measurements and the absorbance of the films was calculated using the equation:

$$A = 2 - \log(T\%) \quad (2)$$

Highest transmittance and lowest absorbance can be observed in ZG within the ultraviolet-visible region, while the lowest transmittance and highest absorbance can be observed in specimen ZA. The increase in slope of the transmittance curve of ZD may be a result of drying retardation during decomposition of ZnS precursor due to solvent type. The smoothness of

the absorption spectra is an evidence of homogeneity in all the specimens. It can be observed that the absorption edge is redshifted with decreasing solvent polarity as expected of a window layer in thin-film solar cell. The optical bandgap of the spray-deposited ZnS thin films was calculated from the Tauc plot. The plot is derived from the expression:

$$(\alpha hf)^{1/n} = A(hf - E_g) \quad (3)$$

where  $\alpha$  is the absorption coefficient,  $h$  represents Planck's constant,  $f$  represents photon frequency,  $E_g$  represents the energy band-gap and  $A$  is a constant of proportionality.  $n$  depends on the nature of radiative transition and is given as  $n = 1/2$  for directed allowed band-gap.

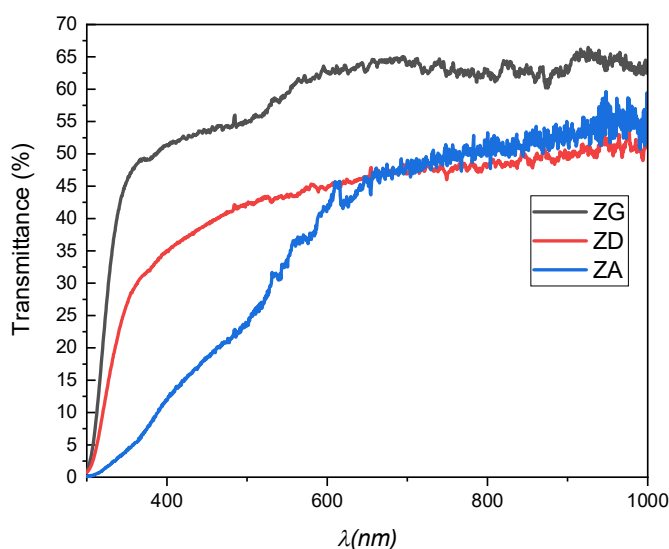


FIG. 7. Variation of transmission spectra of ZnS thin films with solvents of ethylene glycol, deionized water and alcohol.

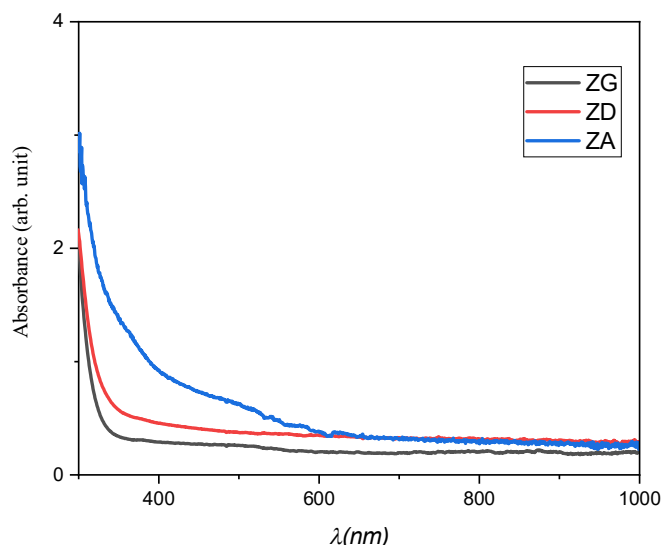


FIG. 8. Variation of absorption spectra of ZnS thin films with solvents of ethylene glycol, deionized water and alcohol.

Fig. 9 shows the plot of  $(\alpha hf)^2$  versus  $hf$ . The bandgap  $E_g$  is obtained from the intercept with axis  $hf$  after extrapolating the linear region of the plot. Fig. 9 shows the Tauc's plot for ZG, ZD and ZA, where a superior bandgap of 3.61 eV can be observed in ZG, while ZD and ZA showed lower energy bandgaps of 3.56 eV and

3.38 eV, respectively. The bandgap is not widely influenced by solvent variation and matches those frequently reported in literature [25-28]. This is an indication that bond length and quinoidal character (higher energy state due to replacement of single bonds with double ones) have not been affected by solvent type.

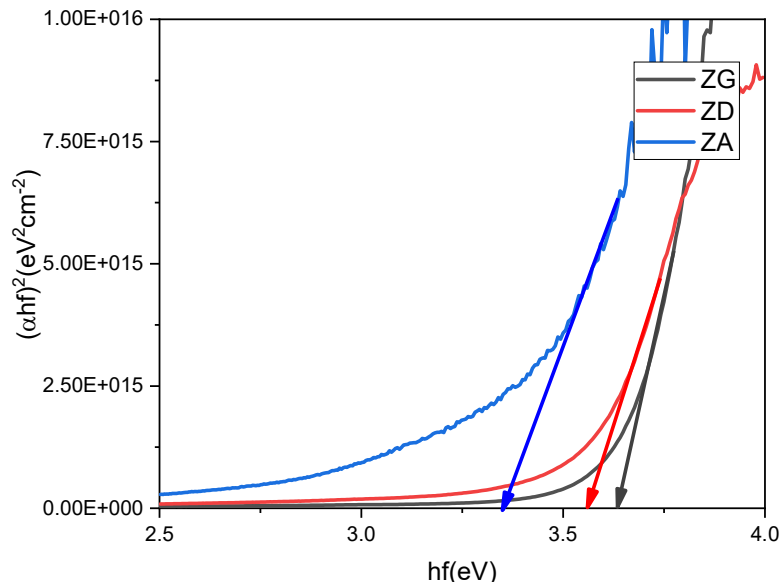


FIG. 9. Variation of optical bandgap of ZnS thin films with solvents of ethylene glycol, deionized water and alcohol.

### Morphological Properties

The surface morphology of spray-deposited ZnS thin films was studied using scanning electron microscope. The scanning electron micrographs (SEM) of ZG, ZD and ZA are shown in Fig. 10. The surface morphology of the films is influenced by solvent variation to some extent, where ridges can be observed in ZnS thin films prepared using ethylene glycol as a solvent. Some voids can be seen in the SEM of

ZG and ZA and the greater grain size of ZD is clearly confirmed by the SEM results. The ridges notwithstanding, it can be observed that ZG has a greater uniform surface morphology compared to the other two specimens. It has been reported in some research works on thin-film semiconductors that uniform surface morphology leads to less grain boundaries [29-31].

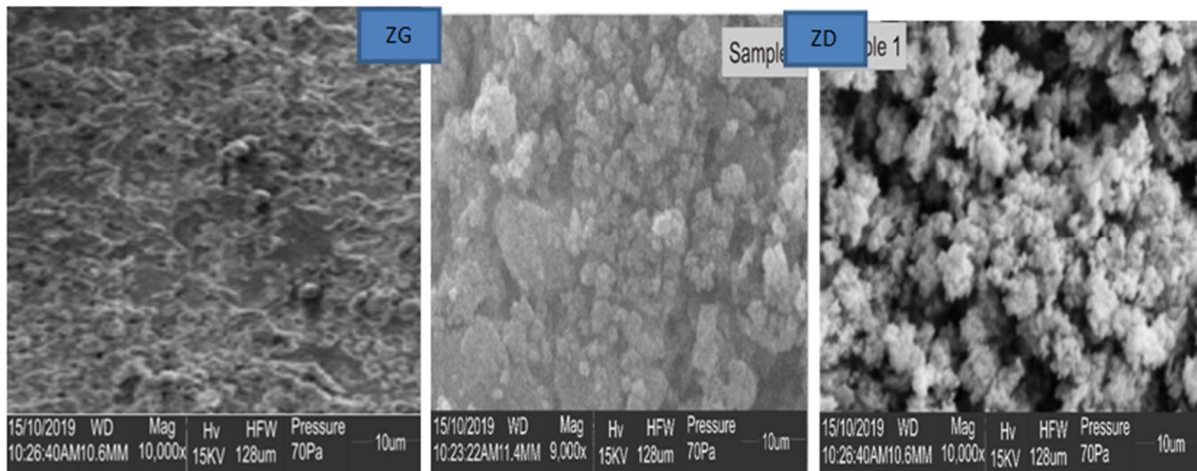


FIG. 10. SEM micrographs of ZG, ZD and ZA.

### Compositional Analysis

The composition of the solvent-varied ZnS thin films was analyzed by energy dispersive X-ray spectroscopy (EDX). The EDX spectra of ZG, ZD and ZA are shown in Fig 11. The ZnS compound is confirmed by the peaks of zinc (Zn) and sulphur (S) in the EDX. It can also be observed that all synthesized films are highly Sulphur-deficient, which may be attributed to

affinity of sulphur towards oxygen leading to formation of sulphur (IV) oxide which is lost during pyrolysis [33] [34]. However, the highest atomic percentage of sulphur can be found in specimen ZG, as shown in Table 2, which may be due to drying retardation during the spraying process. Oxygen peaks observed may be due to air used as carrier gas and the carbon peak may be attributed to C=O functional group in ZG.

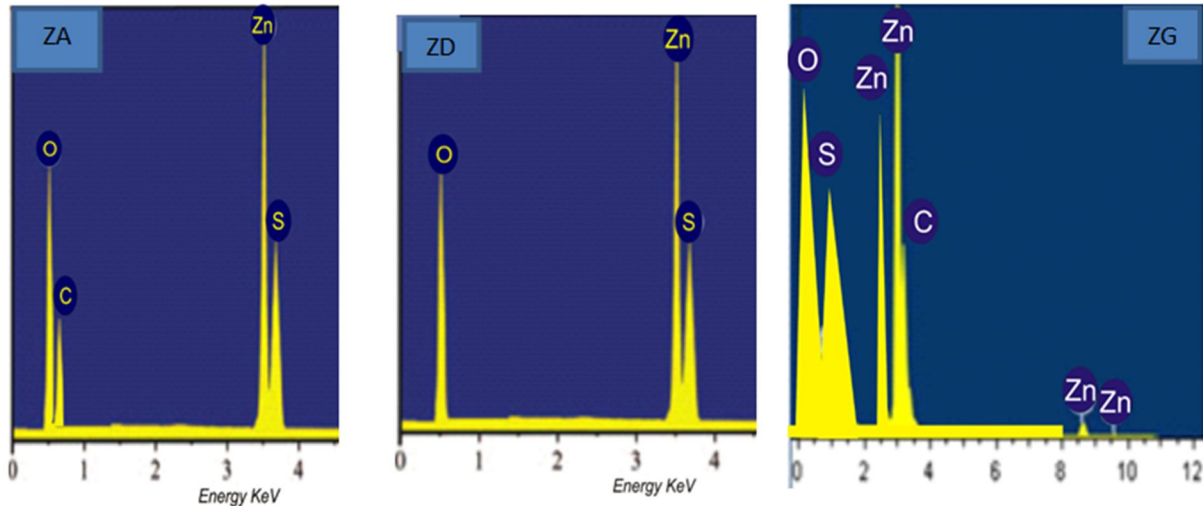


FIG. 11. EDX spectra of ZG, ZD and ZA.

TABLE 2. Elemental composition of solvent-varied ZnS thin films.

Specimen	Zn	S	O	C
	Atomic %	Atomic %	Atomic %	Atomic %
ZG	50.46	15.75	20.50	7.22
ZD	60.29	9.25	30.46	-
ZA	68.00	7.60	20.00	4.40

### Electrical Properties

Resistivity of solvent-varied ZnS thin films was obtained from current-voltage measurements carried out by a Keithley source meter instrument with Tracer software using Vander pauw array mode with indium pellet as ohmic contact. Resistivity was calculated using the following equation:

$$\rho = Rt \quad (4)$$

where  $\rho$  is resistivity,  $R$  is the sheet resistance and  $t$  is the thickness of the film. The thickness

of the films was evaluated using the weight difference method [35] expressed as:

$$t = \frac{m}{\rho A} \quad (5)$$

where  $t$  is thickness,  $\rho$  is density of cubic phase of ZnS, equal to  $4.1 \text{ g cm}^{-3}$  [35],  $A$  is the area of the film and  $m$  is the mass of deposited films.

The resistivity values of ZG, ZD and ZA are shown in Table 3 with ZG observed to have the lowest value of resistivity.

TABLE 3. Resistivity of Solvent-varied ZnS thin films.

Specimen	$\rho (\times 10^5)(\Omega.\text{cm})$	$t (\mu\text{m})$
ZG	2.47	0.25
ZD	74.28	0.75
ZA	35.66	0.34

## Conclusion

In this study, ZnS thin films have been synthesized *via* a simple and cheap chemical technique: spray pyrolysis. The influence of solvents on the structural, optical, surface and electrical properties of spray-deposited ZnS thin films has been studied. Ethylene glycol, deionized water and alcohol are solvents used in preparation of the precursor mixture containing zinc salt and thiocarbamide. The films developed from precursor mixture with ethylene glycol used as solvent exhibited cubic phase of ZnS only, while those developed from deionized water and alcohol showed both cubic and tetragonal phases. It can be suggested from the small grain size (2.67 nm) of ZG that the film is nanocrystalline, while ZnS thin film synthesized from deionized water has the largest grain size of 264.80 nm. The ZnS thin film synthesized from

ethylene glycol exhibited the highest percentage transmittance in the ultraviolet-visible region of the electromagnetic spectrum with a superior bandgap of 3.61 eV; though the effect of solvent type on sprayed ZnS thin film was not far-reaching. Voids and pinholes are absent in the surface of ethylene glycol-synthesized films. In the case of ZnS films prepared from deionized water and alcohol, some voids can be noticed though the particle sizes are more distinguishable compared to those of ethylene glycol. Evaluation of current-voltage characteristics of the films showed that ZnS thin film synthesized from ethylene glycol is less resistive ( $2.47 \times 10^5 \Omega \cdot \text{cm}$ ) compared to the large values of the resistivity of specimens ZD and ZA which are  $74.28 \times 10^5 \Omega \cdot \text{cm}$  and  $35.66 \times 10^5 \Omega \cdot \text{cm}$ , respectively.

## References

- [1] Boutebakh, F.Z., Beloucif, A., Aida, M.S., Chettah, A. and Attaf, N., *Journal of Materials Science: Material in Electronics*, 29 (2017) 4089.
- [2] Kassim, A., Nagalingam, S., Min, H.S. and Karrim, N., *Arabian Journal of Chemistry*, 3 (2010) 243.
- [3] Hassan, M.A., Johar, M.A., Waseem, A., Bagal, I.V., Ha, J. and Ryu, S., *Optics Express*, 27 (4) (2019) A184.
- [4] Offor, P.O., Okorie, B.A., Ezekoye, B.A., Ezekoye, V.A. and Ezema, J.I., *Journal of Ovonic Research*, 11 (2) (2015) 73.
- [5] Manjulavalli, T.E. and Kannan, A.G., *International Journal of ChemTech Research*, 8 (11) (2015) 396.
- [6] Offor, P.O., Whyte, G.M., Otung, F.U., Nnamchi, P.S., Ude, S.N., Omah, A.D., Daniel-Mkpume, C.C., Neife, S.I., Aigbodun, V.S., Madu, S., Okorie, B.A. and Ezema, F.I., *Surfaces and Interfaces*, 16 (2019) 157.
- [7] Djelloul, A., Adanne, M., Larbah, Y., Sahraoui, T., Zegadi, C., Maha, A. and Rahal, B., *Journal of Nano-and Electronic Physics*, 7 (4) (2015) 1.
- [8] Liu, W., Chen, W., Hsieh, S. and Yu, J., *Procedia-Engineering*, 36 (2012) 46.
- [9] Ashith, V.K. and Gowrish, R.K., *IOP Conf. Series: Materials Science and Engineering*, 360 (2018) 012058.
- [10] Ates, A., Yildirim, M.A., Kundakci, M. and Astam, A., *Materials Science in Semiconductor Processing*, 10 (6) (2007) 281.
- [11] Palve, A.M., *Thin Solid Films*, 6 (42) (2019) 1.
- [12] Vishwakarma, R., *Ukrainian Journal of Physics*, 62(5), (2017) 422.
- [13] Ahktar, M.S., Riaz, S. and Nazeem, S., *Materials Today: Proceedings*, 2 (10) (2015) 5497.
- [14] Anila, E.I., Safeera, T.A. and Raman, R., *Journal of Fluorescence*, 25 (2) (2015) 227.
- [15] Zaman, M.B., Chandel, T., Dehury, K. and Rajaram, P., *AIP Conference Proceedings*, 1953 (1) (2018) 100066.
- [16] Falcony, C., Aguilar-Frutis, M.A. and Garcia-Hippolito, M., *Micromachines*, 9 (414) (2018) 1.
- [17] Xiong, H. and Sun, W., *Coatings*, 7 (207) (2017) 1.
- [18] Eid, A.H., Salim, S.M., Sedik, M.B., Omar, H., Dahy, T. and Abou elkhair, H.M., *Journal of Applied Sciences Research*, 6 (6) (2010) 777.

- [19] Yu, F., Ou, S., Yao, P., Wu, B. and Wu, D., *Journal of Nanomaterials*, 594952 (2014) 1.
- [20] Padmavathy, V. and Sankar, S., *Journal of Materials Science: Materials in Electronics*, 29 (2018) 7739.
- [21] Zein, R. and Alghoraibi, I., *Journal of Nanomaterials*, 7541863 (2019) 1.
- [22] Ahmed, M., Rasool, K., Imran, Z., Rafiq, M.A. and Hassan, M.M., *Saudi International Electronics, Communications and Photonics Conference, Riyadh, Saudi Arabia, IEEE Conference Proceedings*, (2011).
- [23] Kannappan, P. and Dhanasekaran, R., *International Journal of Recent Technology and Engineering*, 7 (4s) (2018) 2277.
- [24] Bioki, A.H. and Zarandi, M.B., *International Journal of Optics and Photonics*, 5 (2) (2011) 121.
- [25] Ofor, P.O., Whyte, G.M., Otung, F.U., Nnamchi, P.S., Ude, S.N., Omah, A.D., Daniel-Npkume, C.C., Neife, S.I., Aigbodion, V.S., Madu, S., Okorie, B.A., Mazza, M. and Ezema, F.I., *Surfaces and Interfaces*, 16 (2019) 157.
- [26] Vishwakarma, R., *Journal of Theoretical and Applied Physics*, 2015 (9) (2015) 185.
- [27] Agbo, P.O., Nwofe, P. and Odo, L.O., *Chalcogenide Letters*, 14 (8) (2017) 357.
- [28] Ebrahimi, S., Yarmand, B. and Naderi, N., *Advanced Ceramics Progress*, 3 (4) (2017) 3.
- [29] Patel, S.B. and Gohel, V.J., *Physics and Astronomy International Journal*, 1 (4) (2017) 1.
- [30] Lanjewar, M., Gohel, J.V., *Inorganic and Nano-Metal Chemistry*, 47 (7) (2017) 1090.
- [31] Gohel, J.V., Jana, A.K. and Singh, M., *Applied Physics A*, 123 (8) (2017) 1.
- [32] Kumari, N., Gohel, J.V. and Patel, S.R., *International Journal for Light and Electron Optics*, 144 (2017) 422.
- [33] Rahman, F., Podder, J. and Ichimura, M., *Optik-International Journal of Optics and Photonics*, 5 (2) (2011) 79.
- [34] Poornima, N., Jose, A., Kartha, C.S. and Vijayakumar, K.P., *Procedia-Energy*, 15 (2012) 347.
- [35] Derbali, A., Attaf, A., Saidi, H., Benamra, H., Nouadji, M., Aida, M.S., Attaf, N. and Ezzaouia, H., *Optik-International Journal of Light and Electron Optics*, 154 (2018) 286.
- [36] Chin, S., Choi, J.W., Woo, H.E., Kim, J.H., Lee, H.S. and Lee, C.L., *Nanoscale*, 11 (13) (2019) 5775.
- [37] Mohan, S.R., Joshi, M., Dhimi, T., Awasthi, V., Shalu, C., Singh, B. and Singh, V., *Synthesis Methods*, 224 (2017) 80.
- [38] Margoni, M.M., Mathuri, S., Ramamurthi, K., Babu, P.R. and Sethuraman, K., *Applied Surface Science*, 418 (A) (2017) 280.
- [39] Wu, S., Ysng, H., Hu, J., Shen, D., Zhang, H. and Xiao, R., *Final Processing Technology*, 161 (2017) 162.
- [40] Rizk, H.A. and Elanwar, I.M., *Canadian Journal of Chemistry*, 46 (4) (2011) 507.
- [41] Liu, K., Li, J., Xu, Y., Li, H. and Gao, W., *Results in Physics*, 11 (2018) 749.

## Retrieval of Optical Constants of Undoped Flash-Evaporated Lead Iodide Films from an Analysis of Their Normal Incidence Transmission Spectra Using Swanepoel's Transmission Envelope Theory of Non-Uniform Films

Mousa M. A-G. Jafar<sup>a</sup>, Nidal M. Ershaidat<sup>a</sup>, Mais J. A. Ahmad<sup>b</sup>, Mahmoud H. Saleh<sup>c</sup> and Basim N. Bulos<sup>a</sup>

<sup>a</sup> Department of Physics, School of Science, The University of Jordan, Amman 11942, Jordan.

<sup>b</sup> Leibniz Institute für Analytische Wissenschaften-ISAS e. V., Bunsen-Kirchhoff-Straße 11, D-44139 Dortmund, Germany.

<sup>c</sup> Department of Physics, Faculty of Science, Al-Balqa Applied University, Al-Salt 19117, Jordan.

**Doi:** <https://doi.org/10.47011/14.4.10>

Received on: 17/09/2020;

Accepted on: 12/01/2021

---

**Abstract:** Normal-incidence transmission-wavelength ( $T_{\text{exp}}(\lambda) - \lambda$ ) spectra of 1 and 1.2  $\mu\text{m}$  thick flash-evaporated lead iodide ( $\text{PbI}_2$ ) films on 1.1 mm thick glass slides held at 200 °C display well-spaced several interference-fringe maxima and minima in the  $\lambda$ -range 520-900 nm, without exhibiting a transparent region and with the maxima lying well below the substrate transmission. Below 520 nm, these  $T_{\text{exp}}(\lambda) - \lambda$  curves drop steeply to zero (at  $\lambda \leq 505$  nm), signifying crystalline-like  $\text{PbI}_2$  film absorption. As corrections of measured ( $\text{PbI}_2$  film/substrate) transmittance data for substrate absorption and spectrometer slit-width effect were marginal over the studied  $\lambda$ -range, the observed low transmittance of ( $\text{PbI}_2$  film/substrate) system was related to  $\text{PbI}_2$  film thickness non-uniformity ( $\Delta d$ ), which causes shrinkage of both maxima and minima and leads to significant film optical absorption that reduces both maxima and minima. The McClain ENVELOPE algorithm was utilized, with a minor modification, to construct maxima  $T_{\text{M}}(\lambda_{\text{max}}/\lambda_{\text{min}})$  and minima  $T_{\text{m}}(\lambda_{\text{min}}/\lambda_{\text{max}})$  envelope curves, which were analyzed by Swanepoel's envelope method of non-uniform films using an approach that takes account of dispersive substrate refractive index  $n_s(\lambda)$  and circumvents the non-availability of a high- $\lambda$  transparency region. In such analytical approach,  $\Delta d$  was varied till a re-generated  $T_{\text{gen}}(\lambda) - \lambda$  curve matches the  $T_{\text{exp}}(\lambda) - \lambda$  curve. An average thickness  $\bar{d}$  of the film, besides its refractive index  $n(\lambda)$  and absorption coefficient  $\alpha(\lambda)$  in the weak, medium and strong absorption regions, were then obtained. The energy-dependence of  $\alpha(\lambda)$  is discussed in view of interband electronic transition models. The obtained results are consistent with other literature studies on similar flash-evaporated  $\text{PbI}_2$  films.

**Keywords:**  $\text{PbI}_2$ , Optical constants and bandgap, Swanepoel's transmission envelope method, Non-uniform films.

## Introduction

Single crystals and films of lead iodide ( $\text{PbI}_2$ ) have emerged to be prospective candidates for use in many electronic devices, including room-temperature radiation detectors and x-ray imaging systems [1-3] and in perovskite solar-cell photovoltaics and photodetectors [4-6]. This is because  $\text{PbI}_2$  has useful structural, electrical and optical properties [7-18]. The quality and properties of a  $\text{PbI}_2$  film depend on its purity, stoichiometry, crystallinity and homogeneity, which are governed by the used fabrication route. Crystals/films of lead iodide can be prepared from solution, vapor, gel and melt at different temperatures up to its melting point ( $\sim 410^\circ\text{C}$ ) [7-21].

An accurate and reliable determination of optical constants and thickness of semiconducting films is of importance for basic understanding of their optical and dielectric properties and for the design, fabrication and development of electronic devices integrating them. The refractive index and extinction coefficient of a material sample are common optical constants that are valuable for explicating its optical/dielectric behavior and dissipation under various experimental conditions. However, their measurement is not straightforward, but can be retrieved from a measurable macroscopic physical quantity of the specimen, such as its transmittance  $T(\lambda)$  and/or reflectance  $R(\lambda)$  that can be measured directly using spectrophotometers as a function of wavelength  $\lambda$  of quasi-monochromatic light incident upon it.

As the transmittance or reflectance of a material film is not an inherent material property, one has to analyze its  $T_{\text{exp}}(\lambda) - \lambda$  and/or  $R_{\text{exp}}(\lambda) - \lambda$  data to determine the real  $n(\lambda)$  and imaginary  $\kappa(\lambda)$  components of its complex refractive index  $\hat{n}(\lambda) = n(\lambda) - i\kappa(\lambda)$  as a function of  $\lambda$ . The  $\kappa(\lambda)$  data can be used to find its optical absorption coefficient  $\alpha(\lambda)$  and *vice versa* using the relation  $\alpha(\lambda) \equiv 4\pi\kappa(\lambda)/\lambda$ . This requires mathematical formulae for  $T(\lambda)$  or  $R(\lambda)$  that incorporate  $n(\lambda)$  and  $\kappa(\lambda)$  and a method for analyzing  $T_{\text{exp}}(\lambda) - \lambda$  and  $R_{\text{exp}}(\lambda) - \lambda$  data using such formulae, which depend on the type of optical system. Here, we will be concerned with an optical system in the form of an absorbing film on a thicker slab (substrate), immersed in air ( $n_a(\lambda) = 1$  and  $\kappa_a(\lambda) = 0$ ).

Theoretical formulae that describe  $T(\lambda)$  or  $R(\lambda)$  of an absorbing slab of geometrical thickness  $d_s$  and complex refractive index  $\hat{n}_s(\lambda) = n_s(\lambda) - i\kappa_s(\lambda)$  are relatively simple, but those of {absorbing film/absorbing substrate} systems are elaborate, particularly  $R(\lambda)$  formula [22-27]. In practice, laboratory fabricated films are not ideal in the sense they are not homogeneous and suffer from surface roughness, interfacial layers and inhomogeneity (in composition and thickness non-uniformity), which are governed by the substrate quality, film thickness, deposition method, preparation conditions and post-growth treatment. This makes the  $T(\lambda)$ -/ $R(\lambda)$ -formulations for such non-ideal optical systems much more unwieldy and somewhat inadequate for a rigorous optical analysis.

A variety of conventional curve-fitting programs, numeric optimization and purely algebraic methods were employed to analyze  $T_{\text{exp}}(\lambda) - \lambda$  or  $R_{\text{exp}}(\lambda) - \lambda$  data of various {film/substrate} structures incorporating uniform or non-uniform absorbing films, each of which has its own reliability, curbs and difficulties in application [28-54]. Conventional curve-fitting iterative methods entail a prior knowledge of models that describe spectral dispersion of  $n(\lambda)$  and  $\kappa(\lambda)$  and require sophisticated software that should yield a global solution of the problem and not multi-local solutions, which all give remarkable curve fits with diverse output results, most of which are unreliable or physically meaningless. The former requirement is difficult to accomplish for certain, while the latter is not always at hand and very expensive [28-31, 38, 42]. Nevertheless, conventional data curve-fitting is demandable and inevitable, particularly in case of complex, multi-layered structures of different optical properties.

Alternatively, a numeric optimization (so-called PUMA) method can be used to analyze  $R_{\text{exp}}(\lambda) - \lambda$  data [32] or  $T_{\text{exp}}(\lambda) - \lambda$  data [33-35] of air-supported {uniform absorbing film/transparent substrate} structures to determine  $n(\lambda)$  and  $\kappa(\lambda)$  of the film with no requisite of spectral dispersion relations in advance. The algebraic Swanepoel's envelope method (EM) of uniform films [36] is often employed to analyze  $T_{\text{exp}}(\lambda) - \lambda$  spectra of such structures [37] also with no prior need to  $n(\lambda)$  and  $\kappa(\lambda)$  dispersion relations; but it is solely

limited to  $T_{\text{exp}}(\lambda) - \lambda$  spectra that display many interference-fringe maxima and minima and exhibit wide portion of optically transparent region close to the substrate transmission, which are ideal systems that are not always realized in practice. A variety of modifications were reported in literature to include film inhomogeneity and substrate optical properties (absorption/dispersion) to improve analysis of  $T_{\text{exp}}(\lambda) - \lambda$  or  $R_{\text{exp}}(\lambda) - \lambda$  spectra of non-ideal air-supported {film/substrate} systems using Swanepoel's envelope methods (EMs) of uniform or non-uniform films [28, 38-54].

Normal-incidence transmission can be easily measured to a greater accuracy by most spectrophotometers covering ultraviolet (UV), visible (Vis) and near infrared (NIR) spectral regions compared to measurements of non-zero angle reflection that require calibration procedures using high-quality reference mirrors [29], besides involving analysis of more unwieldy  $R(\lambda)$ -formulae [22-27, 50, 51]. Thus, we shall here deal only with normal-incidence transmission of air-supported {non-uniform absorbing film/slightly-absorbing substrate} systems and with formulations required for analyzing their normal-incidence  $T_{\text{exp}}(\lambda) - \lambda$  spectra on the basis of Swanepoel EM of non-uniform films [28, 38-45, 52-54] using the approach of Richards et al. [42, 43]. This EM analytical approach proves to be conceivable for non-uniform films that are significantly absorbing over the whole wavelength range of interest and whose  $T_{\text{exp}}(\lambda) - \lambda$  spectra do not exhibit a transparent region at the high- $\lambda$  side [17, 31, 42, 43, 48, 49, 54], which is viable in analysis of non-uniform films using procedures of original Swanepoel's EM when  $T_M(\lambda) \approx T_S(\lambda)$  [39-41, 44-47, 52, 53].

Furthermore, there is significant variety in the reported optical constants of  $\text{PbI}_2$  films prepared by various deposition routes and in their retrieved values of bandgap energy  $E_g$ , which are scattered in the range 2.1-2.6 eV [8-21, 31]. These diversities can be linked to the use of different film thicknesses, preparation conditions, optical characterization techniques and to the use of diverse/simple analytical approaches that sometimes exploited irrational/meek theoretical formulations for analyzing the measured optical data, besides implementing unlike models to typify the

dispersion and absorption phenomena in studied lead iodide films.

To get further insight into some of unsettled issues of optical properties of  $\text{PbI}_2$  films and features of their optical transmission, the normal-incidence  $T_{\text{exp}}(\lambda) - \lambda$  spectra of undoped flash-evaporated  $\text{PbI}_2$  films on glass slides held at 200 °C were measured at room temperature (RT) in the range 400-900 nm and analyzed on the basis of Swanepoel EM of non-uniform films [39] using an extended approach reported by Richards et al. [42, 43]. This type of optical analysis has not yet been used to retrieve  $n(\lambda)$  and  $\kappa(\lambda)$  of  $\text{PbI}_2$  films, a study that will shed more light on the spectral dispersion and electronic transition phenomena operative in lead iodide substance.

## Experimental Details

A couple of physically and chemically pre-cleaned and heat-treated 1.1 mm thick microscopic glass slides were installed inside the bell-jar chamber of a Leybold coating's system, pumped down to less than  $10^{-5}$  mbar base pressure. These slides were mounted tightly underneath a home-designed/constructed sample holder made of a massive copper (Cu) block, equipped with a thermocouple and cylindrical-shaped heater, energized from an electric heating/controller kit outside the chamber [17]. The slides were first heated to the required temperature (200 °C), which was controlled and kept steady there within  $\pm 1$  °C for several hours.

Undoped lead iodide films were deposited onto such pre-heated slides using a home-made flash-evaporation unit described elsewhere [17, 18]. This piece of apparatus is composed of an electrically-energized trigger system and a container filled in prior with finely-grinded lead iodide powder, which can be fed in tiny amounts through a perforated sieve into a long stainless steel (SS) tube that extends down close above a box-shaped molybdenum (Mo) crucible connected to two massive Cu electrodes [17, 18]. The Mo-crucible is first electrically heated to around 600 °C, held constant within  $\pm 2$  °C for several hours. The thickness  $d$  of deposited film was monitored and recorded by a quartz-crystal unit during evaporation at a low rate (1 nm/s) until the required final thickness was reached. The evaporation process was then stopped and the samples (film/substrate) were left to cool

down in vacuum to RT. The final recorded  $d$  values of obtained flash-evaporated lead iodide films were 1  $\mu\text{m}$  and 1.2  $\mu\text{m}$ .

The structure and surface morphology of obtained flash-evaporated undoped lead iodide films were examined by conventional x-ray diffraction (XRD) and scanning electron microscopy (SEM), while electron dispersive spectroscopy (EDS) was used to determine their compositions. The flash-evaporated lead iodide films deposited on glass substrates sustained at 200  $^{\circ}\text{C}$  were found to be highly stoichiometric ( $\text{PbI}_{1.9}$ ) and of a 2H-polytype hexagonal crystal structure [8, 16], with preferential crystalline orientation along the  $c$ -axis normal to the substrate surface [17, 18, 30]. Microscopic visualization showed that flash-evaporated  $\text{PbI}_2$  films deposited on glass slides held at stable temperatures in the range 150 – 200  $^{\circ}\text{C}$  were pinhole-/crack-free and having virtuous smooth surfaces with hexagonal-shaped grains [17, 18, 30].

Room-temperature transmittance  $T_s(\lambda)$  of a 1.1 mm thick microscopic glass slide and transmittance  $T_{\text{exp}}(\lambda)$  of the 1  $\mu\text{m}$  and 1.2  $\mu\text{m}$  thick undoped flash-evaporated  $\text{PbI}_2$  films deposited on identical glass slides were measured as a function of the wavelength  $\lambda$  of light in the range 400-900 nm. Transmittance measurements were taken using a double-beam UV-Vis-NIR spectrophotometer (Varian Carry 100) at a scan rate of 120 nm/min and at 0.5 nm intervals, with the light beam being normally incident on surface of bare glass-slide and on the film surface of the {film/substrate} sample. Measurements of sample transmittance were made relative to corrected air-baseline transmission normalized to 100%, made first with both of the sample and the reference paths were open. The sample's transmittance was then measured with the sample being mounted vertically at its spectrophotometer entrance place along the path of its light beam, leaving the entrance of the reference light beam path uncovered.

Spectrophotometric transmission measurements are often affected by the sizes/widths of its slits and by natural line width of emerging light beam hitting the sample, the collective

effect of which is embodied in spectrophotometer spectral band width (SBW) [36]. Thus, the choice of an SBW value is crucial to attain “uninfluenced” and accurately measurable transmission of studied sample. In this work, a 2 nm SBW was adopted in measurements of normal-incidence transmittance of air-supported {flash-evaporated  $\text{PbI}_2$  film/glass slide} structures to ensure good signal-to-noise ratio of detected light and to reduce slit-size effect on transmission spectra [36]. Elimination of SBW effect on measured transmission can be made using Swanepoel procedure [36], but was found to be insignificant for experimental transmittance-wavelength ( $T_{\text{exp}}(\lambda) - \lambda$ ) spectra of our samples.

## Results and Discussion

### Measured Normal-Incidence Transmission-Wavelength Curves

Fig. 1 displays normal-incidence  $T_{\text{exp}}(\lambda) - \lambda$  spectra of ( $\text{PbI}_2$  film/glass-slide) samples F1 and F2 of the 1  $\mu\text{m}$  and 1.2  $\mu\text{m}$  thick flash-evaporated  $\text{PbI}_2$  films, respectively, as well as the  $T_s(\lambda) - \lambda$  spectrum of a typical free-standing 1.1 mm thick bare glass slide, in the wavelength-range 400-900 nm. Several interesting features of these measured normal-incidence transmission spectra are worth discussing, as they provoke optical analysis of such spectra (to be carried out in later sections).

It is noted that the substrate transmittance is almost flat, with nearly constant  $T_s(\lambda)$ -values ranging from 89% to 91% in the  $\lambda$ -range covering the entire transmission and absorption regions of { $\text{PbI}_2$  film/substrate} samples. Figure 1 shows that the  $T_{\text{exp}}(\lambda) - \lambda$  curves of both { $\text{PbI}_2$  film/substrate} samples exhibit in the  $\lambda$ -range 520-900 nm several well-separated interference-fringe maxima and minima, the number of which increases and their spectral width becomes narrower with increasing film thickness. The presence of numerous well-resolved interference-fringe maxima and minima on experimental transmission curves of air-supported {film/substrate} structures facilitates the workability and accuracy of their optical analysis on the basis of Swanepoel EMs [36-42].

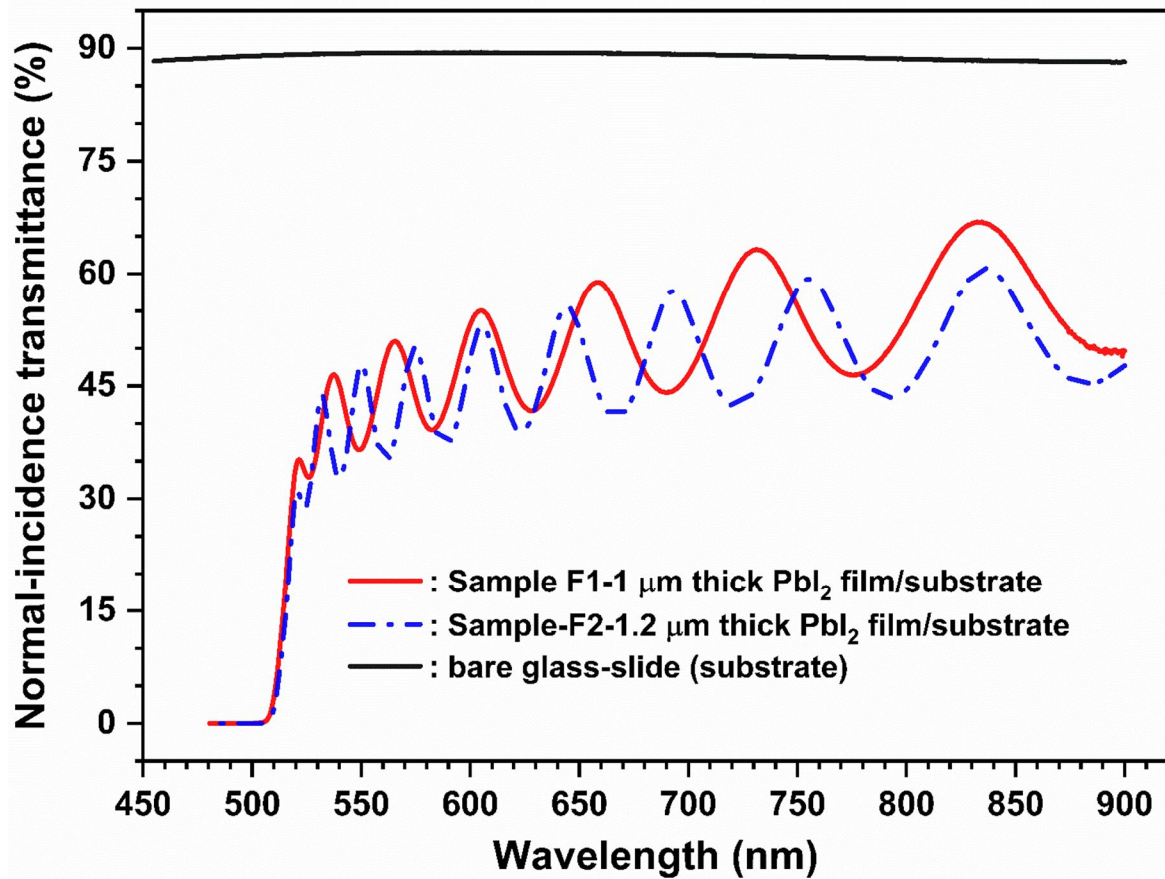


FIG. 1. Wavelength dependency of measured room temperature normal-incidence transmittances of a typical bare glass slide and of samples F1 and F2 which are air-supported {1  $\mu\text{m}$ /1.2  $\mu\text{m}$  thick flash-evaporated  $\text{PbI}_2$  films/glass-slide (at 200  $^\circ\text{C}$ )} structures.

Below  $\lambda \sim 520$  nm, the  $T_{\text{exp}}(\lambda) - \lambda$  curves of both optical structures start to fall down steeply over a narrow  $\lambda$ -range towards zero transmission that initiates at  $\lambda \sim 505$  nm. This abrupt decline in the  $T_{\text{exp}}(\lambda) - \lambda$  curves of studied samples is merely due to light absorption in the flash-evaporated  $\text{PbI}_2$  films themselves. An abrupt optical absorption trend is a characteristic of crystalline materials, which commonly have a vertically sharp fundamental optical absorption edge, with minor bandgap-tailing often encountered in amorphous material films [56-58]. These results are in good accord with the measured XRD patterns of flash-evaporated  $\text{PbI}_2$  films that possess highly hexagonal 2H-polytypic structure [17, 18, 30].

Nevertheless, there are some features in the  $T_{\text{exp}}(\lambda) - \lambda$  spectra of { $\text{PbI}_2$  film/substrate} samples of Fig. 1 that render their analysis rather challenging. Such transmission curves show that the maxima  $T_{\text{M}}(\lambda)$  of their interference-fringe patterns are much lower than  $T_{\text{S}}(\lambda)$  in the studied

$\lambda$ -range, with a depression  $\Delta T(\lambda) = T_{\text{S}}(\lambda) - T_{\text{M}}(\lambda)$  ranging between 55% at  $\lambda \sim 525$  nm and 25% at  $\lambda \sim 835$  nm for sample F1 of 1  $\mu\text{m}$  thick  $\text{PbI}_2$  film, and much larger for that of sample F2 of the 1.2  $\mu\text{m}$  thick  $\text{PbI}_2$  film. This implies that these transmittance spectra do not exhibit at the high- $\lambda$  side any optical transparent region, the existence of which is useful for applying the procedures of traditional Swanepoel's EMs of uniform and non-uniform films to some optical systems [36, 37, 39, 44-47, 52, 53].

#### Optical Analysis of $T_{\text{exp}}(\lambda) - \lambda$ Spectra of {Air/Flash-evaporated $\text{PbI}_2$ Film/Glass-Slide/Air} Structures

The diminishing of normal-incidence transmittance and its interference-fringe maxima of our { $\text{PbI}_2$  film/glass-slide} samples F1 and F2 can then be related to true optical absorption in the film itself and to other causes of different origins. The former cause is undoubtedly the leading term in the strong optical absorption region that becomes more operative with

progressive decrease in wavelength towards the fundamental absorption edge of the substance; however, optical absorption cannot be exclusively responsible for observed drastic transmittance decrease in the weak and intermediate optical absorption regions of studied {PbI<sub>2</sub> film/glass-slide} samples F1 and F2. Studies on many {film/substrate} systems suggested that diminution in the weak and medium absorption region of transmission spectra can be related to interference-fringe shrinking due to spectral bandwidth (SBW) [36], inhomogeneity in the film refractive index ( $\Delta n$ ) and its thickness non-uniformity ( $\Delta d$ ) [36, 38-49], absorption in substrate [38, 42, 43, 48, 49] and light scattering from surface bumpiness [25]. The latter is an unwieldy issue to treat and was tolerated here as visual inspection of our stoichiometric PbI<sub>2</sub> films revealed good surface smoothness and their SEM patterns showed no surface cracks/pinholes, but close-tight hexagonal structure grains [17, 18, 31]. Here, we shall explore the effect of these causes on the measured  $T_{\text{exp}}(\lambda) - \lambda$  spectra of our samples F1 and F2 in some detail.

Large widths of the spectrophotometer slits, effected *via* SBW, often cause shrinkage of the interference-fringe maxima and minima and should be corrected for to achieve accurate optical analysis of transmission spectra of films (uniform or non-uniform) [36, 39, 42]. A large width of spectrometer slit affects significantly and erroneously the determined thickness of the film and its refractive index in the region that is crowded in maxima/minima peaks with small spectral widths and separations [36]. Before starting analysis of the  $T_{\text{exp}}(\lambda) - \lambda$  spectra of our samples by the analytical approach of Richards et al. [42, 43], we carried out slit-width correction to measured  $T_{\text{M}}(\lambda_{\text{tang}})/T_{\text{m}}(\lambda_{\text{tang}})$  using the procedure of Swanepoel [36] (cf. Eq. (A.14) and Eq. (A.15) in supplementary material). But, the 2 nm SBW chosen in the present work was found to be conceivable for minimizing possible slit-width induced influence on such measured maxima and minima, with negligible SBW-corrections to their magnitudes.

Substrate absorption alters the magnitude of measured transmission maxima/minima of films deposited on weakly-absorbed substrates [38,

40-49]. Close inspection of  $T_{\text{s}}(\lambda) - \lambda$  spectrum of Fig. 1 reveals minor absorption inside the 1.1 mm thick glass slide in the range 400-900 nm and marginally affects  $T_{\text{exp}}(\lambda) - \lambda$  spectra of Fig. 1 if divided, to a first approximation [38, 42], at each  $\lambda$  by  $x_{\text{s}}(\lambda) = \exp(-\alpha_{\text{s}}(\lambda)d_{\text{s}})$  [42, 43]. This term is solely originating from the absorption of primary light beam passing through the substrate, as the contribution of all internally reflected beams inside it is trivial in its weak absorption region. So, correction for substrate absorption was abandoned in our analysis, supported by the results of a thorough curve-fitting of the  $T_{\text{s}}(\lambda) - \lambda$  data of Fig. 1 [30, 31]. Yet, instead of using a constant  $n_{\text{s}}(\lambda)$  [36, 37, 39], we fitted part (in the  $\lambda$ -range 400-900 nm) of the  $n_{\text{s}}(\lambda) - \lambda$  data obtained from such curve-fitting analysis to a 5-constant Cauchy dispersion relation of the form:

$$n_{\text{s}}(\lambda) = A_0 + \frac{A_2}{\lambda^2} + \frac{A_4}{\lambda^4} + \frac{A_6}{\lambda^6} + \frac{A_8}{\lambda^8} \quad (1)$$

where  $A_0, A_2, A_4, \dots$  etc. are constants that were determined from the curve fit. The obtained fit equation was exploited to find directly  $n_{\text{s}}(\lambda_{\text{M}}/\lambda_{\text{m}})$  at any wavelength of the measured maxima/minima of studied air-supported {PbI<sub>2</sub> film/glass-slide} samples F1 and F2. The results of  $n_{\text{s}}(\lambda) - \lambda$  data and its fit curve are as shown in Fig. 2.

Further, a lateral variation in the refractive index  $\Delta n$  of a uniformly thick film of thickness  $d$  and an average refractive index  $\bar{n}$  can be modelled in a similar way to that adopted for a lateral thickness variation  $\Delta d$  of a non-uniform film of an average thickness  $\bar{d}$  and refractive index  $n$  [39]. Both non-uniformities compress the interference fringes maxima and minima and their formulations in  $\Delta n$  and  $\Delta d$  are similar, as  $\Delta n d \equiv n \Delta d$  [39]. Thus, it is practically difficult to determine whether  $\Delta n$  or  $\Delta d$  is causing the shrinking of transmission spectra, even if SBW-effect is the same with no variation in  $n$  along the film depth [39, 42, 43]. So, we here have adopted only the effect of thickness non-uniformity, besides the effect of optical absorption in the film, to treat measured  $T_{\text{exp}}(\lambda) - \lambda$  spectra of Fig.1 on the basis of Swanepoel EM of non-uniform films using the analytical procedures of Richards et al. [42, 43].

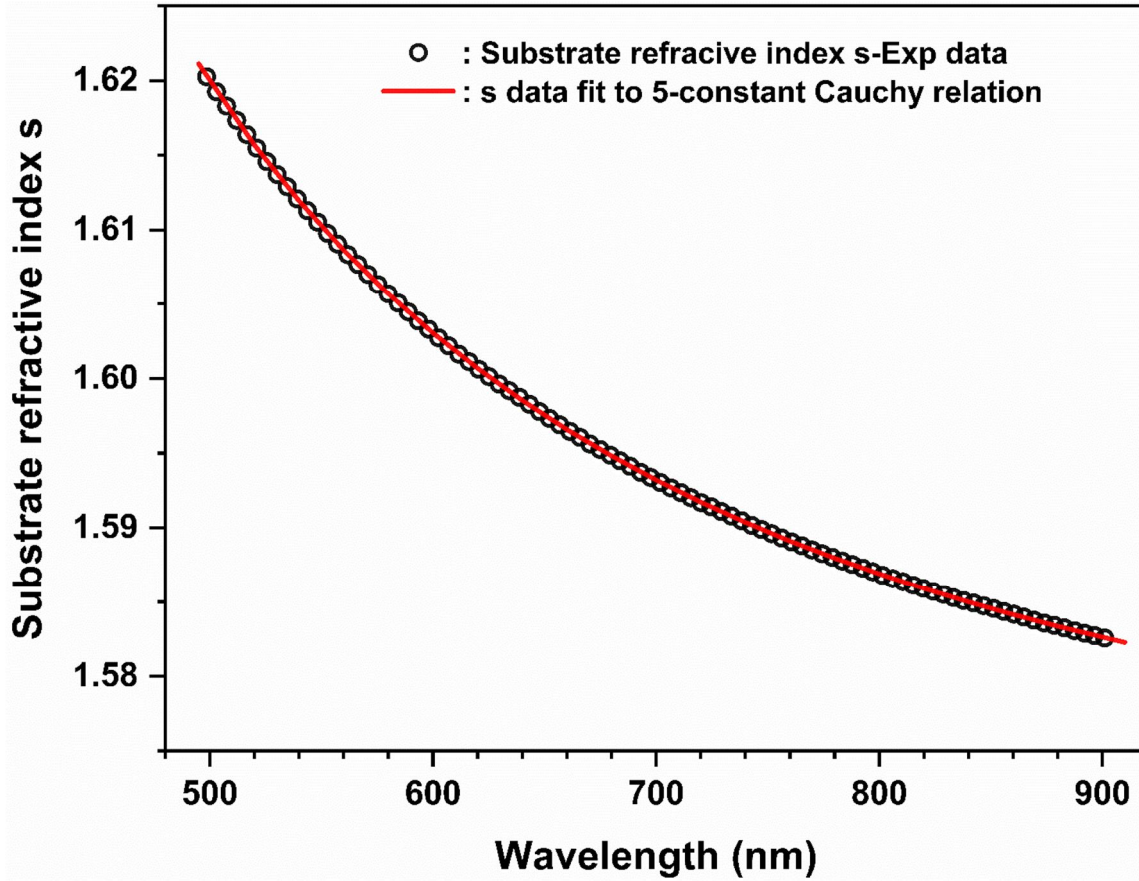


FIG. 2. Data (open circles) of index of refraction  $s$  as a function of wavelength  $\lambda$  for a typical glass slide similar to those used as substrates for studied flash-evaporated lead iodide films. The solid curve represents a curve fit of this data to the 5-constant Cauchy dispersion equation described in Eq. (1).

### The Basic Formulations of Swanepoel Envelope Method (EM) of Non-Uniform Films

Optical analysis presented in supplementary material is exclusively based on Swanepoel's envelope theory of non-uniform films [39] and is limited for transmission spectra exhibiting transparent region at the high- $\lambda$  side. It is assumed that  $T_M(\lambda) \approx T_S(\lambda)$  to find  $\Delta d$  and  $n(\lambda)$  in this transparent region and in the weak and medium absorption regions, besides adopting the formulae relating the measured  $T_M$  and  $T_m$  of non-uniform films to  $T_{M0}$  and  $T_{m0}$  of uniform films of same material and thickness  $d = \bar{d}$ , the average thickness of non-uniform film [39, 44-47, 52, 53].

The measured transmittance  $T_{\Delta d}(\lambda)$  of a non-uniform film of refractive index  $n(\lambda)$ , average thickness  $\bar{d}$  and thickness non-uniformity  $\Delta d$  ( $\ll \bar{d}$ ) on a transparent/weakly-absorbing substrate can be approximately described in the range  $0 < \Delta d < \lambda/4 n(\lambda)$  by an expression of

the form (Appendix A in supplementary material) [38-45]:

$$T_{\Delta d} = \frac{1}{d_{\max} - d_{\min}} \times \int_{d_{\min}}^{d_{\max}} \frac{A \exp[-\alpha(\lambda)\bar{d}]}{\left( B - C \cos \left[ \frac{4\pi n(\lambda)d'}{\lambda} \right] \exp[-\alpha(\lambda)\bar{d}] + D \exp[-2\alpha(\lambda)\bar{d}] \right)} \times dd' \quad (2)$$

where  $d_{\min} = \bar{d} - \Delta d$  and  $d_{\max} = \bar{d} + \Delta d$ , while the constants  $A$ ,  $B$ ,  $C$  and  $D$  are given by the relations below [36]:

$$\begin{aligned} A &= 16n_s n^2, B = (n+1)^3(n+n_s^2), \\ C &= 2(n^2-1)(n^2-n_s^2), \\ D &= (n-1)^3(n-n_s^2). \end{aligned} \quad (3)$$

As discussed in some detail in Appendix A of supplementary material, the measured/calculated maxima  $T_{M\Delta d,x}(\lambda_M/\lambda_m)$  and minima

$T_{m\Delta d,x}(\lambda_m/\lambda_M)$  of a non-uniform film of refractive index  $n(\lambda)$ , absorption coefficient  $\alpha(\lambda)$ , average thickness  $\bar{d}$ , absorbing parameter  $\bar{x}(\lambda) = \exp[-\alpha(\lambda)\bar{d}]$  and thickness non-uniformity  $\Delta d$  can be shown to be described by the following formulae [39-45]:

$$T_{M\Delta d,x} \approx \left( \frac{\lambda}{2\pi n \Delta d} \right) \frac{a_x}{\sqrt{1-b_x^2}} \tan^{-1} \left[ \frac{1+b_x}{\sqrt{1-b_x^2}} \tan \left( \frac{2\pi n \Delta d}{\lambda} \right) \right] \quad (4)$$

$$T_{m\Delta d,x} \approx \left( \frac{\lambda}{2\pi n \Delta d} \right) \frac{a_x}{\sqrt{1-b_x^2}} \tan^{-1} \left[ \frac{1-b_x}{\sqrt{1-b_x^2}} \tan \left( \frac{2\pi n \Delta d}{\lambda} \right) \right]. \quad (5)$$

The parameters  $a_x$  and  $b_x$  are given by the relations below:

$$a_x = \frac{A\bar{x}}{B + D\bar{x}^2} \text{ and } b_x = \frac{C\bar{x}}{B + D\bar{x}^2}. \quad (6)$$

Eqs. (4) and (5), combined with Eq. (6), are valid for both transparent region ( $\bar{x} = 1$ ) and weak and medium absorption regions ( $\bar{x} < 1$ ) of transmission spectra of air-supported {non-uniform film/substrate} structures and are independent transcendental equations that can be solved simultaneously to get a unique solution of their two unknowns. They form the basic expressions on which algebraic analysis of transmission spectra of such structures in these optical absorption regions by the conventional Swanepoel EM of non-uniform films is exclusively based to evaluate  $\Delta d$ ,  $\bar{d}$  and  $n(\lambda)$  of the film under consideration once the values of maxima  $T_M(\lambda_M/\lambda_m)$  and minima  $T_m(\lambda_m/\lambda_M)$  are obtainable, combined with the corresponding values of  $n_s(\lambda_M/\lambda_m)$ . In the present analysis, the latter can be found from Fig. 2 and its numerical fit relation (Eq. (1)). Eventually,  $\alpha(\lambda)$  and bandgap energy  $E_g$  of the film sample can then be determined once the respective values of  $\bar{x}(\lambda)$  are appropriately determined [39-45].

### Procedure for Constructing Transmission Interference-Fringe Maxima and Minima Envelope Curves

It is clear that the first step to proceed with the above-described optical analysis is to determine accurately the values of interference-fringe transmission maxima  $T_M(\lambda_M/\lambda_m)$  and minima  $T_m(\lambda_m/\lambda_M)$  at the corresponding tangent wavelengths  $\lambda_M$  and  $\lambda_m$ , which were here accomplished using the source package

ENVELOPE computer program of McClain *et al.* [55] (<http://dlmf.nist.gov>). The McClain ENVELOPE program usually finds the measured  $T_M(\lambda_M)$  and minima  $T_m(\lambda_m)$  and then constructs continuous, monotonic  $T_M(\lambda_M/\lambda_m)$  and  $T_m(\lambda_m/\lambda_M)$  envelope curves, which are bound and tangent to these transmission maxima and minima.

This ENVELOPE program was applied to maxima and minima of transmission spectra of our samples few times *via* decreasing progressively the tolerance of computation to get optimal numerals of  $T_M$  and  $T_m$  and their  $\lambda_M$  and  $\lambda_m$ . The section of code in the original ENVELOPE program where each pair of transmission maxima and minima data ( $x, y$ ) is replaced by the average of itself and its two nearest neighbor points was commented out as done by Richards *et al.* [42, 43]. This is justified by low noise in our  $T_{\text{exp}}(\lambda)$  data, a valuable aspect for smoothing envelope curves and using  $T_{\text{exp}}(\lambda) > 0.1\%$  to avoid noisy (due to fluctuations in detected signal) data points from being treated by ENVELOPE algorithm as extrema. A second modification in this program was increasing the dimension of the array to improve final smoothing [42, 43] before ENVELOPE code was re-compiled.

The ENVELOPE program starts by an initial smoothing process using a ‘‘piecewise cubic polynomial’’ fit to the experimental data points and a second smoothing when a first estimate of the tangent points is achieved. Several trials of tolerance factors were performed. The ENVELOPE calculations converge and highly acceptable fitted envelope curves were obtained when the values 0.04 and 0.003 of tolerance factors were used for the initial and final smoothing process. Using the new smoothed data, the program then attempts to find estimates for the tangent points where the envelope curves will touch the data curve. This is done by locating intervals where smoothed data curve is either concave or convex, with the tangent points for top envelope were initialized to be the midpoints of each concave interval, while those for bottom envelope were set at the midpoints of each convex interval. The first or last data point is excluded from the last smoothing process. These points were used only if they represent a local maximum or minimum and in this case, the tangent point estimate was taken to be the local

maximum or minimum point rather than the midpoint of the interval.

The true tangent point for an endpoint interval may lie outside the range of the original data points and the ENVELOPE algorithm will not converge correctly. If the endpoint interval contains a local maximum or minimum, the true tangent point is guaranteed to lie nearby and the algorithm will then converge properly. The output of the ENVELOPE consists of two files: one is the number of tangent points having been found for each envelope and the coordinates of each "top" and "bottom" extrema in the oscillating data. The second file contains the smoothed data for both the top and bottom

curves. It is worth noting here that no visible improvement of the resulting top and bottom tangent points was noticed upon performing the second modification. Nevertheless, this minor modification was kept in the executable version. The data file containing the finally determined values of  $T_M(\lambda_M/\lambda_m)$  and  $T_m(\lambda_m/\lambda_M)$  is stored and kept for use in the required optical analysis. An example of such ENVELOPE points corresponding to interference-fringe maxima and minima of measured transmission spectra of samples F1 and F2 of the 1  $\mu\text{m}$  and 1.2  $\mu\text{m}$  thick flash-evaporated  $\text{PbI}_2$  films, respectively, is shown in Fig. 3.

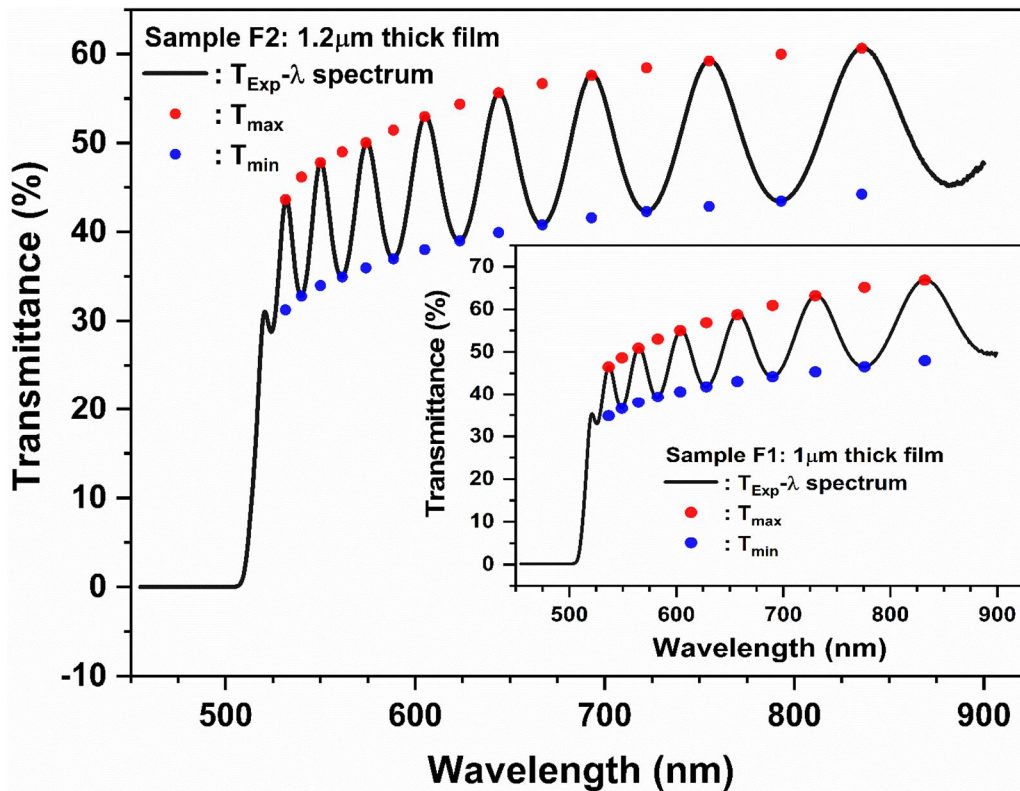


FIG. 3. The interference-fringe maxima and minima points of measured transmission spectra of samples F1 and F2 of the 1  $\mu\text{m}$  and 1.2  $\mu\text{m}$  thick flash-evaporated  $\text{PbI}_2$  films, respectively, as determined from ENVELOPE program of McClain et al. [55].

### Determination of $\text{PbI}_2$ Film Optical Constants Using the Extended Swanepoel EM of Non-Uniform Films

The thickness non-uniformity  $\Delta d$  and  $n(\lambda)$  of the non-uniform film are usually evaluated by solving simultaneously the two transcendental equations given in Eq. (4) and Eq. (5) with  $\bar{x} = 1$  being inserted in Eq. (6) using the measured/calculated maxima  $T_M(\lambda_M/\lambda_m)$  and minima  $T_m(\lambda_m/\lambda_M)$  [39-41]. However, the

calculated values of  $\Delta d$  are often drastically varying with wavelength, so a feasible  $\Delta d$ -value had to be chosen for use in the calculations of  $n(\lambda)$  and  $\alpha(\lambda)$  in the weak and medium ( $\bar{x} < 1$ ) region. In many studies based on Swanepoel EM of non-uniform films [39], this was often made by selecting arbitrarily/luckily few of the calculated  $\Delta d$ -values and taking their average to be that optimum value of  $\Delta d$ .

Further, some {non-uniform film/substrate} samples do not exhibit a transparent region and are absorbing in the whole wavelength range [42, 43, 48, 49, 54], as is also seen from Fig. 1. Assuming  $T_M \approx T_s$  for such transmission spectra for use in the formulae relating  $T_M$  and  $T_m$  of a non-uniform film to  $T_{M0}$  and  $T_{m0}$  of a uniform one with  $d = \bar{d}$  [39, 44-47, 52, 53] or picking a capricious  $\Delta d$ -value [39-41, 54] sometimes yield irrational results and is questionable. An extended version of Swanepoel's EM of non-uniform films has been suggested by Richards et al. [42, 43] for treating transmission spectra of non-uniform films that are absorbing even at high- $\lambda$  side *via* choosing an initial value for  $\Delta d$  and varying it till a coincidence between the calculated (simulated) and measured transmission curves is obtained. This approach is adopted to analyze  $T_{\text{exp}}(\lambda) - \lambda$  spectra of Fig. 1. As discussed above, however, no correction was made to these  $T_{\text{exp}}(\lambda)$  spectra at each  $\lambda$  or to respective  $T_M(\lambda_M/\lambda_m)$  and  $T_m(\lambda_m/\lambda_M)$  at each  $\lambda_M$  and  $\lambda_m$  for slit-width effect or absorption in the substrate. Our analysis only includes the substrate dispersive  $s(\lambda_M/\lambda_m)$ -values in the formulae containing  $T_M(\lambda_M/\lambda_m)$  and  $T_m(\lambda_m/\lambda_M)$ , as done by Richards et al. [42, 43]. This was not used by Swanepoel [39], but is also adopted in other studies using procedures of conventional Swanepoel's EM of non-uniform films [38, 40-49, 52-54].

Lastly, we applied the approach of Richards et al. [42, 43] to analyze the  $T_M(\lambda_M/\lambda_m)$  and  $T_m(\lambda_m/\lambda_M)$  to calculate  $\Delta d$  at each  $\lambda_M$  and  $\lambda_m$ , the value of which was varied until the calculated values of  $\Delta d$ ,  $n(\lambda)$ ,  $\alpha(\lambda)$  and  $\bar{d}$  of studied flash-evaporated  $\text{PbI}_2$  films re-generated their respective measured transmission curves. The finally-approved  $n(\lambda) - \lambda$  and  $\alpha(\lambda) - \lambda$  data was then used to elucidate the spectral dispersion and electronic transitions operating in these undoped flash-evaporated  $\text{PbI}_2$  films.

All of the implemented procedures and the algebraic calculation stages of this extended version of Swanepoel EM of non-uniform films have been integrated in a compact computational program written in Mathematica. Before executing the entire program in a single run, all of its individual steps were first checked in sequence for their workability and correctness.

## Determination of the Thickness Variation $\Delta d$ for the Non-uniform Flash-Evaporated $\text{PbI}_2$ Films

Thickness non-uniformity  $\Delta d$  of a film and its optical absorption affect dissimilarly its transmission spectrum, in the sense that an increase in  $\Delta d$  shrinks the interference-fringe minima and maxima at all wavelengths, while an increase in film absorption coefficient  $\alpha(\lambda)$  reduces progressively the magnitude of both maxima and minima fringes (it reduces the geometric mean of transmission spectrum) [39, 43]. In this analysis, we assumed that the observed transmission interference-fringe pattern of our samples F1 and F2 is related to non-uniformity in the thickness of the  $\text{PbI}_2$  film itself and the film is also optically absorbing over the whole wavelength range studied.

To complete analyzing transmission spectra of the non-uniform, absorbing  $\text{PbI}_2$  films shown in Fig. 1, where no transparent region can be seen, on the basis of Swanepoel EM of non-uniform films, it is indispensable to determine first an accurate value for their thickness non-uniformity  $\Delta d$ . Put  $\bar{x} = 1$  in the coefficients  $a_x$  and  $b_x$  given in Eq. (6) and insert their coefficients  $A, B, C$  and  $D$  defined in Eq. (3) in Eq. (4) and Eq. (5) to reduce them to two independent transcendental equations in  $\Delta d$  and  $n$  only, as substrate's refractive index  $n_s$  is already known.

Now, the measured/calculated values of  $T_M(\lambda_{\text{max}}/\lambda_{\text{min}})$  and  $T_m(\lambda_{\text{min}}/\lambda_{\text{max}})$  were inserted into them, which were solved simultaneously to find the two unknowns  $\Delta d$  and  $n(\lambda_{\text{tang}})$  at each tangent wavelength  $\lambda_{\text{tang}}$  ( $= \lambda_{\text{max}}$  and  $\lambda_{\text{min}}$ ) using the rigorous Mathematica 'FindRoot package'. At this computational stage, the optical absorption in the film is ignored and the obtained values of  $n(\lambda_{\text{tang}})$  are usually overlooked, as the purpose here is exclusively to determine a value for  $\Delta d$ , which should be a  $\lambda$ -independent inherent constant film quantity. However, the values of  $\Delta d$  calculated by this tactic usually show drastic variation with  $\lambda$  [38-43, 54], so selecting an acceptable value for  $\Delta d$  becomes a challenging issue and is crucial for subsequent procedures used to determine optical constants of the film in weak, medium and strong absorption regions.

Adopting an average of the whole/part of the obtained  $\Delta d$ -values and/or a lucky/arbitrary choice of a  $\Delta d$ -value [39-41, 54] is not a good methodology for determining an accurate value for this parameter; thus, finding a more reliable value for  $\Delta d$  turns out to be tricky. A rational value for  $\Delta d$  might be inferred from a plot of  $\Delta d(\lambda_{\text{tang}})$ -Vs- $\lambda_{\text{tang}}$  and picking a reminiscent value of  $\Delta d$  if a saddle-like portion exists on such a plot in the medium absorption region [38]. If the film transmission exhibits a transparent region at high- $\lambda$  side, then  $\Delta d$  might be the asymptotic value at such high wavelengths [42]. However, if the film is absorbing over the whole transmission spectrum with no transparent region, as displayed in Fig. 1, and if no real asymptotic  $\Delta d$  value or saddle-like part on  $\Delta d(\lambda_{\text{tang}})$ -Vs- $\lambda_{\text{tang}}$  plot can be adopted, as for our  $\text{PbI}_2$  films, the  $\Delta d$  values of which calculated from simultaneous solution of Eq. (4) and Eq. (5) with  $\bar{x} = 1$  are depicted in Fig. 4, the situation becomes more problematic. Richards et al. [42, 43] suggested that even choosing a  $\Delta d$ -value from asymptotic regime should be used as an initial guess for succeeding calculations underlying the optical analysis based on Swanepoel's EM of non-uniform films

that are optically absorbing over the entire wavelength range of interest. In the absence of both asymptotic-type or saddle-like  $\Delta d$  region, such initial  $\Delta d$  can be selected from calculated  $\Delta d$  values scattered in medium absorption region [38].

An incorrect attribution of actual optical absorption in the film to be due to the thickness variation that has dissimilar effect on the maxima and minima should be evident when the calculated values of optical constants and film thickness are used to regenerate the measured transmission spectrum. If the generated data does not lie correctly on the measured transmission curve, then the value of  $\Delta d$  has to be adjusted accordingly, most likely to lower values, until an optimum is acquired and a virtuous match between the measured and generated transmission data is realized. This method forms the basis of a checking procedure for the uniqueness solution of Eq. (4) and Eq. (5) that can be considered to be reliable, as there should be only one unique solution for them [39]. The procedures of this EM analytical approach and associated formulations are adopted to analyze measured normal-incidence  $T_{\text{exp}}(\lambda) - \lambda$  spectra of our  $\{\text{PbI}_2 \text{ film/substrate}\}$  samples.

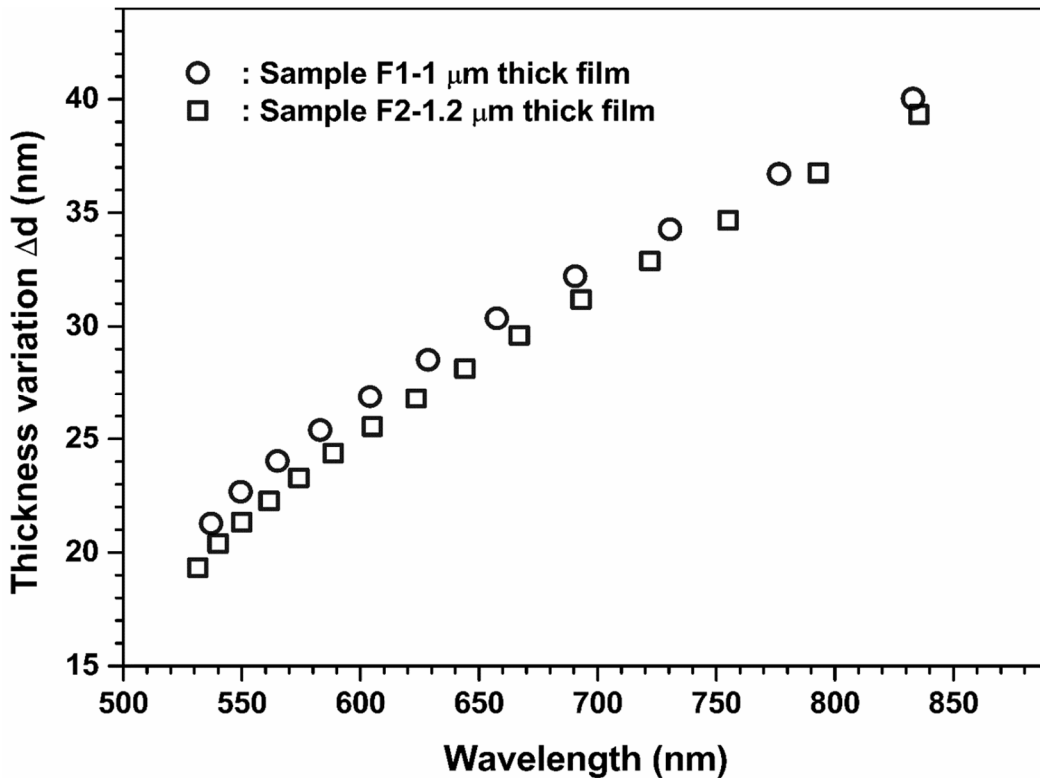


FIG. 4. Wavelength variation of thickness non-uniformity  $\Delta d$  calculated from simultaneous solution of the two transcendental formulae in Eq. (4) and Eq. (5), assuming  $\bar{x} = 1$ , for samples F1 and F2 of the 1  $\mu\text{m}$  and 1.2  $\mu\text{m}$  thick flash-evaporated  $\text{PbI}_2$  films, respectively.

### Determination of Film's Optical Constants and Average Thickness in Weak and Medium Absorption Regions

In principle, having a reasonable value for  $\Delta d$ , Eq. (4) and Eq. (5) can then be solved simultaneously, this time to find the two unknowns  $n(\lambda_{\text{tang}})$  and  $\bar{x}(\lambda_{\text{tang}})$  at each extreme wavelength  $\lambda_{\text{tang}}$  ( $= \lambda_{\text{max}}$  and  $\lambda_{\text{min}}$ ) in the weak and medium absorption regions ( $\bar{x} < 1$ ) using the absorbing coefficients  $a_x$  and  $b_x$  given in Eq. (6) with their  $A$ ,  $B$ ,  $C$  and  $D$  coefficients given in Eq. (3) that incorporate  $n$  and  $s$ , which is determined separately in advance. These expressions are another two independent transcendental equations that have one unique solution for  $n(\lambda_{\text{tang}})$  and  $\bar{x}(\lambda_{\text{tang}})$  at each  $\lambda_{\text{max}}$  or  $\lambda_{\text{min}}$  in the validity range  $0 < \bar{x} \leq 1$  [39].

The absorption coefficient  $\alpha(\lambda_{\text{tang}})$  in the weak and medium absorption regions can be found from the determined  $\bar{x}(\lambda_{\text{tang}})$  using the relation  $\alpha(\lambda_{\text{tang}}) = -\ln \bar{x}(\lambda_{\text{tang}})/\bar{d}$ , if we have at hand an accurate value for the film average thickness  $\bar{d}$ , which, however, is practically difficult to measure. In optical analysis based on Swanepoel's EM of non-uniform films,  $\bar{d}$  can be found from the interference condition given by [39]:

$$2\bar{d}n(\lambda_{\text{tang}}) = m\lambda_{\text{tang}}. \quad (7)$$

This can be attained by using  $n(\lambda_{\text{tang}})$  values at  $\lambda_{\text{max}}$  or  $\lambda_{\text{min}}$  of the nearest neighboring extrema [36, 39], with  $m$  being the interference order (integer for maxima and half-integer for minima displayed on measured transmission spectrum). However, a more feasible value of  $\bar{d}$  can be attained by the use of the expression given below [39]:

$$\frac{\ell}{2} = 2\bar{d} \left[ \frac{n(\lambda)}{\lambda} \right] - m_1, \quad (8)$$

where  $\ell = 0, 1, 2, 3, 4, \dots$ , with  $\ell = 0$  for the first observable extrema on the high-wavelength side, which corresponds to interference order  $m_1$  that should be an integer for maxima and half-integer for minima.

A proper linear portion of a plot of  $\ell/2$  against  $n(\lambda_{\text{tang}})/\lambda_{\text{tang}}$  for  $\ell = 0, 1, 2, 3, 4, \dots$  can be fitted to Eq. (8), with its slope giving  $2\bar{d}$  and its negative intercept is  $m_1$ , which should be then round off to the nearest integer/half-integer

numeral  $m_0$  for the first visible maxima/minima in the long- $\lambda$  region. An improved value for  $\bar{d}$  can then be found from a linear portion of a new  $\ell/2 - n(\lambda_{\text{tang}})/\lambda_{\text{tang}}$  plot, with  $m_0$  being now kept fixed and treated as a constant parameter in the fitting process on basis of Eq. (8). The straight line is normally a poor fit to the points if the wrong  $m_0$  value is used; thus, unity (1) would sometimes be added or subtracted from the used  $m_0$ -value and the fit procedure has to be repeated.

The finally obtained values of  $\bar{d}$  and  $m_0$ , with the interference-order  $m$  being increased progressively from  $m_0$  by  $1/2$  for the maxima and minima at shorter  $\lambda_{\text{tang}}$ , are then fed back into Eq. (7) to determine more accurate values for  $n(\lambda_{\text{tang}})$  at  $\lambda_{\text{max}}/\lambda_{\text{min}}$  of the observed transmission interference-fringe pattern in the weak and medium absorption regions. Further, once an improved value of  $\bar{d}$  is determined, the values of  $\alpha(\lambda_{\text{tang}})$ , hence  $\kappa(\lambda_{\text{tang}}) = \alpha(\lambda_{\text{tang}})\lambda_{\text{tang}}/4\pi$ , can be determined in weak and medium absorption regions using the determined  $\bar{x}(\lambda_{\text{tang}})$ .

### Determination of Optical Constants of the Film in the Strong Optical Absorption Region

In the region of medium to nearby strong optical absorption, the interference fringes become rather small and experimental uncertainties in the magnitude of the last few resolved extrema often lead to erroneous calculated values of  $\alpha(\lambda_{\text{tang}})$  [36, 39]. Hence, one has to choose only the number of data points, counted from the long- $\lambda$  side, which do not produce randomly varying and noisy  $\alpha(\lambda_{\text{tang}})$  values. Values of  $\alpha(\lambda)$  at wavelengths of non-adopted last extrema in the medium absorption region and at shorter wavelengths in the strong absorption region cannot be determined by the use of interference condition given in Eq. (7), which is not strictly valid in the absorption region, and there is no means of extracting  $n(\lambda)$  values from the interference-free transmission curve alone. The values of  $\alpha(\lambda)$  in the quasi-/strong- optical absorption regions can be obtained by the use of different means [36, 37, 39-43].

A tactic to achieve such goal is to extrapolate the non-noisy  $n(\lambda_{\text{tang}})$  of the weak and medium absorption regions in the remainder of the

spectrum *via* fitting such  $n(\lambda_{\text{tang}}) - \lambda_{\text{tang}}$  data to an appropriate dispersion formulation. The obtained fit  $n(\lambda)$ -formula can then be utilized to determine the respective values of  $x(\lambda)$ , and hence of  $\alpha(\lambda)$ , in the weak and medium absorption regions using an evocative formulation relating  $n(\lambda)$  and  $x(\lambda)$ , which involves the transmission maxima  $T_M$  as that described by the expression given below [36, 40, 42-45]:

$$x = \frac{E_M - [E_M^2 - (n^2 - 1)^3(n^2 - n_s^4)]^{\frac{1}{2}}}{(n - 1)^3(n - n_s^2)};$$

$$E_M = \frac{8n^2n_s}{T_M} + (n^2 - 1)(n^2 - n_s^2). \quad (9)$$

Eq. 9 has been frequently used to determine  $\alpha(\lambda)$  for films with uniform thickness in the weak and medium absorption regions since  $n(\lambda)$  and  $n_s(\lambda)$  are already known [36, 37]; nonetheless, it has been argued that Eq. 9 can also be valid for non-uniform films in the spectral region where the interference fringes start to disappear and thus the maxima and minima envelope curves converge to a single curve in the strong absorption region, in which  $T_M \approx T_m \approx T$  [42-45]. Alternatively, a formula that includes interference-free transmission geometric mean  $T_\alpha = \sqrt{T_M T_m}$  [36, 42, 43] can also be utilized to determine  $x(\lambda)$  in weak, medium and strong absorption regions. This formula is often used in optical and infrared studies and is described in the expression given by [39]:

$$x = \frac{\left\{ G - [G^2 - (n^2 - 1)^6(n^2 - n_s^4)^2]^{\frac{1}{2}} \right\}^{\frac{1}{2}}}{(n - 1)^3(n - n_s^2)},$$

$$G = \frac{128n^4n_s^2}{T_\alpha^2} + n^2(n^2 - 1)^2(n_s^2 - 1)^2 + (n^2 - 1)^2(n^2 - n_s^2)^2. \quad (10)$$

For spectral wavelengths shorter than where the last extrema is resolved, Eq. (9) and Eq. (10) can be used for calculating  $x(\lambda)$ , but with taking the transmission value incorporated into them directly from the original spectrum and using the extrapolated  $n(\lambda)$  values [40-45]. In the present study, Eq. (10) has been found to yield more satisfactory results for the transmission spectrum of our non-uniform undoped flash-evaporated PbI<sub>2</sub> films.

The above-described comprehensive optical analytical procedures based on Swanepoel's EM of non-uniform films [39] and extended to deal with transmission spectra of films that are absorbing in the whole  $\lambda$ -range of interest [42, 43] complete the determination of the optical constants  $n(\lambda)$ ,  $\alpha(\lambda)$  and  $\kappa(\lambda)$  of PbI<sub>2</sub> films, in addition to optimal values of their average thickness  $\bar{d}$  and thickness non-uniformity  $\Delta d$ . The obtained optical constants as a function of wavelength  $\lambda$  in the interference-fringe maxima and minima region (520-900 nm) and in strong absorption region over the whole spectral range studied are plotted as a function of wavelength  $\lambda$  or of the respective photon energy  $E_{\text{ph}} = h\nu = hc/\lambda$  ( $= 1240/\lambda(\text{nm})$  eV) of light incident on the film to explicate spectral dispersion and inter-bandgap electronic transitions operative in studied flash-evaporated PbI<sub>2</sub> films, as discussed later.

Implementation of the above-described procedures for analyzing the transmittance spectra of our samples F1 and F2 displayed in Fig. 1 was started by choosing an initial guess value of  $\Delta d = 25$  nm in the Mathematica program to solve Eq. (4) and Eq. (5) with  $\bar{x} = 0$  to find initial values of  $n(\lambda_{\text{tang}})$ , which are labelled as  $n_2(\lambda_{\text{tang}})$  in Table 1 and the values of  $\Delta d(\lambda_{\text{tang}})$  depicted in Fig. 4 which are labelled in Table 1 as  $\Delta d_{\text{cal}}(\lambda_{\text{tang}})$ . This initial value of  $\Delta d$  did not give viable results of subsequent calculations or simulated transmittance spectra, which was then varied until feasible results were achieved. The optimum values of  $\Delta d$ , found to be 14 nm for sample F1 and 14.5 nm for sample F2, were then used to determine more reasonable values for refractive index  $n(\lambda_{\text{tang}})$  and  $x(\lambda_{\text{tang}})$  in the weak and medium absorption regions, which are designated as  $n_3(\lambda_{\text{tang}})$  and  $x_3(\lambda_{\text{tang}})$  in Table 1. The  $x_3(\lambda_{\text{tang}})$  values were determined from Eq. (10) using the values of  $n_3(\lambda_{\text{tang}})$ ,  $n_s(\lambda_{\text{tang}})$  and  $T_\alpha(\lambda_{\text{tang}})$ .

However, as discussed above, the last extremes were recalculated to give more viable values for  $n(\lambda_{\text{tang}})$  by extrapolating their values in the long- $\lambda$  region by the use of a 4-constant Cauchy dispersion relation [28-30] and the values of noisy  $n_3(\lambda_{\text{tang}})$  data were being replaced with the extrapolated values [42]. In

Table 1, the  $n(\lambda_{\text{tang}})$  values found from such extrapolation procedure are denoted by  $n_4(\lambda_{\text{tang}})$ , which were used to plot  $\ell/2$ -vs-  $n_4(\lambda_{\text{tang}})/\lambda_{\text{tang}}$  (nm) with  $\ell = 0, 1, 2, 3, \dots$ , in accordance with Eq. (8), the fit of which for the samples F1 and F2 gave an initial value for  $m_1$  ( $\ell = 0$ ) that was rounded off to integers  $m_0 = 7$  and 8 as the first extremes observed in their spectra were maxima. The obtained  $m_0$  was then set constant in Eq. (8) to find improved values for average thickness  $\bar{d}$  of their films, which were 1072 nm for sample F1 and 1229 nm for sample F2. These results are shown in Fig. 5, with the values of interference order labelled as  $m$  in Table 1. The obtained  $\bar{d}$  value and order  $m$  were then inserted in Eq. (7) to find a more improved values of  $n(\lambda_{\text{tang}})$ , labelled as

$n_5(\lambda_{\text{tang}})$  in Table 1. The values of  $n_5(\lambda_{\text{tang}})$ ,  $n_s(\lambda_{\text{tang}})$  and  $T_\alpha(\lambda_{\text{tang}})$  were inserted in Eq. (10) to find  $x_5(\lambda_{\text{tang}})$  values, which were then used to evaluate the corresponding values of film absorption coefficient  $\alpha(\lambda_{\text{tang}})$  listed in Table 1.

The obtained  $n_5(\lambda_{\text{tang}})$ - $\lambda_{\text{tang}}$  data was then fitted to a 4-constant Cauchy dispersion relation, the fit formula of which was used to extrapolate the  $n(\lambda)$  at shorter wavelengths down to  $\lambda = 500$  nm, lying into the strong absorption region and beyond. The final results were then used in Eq. (10) to find the corresponding values of  $x(\lambda)$  and hence the matching values of  $\alpha(\lambda)$  from the relation  $\alpha(\lambda) = -\ln \bar{x}(\lambda)/\bar{d}$ , using the above-deduced values of average film thickness  $\bar{d}$ .

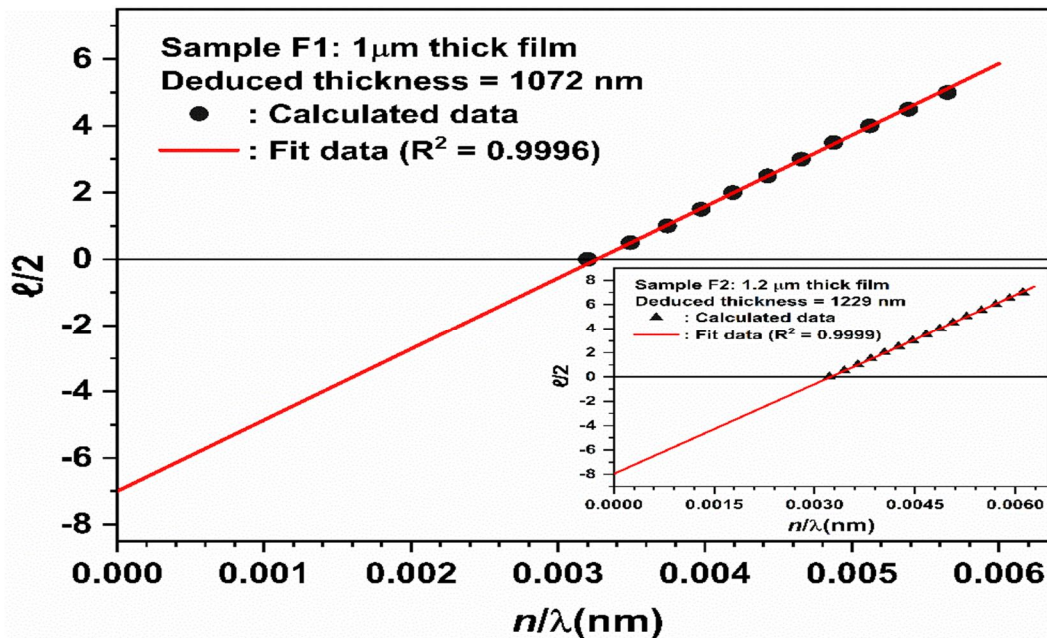


FIG. 5. Plot of  $\ell/2$ -Vs-  $n/\lambda$ (nm) for samples F1 and F2 of the 1  $\mu\text{m}$  and 1.2  $\mu\text{m}$  thick flash-evaporated  $\text{PbI}_2$  films.

TABLE 1. Values of  $\lambda$ ,  $T_M$  and  $T_m$  for the two samples F1 and F2 transmission spectra of Fig. 1; the underlined transmittance values are those calculated by the McClain envelope program. The rest of symbols in the table are explained in the text. The uncertainty in the finally calculated values of the film index of refraction was estimated to be better than 3%, while the uncertainty in the finally calculated average thicknesses of the studied films was around 5%.

Sample	$\lambda$ (nm)	$s$	$T_M$	$T_m$	$n_2$	$\Delta d_{\text{cal}}$ (nm)	$n_3$	$x_3$	$n_4$	$m$	$n_5$	$x_5$	$\alpha$ ( $\text{cm}^{-1}$ )
F1 $\Delta d_{\text{opt}} =$ 14 nm $\bar{d} =$ 1072 nm	833	1.585	0.6681	<u>0.4792</u>	3.608	40.0	2.666	0.791	2.666	7	2.720	0.791	2184
	776.5	1.588	<u>0.6512</u>	0.4647	3.730	36.8	2.711	0.778	2.711	7.5	2.716	0.778	2338
	730.5	1.591	0.6317	<u>0.4528</u>	3.857	34.3	2.734	0.762	2.734	8	2.726	0.762	2541
	690.5	1.594	<u>0.6088</u>	0.4412	4.004	32.2	2.744	0.740	2.744	8.5	2.737	0.740	2805
	657.5	1.597	0.5870	<u>0.4296</u>	4.156	30.4	2.754	0.720	2.754	9	2.760	0.720	3069
	628.5	1.600	<u>0.5682</u>	0.4175	4.305	28.5	2.781	0.703	2.781	9.5	2.785	0.703	3284
	604	1.603	0.5499	<u>0.4053</u>	4.461	26.9	2.812	0.687	2.812	10	2.817	0.687	3499
583	1.605	<u>0.5297</u>	0.3926	4.640	25.4	2.838	0.669	2.842	10.5	2.855	0.670	3742	

Sample	$\lambda$ (nm)	$s$	$T_M$	$T_m$	$n_2$	$\Delta d_{cal}$ (nm)	$n_3$	$x_3$	$n_4$	$m$	$n_5$	$x_5$	$\alpha$ ( $cm^{-1}$ )
F2 $\Delta d_{opt} = 14.5$ nm $\bar{d} =$ 1229 nm	565	1.608	0.5084	<b>0.3797</b>	4.839	24.0	2.860	0.648	2.893	11	2.899	0.653	3983
	549.5	1.610	<b>0.4857</b>	0.3651	5.074	22.7	2.890	0.627	2.960	11.5	2.947	0.633	4260
	537	1.613	0.4643	<b>0.3476</b>	5.334	21.3	2.965	0.610	3.034	12	3.006	0.613	4559
	835.5	1.585	0.6064	<b>0.4426</b>	4.004	39.3	2.696	0.731	2.696	8	2.719	0.731	2547
	793	1.587	<b>0.5998</b>	0.4346	4.069	36.8	2.736	0.728	2.736	8.5	2.743	0.728	2584
	755	1.589	0.5923	<b>0.4287</b>	4.130	34.7	2.759	0.723	2.759	9	2.765	0.723	2642
	722	1.592	<b>0.5845</b>	0.4230	4.193	32.9	2.779	0.717	2.779	9.5	2.791	0.717	2706
	693	1.594	0.5761	<b>0.4160</b>	4.267	31.2	2.809	0.712	2.808	10	2.820	0.712	2770
	667	1.596	<b>0.5668</b>	0.4081	4.352	29.6	2.843	0.705	2.843	10.5	2.850	0.705	2841
	644	1.598	0.5564	<b>0.3994</b>	4.449	28.1	2.881	0.698	2.881	11	2.883	0.698	2923
	623.5	1.600	<b>0.5437</b>	0.3901	4.565	26.8	2.917	0.689	2.917	11.5	2.918	0.689	3034
	605	1.602	0.5296	<b>0.3802</b>	4.697	25.5	2.953	0.677	2.953	12	2.954	0.677	3170
	588.5	1.605	<b>0.5145</b>	0.3699	4.844	24.4	2.989	0.665	2.989	12.5	2.994	0.665	3320
	574	1.607	0.5004	<b>0.3597</b>	4.993	23.3	3.031	0.655	3.031	13	3.037	0.654	3457
	561.5	1.608	<b>0.4900</b>	0.3495	5.121	22.2	3.098	0.650	3.090	13.5	3.085	0.644	3585
550	1.610	0.4781	<b>0.3397</b>	5.264	21.3	3.155	0.642	3.144	14	3.133	0.635	3700	
540	1.612	<b>0.4617</b>	0.3280	5.461	20.4	3.212	0.629	3.200	14.5	3.186	0.621	3874	
531.5	1.614	0.4364	<b>0.3125</b>	5.776	19.3	3.262	0.605	3.255	15	3.244	0.599	4175	

The final values of  $\bar{d}$ ,  $\Delta d$ ,  $s(\lambda)$ ,  $n(\lambda)$  and  $\alpha(\lambda)$  determined from the optical analysis of our non-uniform, absorbing flash-evaporated lead iodide films of samples F1 and F2 on the basis of extended version [42, 43] of Swanepoel EM of non-uniform films were inserted in Eq. (2),

which was then evaluated numerically at adopted wavelengths to get their simulated transmission curves. The obtained results yielded good match between their measured transmission spectra and the re-generated (simulated) curves, as illustrated in Fig. 6 for the two samples F1 and F2.

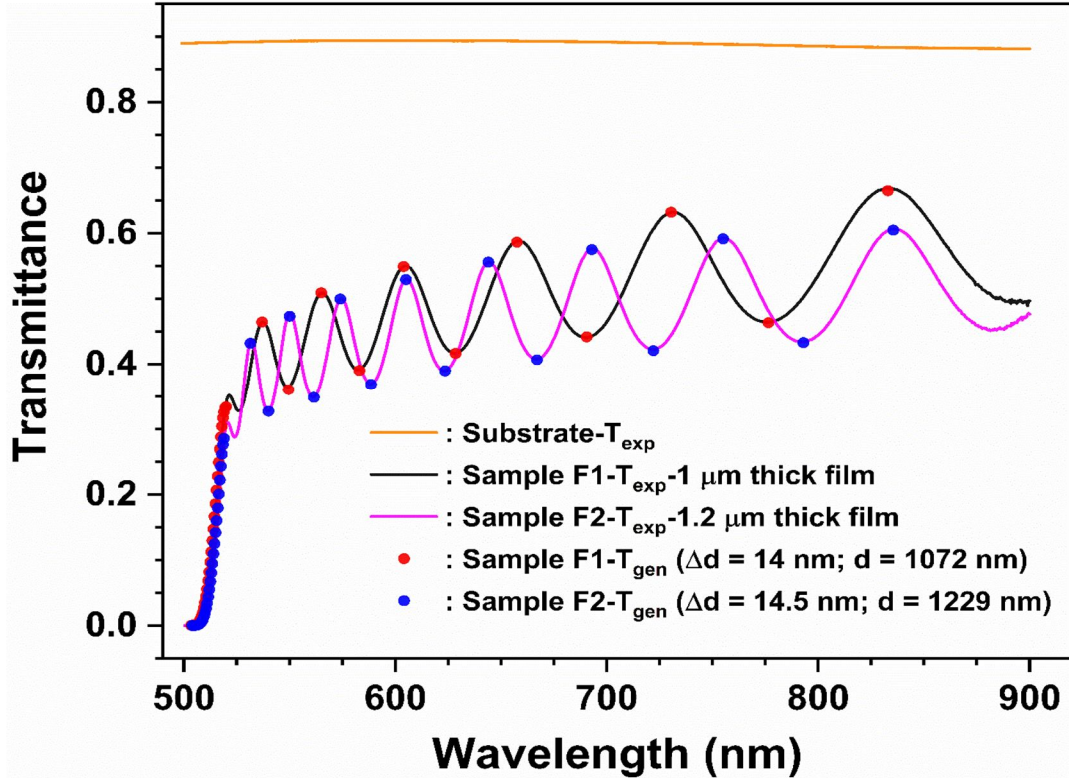


FIG. 6. A plot showing the coincidence of measured transmittance spectra (solid curves) for samples F1 ( $\bar{d} = 1072$  nm) and F2 ( $\bar{d} = 1229$  nm) and their re-generated (simulated) transmission curves and maxima/minima points (solid circles) by integrating numerically Eq. (2) using the attained improved values of their optical constants, their average thicknesses and substrate refractive index  $n_s$  over the whole studied wavelength range.

### Spectral Dispersion of Refractive Index of Flash-evaporated PbI<sub>2</sub> Films

Fig. 7 illustrates the spectral dispersion of the refractive index  $n(\lambda)$  of 1.2  $\mu\text{m}$  thick undoped flash-evaporated PbI<sub>2</sub> film of sample F2 as a function of  $\lambda$  of the light incident on film surface. The plot includes  $n(\lambda_{\text{tang}}) - \lambda_{\text{tang}}$  values determined by the extended analytical EM using constructed maxima and minima envelope curves in weak and medium absorption regions and extrapolated  $n(\lambda)$  values in the strong absorption region using a fit of a 4-constant Cauchy relation to the finally-improved  $n(\lambda_{\text{tang}}) - \lambda_{\text{tang}}$  data. Similar results were found for the 1  $\mu\text{m}$  thick PbI<sub>2</sub> film of sample F1. The inset to Fig. 7 illustrates the validity wavelength range of the Wemple-DiDomenico (WDD) relation that describes the dielectric behavior of a forced-damped single harmonic oscillator [61] above the fundamental absorption edge of the material that is expressed in the following form:

$$[n(\lambda)]^2 = 1 + \frac{E_0 E_d}{E_0^2 - E^2} \quad (11)$$

The oscillator energy  $E_0$  is a measure of the ‘average’ bandgap energy that is reported to scale with the Tauc bandgap energy  $E_g^{\text{opt}}$  or the direct bandgap energy  $E_g$  of the material as  $E_0 = C E_g^{\text{opt}}$ , where  $C$  is a constant having values in the range 1.5 – 2, depending on the type of material. The oscillator strength  $E_d$  is a dispersion energy that is a measure of the average strength of interband optical transition.

Using the obtained fit value of  $E_0 = 3.75$  eV, one can obtain  $E_g^{\text{opt}} = 2.3$  eV for  $C = 1.6$ . The value of  $E_d$  determined from the fit of WDD formula to the data chosen in the inset of Fig. 7 was almost near 20.2 eV. These results are in good agreement with the literature findings of other studies on similar flash-evaporated films whose transmission curves were analyzed using rigorous conventional curve-fitting programs [31].

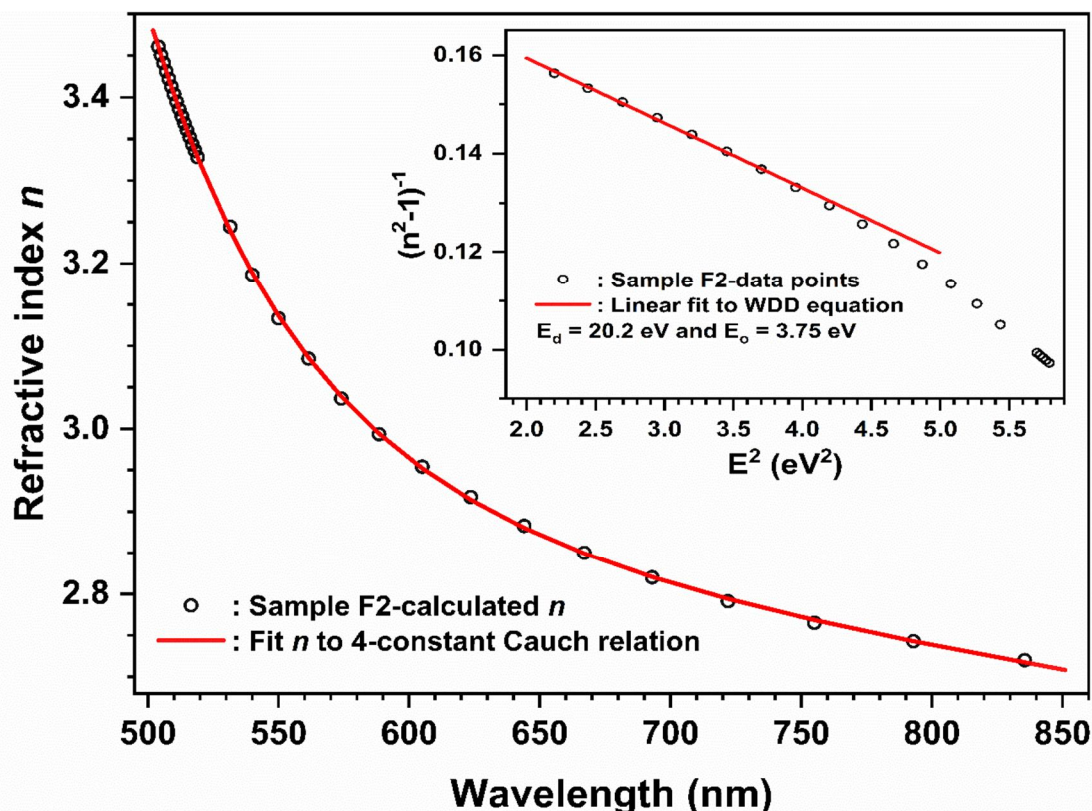


FIG. 7. Spectral dispersion of refractive index  $n(\lambda)$  of the 1.2  $\mu\text{m}$  thick flash-evaporated PbI<sub>2</sub> film of sample F2 over the entire weak, medium and strong optical absorption regions. Details of determining  $n(\lambda) - \lambda$  data are given in text. Solid curves are curve-fits of  $n(\lambda_{\text{tang}}) - \lambda_{\text{tang}}$  data to a 4-constant Cauchy relation. The inset is a fit for the WDD relation.

### Determination of Interband Transition Bandgap Energy of Flash-evaporated $\text{PbI}_2$ Films

The variation of absorption coefficient  $\alpha(\lambda)$  with photon energy of the light incident on a film specimen below its fundamental absorption edge can be described by simplified expressions that exemplify band-to-band (interband) electronic transitions as given below:

$$\alpha(h\nu) = B \frac{(h\nu - E_g)^m}{h\nu} \quad (12)$$

The constant  $B$  is characteristic of the material, related to the extent of band tailing into the bandgap,  $E_g$  defines the optical bandgap energy  $E_{g0}$  in case of defect-free, perfectly crystalline semiconductors/dielectrics or the Tauc (optical) bandgap energy  $E_g^{\text{opt}}$  in case of non-crystalline (amorphous) semiconducting

materials with disorder that causes broadening of the absorption tail. The numeral exponent  $m$  has a variety of values, which depend on the nature of interband optical transition [23, 24, 30, 56-63]. For allowed direct interband transitions,  $m = 1/2$ , while for Tauc model  $m = 2$ , which can closely be assigned to allowed indirect phonon-assisted interband transitions.

Fig. 8 illustrates the variation of  $\alpha(\lambda)$  of the 1  $\mu\text{m}$  and 1.2  $\mu\text{m}$  thick crystalline, stoichiometric flash-evaporated  $\text{PbI}_2$  films of samples F1 and F2 with the photon energy of monochromatic light incident onto them on the basis of interband transition model with  $m = 1/2$ . The fits are virtuous in the strong absorption region and yield a bandgap energy  $E_{g0} \approx 2.43 \text{ eV}$  ( $< 3\%$ ) for their films, in good agreement with the results of other studies on similar flash-evaporated  $\text{PbI}_2$  films [31].

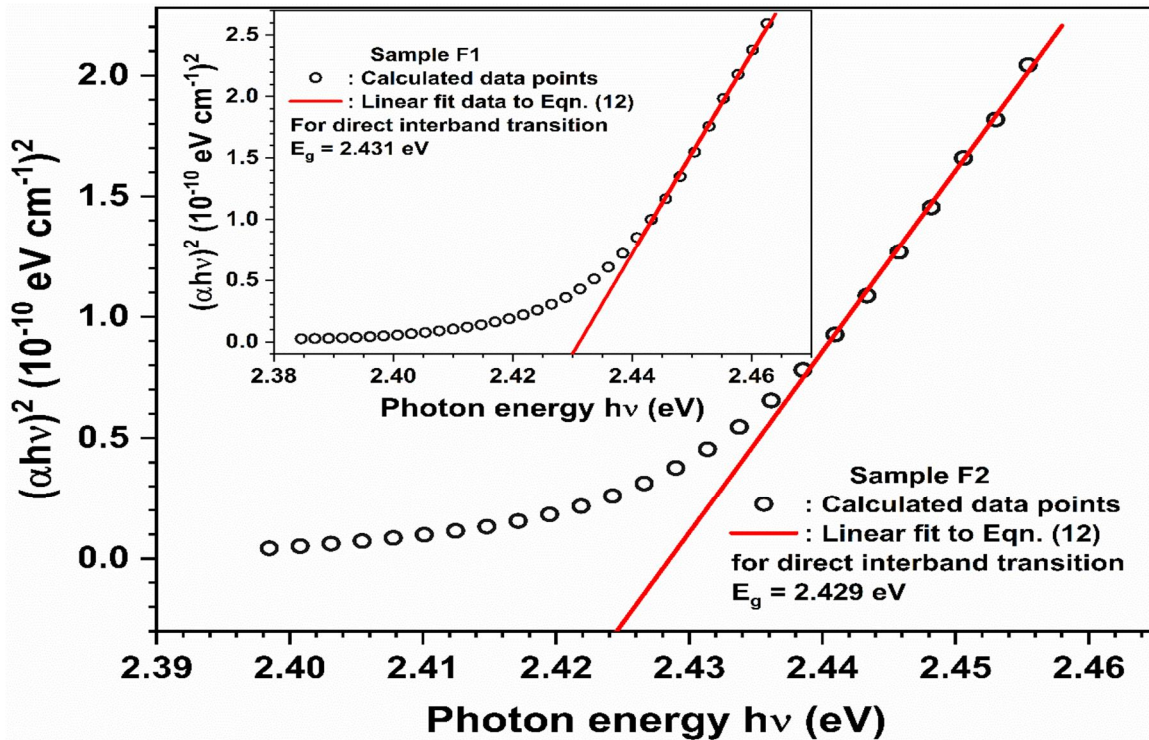


FIG. 8. Variation of absorption coefficient  $\alpha(h\nu)$  of the 1  $\mu\text{m}$  and 1.2  $\mu\text{m}$  thick crystalline, stoichiometric flash-evaporated  $\text{PbI}_2$  films of samples F1 and F2 with photon energy ( $h\nu$ ) of light incident onto them in the strong absorption region below the respective fundamental absorption edge. Data is represented by open circles and fits of the linear portions of the  $(\alpha h\nu)^2$ -Vs-  $h\nu$  plots were fitted to Eq. (12) and gave a bandgap energy  $E_{g0} \approx 2.43 \text{ eV}$  for both films.

### Conclusions

Normal-incidence transmission-wavelength ( $T_{\text{exp}}(\lambda) - \lambda$ ) spectra of 1  $\mu\text{m}$  and 1.2  $\mu\text{m}$  thick flash-evaporated lead iodide ( $\text{PbI}_2$ ) films

deposited on 1.1 mm thick glass slides held at 200  $^\circ\text{C}$  display well-spaced several interference-fringe maxima and minima in the  $\lambda$ -range 520-900 nm. No transparent region exists at the high  $\lambda$ -side, where the maxima are well below the

normal-incidence transmittance  $T_s$  of the glass-slides used as substrates for such films. Below 520 nm, the  $T_{\text{exp}}(\lambda) - \lambda$  curves decline sharply to zero transmission values (at  $\lambda \approx 505$  nm) with no significant band-tailing effects, indicating stoichiometric, crystalline-like  $\text{PbI}_2$  film absorption. The McClain ENVELOPE algorithm was exploited, with few minor modifications, to construct the maxima  $T_M(\lambda_{\text{max}}/\lambda_{\text{min}})$  and minima  $T_m(\lambda_{\text{min}}/\lambda_{\text{max}})$  envelope curves from respective  $T_{\text{exp}}(\lambda) - \lambda$  spectra of studied films.

No corrections of the measured ( $\text{PbI}_2$  film/substrate) transmittance data for substrate absorption and for spectrometer slit-width effect were made, as they were found to be negligible over the studied  $\lambda$ -range. The observed low transmittance of ( $\text{PbI}_2$  film/substrate) system and drastic depression of interference-fringe maxima far below  $T_s$  has been related to  $\text{PbI}_2$  film thickness non-uniformity ( $\Delta d$ ), which causes shrinkage of both maxima and minima, as well as to film optical absorption that reduces both maxima and minima. Thus, application of conventional Swanepoel envelope method (EM) of non-uniform films cannot be used as described by Swanepoel [39], but its extended version suggested by Richards et al. [42, 43] has been adopted.

In the latter optical analysis, values of thickness non-uniformity  $\Delta d$  was varied, in addition to implementing the improvement procedures utilized for determining optical constants of the film under study till a good

match between the re-generated (simulated) and measured transmission curves was obtained. Excellent results were achieved from the application of such optical analysis method, which yields plausible values for the average thickness  $\bar{d}$  of studied flash-evaporated  $\text{PbI}_2$  films, besides their refractive index  $n(\lambda)$  and absorption coefficient  $\alpha(\lambda)$  in weak, medium and strong absorption regions. The energy-dependence of  $\alpha(\lambda)$  is discussed in view of interband electronic transition models and it was found that the direct interband electronic transition model described by Eq. (12) with  $m = 1/2$  represents well the variation of  $\alpha(h\nu)$  with the photon energy  $h\nu$ . The value of respective bandgap energy  $E_{g0} \approx 2.43$  eV indicates that the produced flash-evaporated  $\text{PbI}_2$  films are stoichiometric with 2H-type hexagonal crystallinity, in good agreement with the findings of other studies on similar  $\text{PbI}_2$  films the transmission curves of which were analyzed by different means [31].

## Acknowledgments

Mousa M. Abdul-Gader Jafar acknowledges The University of Jordan (Amman, Jordan) for offering him the sabbatical leave of absence for the year 2019-2020, during which this manuscript has been completed.

## Compliance with ethical standards

**Conflict of interest** The authors declare that they have no conflict of interest.

## References

- [1] Moy, J.P., Nucl. Instrum. Meth. A, 442 (2000) 26.
- [2] Bennet, P.R., Shah, K.S., Dmitriev, Y., Klugerman, M., Gupta, T., Squillante, M., Street, R., Partian, L., Zantai, G. and Pavlyuchkova, R., Nucl. Instrum. Methods A, 505 (2003) 259.
- [3] Zhu, X.H., Wei, Z.R., Jin, Y.R. and Xiang, A.P., Cryst. Res. Tech., 42 (2007) 456.
- [4] Green, M.A., Ho-Baillie, A. and Snaith, H.J., Nature Photonics, 8 (2014) 506.
- [5] Stranks, S.D. and Snaith, H.J., Nature Nanotechnology, 10 (2015) 391.
- [6] Wang, H. and Kim, D.H., Chem. Soc. Rev., 46 (2017) 5204.
- [7] Unagami, T., J. Electrochem. Soc., 146 (1999) 3110.
- [8] Almalaji, B.R., M.Sc. Thesis, The University of Jordan, (2014), Jordan.
- [9] Ghosh, T., Bandyopadhyay, S., Roy, K.K., Kar, S., Lahiri, A.K., Maiti, A.K. and Goswami, K., Cryst. Res. Technol., 43 (2008) 959.
- [10] Caldeira Filho, A.M. and Mulato, M., Nucl. Instrum. Meth. A, 636 (2011) 82.
- [11] Shkir, M., Abbas, H. and Khan, Z.R., Journal of Physics and Chemistry of Solids, 73 (2012) 1309.
- [12] Condeles, J.F. and Mulato, M., J. Mater. Sci., 46 (2011) 1462.

- [13] Condeles, J.F. and Mulato, M., *J. Phys. Chem. Solids*, 89 (2016) 39.
- [14] Veissid, N., An, C.Y., Ferreira da Silva, A. and Pinto de Souza, J.I., *Mater. Res.*, 2 (1999) 279.
- [15] Ahuja, R., Arwin, H., Ferreira, A., Persson, C., Osorio-Guillen, J.M., Souza de Almeida, J., Moyses Araujo, C., Veje, E., Veissid, N., An, C.Y., Pepe, I. and Johansson, B., *Journal of Applied Physics*, 92 (2002) 7219.
- [16] Matuchova, M., Zdansky, K., Zavadil, J., Tonn, J., Jafar, M.M.A-G., Danilewsky, A.N., Cröll, A. and Maixner, J., *Journal of Crystal Growth*, 312 (2010) 1233.
- [17] Al-Daraghme, T.M., Saleh, M.H., Ahmad, M.J.A., Bulos, B.N., Shehadeh, K.M. and Jafar, M.M.A-G., *Journal of Electronic Materials*, 47 (2018) 1806.
- [18] Saleh, M.H., PhD Thesis, The University of Jordan, Amman, (2011), Jordan.
- [19] Acuña, D., Krishnan, B., Shaji, S., Sepúlveda, S. and Menchaca, J.L., *Bull. Mater. Sci.*, 39 (2016) 1453.
- [20] Kariper, I.A., *Opt. Rev.*, 23 (2016) 401.
- [21] AbuEid, M.A., M.Sc. Thesis, The University of Jordan, Amman, (2018) Jordan.
- [22] Ward, L., "The optical constants of bulk materials and films", 2<sup>nd</sup> Ed., (Institute of Physics Publishing, Bristol, UK, 1994).
- [23] Born, M. and Wolf, E., "Principles of Optics: Electromagnetic Theory of Propagation, Interference and Diffraction of Light", (Cambridge University Press, Cambridge, 2002).
- [24] Dragoman, D. and Dragoman, M., "Optical Characterization of Solids", (Springer-Verlag, Berlin, 2002).
- [25] Stenzel, O., "The physics of thin-film optical spectra: An introduction", (Springer, Berlin, 2005).
- [26] Chambouleyron, I. and Martínez, J.M., "Optical properties of dielectric and semiconducting thin films; in: Handbook of Thin-film Materials", Ed. Nalwa, H.S., (Academic Press, San Diego, USA, 2001), pp. 593-622.
- [27] Jafar, M.M.A-G., *European Int. J. Sci. Technol.*, 2 (2013) 274.
- [28] Kasap, S.O., Tan, W.C., Jai Singh, A. and Ray, K., "Fundamental Optical Properties of Materials I; in: Optical Properties of Materials and Their Applications", 2<sup>nd</sup> Ed., Ed. Jai Singh, (John Wiley & Sons, Ltd., Chichester, West Sussex, 2020), pp. 1-66.
- [29] Poelman, D. and Smet, P.F., *J. Phys. D: Appl. Phys.*, 36 (2003) 1850.
- [30] Saleh, M.H., Jafar, M.M.A-G., Bulos, B.N. and Al-Daraghme, T.M.F., *Appl. Phys. Res.*, 6 (2014) 10.
- [31] Jafar, M.M.A-G., Saleh, M.H., Al-Daraghme, T.M., Ahmad, M.J.A., AbuEid, M.A., Ershaidat, N.M. and Bulos, B.N., *Appl. Phys. A*, 125 (2019) 672.
- [32] Ventura, S.D., Birgin, E.G., Martínez, J.M. and Chambouleyron, I., *J. Appl. Phys.*, 97 (2005) 043512.
- [33] Andrade, R., Birgin, E.G., Chambouleyron, I., Martínez, J.M. and Ventura, S.D., *Appl. Optics*, 47 (2008) 5208.
- [34] Mulato, M., Chambouleyron, I., Birgin, E.G. and Martínez, J.M., *Appl. Phys. Lett.*, 77 (2000) 2133.
- [35] Jafar M.M.A-G., Saleh, M.H., Ahmed, M.J.A., Bulos, B.N. and Al-Daraghme, T.M., *J. Mater. Sci: Mater. Electron.*, 27 (2016) 3281.
- [36] Swanepoel, R., *J. Phys. E: Sci. Instrum.*, 16 (1983) 1214.
- [37] Saleh, M.H., Ershaidat, N.M., Ahmad, M.J.A., Bulos, B.N. and Jafar, M.M.A-G., *Opt. Rev.*, 24 (2017) 260.
- [38] González-Leal, J.M., Prieto-Alcon, R., Angel, J-A., Minkov, D.A. and Márquez, E., *Appl. Optics*, 41 (2002) 7300.
- [39] Swanepoel, R., *J. Phys. E: Sci. Instrum.*, 17 (1984) 896.
- [40] Ramírez-Malo, J.B., Corrales, R., Márquez, E., Reyes, J. and Fernández-Peña, J.P., *Mater. Chem. Phys.*, 40 (1995) 30.
- [41] Nagels, P., Sleenckx, E., Callaerts, R., Márquez, E., González, J.M. and Bernal-Oliva, A.M., *Solid State Communications*, 102 (1997) 539.

- [42] Richards, B.S., MEngSci. Thesis, University of New South Wales, New South Wales, (1998), Australia.
- [43] Richards, B.S., Lambertz, A. and Sproul, A.B., *Thin Solid Films*, 460 (2004) 247.
- [44] Márquez, E., Bernal-Oliva, A.M., González-Leal, J.M., Prieto-Alcón, R., Ledesma, A., Jiménez-Garay, R. and Mártil, T., *Mater. Chem. Phys.*, 60 (1999) 231.
- [45] Márquez, E., Ramírez-Malo, J.B., Villares, P., Jiménez-Garay, R. and Swanepoel, R., *Thin Solid Films*, 254 (1995) 83.
- [46] Bennouna, A., Laaziz, Y. and Idrissi, M.A., *Thin Solid Films*, 213 (1992) 55.
- [47] Bah, K., Czapla, A. and Pisarkiewicz, T., *Thin Solid Films*, 232 (1993) 18.
- [48] Minkov, D.A., Gavrilov, G.M., Moreno, J.M.D., Vazquez, C.G. and Marquez, E., *Meas. Sci. Technol.*, 28 (2017) 035202.
- [49] Minkov, D.A., Gavrilov, G.M., Angelov, G.V., Moreno, J.M.D., Vazquez, C.G., Ruano, S.M.F. and Marquez, E., *Thin Solid Films*, 645 (2018) 370.
- [50] Minkov, D.A., Gavrilov, G.M., Marquez, E., Ruano, S.M.F. and Stoyanova, A.V., *Optik*, 132 (2017) 320.
- [51] Ruíz-Pérez, J.J., González-Leal, J.M., Minkov, D.A. and Márquez, E., *J. Phys. D: Appl. Phys.*, 34 (2001) 2489.
- [52] Qasem, A., Shaaban, E.R., Hassan, M.Y., Moustafa, M.G. and Hammam, M.A.S., *J. Electron. Mater.*, 49 (2020) 5750.
- [53] Shaaban, E.R., *Philosophical Magazine*, 88 (2008) 781.
- [54] Marquez, E., Ramirez-Malo, J.B., Fernandez-Pena, J., Jimenez-Garay, R., Ewen, P.J.S. and Owen, A.E., *Opt. Mater.*, 2 (1993) 143.
- [55] McClain, M., Feldman, A., Kahaner, D. and Ying, X., *Comput. Phys.*, 5 (1991) 45.
- [56] O'Leary, S.K., Johnson, S.R. and Lim, P.K., *J. Appl. Phys.*, 82 (1997) 3334.
- [57] Studenyak, I., Kranjčec, M. and Kurik, M., *Inter. J. Optics Appl.*, 4 (2014) 76.
- [58] Jellison, G.E. and Modine, F.A., *App. Phys. Lett.*, 69 (1996) 371.
- [59] Forouhi, A.R. and Bloomer, I., *Phys. Rev. B*, 34 (1986) 7018.
- [60] Forouhi, A.R. and Bloomer, I., *Phys. Rev. B*, 38 (1988) 1865.
- [61] Wemple, S.H. and DiDomenico, S., *Phys. Rev. B*, 3 (1971) 1338.
- [62] Tauc, J., "Optical Properties of Amorphous Semiconductors; In: *Amorphous and Liquid Semiconductors*", Ed. Tauc, J., (Plenum Press, London, New York, 1974), pp. 159-220.
- [63] Zanatta, A.R., *Scientific Reports* 9 (2019) 11125: 1-12.

**المراجع:** يجب طباعة المراجع بأسطر مزدوجة ومرقمة حسب تسلسلها في النص. وتكتب المراجع في النص بين قوسين مربعين. ويتم اعتماد اختصارات الدوريات حسب نظام Wordlist of Scientific Reviewers.

**الجدول:** تعطى الجداول أرقاماً متسلسلة يشار إليها في النص. ويجب طباعة كل جدول على صفحة منفصلة مع عنوان فوق الجدول. أما الحواشي التفسيرية، التي يشار إليها بحرف فوقي، فتكتب أسفل الجدول.

**الرسوم التوضيحية:** يتم ترقيم الأشكال والرسومات والرسومات البيانية (المخططات) والصور، بصورة متسلسلة كما وردت في النص.

تقبل الرسوم التوضيحية المستخرجة من الحاسوب والصور الرقمية ذات النوعية الجيدة بالأبيض والأسود، على أن تكون أصيلة وليست نسخة عنها، وكل منها على ورقة منفصلة ومعرفة برقمها بالمقابل. ويجب تزويد المجلة بالرسومات بحجمها الأصلي بحيث لا تحتاج إلى معالجة لاحقة، وألا تقل الحروف عن الحجم 8 من نوع Times New Roman، وألا تقل سماكة الخطوط عن 0.5 وكتافة متجانسة. ويجب إزالة جميع الألوان من الرسومات ما عدا تلك التي ستنتشر ملونة. وفي حالة إرسال الرسومات بصورة رقمية، يجب أن تتوافق مع متطلبات الحد الأدنى من التمايز (1200 dpi Resolution) لرسومات الأبيض والأسود الخطية، و 600 dpi للرسومات باللون الرمادي، و 300 dpi للرسومات الملونة. ويجب تخزين جميع ملفات الرسومات على شكل (jpg)، وأن ترسل الرسوم التوضيحية بالحجم الفعلي الذي سيظهر في المجلة. وسواء أرسل المخطوط بالبريد أو عن طريق الشبكة (Online)، يجب إرسال نسخة ورقية أصلية ذات نوعية جيدة للرسومات التوضيحية.

**مواد إضافية:** تشجع المجلة الباحثين على إرفاق جميع المواد الإضافية التي يمكن أن تسهل عملية التحكيم. وتشمل المواد الإضافية أي اشتقاقات رياضية مفصلة لا تظهر في المخطوط.

**المخطوط المنقح (المعدل) والأقراص المدمجة:** بعد قبول البحث للنشر وإجراء جميع التعديلات المطلوبة، فعلى الباحثين تقديم نسخة أصلية ونسخة أخرى مطابقة للأصلية مطبوعة بأسطر مزدوجة، وكذلك تقديم نسخة إلكترونية تحتوي على المخطوط كاملاً مكتوباً على Microsoft Word for Windows 2000 أو ما هو استجد منه. ويجب إرفاق الأشكال الأصلية مع المخطوط النهائي المعدل حتى لو تم تقديم الأشكال إلكترونياً. وتخزن جميع ملفات الرسومات على شكل (jpg)، وتقدم جميع الرسومات التوضيحية بالحجم الحقيقي الذي ستظهر به في المجلة. ويجب إرفاق قائمة ببرامج الحاسوب التي استعملت في كتابة النص، وأسماء الملفات على قرص مدمج، حيث يعلم القرص بالاسم الأخير للباحث، وبالرقم المرجعي للمخطوط للمراسلة، وعنوان المقالة، والتاريخ. ويحفظ في مغلف واقٍ.

### حقوق الطبع

يُشكّل تقديم مخطوط البحث للمجلة اعترافاً صريحاً من الباحثين بأن مخطوط البحث لم يُنشر ولم يُقدّم للنشر لدى أي جهة أخرى كانت وبأي صيغة ورقية أو إلكترونية أو غيرها. ويشتترط على الباحثين ملء نموذج ينصّ على نقل حقوق الطبع لتصبح ملكاً لجامعة اليرموك قبل الموافقة على نشر المخطوط. ويقوم رئيس التحرير بتزويد الباحثين بإنموذج نقل حقوق الطبع مع النسخة المُرسلة للتتقيح. كما ويمنع إعادة إنتاج أي جزء من الأعمال المنشورة في المجلة من دون إذن خطّي مُسبق من رئيس التحرير.

### إخلاء المسؤولية

إن ما ورد في هذه المجلة يعبر عن آراء المؤلفين، ولا يعكس بالضرورة آراء هيئة التحرير أو الجامعة أو سياسة اللجنة العليا للبحث العلمي أو وزارة التعليم العالي والبحث العلمي. ولا يتحمل ناشر المجلة أي تبعات مادية أو معنوية أو مسؤوليات عن استعمال المعلومات المنشورة في المجلة أو سوء استعمالها.

**الفهرسة:** المجلة مفهرسة في:



المجلة الأردنية للفيزياء هي مجلة بحوث علمية عالمية متخصصة مُحكمة تصدر بدعم من صندوق دعم البحث العلمي، وزارة التعليم العالي والبحث العلمي، عمان، الأردن. وتقوم بنشر المجلة عمادة البحث العلمي والدراسات العليا في جامعة اليرموك، إربد، الأردن. وتنتشر البحوث العلمية الأصيلة، إضافة إلى المراسلات القصيرة Short Communications، والملاحظات الفنية Technical Notes، والمقالات الخاصة Feature Articles، ومقالات المراجعة Review Articles، في مجالات الفيزياء النظرية والتجريبية، باللغتين العربية والإنجليزية.

#### تقديم مخطوط البحث

تقدم البحوث عن طريق إرسالها إلى البريد الإلكتروني : [jjp@yu.edu.jo](mailto:jjp@yu.edu.jo)

تقديم المخطوطات إلكترونياً: اتبع التعليمات في موقع المجلة على الشبكة العنكبوتية.

ويجري تحكيم البحوث الأصيلة والمراسلات القصيرة والملاحظات الفنية من جانب مُحكمين اثنين في الأقل من ذوي الاختصاص والخبرة. وتُشجّع المجلة الباحثين على اقتراح أسماء المحكمين. أما نشر المقالات الخاصة في المجالات الفيزيائية النشطة، فيتم بدعوة من هيئة التحرير، ويُشار إليها كذلك عند النشر. ويُطلب من كاتب المقال الخاص تقديم تقرير واضح يتسم بالدقة والإيجاز عن مجال البحث تمهيداً للمقال. وتنتشر المجلة أيضاً مقالات المراجعة في الحقول الفيزيائية النشطة سريعة التغير، وتشجّع كاتبي مقالات المراجعة أو مُستكثبيها على إرسال مقترح من صفحتين إلى رئيس التحرير. ويُرفق مع البحث المكتوب باللغة العربية ملخص (Abstract) وكلمات دالة (Keywords) باللغة الإنجليزية.

#### ترتيب مخطوط البحث

يجب أن تتم طباعة مخطوط البحث ببنت 12 نوعه Times New Roman، وبسطر مزدوج، على وجه واحد من ورق A4 (21.6 × 27.9 سم) مع حواشي 3.71 سم، باستخدام معالج كلمات ميكروسوفت وورد 2000 أو ما استُجد منه. ويجري تنظيم أجزاء المخطوط وفق الترتيب التالي: صفحة العنوان، الملخص، رموز التصنيف (PACS)، المقدمة، طرق البحث، النتائج، المناقشة، الخلاصة، الشكر والعرفان، المراجع، الجداول، قائمة بدليل الأشكال والصور والإيضاحات، ثم الأشكال والصور والإيضاحات. وتُكتب العناوين الرئيسة بخط غامق، بينما تُكتب العناوين الفرعية بخط مائل.

**صفحة العنوان:** وتشمل عنوان المقالة، أسماء الباحثين الكاملة وعناوين العمل كاملة. ويكتب الباحث المسؤول عن المراسلات اسمه مشاراً إليه بنجمة، والبريد الإلكتروني الخاص به. ويجب أن يكون عنوان المقالة موجزاً وواضحاً ومعبراً عن فحوى (محتوى) المخطوط، وذلك لأهمية هذا العنوان لأغراض استرجاع المعلومات.

**الملخص:** المطلوب كتابة فقرة واحدة لا تزيد على مائتي كلمة، موضحة هدف البحث، والمنهج المتبع فيه والنتائج وأهم ما توصل إليه الباحثون.

**الكلمات الدالة:** يجب أن يلي الملخص قائمة من 4-6 كلمات دالة تعبر عن المحتوى الدقيق للمخطوط لأغراض الفهرسة.

**PACS:** يجب إرفاق الرموز التصنيفية، وهي متوفرة في الموقع <http://www.aip.org/pacs/pacs06/pacs06-toc.html>.

**المقدمة:** يجب أن توضّح الهدف من الدراسة وعلاقتها بالأعمال السابقة في المجال، لا أن تكون مراجعة مكثفة لما نشر (لا تزيد المقدمة عن صفحة ونصف الصفحة مطبوعة).

**طرائق البحث (التجريبية / النظرية):** يجب أن تكون هذه الطرائق موضحة بتفصيل كاف لإتاحة إعادة إجرائها بكفاءة. ولكن باختصار مناسب، حتى لا تكون تكراراً للطرائق المنشورة سابقاً.

**النتائج:** يستحسن عرض النتائج على صورة جداول وأشكال حيثما أمكن، مع شرح قليل في النص ومن دون مناقشة تفصيلية.

**المناقشة:** يجب أن تكون موجزة وتركز على تفسير النتائج.

**الاستنتاج:** يجب أن يكون وصفاً موجزاً لأهم ما توصلت إليه الدراسة ولا يزيد عن صفحة مطبوعة واحدة.

**الشكر والعرفان:** الشكر والإشارة إلى مصدر المنح والدعم المالي يكتبان في فقرة واحدة تسبق المراجع مباشرة.



Jordan Journal of

**PHYSICS**An International Peer-Reviewed Research Journal issued by the  
Support of the Scientific Research Support Fund

Published by the Deanship of Research &amp; Graduate Studies, Yarmouk University, Irbid, Jordan

Name: ..... الأسم:  
 Specialty:..... التخصص:  
 Address: ..... العنوان:  
 P.O. Box:..... صندوق البريد:  
 City & Postal Code: ..... المدينة/الرمز البريدي:  
 Country: ..... الدولة:  
 Phone: ..... رقم الهاتف:  
 Fax No:..... رقم الفاكس:  
 E-mail:..... البريد الإلكتروني:  
 No. of Subscription: ..... عدد الاشتراكات:  
 Method of Payment:..... طريقة الدفع:  
 Amount Enclosed:..... المبلغ المرفق:  
 Signature: ..... التوقيع:

Cheques should be paid to Deanship of Research and Graduate Studies - Yarmouk University.

I would like to subscribe to the Journal  
For

- One Year  
 Two Years  
 Three Years

**One Year Subscription Rates**

	Inside Jordan	Outside Jordan
Individuals	JD 8	€ 40
Students	JD 4	€ 20
Institutions	JD 12	€ 60

**Correspondence****Subscriptions and Sales:**

**Prof. Ibrahim O. Abu Al-Jarayesh**  
 Deanship of Research and Graduate Studies  
 Yarmouk University  
 Irbid – Jordan  
**Telephone:** 00 962 2 711111 Ext. 2075  
**Fax No.:** 00 962 2 721121



المجلة الأردنية

# للفيزياء

مجلة بحوث علمية عالية متخصصة محكمة  
تصدر بدعم من صندوق دعم البحث العلمي

المجلة الأردنية  
**للفيزياء**  
مجلة بحوث علمية عالمية محكمة

المجلد (14)، العدد (4)، كانون الأول 2021م / جمادى الأولى 1443هـ

المجلة الأردنية للفيزياء: مجلة علمية عالمية متخصصة محكمة تصدر بدعم من صندوق دعم البحث العلمي، عمان، الأردن، وتصدر عن عمادة البحث العلمي والدراسات العليا، جامعة اليرموك، إربد، الأردن.

رئيس التحرير:

ابراهيم عثمان أبو الجرايش

قسم الفيزياء، جامعة اليرموك، إربد، الأردن.  
[ijaraysh@yu.edu.jo](mailto:ijaraysh@yu.edu.jo)

هيئة التحرير:

نبيل يوسف أيوب

رئيس الجامعة الأمريكية في مادبا، مادبا، الأردن.  
[nabil.ayoub@gju.edu.jo](mailto:nabil.ayoub@gju.edu.jo)

طارق فتحي حسين

قسم الفيزياء، الجامعة الأردنية، عمان، الأردن.  
[t.hussein@ju.edu.jo](mailto:t.hussein@ju.edu.jo)

مروان سليمان موسى

قسم الفيزياء، جامعة مؤتة، الكرك، الأردن.  
[mmousa@mutah.edu.jo](mailto:mmousa@mutah.edu.jo)

محمد خالد الصغير

قسم الفيزياء، الجامعة الهاشمية، الزرقاء، الأردن.  
[msugh@hu.edu.jo](mailto:msugh@hu.edu.jo)

عبد المجيد الياسين

قسم الفيزياء، جامعة اليرموك، إربد، الأردن.  
[alyassin@yu.edu.jo](mailto:alyassin@yu.edu.jo)

محمد العمري

قسم الفيزياء، جامعة العلوم والتكنولوجيا، إربد، الأردن.  
[alakmoh@just.edu.jo](mailto:alakmoh@just.edu.jo)

إبراهيم البصول

قسم الفيزياء، جامعة آل البيت، المفرق، الأردن.  
[Ibrahimbsoul@yahoo.com](mailto:Ibrahimbsoul@yahoo.com)

سكرتير التحرير: مجدي الشناق

ترسل البحوث إلى العنوان التالي:

الأستاذ الدكتور إبراهيم عثمان أبو الجرايش  
رئيس تحرير المجلة الأردنية للفيزياء  
عمادة البحث العلمي والدراسات العليا، جامعة اليرموك  
إربد، الأردن

هاتف 00 962 2 7211111 فرعي 2075

E-mail: [jpp@yu.edu.jo](mailto:jpp@yu.edu.jo) Website: <http://Journals.yu.edu.jo/jpp>

